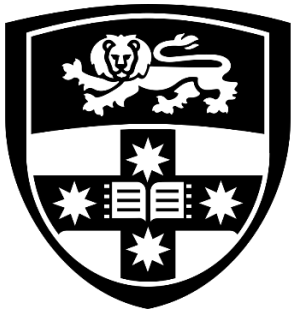

THE UNIVERSITY OF SYDNEY

Engineering efficient and sustainable catalysts for hydrogen production through (photo)electrochemical water splitting

Xuan Minh Chau Ta

A thesis submitted in fulfilment of the requirements for the degree of

Doctor of Philosophy

School of Biomedical Engineering

Faculty of Engineering

The University of Sydney

2024

Authorship attribution statement

- This thesis contains published material in: *Xuan Minh Chau Ta, Thành Trần-Phú, Thi Kim Anh Nguyen, Manjunath Chatti, Rahman Daiyan; Engineering oxygen-evolving catalysts for acidic water electrolysis. Appl. Phys. Rev. 1 June 2024; 11 (2): 021321. 10.1063/5.0200438*. This publication forms a part of "**chapter 2 Acidic oxygen evolution reaction electrocatalyst**". I wrote, formatted, and prepared the draft and manuscript.
- This thesis contains published material in: *Ta, X. M. C., Daiyan, R., Nguyen, T. K. A., Amal, R., Tran-Phu, T., Tricoli, A., Alternatives to Water Photooxidation for Photoelectrochemical Solar Energy Conversion and Green H_2 Production. Adv. Energy Mater. 2022, 12, 2201358. 10.1002/aenm.202201358*. This publication forms a part of "**chapter 3 Photoelectrochemical water splitting**". I wrote, formatted, and prepared the draft and manuscript.
- This thesis contains published material in: *Ta, X. M. C., Trần-Phú, T., Yuwono, J. A., Nguyen, T. K. A., Bui, A. D., Truong, T. N., Chang, L., Magnano, E., Daiyan, R., Simonov, A. N., Tricoli, A., Optimal Coatings of Co_3O_4 Anodes for Acidic Water Electrooxidation. Small 2023, 2304650. 10.1002/smll.202304650***.** This publication forms "**chapter 4 Optimal Coatings of Co_3O_4 Anodes for Acidic Water Electrooxidation**". I performed all the required data analysis. I wrote, formatted, and prepared the draft and manuscript. I designed and performed all the experiments described in "experimental section" of this manuscript with the support of co-authors. (DFT calculation was conducted by co-author with my contribution).
- This thesis contains published material in: *Ta, X. M. C., Trần-Phú, T., Nguyen, T. K. A., Wang, Q., Tricoli, A., Environmental-friendly and earth-abundant self-healing electrocatalyst systems for durable and efficient acidic water splitting. ACS Applied Materials & Interfaces 2025 17 (17), 25327-25336 DOI: 10.1021/acsami.5c01637*. This publication forms "**chapter 5 Environmental-friendly and earth-abundant self-healing electrocatalyst systems for durable and efficient acidic water splitting**". I performed all the required data analysis. I wrote, formatted, and prepared the draft and manuscript. I designed and performed all the experiments described in "experimental section" of this manuscript.
- This thesis contains published material in: *Ta, X. M. C., Nguyen, T. K. A., Bui, A. D., Nguyen, H. T., Daiyan, R., Amal, R., Tran-Phu, T., Tricoli, A., Optimizing Surface Composition and Structure of $FeWO_4$ Photoanodes for Enhanced Water Photooxidation. Adv. Mater. Technol. 2023, 8, 2201760. 10.1002/admt.202201760***.** This publication forms "**chapter 6 Optimizing Surface Composition and Structure of $FeWO_4$ Photoanodes for Enhanced**

Water Photooxidation". I performed all the required data analysis. I wrote, formatted, and prepared the draft and manuscript. I designed and performed all the experiments described in "experimental section" of this manuscript with the support of co-authors.

In addition to the statements above, permission to include the published material has been granted by the supervisor of the project.

Student Name: Xuan Minh Chau Ta

Signature: Date: December 19th, 2024

As supervisor for the candidature upon which this thesis is based, I can confirm that the authorship attribution statements above are correct.

Supervisor Name: Antonio Tricoli Date: December 19th, 2024

Signature:

Statement of originality

This is to certify that to the best of my knowledge; the content of this thesis is my own work. This thesis has not been submitted for any degree or other purposes.

I certify that the intellectual content of this thesis is the product of my own work and that all the assistance received in preparing this thesis and sources have been acknowledged.

Signature
Name: Xuan Minh Chau Ta Date: December 19th, 2024

Acknowledgments

The Ph.D. thesis was studied and conducted in the Nanotechnology Research Laboratory (NRL) at the Faculty of Engineering at the University of Sydney and Australian National University. First and foremost, I would like to express my biggest gratitude to my primary supervisor, Professor Antonio Tricoli, for giving me the opportunity to pursue the doctoral degree under his supervision, continuous support, scientific instruction, and critical feedback. All the collaboration opportunities he gave me with some leading research institutes and companies were useful and beneficial experiences for my research career. I am also deeply thankful to Dr. Thành Trần-Phú, whose mentorship has been one of the most important supports that I have received in my Ph.D. journey. I could not go this far without his guidance, scientific advice, and guidance when I started my experimental work. Besides, I sincerely thank Professor Anita Ho-Baillie, my co-supervisor, for her assistance throughout my work.

I would also like to acknowledge the generous support from the Faculty of Engineering Research Scholarship to provide scholarship covering the tuition fee and living expenses for my PhD time. I am thankful for several organizations that are providing facilities for this research, including the Australian National Fabrication Facility (ANFF) – ACT and NSW nodes, the Sydney Analytical Center, the Centre for Advanced Microscopy (CAM), and the University of New South Wales Analytical Centre. I am deeply grateful to their dedicated staff for their expert guidance and technical assistance.

Besides, I would like to give special thanks to my lab mates: Thi Kim Anh Nguyen, Elena Magnano, Qi Wang, Zahra Lotfibakalani, Dr. Borui Liu, Dr. Siu-Fung Leng, Dr. Nuwan Bandara, for all the inspiring discussion, happy adventures, and your unwavering support made my enjoyable Ph.D. experience. I am also indebted to my co-authors from other research institutes: Dr. Rahman Daiyan, Professor Rose Amal, Professor Alexandr N. Simonov, Dr. Jodie Yuwono, Dr. Anh Dinh Bui, Dr. Thien Truong, Dr. Hieu Nguyen, Li-chun Chang for their professional contribution in my research. I am grateful to everyone at the University of Sydney and the Australian National University, especially to Mrs. Christine Kueh, whose assistance with administrative and logistical challenges significantly facilitated my research progress.

Finally, I want to express my deepest love and gratitude to my wonderful husband, Nguyễn Vũ Linh. Your unconditional love, selfless sacrifices, efforts in managing household responsibilities, and unwavering emotional support have helped me go through this journey. I also would like to thank my homeland family, my father (Tạ Xuân Thùy), my mother (Lê Minh Chánh), my brother and sister-in-law (Tạ Minh Khải and Trương Thị Thiên Lý), who gave me a life, endless love, and belief in me. Even though you may not fully understand the specifics of my work, striving to make you proud and honor your sacrifices has been my greatest motivation in this challenging journey.

Research outcomes

List of publications included in this thesis:

1. **Ta, X. M. C**., Trần-Phú, T., Nguyen, T. K. A., Wang, Q., Tricoli, A., Environmental-friendly and earth-abundant self-healing electrocatalyst systems for durable and efficient acidic water splitting. **ACS Applied Materials & Interfaces** 2025 17 (17), 25327-25336 DOI: 10.1021/acsami.5c01637
2. **Xuan Minh Chau Ta**, Thành Trần-Phú, Thi Kim Anh Nguyen, Manjunath Chatti, Rahman Daiyan; Engineering oxygen-evolving catalysts for acidic water electrolysis. **Appl. Phys. Rev**. 1 June 2024; 11 (2): 021321. 10.1063/5.0200438
3. **Ta, X. M. C**., Trần-Phú, T., Yuwono, J. A., Nguyen, T. K. A., Bui, A. D., Truong, T. N., Chang, L., Magnano, E., Daiyan, R., Simonov, A. N., Tricoli, A., Optimal Coatings of Co_3O_4 Anodes for Acidic Water Electrooxidation. **Small** 2023, 2304650. 10.1002/smll.202304650
4. **Ta, X. M. C.**, Nguyen, T. K. A., Bui, A. D., Nguyen, H. T., Daiyan, R., Amal, R., Tran-Phu, T., Tricoli, A., Optimizing Surface Composition and Structure of $FeWO_4$ Photoanodes for Enhanced Water Photooxidation. **Adv. Mater. Technol**. 2023, 8, 2201760. 10.1002/admt.202201760
5. **Ta, X. M. C**., Daiyan, R., Nguyen, T. K. A., Amal, R., Tran-Phu, T., Tricoli, A., Alternatives to Water Photooxidation for Photoelectrochemical Solar Energy Conversion and Green H_2 Production. **Adv. Energy Mater**. 2022, 12, 2201358. 10.1002/aenm.202201358

Other publications in the Doctoral course:

1. Nguyen, Dang-Thuan, Anh Dinh Bui, Daniel Walter, Khoa Nguyen, Hualin Zhan, **Xuan Minh Chau Ta**, Grace Dansoa Tabi et al. "Universal buried interface modification with lead iodide for efficient and stable perovskite solar cells." **Journal of Materials Chemistry A** (2025) https://doi.org/10.1039/D5TA01282A
2. Britto, J.S.J., Wong, S.L., Patel, V., Tran, T.K.A., Perumalsamy, V., Morey, M., **Ta, X.M.C.**, Tricoli, A., Bahadur, R., Singh, G., Kumar, P. and Vinu, A. (2025), Copper-Loaded Nitrogen-Rich Mesoporous C_3N_6 Based Nanozymes for Calorimetric Detection of Glutathione and Glucose. **Adv. Sensor Res**., 4: 2400149. https://doi.org/10.1002/adsr.202400149
3. Chang, L.-C., Dinh Bui, A., Huang, K., Kremer, F., Brink, F., Wang, W., Haggren, A., Mayon, A.O., **Ta, X.M.C.**, Duan, L., Lem, O.L.C., Hou, Y., Nguyen, D.-T., Tabi, G.D., Zhan, H., Ahmad, V., Duong, T., white, T., Walter, D., Weber, K., Catchpole, K. and Shen, H. (2024), Enhanced

Efficiency and Stability for the Inverted High-Bandgap Perovskite Solar Cell via Bottom Passivation Strategy. **Sol. RRL**, 8: 2400391. https://doi.org/10.1002/solr.202400391

4. N. Panangattu Dharmarajan, M. Fawaz, C. Sathish, S. N. Talapaneni, K. Ramadass, A. M. Sadanandan, **X. M. C. Ta**, M. Huš, V. Perumalsamy, A. Tricoli, B. Likozar, C.-H. Jeon, J.-H. Yang, A. Vinu, Insights into Atomic Level π-Electron Modulations in Supramolecular Carbon Nitride Nano architectonics for Sustainable Green Hydrogen Production. **Adv. Energy Mater**. 2024, 2400686. 10.1002/aenm.202400686
5. T. K. Anh Nguyen, T. Trần-Phú, R. Daiyan, **X. Minh Chau Ta**, R. Amal, A. Tricoli, **Angew. Chem. Int. Ed.** 2024, e202401746. From Plastic Waste to Green Hydrogen and Valuable Chemicals Using Sunlight and Water. https://doi.org/10.1002/anie.202401746
6. T. K. A. Nguyen, T. Trần-Phú, **X. M. C. Ta**, T. N. Truong, J. Leverett, R. Daiyan, R. Amal, A. Tricoli, Understanding Structure-Activity Relationship in Pt-loaded g-C_3N_4 for Efficient Solar-Photoreforming of Polyethylene Terephthalate Plastic and Hydrogen Production. **Small Methods** 2024, 8, 2300427. 10.1002/smtd.202300427
7. Tran-Phu, T., Daiyan, R., **Ta, X. M. C**., Amal, R., Tricoli, A., From Stochastic Self˜-Assembly of Nanoparticles to Nanostructured (Photo)Electrocatalysts for Renewable Power-to-X Applications via Scalable Flame Synthesis. **Adv. Funct. Mater**. 2022, 32, 21100200. 10.1002/adfm.202110020

Publications under preparation/submission:

1. Putri Ramadhany, Thành Trần-Phú, Zhipeng Ma, **Xuan Minh Chau Ta**, Priyank Kumar, Jodie A. Yuwono, Rosalie K. Hocking, Bernt Johannessen, Antonio Tricoli, Alexandr N. Simonov, Rose Amal, and Rahman Daiyan, *Electrochemical reduction of CO_2 and nitrite on tandem Copper Cobalt co-sputtered catalysts for urea synthesis*
2. Navneet Matharoo, Mohammed Fawaz, Nithinraj P. D., **Xuan Minh Chau Ta**, Vibin Perumalsamy, Yuwei Wang, Antonio Tricoli, Prashant Kumar, Ramaswamy Murugavel, Ajayan Vinu, *Two-Dimensional Cobalt Dialkyl Phosphate rectangular grids-Graphitic Carbon Nitride (gC_3N_4) Synergistic Hybrids for Photocatalytic Hydrogen Evolution Reaction*
3. Navneet Matharoo, Mohammed Fawaz, Nithinraj P. D., **Xuan Minh Chau Ta**, Harleen Kaur, Yuwei Wang, Antonio Tricoli, Prashant Kumar, Ramaswamy Murugavel, Ajayan Vinu, *Sulfoxide-functionalized Graphitic Carbon Nitride (SGCN)-Cobalt Dialkyl Phosphate Bipyridine (CDPB) Heterojunction for Photocatalytic Hydrogen Production*
4. Aathira M. Sadanandan, Jae-Hun Yang, Mohammed Fawaz, Ayona K. P Jose, Nithinraj Panangattu Dharmarajan, **Xuan Minh Chau Ta**, Vaishwik Patel, Yuwei Wang, Zhixuan Li,

Gurwinder Singh, Prashant Kumar, Antonio Tricoli, and Ajayan Vinu, *Mesoporous C_3N_5 with high efficiency for photocatalytic CO_2 reduction*

5. Aathira M. Sadanandan, Mohammed Fawaz, Ayona K. P Jose, Nithinraj Panangattu Dharmarajan, Matej Huš, **Xuan Minh Chau Ta**, Vibin Perumalsamy, Jae-Hun Yang, Ana Oberlintner, Gurwinder Singh, Antonio Tricoli, Blaž Likozar, Prashant Kumar, and Ajayan Vinu, *Sulfoxide-functionalized mesoporous C_3N_5 as a metal-free and visible-light-driven efficient photocatalyst for CO_2 reduction*
6. Nithinraj Panangattu Dharmarajan, Mohammed Fawaz, Jae-Hun Yang, Matej Huš, **Xuan Minh Chau Ta**, Vibin Perumalsamy, Aathira Sadanandan, CI Sathish, Blaž Likozar, Antonio Tricoli, Ajayan Vinu, *Lithium-Potassium-Regulated Crystalline Lamellar Carbon Nitride for Sustainable Photocatalytic Hydrogen Generation*

Conference presentation and award:

1. Oral presentation "Engineering earth-abundant oxygen-evolving electrocatalyst for stable acidic water electrolysis" – 5th International Conference on Emerging Advanced Nanomaterials ICEAN 2024
2. Oral presentation "Effect of nanoscale passivation layer on the activity and stability of acidic oxygen evolution catalyst" – Australian Hydrogen Research Conference AHRC 2024
3. Poster Presentation Winner – 1st NSW Electrochemistry Symposium – Royal Australian Chemical Institute **(**RACI) 2024
4. 2024 Soft X-ray Spectroscopy Workshop – Australian Nuclear Science and Technology Organisation (ANSTO)
5. Best Poster Award at the 2022 International Symposium on Clean Energy Materials
6. Faculty of Engineering Career Advancement Award 2024 – Faculty of Engineering – The University of Sydney
7. Faculty of Engineering Research Scholarship 2021 – Faculty of Engineering – The University of Sydney

Table of Contents

List of Figures

List of Table

List of abbreviations

Notation	Definition	Notation	Definition
AEMWE	Anion-exchange membrane water electrolysis	M	Molarity
ALD	Atomic layer deposition	MS	Mott-Schottky
AM	Air Mass	MEA	Membrane electrode assembly
AMS	Aqueous model system	ND	Donor density
ASF	Activity-stability factor	NHE	Normal hydrogen electrode
ATO	Antimony-doped tin oxide	NIR	Near infrared
AWE	Alkaline water electrolysis	O_2	Oxygen
CA	Chronoamperometry	OECs	Oxygen evolution catalysts
CB	Conduction band	OER	Oxygen evolution reaction
Cdl	Double layer capacitance	PA-ALD	Plasma-assisted atomic layer deposition
CE	Counter electrode	PC	Photocatalysis
CO_2	Carbon dioxide	PCET	Proton-coupled electron transfer
CP	Chronopotentiometry	PEC	Photoelectrochemical
CV	Cyclic voltammetry	PEM	Polymer electrolyte membrane
DFT	Density functional theory	PEMWE	Proton-exchange-membrane water electrolysis
DI	Deionized	PFSA	Perfluorosulfonic acid
ECSA	Electrochemically active surface area	PGM	Platinum group metal
EDS	Energy-dispersive X-ray spectroscopy	PV-EC	Photovoltaic-electrolysis
EIS	Electrochemical impedance spectroscopy	RE	Reference electrode
EQCN	Electrochemical quartz crystal nanobalance	RHE	Reversible hydrogen electrode
FESEM	Field-emission scanning electron microscope	SEM	Scanning electron microscopy
FSP	Flame spray pyrolysis	SOE	Solid oxide electrolysis
FTIR	Fourier-transform infrared spectroscopy	SOWE	Solid oxide water electrolysis
FTO	Fluorine-doped tin oxide	STH	Solar-to-hydrogen
H_2	Hydrogen	TEM	Transmission electron microscopy
HAB	Height above burner	UV–Vis	Ultraviolet-visible spectrophotometer
HER	Hydrogen evolution reaction	V vs Ag/AgCl	Voltage versus the silver/silver chloride electrode
HR-TEM	High-resolution transmission electron microscope	V vs RHE	Voltage versus the reversible hydrogen electrode
ICP-MS	Inductively coupled plasma mass spectroscopy	WE	Working electrode
ICP-OES	Inductively coupled plasma optical emission spectroscopy	XAS	X-ray absorption spectroscopy
IPCE	Incident photon-to-current conversion efficiencies	XPS	X-ray photoelectron spectroscopy
j	Current density	XRD	X-ray diffraction
LSV	Linear sweep voltammetry		

Abstract

Hydrogen (H_2) is regarded as one of the most important energy sources for a wide range of sectors (transportation, chemical production, power generation) in the sustainable economy. Among various methods, water electrolysis emerges as a critical technology for green H_2 production based on renewable energy with no carbon emission. Between two half-cell reactions in the water electrolysis system, oxygen evolution reaction (OER) is a more complex process with a proton-coupled four-electron transfer-step and slower kinetics requiring high voltage to drive a reaction. Thus, it is a crucial step limiting the efficiency of H_2 generation from water electrolysis. Moreover, most oxygen evolution catalysts (OECs) are also constrained by poor stability, especially at extreme pH conditions. It results in the dependence on OECs-based noble metals in most large-scale water electrolysis systems, causing consideration of the high cost and scarcity of materials. To efficiently drive H_2 production by water electrolysis in a sustainable pathway, this thesis concentrates on developing efficient and stable electrocatalysts based on sustainable materials to fuel OER. Sustainable (photo)electrocatalysts studied in this work are expected to be non-toxic, low-cost, and synthesized by environmentally friendly approaches based on earth-abundant materials.

The first work concentrated on acidic OECs, the indispensable research pathway to improve the application of green H_2 production by proton-exchange-membrane water electrolyzer (PEMWE). PEMWE is one of the most favorable water electrolysis technologies in light of their multiple advantages relating to high production efficiency and compact system design. However, its sustainable application is limited by the reliance on noble metals (Ir, Ru) to drive OER, while non-noble-metal-based OECs usually suffer due to their poor stability in acidic electrolytes with high oxidation potential conditions. In the attempt to promote the economic value and sustainability of this approach, this work focused on developing stabilization strategies to enhance the stability of earth-abundant-based OECs, along with the activity of catalysts. The first research approach proposed a nanoscale protective layer to prolong the stability of active cobalt oxide catalysts at near-zero pH conditions. The material characterizations revealed the acidic corrosion occurring with OECs and the protective effects of the coating layer on the stability of catalysts. The second research work utilized the self-healing concept to engineer mixed metal oxide materials, which have the potential for long-lasting applications in acidic conditions. The self-healing concept implies a quasi-equilibrium state where the loss of catalyst due to corrosion occurs at the same or slower rate than its re-electrodeposition. The self-healing OECs were constructed based on integrating active components (Co, Ni) with the acidic stable structure of bismuth oxides. A comprehensive structural-

performance investigation provided insights into the role of electrolyte conditions in the self-healing behavior of OECs. Therefore, the best conditions for the acidic stable performance of self-healing OECs were defined.

The second part of this thesis investigated OECs in photoelectrochemical (PEC) water splitting, a complementary device focusing on direct use of solar energy, a clean and renewable source, for green H_2 production. In addition to high OER activity and stability, anodic photoelectrocatalysts are required to be semiconductor materials with good photoabsorption capability to boost the water photooxidation reaction. Herein, nanostructured ternary metal oxide, iron tungstate, was proposed as a photoanode based on its narrow bandgap and suitable band edge. Flame spray pyrolysis, an ultra-fast synthesis route, offers potential opportunities to optimize the structural and morphological properties, which resulted in a significant improvement in the optical and PEC activity of photoanode. Further modification strategy was conducted by coupling photoanode with FeOOH/NiOOH co-catalyst layer to enhance the photostability.

Chapter 1. Introduction

1.1. Research background

In recent decades, humans have been facing escalating global environmental issues, such as global warming, air pollution, rising sea levels, and resource depletion, due to the emerging reliance on fossil fuels.[1–4] These issues underscore the need to transition to alternative clean and renewable energy resources to mitigate greenhouse gas emissions. Within this context, hydrogen (H_2) is one of the most attractive replacement options since it is an efficient energy carrier with high energy density (140 MJ/kg), versatility for a wide range of applications (transportation, fertilizers, electricity production, *etc*.), and no emissions in use. [5–9] There are various H_2 production technologies, which are classified as color based the energy resources and the level of carbon emissions. Till now, black, gray, and brown production technologies utilizing the gasification, steam reforming, or pyrolysis process play a dominant role in H_2 market.[10,11] Nevertheless, the use of fossil fuel resources (coal, natural gas) and the emission of carbon dioxide (CO_2) gas and other harmful by-products in these production methods are not suitable for the sustainable development goal. It provoked the need to transition to the clean production process, water electrolysis, driven by renewable energy resources (*e.g.,* solar, wind, or geothermal energy) with no toxic emission, named green H_2.[11–13]

Green H_2 production by water electrolysis stands as a potential strategy for achieving decarbonization targets and developing a net-zero economy by providing clean and flexible energy storage. There are two half-reactions occurring in the water electrolysis system, including hydrogen evolution reaction (HER) and oxygen evolution reaction (OER), but OER is the main bottleneck to obstruct this process in terms of efficiency, stability, and price. Firstly, owing to a four-proton-electron coupled pathway, OER is kinetically more sluggish than HER (two-electron transfer process) and requires a higher external driving force (*e.g.*, overpotential) to drive the reaction.[14,15] Therefore, oxygen evolution catalysts (OECs) are desirable to have high catalytical activity to overcome this energy barrier and enhance the H_2 production efficiency. In addition to the intrinsic catalytic activity, there are some related factors controlling overall efficiency of OECs, depending on their working condition of electrolyzer. For example, due to the high applied oxidation potential and the extremely harsh operation conditions of industrial water electrolyzers, stability is also a considerable factor with OECs.[16–18] Especially when considering industrial application, which usually requires up to a thousand hours of stable performance, stability becomes a more prioritized

factor than activity regarding economic efficiency. In case of solar-driven water electrolyzers, the performance of OECs is also considerably affected by the light absorption and behavior of the photogenerated charge carriers under illumination, which will be discussed further in below. [19–22] In addition to the activity and stability, another factor which should be considered to assess the possibility of this technology is the capital cost of OECs materials. Up till now, almost the top OECs which can satisfy the industrial requirements in conventional water electrolysis relating to stability and activity are developed based on the noble-metal-based materials.[17] However, the high price and the scarcity are the significant challenges in the sustainable development of green H_2 production. For this reason, considerable research has been devoted to engineering alternative OECs from affordable and sustainable materials with good OER activity and stability. The targeted sustainable OECs are non-toxic, low-cost, and synthesized by the environmentally production technology based on earth-abundant-based metals.

To date, there are four most investigated types of water electrolysis, including: (i) solid oxide water electrolysis (SOWE), (ii) alkaline water electrolysis (AWE), (iii) proton-exchange membrane water electrolysis (PEMWE), and (iv) anion-exchange membrane water electrolysis (AEMWE), which are classified based on the electrolyzer design.[23–25] The most mature technology is AWE, which has been developed for a long time and is widely employed in commercial systems.[26–28] However, it faces several limitations, including the corrosive condition of the alkaline liquid electrolyte, low operating pressures, and limited current densities, all of which hinder its overall productivity.[27] Another notable technology, SOWE, is considered to have the advantages of high operating pressures and excellent efficiency. Nevertheless, SOWE is constrained by low durability resulting from its fragile ceramic structure, keeping it confined mainly to the research and development phase with minimal industrial deployment.[29,30] In the meanwhile, PEMWE stands out as a promising solution, owning several advantages over AWE and SOWE, such as rapid ion conductivity, faster start-up, high operating currents, low gas crossover at high operating pressure, and compact system design.[23,31,32] Although AEMWE is newly developed based on AWE and PEMWE, with the expectation of combining the benefits of AWE and PEMWE, more research is still required to enhance industrial performance.[33] For these reasons, PEMWE can be considered as a leading technology due to its efficiency and scalability. However, its reliance on noble metal-based OECs (*e.g.*, iridium or ruthenium) poses sustainability challenges due to their scarcity and high operation cost.[17] While earth-abundant-based OECs is presented as the low-cost and more sustainable alternative, the application is limited by the corrosive acidic environment and high oxidative potential at the anode of PEMWE.[18,34–37] For this reason, tackling the stability issues and

promoting the catalytic activity offers the great opportunity to employ alternative electrocatalysts from earth-abundant materials in PEMWE, which are expected to enhance the economic feasibility and sustainability of green H_2 produced by water electrolysis.

Besides these electrolysis system, photoelectrochemical (PEC) water splitting offers a complementary pathway for the sustainable solar-driven method for hydrogen production. It utilizes semiconductor materials as photoelectrodes to harvest sunlight, thereby reducing the required external voltage to drive a water-splitting reaction.[19–22] This specialized technology to leverage the direct employment of solar energy offers an alternative promising vision for H_2 production with lower input of external electricity. However, the commercialization prospect is still limited due to their low efficiency and the intermittent nature of solar sources. To tackle the issue of the PEC system, the most straightforward method concentrates on developing a light-absorbing semiconductor photoelectrocatalyst (photoanode) to promote OER, a half-cell reaction with sluggish kinetic limiting the overall production efficiency.[19,38–40] Since the first successful demonstration of water splitting with a TiO_2 photoanode by Honda and Fujishima,[22] there have been various types of materials investigated, but the best performance was observed in n-type metal oxide semiconductors such as TiO_2, $BiVO_4$, WO_3, Fe_2O_3, ZnO, *etc*.[41–46] Besides similar requirements to conventional water electrolysis regarding low cost and long stability, the most important selection criteria of the photoanodes in the PEC system is their activity under light illumination. As such, the efficient photoanodes require the appropriate bandgap energy to absorb light in a broad spectrum, well-aligned band edge positions to catalyze water oxidation reaction, and a low photogenerated electron-hole recombination rate, which is the main factor lowering the energy conversion efficiency.[39,47,48] There have been many studies on popular binary metal oxides and $BiVO_4$, a typical ternary metal oxide, photoanode, and various enhancement strategies have been proposed, resulting in the comprehensive exploration of their potential.[41–46] While further improvements of these photoanodes seem to be challenging, the other research pathway concentrating on exploring more new photoelectrocatalysts in a class of ternary metal oxide, has emerged increasingly.[49–52] It offers promising alternative options for photoanodes with some advantages over binary metal oxide and more research opportunities to optimize and enhance PEC performance in the future.

1.2. Research objectives and scopes

In accordance with the abovementioned discussion, the focus of this thesis is on exploring low-cost, active, and stable OECs in acidic water electrolysis and PEC systems.

Regarding acidic water electrolysis, the research interest in the scope of the thesis is to develop a strategy to enhance the stability of active earth-abundant-based OECs with no negative impact to their activity. My first proposal is to design effective passivation layers to protect the underlayer active materials at low pH conditions with a negligible effect on the electrocatalytic activity. The passivation layers are uniformly coated onto the top of catalysts, with their thickness controlled at the nanometer scale. Structural and electrochemical investigations, along with theoretical calculations, are conducted to prove their protective capability and the enhanced stability of catalysts. Another stabilization strategy studied in this thesis is constructing stable catalysts by implementing self-healing materials in acidic water oxidation. Comprehensive structural-performance investigation of OER electrocatalysts provides insights into the role of the electrolyte composition and pH on the catalyst's self-healing mechanism under anodic conditions. It aims to define the optimal condition for sustainable activity of self-healing materials and evaluate their possibility in PEMWE as the alternative OECs to replace the poorly scalable noble materials.

Regarding PEC water electrolysis, this research attempts to develop low-cost and efficient OER photoelectrocatalysts with suitable band edge to catalyze the sluggish kinetic of water oxidation and narrow band gap to extend the light absorption range. Among various semiconductors investigated for PEC, early studies focused on binary transition metal oxides (*e.g.* TiO_2, Fe_2O_3, WO_3, ZnO, Bi_2O_3) and ternary oxide, $BiVO_4$, with some promising results but faced with several issues for further enhancing PEC performance.[41–46] In recent years, a significant effort has been made to other classes of semiconductor materials from ternary metal oxides (labeled as ABO_x, where A and B are two different cations), aside from $BiVO_4$, that generally are more flexible to tune the optoelectronic and physiochemical properties resulting better theoretical PEC activities compared to its constitutional components.[49,50,52] Herein, nanostructured ternary metal oxide photoanodes are synthesized and optimized by flame spray pyrolysis (FSP), a powerful and scalable technique for direct nanofabrication in very short time.[53–55] It allows to engineer the robust films with tunable morphology and crystallinity, which is beneficial to optimize optoelectronic properties and enhance PEC activity. Besides, surface modification by decorating with co-catalysts is also employed to improve interfacial reaction kinetics and stability against photocorrosion.

1.3. Thesis outline

The thesis is an outcome of my PhD research and has been partially published in the form of research/ review articles. It is divided into seven chapters presented in the following outlines:

- ***Chapter 1*** presents a brief introduction of the research background of OER (photo)electrocatalysts for green production by water splitting in two targeted systems, PEMWE and PEC electrolyzer, the research objectives and scopes, as well as the outline of the thesis.
- The next two chapters, including ***chapter 2*** and ***chapter 3***, are the literature reviews that provide the research background and recent advancements of OER (photo)electrocatalysts. ***Chapter 2*** is a state-of-art review of the acidic OER and strategies to engineer non-precious, stable electrocatalysts at low pH, a crucial component to employ in PEMWE successfully. ***Chapter 3*** is the literature review focusing on overall PEC water splitting, the current research status of some potential ternary metal oxide photoanodes, and the optimization strategies to advance photoelectrodes by flame spray pyrolysis.
- To engineer stable acidic OER electrocatalysts**,** ***chapter 4*** investigates the nano-scale passivation layer coated on the surface, a stabilization strategy reviewed in ***chapter 2***, to protect and enhance the stability of low-cost materials, which were representative by Co_3O_4, a promising high active catalyst at low pH. This chapter focuses on studying five potential passivation layers, TiO_2, Al_2O_3, SnO_2, SiO_2, and HfO_2 layers, to protect the Co_3O_4 anode from acidic water electrooxidation at pH 0. The impacts of the interrelation between the chemical nature, and thickness of the coatings to the electrocatalytic activity and stability of the modified anodes were systematically investigated. They are fundamental knowledge for identifying the most suitable materials for protective layers in the acidic OER application.
- With the aim to further extend the stability of acidic OECs reviewed and studied in ***chapter 2*** and ***chapter 4*****,** ***chapter 5*** reports a systematic investigation of the self-healing materials based on earth-abundant elements and their possibility as OECs at low pH conditions. An optimal composition consisting of stable self-healing bismuth (Bi)-based matrix hosting cobalt (Co) and nickel (Ni) transition metals as active OER sites was determined to be efficient in prolonging the sustainable activity in acidic conditions. In addition, this study attempted to optimize tested conditions for the most efficient self-healing operations. These insights offer design principles to prepare and operate scalable, stable, and efficient electrocatalyst systems for acidic water splitting using earth-abundant and environmentally friendly materials.
- Based on the need to explore new photoelectrocatalysts materials and opportunities of FSP methods in engineering photoelectrodes reviewed in ***chapter 3***, ***chapter 6*** covers a controlled FSP deposition and the post-thermal treatment of iron tungstate materials, a

promising ternary metal oxide which has not been thoughtfully explored as photoanodes. These physical, optical, and electrochemical properties are systematically investigated to evaluate the application possibility of photoanodes made by FSP for water electrolysis, along with understanding the remaining issues of materials. These insights are beneficial to iron tungstate as the role of photoanode for PEC water splitting and explore more possibilities of FSP in designing advanced photoelectrocatalyst materials.

- ***Chapter 7*** concludes this thesis by providing an overview of findings and observations found throughout the PhD study, preceding an outlook into the field and recommendations for future work.

1.4. References

[1] S. A. R. Khan, H. M. Zia-Ul-Haq, P. Ponce, L. Janjua, *Resour. Policy* **2023**, *81*, 103411.

[2] J. Wang, W. Azam, *Geosci. Front.* **2024**, *15*, 101757.

[3] C. Yu, M. Moslehpour, T. K. Tran, L. M. Trung, J. P. Ou, N. H. Tien, *Resour. Policy* **2023**, *80*, 103221.

[4] Y. Xu, F. Zhao, *Resour. Policy* **2023**, *83*, DOI 10.1016/j.resourpol.2023.103531.

[5] J. Chi, H. Yu, *Chinese J. Catal.* **2018**, *39*, 390.

[6] S. J. Davis, N. S. Lewis, M. Shaner, S. Aggarwal, D. Arent, I. L. Azevedo, S. M. Benson, T. Bradley, J. Brouwer, Y. Chiang, C. T. M. Clack, A. Cohen, S. Doig, J. Edmonds, P. Fennell, C. B. Field, B. Hannegan, B. Hodge, M. I. Hoffert, E. Ingersoll, P. Jaramillo, K. S. Lackner, K. J. Mach, M. Mastrandrea, J. Ogden, P. F. Peterson, D. L. Sanchez, D. Sperling, J. Stagner, J. E. Trancik, C. Yang, K. Caldeira, *Science (80-.).* **2018**, *360*, DOI 10.1126/science.aas9793.

[7] M. H. Nehrir, C. Wang, in *Electr. Renew. Energy Syst.* (Ed.: M.H. Rashid), Academic Press, Boston, **2016**, pp. 92–113.

[8] H. Nazir, C. Louis, S. Jose, J. Prakash, N. Muthuswamy, M. E. M. Buan, C. Flox, S. Chavan, X. Shi, P. Kauranen, T. Kallio, G. Maia, K. Tammeveski, N. Lymperopoulos, E. Carcadea, E. Veziroglu, A. Iranzo, A. M. Kannan, *Int. J. Hydrogen Energy* **2020**, *45*, 13777.

[9] P. De Luna, C. Hahn, D. Higgins, S. A. Jaffer, T. F. Jaramillo, E. H. Sargent, *Science (80-.).* **2019**, *364*, DOI 10.1126/science.aav3506.

[10] T. L. Levalley, A. R. Richard, M. Fan, *Int. J. Hydrogen Energy* **2014**, *39*, 16983.

[11] A. Ajanovic, M. Sayer, R. Haas, *Int. J. Hydrogen Energy* **2022**, *47*, 24136.

[12] J. Chi, H. Yu, *Chinese J. Catal.* **2018**, *39*, 390.

[13] O. Bičáková, P. Straka, *Int. J. Hydrogen Energy* **2012**, *37*, 11563.

[14] M. Tahir, L. Pan, F. Idrees, X. Zhang, L. Wang, J. J. Zou, Z. L. Wang, *Nano Energy* **2017**, *37*, 136.

[15] E. Fabbri, T. J. Schmidt, *ACS Catal.* **2018**, *8*, 9765.

[16] F. Y. Chen, Z. Y. Wu, Z. Adler, H. Wang, *Joule* **2021**, *5*, 1704.

[17] K. Ham, S. Bae, J. Lee, *J. Energy Chem.* **2024**, *95*, 554.

[18] S. Cherevko, *Curr. Opin. Electrochem.* **2023**, *38*, 101213.

[19] W. Yang, R. R. Prabhakar, J. Tan, S. D. Tilley, J. Moon, *Chem. Soc. Rev.* **2019**, *48*, 4979.

[20] T. Hisatomi, J. Kubota, K. Domen, *Chem. Soc. Rev.* **2014**, *43*, 7520.

[21] Y. Li, J. Z. Zhang, *Laser Photon. Rev.* **2010**, *4*, 517.

[22] A. FUJISHIMA, K. HONDA, *Nature* **1972**, *238*, 37.

[23] M. Carmo, D. L. Fritz, J. Mergel, D. Stolten, *Int. J. Hydrogen Energy* **2013**, *38*, 4901.

[24] S. Shiva Kumar, V. Himabindu, *Mater. Sci. Energy Technol.* **2019**, *2*, 442.

[25] N. Du, C. Roy, R. Peach, M. Turnbull, S. Thiele, C. Bock, *Chem. Rev.* **2022**, *122*, 11830.

[26] R. M. Navarro, R. Guil, J. L. G. Fierro, in *Compend. Hydrog. Energy*, Elsevier, **2015**, pp. 21–61.

[27] K. Zeng, D. Zhang, *Prog. Energy Combust. Sci.* **2010**, *36*, 307.

[28] T. Smolinka, H. Bergmann, J. Garche, M. Kusnezoff, *The History of Water Electrolysis from Its Beginnings to the Present*, Elsevier B.V., **2021**.

[29] S. A. Grigoriev, V. N. Fateev, D. G. Bessarabov, P. Millet, *Int. J. Hydrogen Energy* **2020**, *45*, 26036.

[30] S. E. Wolf, F. E. Winterhalder, V. Vibhu, L. G. J. (Bert) de Haart, O. Guillon, R.-A. Eichel, N. H. Menzler, *J. Mater. Chem. A* **2023**, *11*, 17977.

[31] L. Zhang, X. Jie, Z.-G. Shao, Z.-M. Zhou, G. Xiao, B. Yi, *Int. J. Hydrogen Energy* **2012**, *37*, 1321.

[32] L. Ma, S. Sui, Y. Zhai, *Int. J. Hydrogen Energy* **2009**, *34*, 678.

[33] H. Ito, N. Kawaguchi, S. Someya, T. Munakata, *Electrochim. Acta* **2019**, *297*, 188.

[34] T. Liu, C. Chen, Z. Pu, Q. Huang, X. Zhang, A. M. Al-Enizi, A. Nafady, S. Huang, D. Chen, S. Mu, *Small* **2024**, *20*, 1.

[35] L. An, C. Wei, M. Lu, H. Liu, Y. Chen, G. G. Scherer, A. C. Fisher, P. Xi, Z. J. Xu, C. H. Yan, *Adv. Mater.* **2021**, *33*, 1.

[36] X. M. C. Ta, T. Trần-Phú, T. K. A. Nguyen, M. Chatti, R. Daiyan, *Appl. Phys. Rev.* **2024**, *11*, DOI 10.1063/5.0200438.

[37] J. Gao, H. Tao, B. Liu, *Adv. Mater.* **2021**, *33*, 1.

[38] M. D. Bhatt, J. S. Lee, *J. Mater. Chem. A* **2015**, *3*, 10632.

[39] C. Jiang, S. J. A. Moniz, A. Wang, T. Zhang, J. Tang, *Chem. Soc. Rev.* **2017**, *46*, 4645.

[40] A. A. Mohd Raub, R. Bahru, S. N. A. Mohd Nashruddin, J. Yunas, *Heliyon* **2024**, *10*, e39079.

[41] Y. Wang, W. Tian, C. Chen, W. Xu, L. Li, *Adv. Funct. Mater.* **2019**, *29*, 1809036.

[42] X. Yao, D. Wang, X. Zhao, S. Ma, P. S. Bassi, G. Yang, W. Chen, Z. Chen, T. Sritharan, *Energy Technol.* **2018**, *6*, 100.

[43] L. Wang, Y. Zhang, W. Li, L. Wang, *Mater. Reports Energy* **2023**, *3*, 100232.

[44] M. H. Sawal, A. A. Jalil, N. F. Khusnun, N. S. Hassan, M. B. Bahari, *Electrochim. Acta* **2023**, *467*, 143142.

[45] Z. Najaf, D. L. T. Nguyen, S. Y. Chae, O.-S. Joo, A. U. H. A. Shah, D.-V. N. Vo, V.-H. Nguyen, Q. Van Le, G. Rahman, *Int. J. Hydrogen Energy* **2021**, *46*, 23334.

[46] R. Abdullah, A. A. Jalil, M. Asmadi, N. S. Hassan, M. B. Bahari, M. Alhassan, N. M. Izzudin, M. H. Sawal, R. Saravanan, H. Karimi-Maleh, *Int. J. Hydrogen Energy* **2024**, DOI 10.1016/j.ijhydene.2024.05.461.

[47] C. W. Moon, M. J. Choi, J. K. Hyun, H. W. Jang, *Nanoscale Adv.* **2021**, *3*, 5981.

[48] L. M. Peter, K. G. Upul Wijayantha, *ChemPhysChem* **2014**, *15*, 1983.

[49] X. Wang, B. Liu, Y. Zhang, T. Butburee, K. (Ken) Ostrikov, S. Wang, W. Huang, *EcoEnergy* **2023**, *1*, 108.

[50] D. K. Lee, D. Lee, M. A. Lumley, K.-S. Choi, *Chem. Soc. Rev.* **2019**, *48*, 2126.

[51] H. He, A. Liao, W. Guo, W. Luo, Y. Zhou, Z. Zou, *Nano Today* **2019**, *28*, 100763.

[52] F. F. Abdi, S. P. Berglund, *J. Phys. D. Appl. Phys.* **2017**, *50*, 193002.

[53] H. Chen, H. K. Mulmudi, A. Tricoli, *Chinese Chem. Lett.* **2020**, *31*, 601.

[54] W. Y. Teoh, R. Amal, L. Mädler, *Nanoscale* **2010**, *2*, 1324.

[55] T. Tran-Phu, R. Daiyan, X. M. C. Ta, R. Amal, A. Tricoli, *Adv. Funct. Mater.* **2022**, *32*, 1.

Chapter 2. Acidic oxygen evolution reaction electrocatalyst

This chapter is a literature review introducing about the oxygen evolution catalysts (OECs) in acidic water electrolysis, an important factor for implementation to proton-exchange-membrane water electrolyzer (PEMWE). It describes the oxygen evolution reaction (OER) pathway at low pH condition associated with the degradation of OECs occurring throughout this process. To tackle the stability issues in acidic OER, this review concentrates on some recent development of stabilization strategies, especially applied for the non-noble-based electrocatalysts, which can be a main contributor to the sustainable growth of this technology. The review concludes by identifying some remaining challenges and proposing opportunities for diverse applications of stable acidic OECs in water electrolysis systems.

This chapter was a part reprinted from Xuan Minh Chau Ta, Thành Trần-Phú, Thi Kim Anh Nguyen, Manjunath Chatti, Rahman Daiyan; Engineering oxygen-evolving catalysts for acidic water electrolysis. Appl. Phys. Rev. 1 June 2024; 11 (2): 021321. 10.1063/5.0200438, with the permission of AIP Publishing.

Authorship Attribution Statement

Xuan Minh Chau Ta is the principal author of this publication, which forms part of her thesis submitted for the examination for the Doctor of Philosophy degree. The corresponding authors below provide their consent for inclusion of a part or whole of the following publication in this thesis and accept the following candidate statement of contribution for this publication.

Candidate contribution

This study reviews the recent development of engineering stable acidic electrocatalyst for oxygen evolution reaction. The manuscript was written, formatted, reviewed, and edited by Xuan Minh Chau Ta.

Corresponding author

Dr. Thành Trần-Phú

Corresponding author

Dr. Rahman Daiyan

2.1. Introduction

In recent decades, the emerging reliance on fossil fuels has engendered a wide range of global environmental issues, including but not limited to air pollution, the greenhouse effect, climate perturbations, and the resource depletion.[1–4] This situation leads to a critical imperative to explore alternative renewable resources with the primary objective of mitigating carbon emissions. Hydrogen (H_2) is one of the most attractive energy carriers to replace carbon-based fuel sources due to its zero emissions in use, high energy density (140 MJ/kg), and versatility across sectors.[5,6] H_2 can be utilized in a wide range of applications, such as transportation, fertilizers, electricity production, *etc*.[7–9] There are various methods to produce H_2, which are classified based on the energy resources and carbon emission of the generation and utilization processes.[8,10] Currently, the most widely used H_2 is derived from the gasification, steam reforming, or pyrolysis process driven by the fossil fuels resources (coal, natural gas).[11] However, it is not suitable with the vision of carbon neutrality objectives, due to the emission of CO_2 gas and various harmful by-products. Meanwhile, green H_2 produced from water electrolysis fueled by renewable energy resources (*e.g.,* solar, wind, or geothermal energy) is more appropriate feedstock to the sustainable growth as it poses no harmful effects on the environment and becoming the strategic development goals around the world.[12–14]

Water electrolysis normally involves two half-reactions: hydrogen evolution reaction (HER) and oxygen evolution reaction (OER). In acidic environment, electrons and protons are produced through OER at anode, and they subsequently migrate to and recombine at the cathode to produce H_2 gas. However, owing to a four-proton-electron coupled pathway, OER is kinetically more sluggish as compared to HER (two-electron transfer process), requiring a higher external driving force (i.e., overpotential). Thus, OER plays a dominant role in the overall efficiency of H_2 production by acidic water electrolysis. Research on Google scholar has shown the emerging increased trend of studies in acidic OER topic as demonstrated in (**Figure 2.1**). Most of the attention have been paid on optimizing the activity of oxygen evolution catalysts (OECs) along with reducing the materials cost,[15–19] whereas, there are fewer efforts devoted to improve stability in harsh acidic OER condition.[20–22] It is due to the inverse relationship between activity and stability, in which the prolonged stability is usually accompanied by the decrease in activity. In fact, stability can be an even more important factor than activity, especially for a practical application which usually requires more than a thousand hours of operation. For instance, Chen et al. illustrated that OECs with lower activity and degradation rate could reduce up to 43% energy cost after over 2000 h continuous operation.[20]

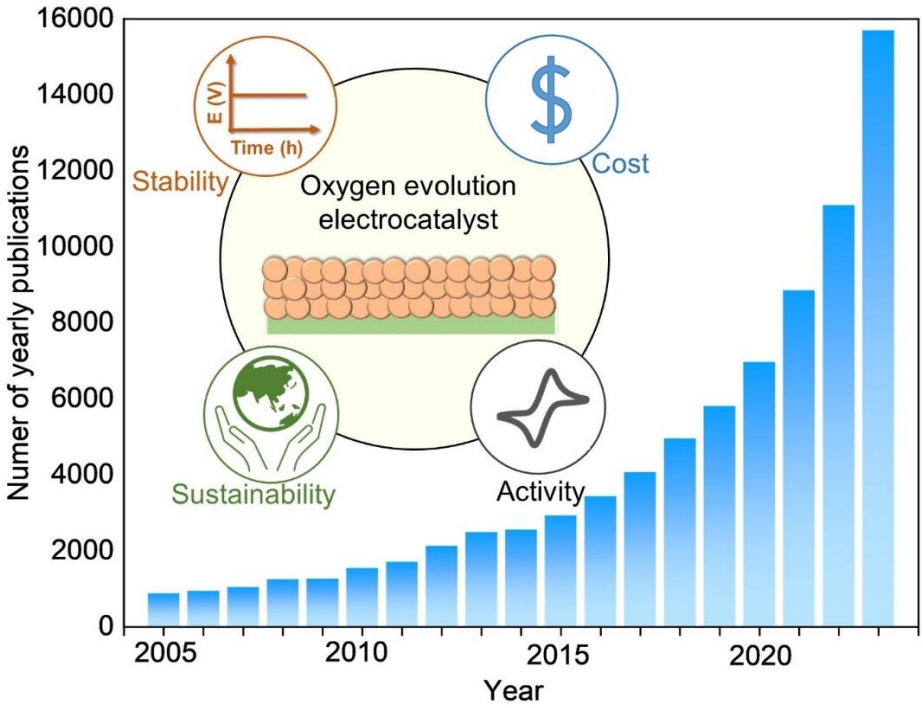

Figure 2.1 Statistical data reflecting the increased interest of the research community toward acidic OER over years. Data obtained by using Boolean operators in Google Scholar' search queries "acidic electrocatalytic water splitting" and "oxygen evolution reaction"

Depending on the operation conditions and electrolyzer components, there are four most investigated water splitting technologies: (i) solid oxide water electrolysis (SOWE), (ii) alkaline water electrolysis (AWE), (iii) proton-exchange membrane water electrolysis (PEMWE), and (iv) anion-exchange membrane water electrolysis (AEMWE).[23–25] Among them, AWE is the most mature technology with a long history and widely employed on the commercial scale.[26–28] Nevertheless, challenges arise from the causticity of the alkaline liquid electrolyte, low operating pressure, and restricted current densities, all of which significantly curtail productivity.[27] Another notable technology is SOWE, which owns the advantages from the high operating pressure and efficiency. Despite these merits, SOWE faces a hurdle in terms of low durability due to its brittle ceramic structure, relegating it to a research and development stage with limited industrial applications.[29,30] In contrast, PEMWE boasts several advantages over AWE and SOWE, such as rapid ion conductivity, faster startup, high operating currents, low gas crossover at high operating pressure, and the compact system design.[23,31,32] However, the sustainable development of PEMWE technology is obstructed by corrosive acidic conditions and the reliance on noble metal-based electrocatalysts (Ir or Ru). Recently, AEMWE is a newly developed technology with the attempt to combine the benefits of AWE and PEMWE, but the working pressure of AEMWE is relatively low

(<10 bars), limiting its industrial performance.[33] As such, PEMWE remains the most promising and efficient candidate for industrial-scale green hydrogen production.

When considering the economic viability of PEMWE, the stack cost, covering all the main components in an electrolyzer, including catalyst-coated membrane, porous transport layer, and bipolar plates, accounts for ~40 % of total system.[34] Among them, catalyst-coated membrane (CCM), in which price of platinum group metal catalyst can be up to 50%, is the dominant part.[24,34] While the costs of most components are challenging to be reduced due to their essential roles in the compact design of the electrolyzer, an exception lies in the use of electrocatalysts, particularly the precious metals employed. At present, noble metals-based OECs from Ir, Ru stand as the sole option for an industrial-relevant balance between activity and stability in acidic media.[18,35–37] Nevertheless, they are expensive and scare materials, contributing to elevated costs within the overall hydrogen (H_2) production system and impeding widespread adoption of PEMWE.[24,38] Thus, to mitigate construction costs for PEMWE and enhance economic viability, a potential solution involves the imperative reduction of precious metals in catalysts and the utilization of low-cost electrocatalysts that meet industrial requirements of higher activity and longer stability. [38] Therefore, considerable efforts have been directed toward exploring alternatives based on earth-abundant OECs. However, their utilization in acidic media is primarily constrained by inherent instability, the important factors governing the efficiency of PEMWE in practical application, as discussed aboved.[39]

There are several review articles have been published on acidic OER in water electrolysis.[35,36,40–43] However, the majority of these studies primarily focus on introducing reaction mechanism of acidic OER and reviewing the strategy to enhance electrocatalytic activity of OECs.[35,36,40–43] Other research works deeply investigated the stability of OECs and related factors affecting the degradation of OECs in acidic conditions.[20,22,37,44,45] Most of these studies concentrated on OECs developed from noble elements such as Ir or Ru, whereas the studies about strategies designed to especially enhance the stability of nonnoble metal oxides are limited.[21,22,46] For this reason, we aim to supplement the literature to systematically review this section and review effective strategies to design stable OECs in acid. In specific, this review will focus on (i) thermodynamics and degradation mechanism of OECs in acidic media, (ii) evaluation parameters and methods to assess the OECs activity and stability, (iii) strategies to develop active and acid-stable OECs, and (iv) challenges and opportunities of acid water electrolysis.

2.2. Acidic water electrolysis

In general, acidic water electrolysis consists of oxygen evolution reaction (OER) at the anode to produce protons and electrons ($2H_2O \rightarrow O_2 + 4H^+ + 4e^-$), which are then combined at the cathode to generate H_2 ($2H^+ + 2e^- \rightarrow H_2$), or hydrogen evolution reaction (HER). Among these two half-cell reactions, the reaction mechanism of HER in acidic condition is simpler, faster, and more straightforward to H_2 products. Although most popular HER catalysts are developed based on platinum (Pt), there have been numerous low-cost and nontoxic electrocatalysts to drive acidic HER at stable electrochemical performance including MoS_2[47–49] and CoP.[50]

Contrasting to HER, the mechanism of acidic OER is more complicated, and the dissolution of OECs is problematic. Among various types of OECs (*e.g.,* metal oxides, sulfides, nitrides, phosphides, or intermetallic alloys), metal oxides remain the most widely investigated OECs materials with more promising OER stability.[16] Therefore, this review will primarily focus on reaction mechanism and degradation process for metal oxides materials. To date, there have been various possible mechanism proposed for OER, but the most widely accepted explanation is developed based on the conventional adsorbate evolution mechanism (AEM) and the lattice oxygen mechanism (LOM) as illustrated in (**Figure 2.2**).[39]. According to the thermodynamics calculated by density functional theory (DFT), the AEM in acidic media can be described through four concerted proton-electron transfer steps with surface metal-ion centers as catalytically active sites to yield O_2 from H_2O molecules. At the first step, water molecules are adsorbed onto the active site, then undergo three subsequent deprotonation steps to generate the M-OH*, M-O*, and M-OOH* intermediate species successively via electron transfer, followed by the oxidation step to release O_2.

Being different from the AEM, LOM involves the lattice oxygen redox reactions and non-concerted proton-electron transfer steps, which does not merely rely on H_2O molecules. In acid electrolyte, LOM could be observed by the experiment of ^{18}O-isotope labeling with differential electrochemical mass spectrometry (DEMS).[40,51] Acidic LOM has been studied to illustrate for different OECs (RuO_2, IrO_2, *etc*.); nevertheless, the general acidic LOM can be concluded to five elementary steps. Similar to AEM, absorbed *O species are generated through the oxidation of H_2O molecules on the active sites, then they couple with lattice oxygen to release oxygen gas and leave the abundant oxygen vacancies on the surface. Finally, these vacancies can react with H_2O molecules to reproduce active sites again.

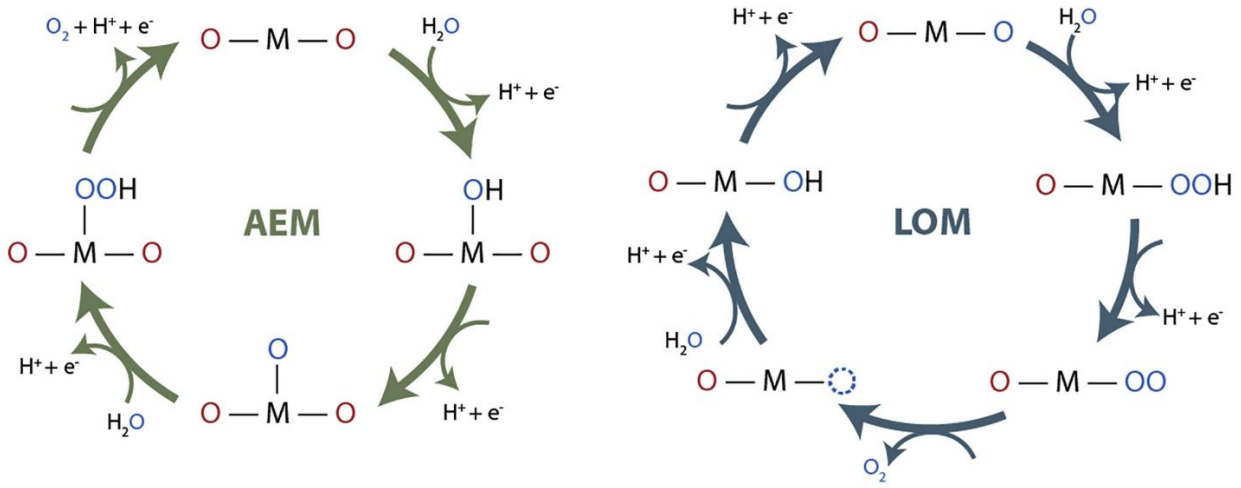

Figure 2.2 Schematic of two reaction pathways of acidic OER: adsorbate evolution mechanism AEM (left) and lattice oxygen mechanism LOM (right). M stands for metal active site and the dashed circle represents the lattice oxygen vacancy. Reproduced with permission.[20] Copyright 2021, Elsevier.

It is reported that AEM and LOM can be two simultaneous mechanisms competing in OER.[36,52,53] The main advantage of LOM over AEM is that it can bypass scaling relation limitation with direct O-O coupling and not be limited by the minimum theoretical potential of 0.37 V.[52] Therefore, it is more beneficial to improve OER ability. However, since LOM requires the participation of active sites of catalysts to generate oxygen vacancies, it usually results in structural instability and more severe dissolution of metal sites. By contrast, AEM theoretically does not suffer from either the surface changes or structure collapse of electrocatalysts.

2.2.1. Degradation mechanisms

In acidic OER, there are various factors governing the stability of catalyst materials.[22,45,54–56] Among them, the most primary driving forces of dissolution comes from the intrinsic stability of catalyst materials when they are in contact with an electrolyte solution.[22,45] Besides, the cause of catalyst degradation can be derived from the electrolyzer support system such as the acidic resistance of substrate, supportive materials, binder, or the bubble formation on catalysts surface. [22,45,54–56] The fundamental understanding of these factors is valuable to elucidate the degradation mechanisms of catalyst materials and will be discussed in this section.

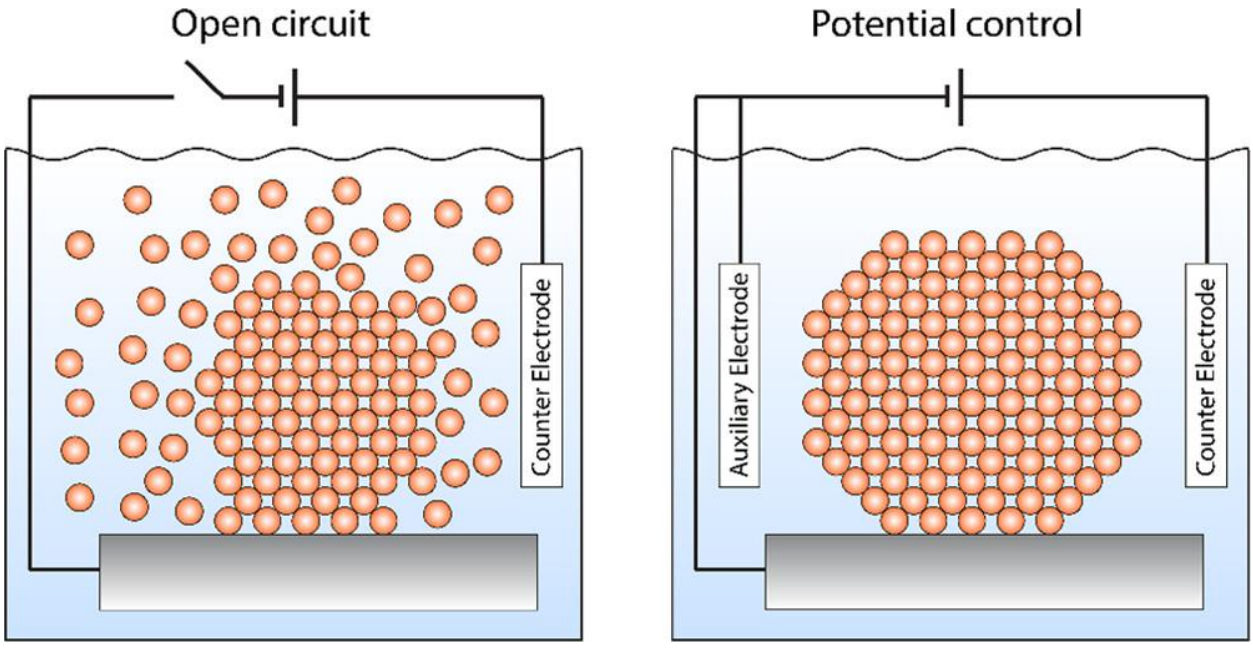

Figure 2.3 Illustration of (left) catalyst dissolution during uncontrolled immersion of the catalyst into the electrolyte and (right) catalyst immersion under potential control to avoid dissolution. Hochfilzer *et al.*, ACS Energy Lett., 8, 3, 1607–1612, 2023;[57] licensed under a Creative Commons Attribution (CC BY) license.

Dissolution of catalysts is considered as the predominant process causing the loss of active sites on the electrode surface and the instability performance. When immersed into the electrolytes, chemical dissolution can occur at an open circuit voltage (OCV) without an applied bias potential (**Figure 2.3a**), resulting in the dissolved metal species and changes of morphological of catalysts prior to the electrochemical tests, which cause the irreproducibility of mateirals.[57,58] For this reason, to eliminate the impact of chemical dissolution, the recommended protocol is immersing catalyst only under the controlled potential to preserve the initial state of as-synthesized catalyst (**Figure 2.3b**).[57,59–61] The prior driving force of dissolution comes from the intrinsic chemical instability of materials, which is corroded via interaction with electrolytes or impurities. This thermodynamic driving force towards decomposition was determined to be derived from the electrode-electrolyte interface potential.[57,58] It is more severe with the first-row transition metal oxides, such as CoO_x, FeO_x, or MnO_x, due to the reaction with protons (H^+) in neutral or acidic conditions.[59]

Nonetheless, during OER, the most significant corrosion of catalysts comes from the oxidative dissolution when applying a high anodic potential. It can be classified into two types, transient dissolution under the fluctuation of potential or current applied and steady-state dissolution under the fixed power input.[20,45,62] Between these two dissolution types, the steady-state dissolution has

been highly considered as a main challenge in almost acidic OER studies, because it directly reflects the actual stability under prolonged operation at continuous and fixed conditions.[20] It was controlled by two factors, the intrinsic thermodynamical stability of materials and the oxygen evolution reaction mechanism, which is mainly driven by LOM. For example, a commercial RuO_2 catalyst exhibited Ru dissolution during prolonged OER operation in 0.5 M H_2SO_4 due to the participation of lattice oxygen, resulting in the formation of oxygen vacancies and unstable RuO_4 intermediates with weakened Ru-O bonds.[63,64] However, the transient dissolution, which is correlated with the surface reconstruction under the fluctuating condition, can also cause the instability of OER catalysts. For instance, the surface reconstruction of amorphous IrO_x under potential cycling resulted in the reduction of Ir oxidation state to +3.[65–67] These undercoordinated sites enhance OER activity by lowering the O–O coupling barrier but weaken Ir–O bonds, accelerating further dissolution in prolonged operation. Recently, Priamushko et al. revealed the transient dissolution in the acidic electrolytes of non-noble electrocatalysts, Co_3O_4.[68] The potential cycling window (1.55–1.65 V_{RHE}) has been considered as stable, which promoted the formation of Co^{III-IV} species to stabilize the surface and reduce the rapid Co dissolution rate. The formation of Co^{III-IV} species also participated in the LOM mechanism when applying the OER operation with a longer-term process, resulting in a direct impact to the lattice destabilization and Co dissolution. As for the above discussion, some key aspects of the transient and steady-state dissolution were summarized in **Table 2.1** as below.

Table 2.1 Comparison between the transient and steady-state dissolution.

Aspect	Transient Dissolution	Steady-state Dissolution
Triggered conditions	The sharp potential/ currents changes	The fixed potential/ current
Rate	Rapid and fluctuated rate	Slow and sustained rate
Representation	Short-term loss of materials during the initial catalyst-electrolyte contacts or potential fluctuations	Long-term stability of materials in the continuous operation.
Mechanism	Correlated with surface reconstruction/ oxidation.	Correlated with oxygen evolution mechanism and thermodynamical stability of materials

Accordingly, Cherevko and co-workers visualized the dissolution profiles during acidic OER of Ir, Ru, and Pt by the potential sweep experiments.[62] It represented that the steady-state dissolution, excluding the first anodic potential step mainly controlled by the transient dissolution, was the dominant corrosion process under galvanostatic condition. Each element would have a different number of dissolved ions in electrolytes, relying on the intrinsic stability and the applied potential. For instance, Ru has a high steady-state dissolution rate, while Ir and Pt have a low steady-state dissolution rate but a relatively high transient dissolution rate. In-depth theoretical knowledge on the potential stability can be referred to the calculated Pourbaix diagrams,[69] which plot the thermodynamic stability (*e.g.,* standard Gibbs free energy) of metal elements with different redox states as a function of specific pH and voltage, at a certain concentration of ions in solution (around 10^{-6} M). They are widely employed tools in corrosion science to provide insights into the thermodynamic stability of used materials. Therefore, they have been used to rapidly screen the potential OECs (*e.g.,* Si, Ti, Mn, Fe, Co, Cu, Mo, Ag, Sn, Te, Ta, W, Tl, Pb, and Bi). However, in practical experiments, there are also various factors that control the oxidation dissolution of materials. Indeed, Pourbaix diagrams consider the thermodynamic equilibrium of elements, but not the structures properties of synthesized materials and reaction conditions, which are closely related to the kinetic rates of corrosion and dissolution.[69,70] For the bulk properties, morphology, especially for nanoparticle sizes, is a critical factor of the dissolution rate: the smaller nanoparticle sizes are more vulnerable to be dissolved owing to their lower dissolution potentials and less cohesive energies.[71–73] For example, Hodnik *et al.* investigated the dissolution of Ru catalysts with different nanoparticle sizes using cyclic voltammograms in 0.1 M $HClO_4$ electrolyte.[72] They found that the small Ru particles (< 100 nm) dissolved completely after 10 cycles, whereas the big particles were only detached from the substrate but not dissolved. Similarly, Abbott *et al.* found that he lower stability and faster deactivation process of small spherical IrO_2 particles (with a diameter of 1.7 nm) than large rod-shape counterparts (with a length ~ 20 nm) in 0.1 M $HClO_4$ electrolyte. [73] Besides, the change of morphology through the kinetic dissolution could result in the agglomeration of nanoparticles, reducing electrochemical active surface area and the degradation of OER performance.[74] Crystalline and electronic structures of OECs can also influence the dissolution kinetics. Cherevko *et al.* studied the correlation between the crystallinity through the calcinated temperatures and the dissolution rate of IrO_x/Ti catalysts.[75] It determined that the stability of IrO_x/Ti increased with the with the increasing in the calcination temperature due to the better crystallinity, which promotes higher degree of surface lattice oxygen and inhibited surface hydroxylation. Cherevko *et al.* also presented that the Ru and Ir metal catalysts had about 2 – 3 orders of magnitude

higher dissolution than their corresponding oxides, indicating the impacts electronic structures or oxidations states of catalyst.[76]

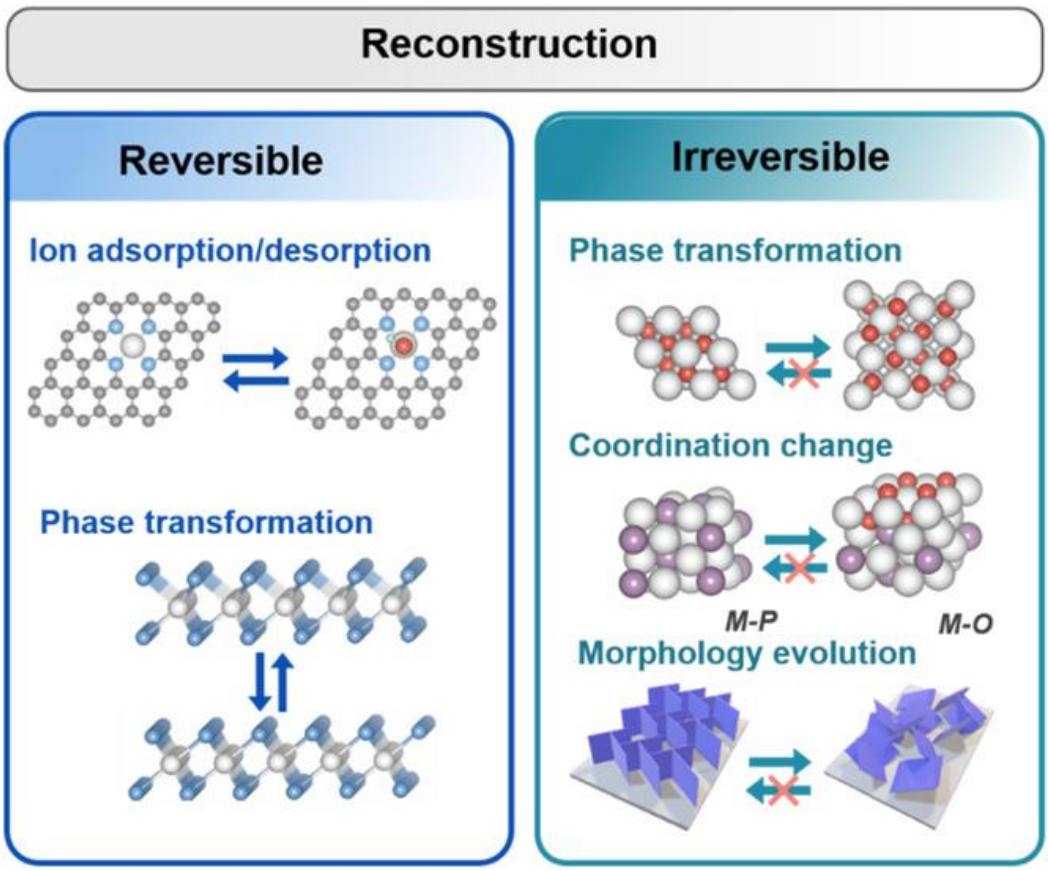

Figure 2.4 Overview of reconstruction processes, which can be classified into reversible and irreversible processes. Kou et al, Small Sci., 1, 7, 2688-4046;[77] licensed under a Creative Commons Attribution (CC BY) license.

Besides, the reconstruction of pre-catalyst properties such as compositions, phases, crystallinity, or structures at various scales may influence the catalyst degradation.[77] There are several driving forces for such transformation including the testing conditions (*e.g.,* pH, applied potentials, concentration of exotic ions, *etc*.) and the reactive nature of metals compounds under the reaction conditions.[77] The reconstruction of pre-catalysts can be divided into reversible and irreversible transformation as depicted in (**Figure 2.4**). The first reconstruction relates to the intermediate absorption and desorption along the varied potentials. For example, a two-dimensional ultrathin perovskite $SrIrO_3$ performed a strong deprotonation capability to quickly store oxidative charges and generate surface O* species during acidic OER, which facilitates the OER kinetics.[78] The leaching of Sr from $SrIrO_3$ matrix at the first atomic layers enabled exposure of the $SrIrO_3$ (001) facet, which restrains the Sr dissolution and prolongs OER stability. The later reconstruction

involves the unrecovered transformation of phase, morphology, or coordination states in the surface of catalysts materials. An example of this is the oxidation of the bulk Ir and Ru metals to form the IrO_2 and RuO_2 oxides, which are more stable phase, under the applied anodic potential.[62,76] Nevertheless, the reconstruction could also lead to some negative impacts to the catalyst dissolution due to the transient dissolution mechanism.[62] Indeed, the formation of amorphous IrO_x in the surface of IrO_2 catalysts resulted in Ir(III) hydrous oxide, which could trigger the LOM mechanism and fasten the Ir dissolution rate.[79–82]

Besides intrinsic properties of OECs and oxidative potentials, the decreased OER performance in an electrochemical system can originate from the instability of substrate materials or the loss of catalysts materials due to peeling off. In fact, with the same catalyst materials and loading amount, varying substrate materials could cause a significantly different degradation behavior of electrodes. For example, the stability of Co_3O_4 deposited on fluorine-doped tin oxide (FTO) glass is significantly better than that on a titanium (Ti) foil (**Figure 2.5a**).[83] It was due to the change of catalyst|substrate interface causing the passivation of Ti foil and promoting the degradation of the catalyst. Similarly, carbon fiber paper or Ti felt substrates are unstable in oxidative acidic conditions, and their degradation causes the exfoliation of coated catalysts, resulting in the unstable OER performance.[84] Among the common substrates, FTO is the most excellent substrate for OER tested in H_2SO_4 electrolyte over a wide range of anodic potential (**Figure 2.5b**).[85] To date, despite various newly developed substrates, Pt/Ti-based materials stands out as the most remarkable candidate, which are widely employed in the accelerated durability tests at high temperature and applied current density in acid.[86–88]

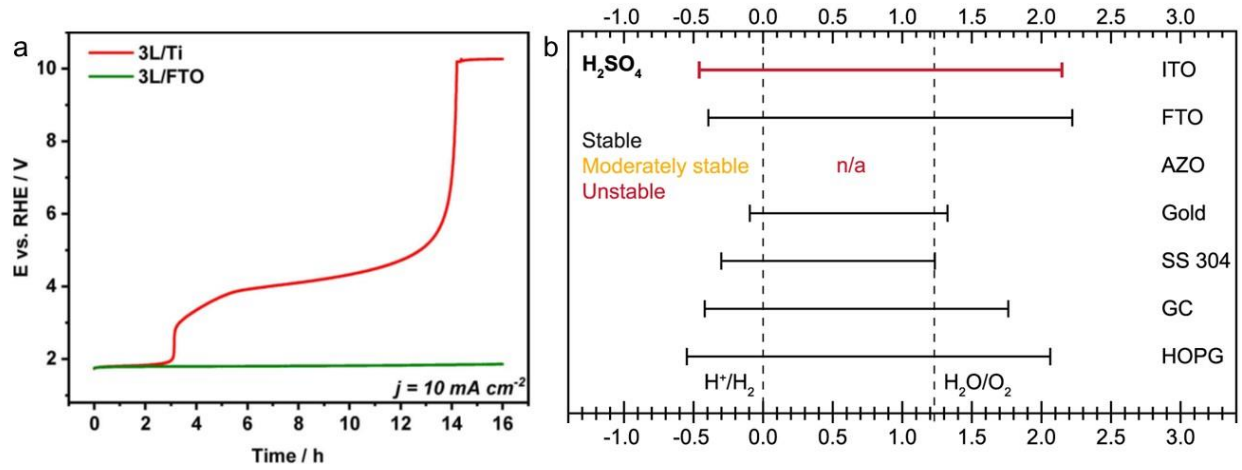

Figure 2.5 a) Comparison chronoamperometry of Co_3O_4 deposited on FTO or Ti foil at 10 mA cm^{-2} in 0.05 M H_2SO_4. Reproduced with permission from ChemCatChem 13, 1 (2020).[83] Copyright 2020

Wiley. b) Stable potential range of various substrates in 0.1 M H_2SO_4 electrolytes. Benck *et al.*, PLOS ONE, 9, 10, 2014;[85] licensed under a Creative Commons Attribution (CC BY) license.

Another reason for the unstable OER performance is the surface blockage of catalyst sites by the accumulation of O_2 gas bubbles due to the limited solubility of molecular oxygen in the electrolyte.[89–91] The bubbles can evolve to the large nucleation before the detachment from the substrate as shown in (**Figure 2.6**).[22,89] This process leads to the undesired coverage of the active site then block the ion conducting pathways at the heterogeneous interfacial area on the catalyst's surface such as pores, cracks, or crevices and weaken the mechanical stability of electrodes. The formation of an insulating layer at a catalyst|substrate interface inhibits electron transport or reduces the electrical conductivity, leading to the degradation of OER performance.[84] For instance, the instability of IrO_2-Ta_2O_5 catalysts in an 0.5 M H_2SO_4 electrolyte is attributed to the formation of the passivation layer between the catalyst layer and Ti substrate.[92]

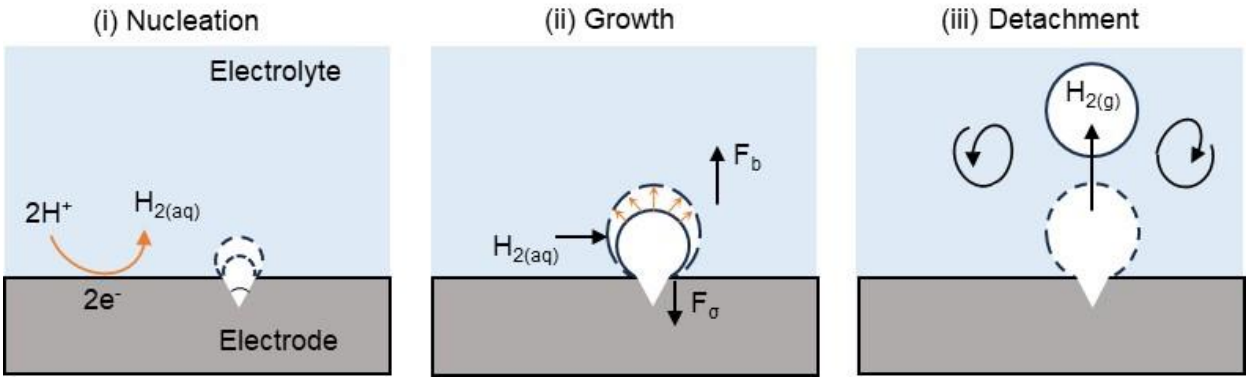

Figure 2.6 Schematic illustrating three stages of O_2 bubble evolution. Gas bubbles are started as i) the nucleation on cracks or crevices, then they ii) grow by accumulated dissolved gas, and (iii) detach from them including i) the nucleation, ii) the growth, and iii) the detachment from the electrode surface. Reproduced with permission from Joule 4, 3 (2020).[89] Copyright 2020 Elsevier.

Additionally, the binding and support materials are crucial to the OER stability. Catalyst powder is usually distributed and fixed in the surface of an electrode using ionomer binders such as Nafion.[23,55,93] However, under the nucleophilic attack of water or oxidation by oxygen radical species through substitution and elimination reaction, or the oxidative potential, the ionomer binders can be degraded, causing in the loss of OER activity. Support materials are also important components which have a wide range of effects on catalyst properties.[22,45,54–56] A strong interaction between catalysts and supported materials is expected to suppress the corrosion or dissolution behavior such as diffusion, aggregation, segregation, or reconstruction. Among varied types of supported materials, carbon-based supports have been widely deployed in electrocatalysis due to

their irreplaceable high conductivity, specific surface area, as well as controllability. One of the prominent carbon-based materials is Vulcan, a commercial carbon black product, which is widely employed to prepare electrocatalysts in the industrial PEMWE scale.[94–96] However, they are prone to dissolution under cumulative acidic and oxidative conditions, especially at a high applied potential. Carbon-based materials are found to be electrochemically oxidized to CO and CO_2 at an applied anodic potential greater than 0.9 V *vs*. reversible hydrogen electrode (RHE: potentials reported in this review are on the RHE scale; unless otherwise specified).[97] Consequently, it causes detrimental effects on catalysts such as the susceptibility of catalyst morphology, which reduces the electroactive surface area of carbon-based materials, the gasification to form gaseous oxidative by-products, and the formation of passivating surface from saturated carbon.[98–100]

2.2.2. Evaluation OECs stability

Several electrochemical techniques have been employed to assess the stability of OECs including cyclic voltammetry (CV), chronoamperometry (CA), and chronopotentiometry (CP). Readers are advised to explore the comprehensive studies available in the literature regarding these techniques, especially the pitfalls during the electrochemical measurements and analyses.[101–111] Briefly, one of the most understandable and straightforward methods to interpret the stability of OECs is recording the change of a cell potential under an applied constant current density (CP curves) over time.[112,113] The decaying of an OEC is interpreted by an increase in operated potential during operation to remain a fixed current. The stable duration is usually determined by the longest operation time before CP curves suddenly rise and halt (**Figure 2.7**) or the fixed time when there is no significant change of overpotentials.[45,114–118] Another electrochemical method for stability evaluation is to track the change of current under a constant voltage (CA curves) versus reaction time. In contrast to the chronopotentiometry, chronoamperometry evaluate catalyst stability by the stable operation time before CA curves degrade.[45,119–122] Sudden increase in CP or decrease in CA curves implies a reduction of loaded catalysts or a catalytic activity. Alternatively, cyclic voltammetry can be used.[45,121,123–126] Dissimilar to CA and CP, a durability test based on CV is conducted by continuously scan currents in an interested potential range (*e.g.*, 1 – 2.5 V vs RHE). The minimal change of currents over time from different cycles implies the high catalyst stability. Cyclic voltammetry offers advantages of reflecting stability in a relatively wide range of overpotential and current under transient conditions; however, its practical application is limited. It can be ascribed to backward scans of CV curves (reduction), which can reverse the degradation of catalyst induced by the anodic polarization in forward scans (oxidation), resulting in less accurate evaluation.

Besides, practical implementation often requires a constant production (such as stable H_2 evolution), which further complicates its use.

However, evaluating the interpretation of OEC stability solely on data derived from these techniques can lead to inaccurate conclusions. As illustrated in (**Figure 2.7**) below, even though the applied potentials may remain relatively unchanged over time intervals t_1, t_2, and t_3, there is a continuous dissolution of the catalysts. The observable changes in potential merely become apparent when the catalyst loading becomes substantially low. Indeed, the longevity of the "stable time" for the same catalyst is dependent on the mass loading. Therefore, it is crucial to report electrochemical data alongside mass activity to accurately evaluate the stability of a catalyst and compare its intrinsic activity across different catalytic materials, especially in case of noble metal-based OECs. The importance of monitoring mass loss was highlighted in Frydendal *et al.* study.[127] Particularly, despite the mass loss of RuO_2, detected by electrochemical quartz crystal microbalance (EQCM) and inductively coupled plasma mass spectrometry (ICP-MS) from stability test at 30 mA cm^{-2}, was higher than that collected from the experiments at 1.8 V in 0.05 M H_2SO_4 electrolyte, the electrochemical measurement showed more significant degradation of OER performance throughout operation in the latter case. Mass activity, denoted as (A g^{-1}), is determined by dividing the current density by the catalyst loading, as expressed in the Equation 1 below.

$$\text{Mass activity} = \frac{j}{m}, \qquad \textbf{(Equation 2.1)}$$

where j and m represent a current density (A cm^{-2}) at the specific overpotential and mass loading of an active component in an electrocatalyst, respectively.[18,128,129] For instance, Shi *et al.* reported the mass activity of Ir:WO_3/Ir (0.72 mg_{Ir} cm^{-2}) at 13.8 A mg^{-1}_{Ir} in 0.5 M H_2SO_4 electrolyte with 260 mV overpotential, which is one of the highest value recorded for low-content-noble materials.[130]

Likewise, Cherevko's group introduced stability number (S-number) to evaluate the catalyst durability.[82] It characterized the correlation between the O_2 formation during OER and the dissolution of a given element in OECs throughout a constant current or potential hold. In practice, S-number could be calculated using the Equation 3 below.

$$\text{S-number} = \frac{n(O_2)}{n(metal)}, \qquad \textbf{(Equation 2.2)}$$

in which $n(O_2)$ and n(metal) are the molar amount of O_2 evolved and metal dissolved during stability test.[131]

For example, Geiger *et al.* utilized S-number to present the dissolution process of IrO_x with the change of current load since it is independent of catalyst loading, surface area, and active sites (**Figure 2.8a**).[82] The data show that a nearly unchanged S-number of crystal IrO_x and other amorphous IrO_x over a wide range of current density (0.1 – 1000 mA cm^{-2}), indicating a direct relation between oxygen evolution and dissolution metal in the tested region. The lower S-number in amorphous compounds could be explained by a weaker bonding of the lattice oxygen in amorphous structures compared to crystalline ones. Indeed, it would enable a direct participation of lattice oxygen in the OER and the formation of metastable with activated iridium complexes, the more prone compound to dissolution.[69]

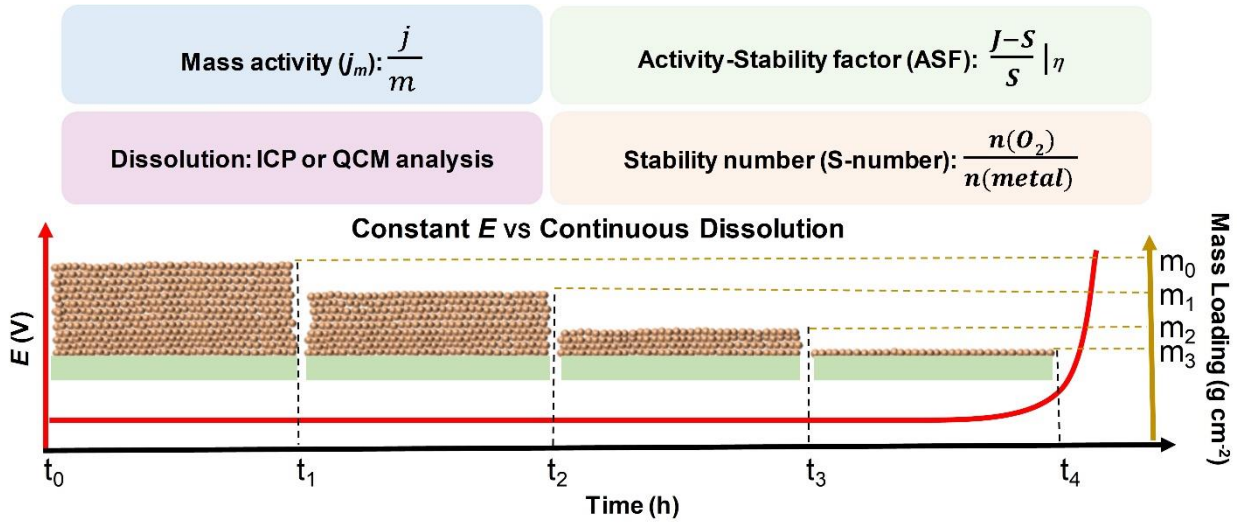

Figure 2.7 Schematic represents the combination of electrochemical and physical characterization to investigate the activity and stability of acidic OECs. The golden circles representing catalysts loaded on light-green rectangle substrates.

Additionally, the intrinsic stability and the degradation of OECs throughout the long-term OER operation is evaluated based on the proposed activity-stability factor (ASF) as expressed in **(Equation 2.3)** below.

$$\text{ASF} = \frac{J-S}{S}|_\eta, \qquad \textbf{(Equation 2.3)}$$

where J and S denote the rate of O_2 formation (expressed as current density, J) and the rate of metal dissolution (equivalent dissolution current density, S) achieved at a constant potential (η), respectively.[132] For instance, Kim *et al.* used ASF parameter to compare OER activity between dealloyed thin films (dtf-$Ir_{25}Os_{75}$) and a colloidal film from nanoparticle materials (dnp-$Ir_{50}Os_{50}$) as shown in **(Figure 2.8b)**. The authors believed that dtf-$Ir_{25}Os_{75}$, owning a good balance between

activity and stability, is more technologically relevant for efficient oxygen production in water electrolyzer.

Both ASF and S-number are more catalyst-specific metrics independent of the active sites, surface area, and loading amount. Therefore, they are expected to provide more accurate information relating to the intrinsic stability of OECs. Especially, S-number particularly attracts significant interest and have been adopted in many publications.[54,82,95,131,133,134]

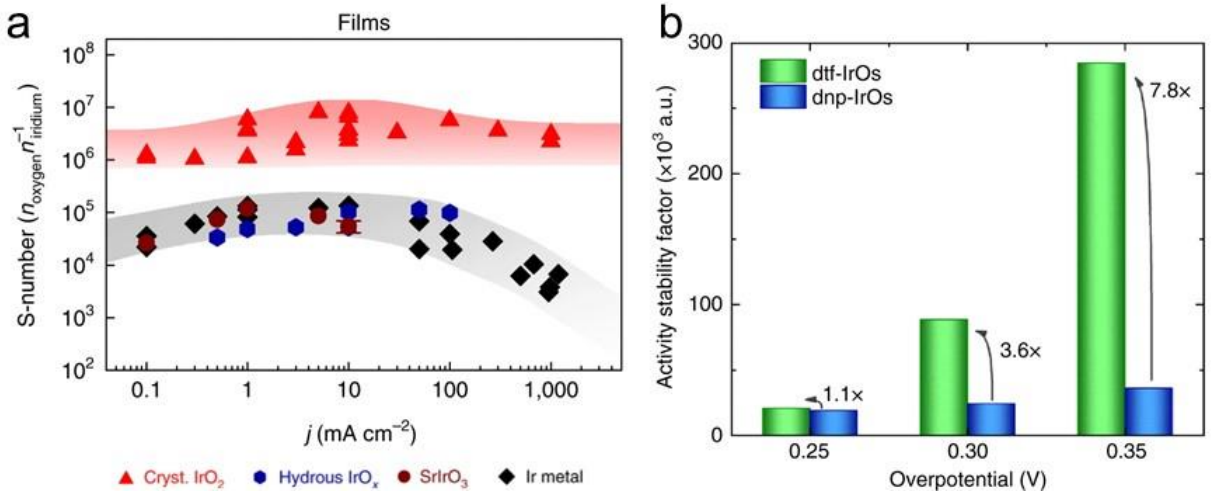

Figure 2.8 a) S–number plotted versus geometric current density for sputtered films IrO_x. Reproduced with permission from Nat Cal, 1, 508–515 (2018).[82] Copyright 2018 Springer Nature. b) Changes in activity-stability factor (ASF) values with overpotentials for dtf-$Ir_{25}Os_{75}$ and dnp-$Ir_{50}Os_{50}$. Kim *et al.*, Nat Commun 8, 1449, 2017;[132] licensed under a Creative Commons Attribution (CC BY) license.

Generally, concentration of dissolved metal cations is monitored by ICP-MS and/or (E)QCM. For instance, Cherevko et al. developed a scanning flow cell coupled with ICP-MS (SFC/ICP-MS) to investigate the electrocatalyst dissolution of six noble metals (*i.e.*, Ru, Au, Ir, Rh, Pt, Pd) in parallel with the interrelated activity.[62] It demonstrated the degradation of OER performance and the etching of OECs in the dissolution profile recorded within the change of electrochemical conditions. Sharing the similar interest, Inzelt *et al.* detected the degradation of Pt-based catalyst through the loss of Pt mass from the soluble Pt species and the formation of PtO_x at high positive potentials and temperatures via an electrochemical quartz crystal nanobalance (EQCN).[135] The incorporation of both QCM and ICP-MS in an online electrochemical system could monitor the mass loss more accurately, and the amount of dissolution materials could be a useful evaluation parameters of stability together with the long-term electrochemical test.[127]

2.3. Designing stable oxide systems

Among the non-precious elements, oxides derived from Co and Mn, such as Co_3O_4 and MnO_x, exhibit considerable promises as active OECs in acid. However, their intrinsic instability at low pH poses a substantial challenge for practical implementation.[136] It underscores the need for a novel strategy aimed at developing a stable matrix in an acidic environment, herein referred to as a 'stable matrix.' Such materials can be achieved by modulating crystal structures of structural elements or compounds and integrating them with more active elements to enhance electrocatalytic activity. Typically, the structural elements are thermodynamically acidic inert in suitable pH and potential ranges, as elucidated by the Pourbaix diagram (**Figure 2.9**).[118] Within this category, lead (Pb) and antimony (Sb) stand out as key elements extensively employed in studies on acidic-stable OECs. Additionally, spinel-type oxides of Co and Mn are modulated through the incorporation of foreign elements to construct stable matrices. The distinctive features of these acidic-stable matrices are elaborated upon in this section, and a comprehensive summary of representative acidic OECs developed within this conceptual framework is provided in (**Table 2.2**).

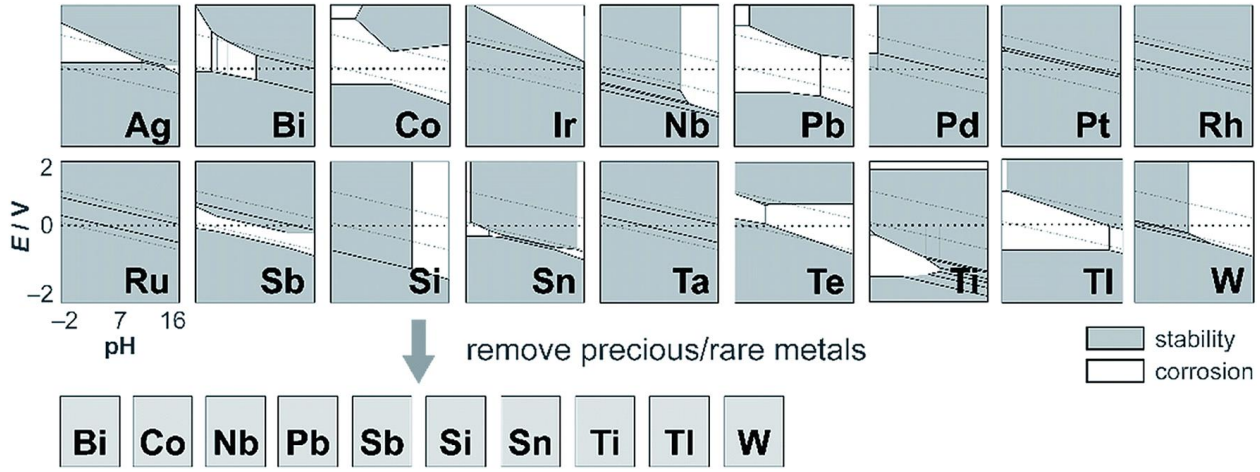

Figure 2.9 Pourbaix diagrams of metals were analyzed for stability in the top left region of the plots (corresponding to high anodic potentials and low pH). The candidates were then filtered by removing precious and rare metals. Huynh et al, Chem. Sci. 8, 4779-4794, 2017;[118] licensed under a Creative Commons Attribution (CC BY) license.

2.3.1. Lead-based catalysts

PbO_x-based materials have long been recognized as robust and acidic-stable OECs, finding application as water oxidation anodes in industrial electrowinning processes in 1.8 M H_2SO_4 at temperatures ranging from 35 – 40 °C.[137] Despite the commendable acidic corrosion resistance of PbO_x materials, their specific activity remains constrained. A promising strategy to address this

limitation is coupling PbO_x with an active component. For example, Bonke *et al.* introduced FePb-based materials to function as self-regenerative OER catalysts with the continuous formation of active FeO_x stabilized by PbO_x in slightly acidic conditions (pH 2.9).[122] This study was conducted in wastewater contaminated by metal cations at low concentrations. An *in situ* generated FePb-based system still performed relatively low OER activity, exhibiting a current density of 4.5 mA cm^{-2} at an overpotential of 0.8 V in pH 2.9. To enhance the performance of PbO_x matrices in acidic OER, Li *et al.* explored the incorporation of MnO_2 into PbO_2 matrices with phosphorus dopants.[138] The phosphorus-doped (P-doped)-PbO_2-MnO_2 anode demonstrated an improved electrocatalytic activity, reducing the overpotential by approximately 139 mV as compared to a P-doped PbO_2 anode and maintaining a current density of 10 mA cm^{-2} for 90 minutes in 1.63 M H_2SO_4 electrolyte.

Likewise, Huynh *et al.* integrated both Co and Fe into PbO_x matrix to generate $CoFePbO_x$ using electrodeposited.[118] $CoFePbO_x$ demonstrated sustained performance, operating continuously at around 1 mA cm^{-2} with a steady 220 mV overpotential for over 50 hours in a sulfate buffer pH 2. Subsequent research in the same group incorporated highly active Ni OER catalysts into the stable PbO_x framework to form $NiPbO_x$ that showed 1 mA cm^{-2} OER activity for an extended 20 hours at an applied bias of approximately 1.8 V in 0.1 M KPi + 1.75 M KNO_3 electrolyte pH 2.5.[139] Notably, these preliminary studies were only conducted under laboratory-scale conditions, and thus further investigations in industrial benchmarking are required.

2.3.2. Antimony-based catalysts

While PbO_2 has established itself as the most stable matrix, its toxic nature has prompted restrictions on its usage within the ecosystems. Alternatively, antimony (Sb) has undergone extensive investigation as the structural element.[69,123,140–144] Moreno-Hernandez *et al.* studied various Mn-Sb structures in conjunction with Ni via sputter coating on antimony-doped tin oxide (ATO)-coated quartz slides electrode.[123] Amongst these structures, $Ni_{0.5}Mn_{0.5}Sb_{1.7}O_y$ electrocatalyst demonstrated the most stable performance, sustaining a current density of 10 mA cm^{-2} with 735 mV overpotential for over 168 hours in 1 M H_2SO_4 electrolyte (**Figure 2.10a**). After 144 hours of continuous operation, ICP-MS analysis showed approximately 56%, 17%, and 11% leaching of Mn, Ni, and Sb, respectively. The inhibited dissolution of Ni and small amount of leached Sb indicated that the stability of the structure originated from the crystalline rutile-phase of the $NiSb_2O_6$ compound, a thermodynamically stable material in acidic media. Moreover, TEM images revealed the maintained stable lattice spacing (110) of the $NiSb_2O_6$ crystal structure after 144 hours of continuous OER operation (**Figure 2.10b−c**). Recently, Mahidashti *et al.* prepared $Ni_{0.5}Mn_{0.5}Sb_yO_x$

electrocatalysts via thermal decomposition on a Ti substrate. The electrocatalyst exhibited an overpotential of 598 mV to generate at 10 mA cm^{-2} and sustained stability over 168 hours in a 0.5 M H_2SO_4 electrolyte. Post-OER characterizations revealed structural and morphological changes during a one-week electrolysis. Significantly, XPS data indicated a notable shift towards higher binding energies of Mn 2p and a reduction in the Sb^{5+}/Sb^{3+} ratio on the surface, suggesting an increase in Mn oxidation state under anodic potential and a decrease in Sb^{5+} ions due to dissolution into the electrolyte. As expected, ICP data recorded the dissolution of the cations in the order of Sb < Ni < Mn, with the number of dissolved ions decreasing at a higher annealing temperature. The data point to the primary corrosion of Ni, Mn, and Sb, likely resulting from preferential etching from regions with poorer crystallinity.

In addition to Ni and Mn, Babaei *et al.* undertook an investigation into the Sb-stable matrix by incorporating Co to generate $CoSb_2O_x$ on a Ti substrate. This composite exhibited superior stability at 1.8 V, facilitating the sustained current to 10 mA cm^{-2} for over 200 hours.[145] In an accelerated lifetime test, $CoSb_2O_x$ displayed an exceptional lifespan of 650 hours within a potential range of 2 – 2.2 V at a current density of 100 mA cm^{-2}. The study emphasized the critical role of controlling Co:Sb ratio (1:2), as $CoSbO_x$ and $CoSb_{1.5}O_x$ failed to match the comparative stability of $CoSb_2O_x$ under identical conditions. However, the usage of high mass loading of 10 mg cm^{-2} raised concerns about the stability evaluation, thus requiring a more comprehensive analysis based on degradation/dissolution rate or mass activity as discussed in part 3. Similarly, Evans *et al.* prepared phase-pure $CoSb_2O_6$ and $MnSb_2O_6$ as OECs under strongly acidic conditions with electrodeposition.[143] The catalysts exhibited similar OER activity, requiring a 0.76 V overpotential to attain 10 mA cm^{-2} in 0.5 M H_2SO_4 and maintaining the stable current throughout 24-hour galvanostatic measurement.

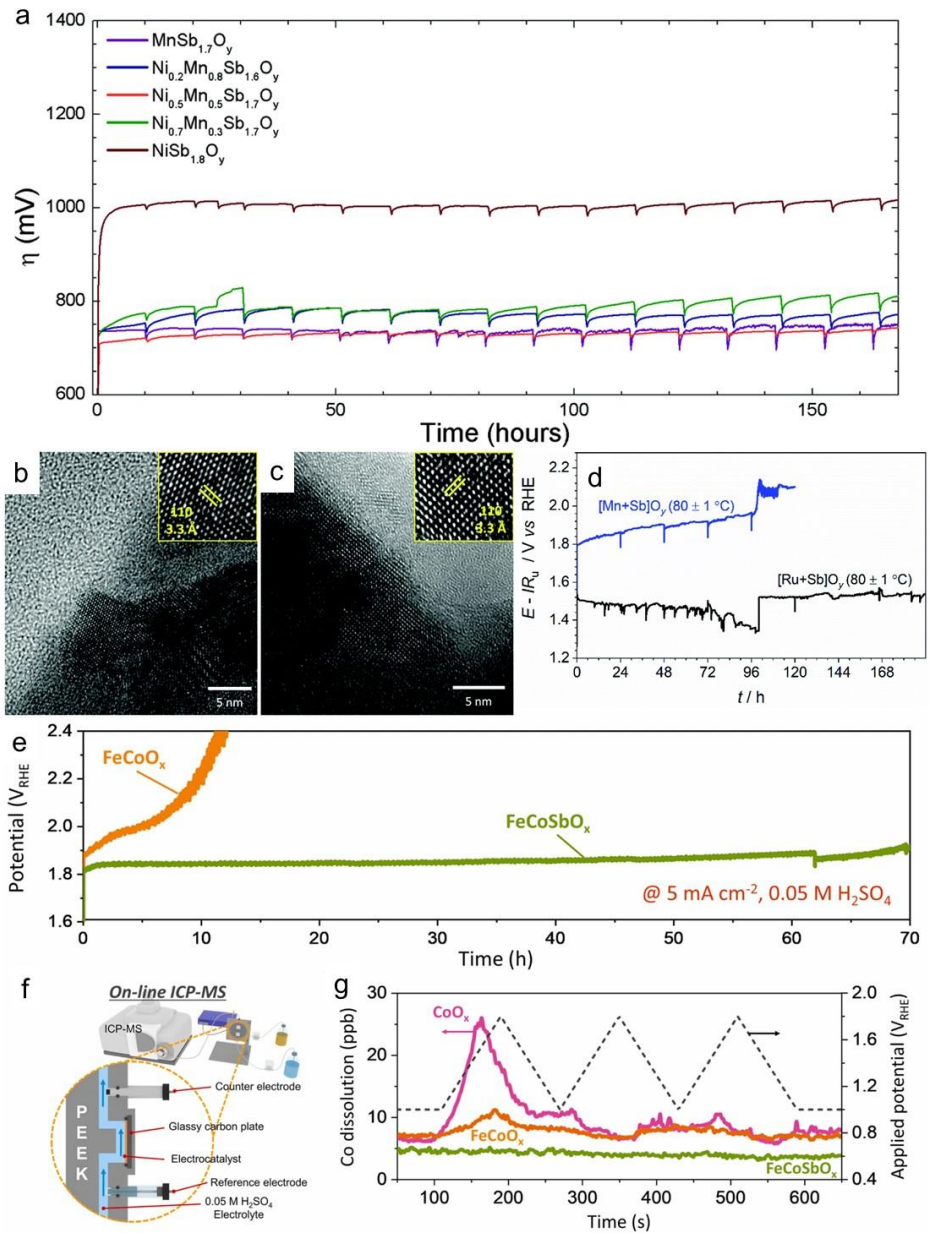

Figure 2.10 a) Chronopotentiometric stability curves at 10 mA cm^{-2} of the $Ni_xMn_{1-x}Sb_{1.6-1.8}O_y$ family in 1.0 M H_2SO_4 electrolyte, b – c) TEM images of $Ni_{0.5}Mn_{0.5}Sb_{1.7}O_y$ b) before and c) after chronopotentiometry for 144 h electrolysis. Reproduced with permission from Energy Environ. Sci. 10, 10 (2017).[123] Copyright 2017 Royal Society of Chemistry. d) Chronopotentiogram of [Ru + Sb]O_y (*black*) and [Mn + Sb]O_y (*blue*) catalysts during the OER in stirred 0.5 M H_2SO_4 at 80 ± 1 °C. Reproduced with permission from J. Mater. Chem. A 9, 48 (2021).[144] Copyright 2021 Royal society of Chemistry. e) Chronopotentiometry curves of $FeCoSbO_x$ and $FeCoO_x$ electrodes in O_2-saturated 0.05 M H_2SO_4 at a constant current density of 5 mA cm^{-2}. f) Schematic of *in situ* ICP–MS experimental setup with a homemade electrochemical

flow cell. g) Co dissolution profiles during cyclic voltammetry measured by on-line ICP-MS. Reproduced with permission from Nano Energy 110, 108355 (2023).[146] Copyright 2023 Elsevier.

In a comparative study, Luke *et al.*, evaluated the OER activity and stability of antimony mixed with either a transition metal or a noble element (Ru). [Ru-Sb]O_x performed the outstanding stability up to 8 day-long tests at 80 ºC, achieving 10 mA cm^{-2} with a stable overpotential of 0.34 V (**Figure 2.10d**).[144] When replacing Ru with a transition metal (*e.g.,* Co, Mn, Ni, or Fe), [Mn-Sb]O_x displayed the robust performance for at least 96 hours to achieve 10 mA cm^{-2} with an overpotential of 0.68 V at high temperature (80 ºC). Subsequent research aimed to explore antimony-manganese matrices by incorporating them with other active elements (*e.g.,* Co, Ru, Pb, or Cr) to create mixed oxide structures.[147] [MnCr + Sb]O_x and [MnRu + Sb]O_x were found to be less stable, while [MnCo + Sb]O_x, [MnPb + Sb]O_x, and [MnCoPb + Sb]O_x maintained a stable performance at a reasonable overpotential to achieve a water oxidation rate of 10 mA cm^{-2}, within 24 hours at both ambient and elevated temperatures. Among them, the [MnPb + Sb]O_x system exhibited the highest OER activity, attributed to the stabilizing effect of lead oxides on catalytically active manganese sites. However, as discussed above, the utilization of lead in mixed oxide OECs is not considered promising due to the toxicity of this element. Wang *et al.* reported the incorporation of Co and Fe with SbO_x matrix to construct $FeCoSbO_x$.[146] The electrocatalyst displayed a stable current density of 5 mA cm^{-2} over 70 hours in 0.05 M H_2SO_4 electrolyte (**Figure 2.10e**). It was attributed to the stronger Sb-O bond, inhibiting distortion during the reaction and preventing the participation of lattice oxygen to enhance thermodynamic stability in the acidic media. Notably, the *in situ* ICP-MS (**Figure 2.10f–g**) shows suppression of Co dissolution from the $FeCoSbO_x$ system as compared to $FeCoO_x$ and CoO_x, suggesting the critical role of Sb in stabilizing this OEC. Nevertheless, the stability test in this work was conducted at a low current density (5 mA cm^{-2}), which is not compatible with the benchmark requirement (10 mA cm^{-2}) in other studies of the same topic.

2.3.3. Manganese-based catalysts

Manganese oxides (MnO_x) emerge as promising earth-abundant catalysts due to their relatively favorable electrocatalytic activity and thermodynamic stability within a specific potential range at low pH, as illustrated by the Pourbaix diagram (**Figure 2.11a**).[148–150] The dissolution of Mn-based oxides in acid was proposed by Peng *et al.* and is briefly described in (**Figure 2.11b)**.[151] This process commences with the release of Mn ions from the surface of the metal oxide structure, followed by solvation with H_2O molecules in the electrolyte. Subsequent protonation of the oxygen sites

polarizes neighboring metal-oxygen bonds, rendering them more susceptible. Consequently, oxygen ions depart from the surface to react with protons in the electrolyte, diffusing into the bulk solution and leading to the complete dissolution of metal oxides. Critical reaction steps of dissolution processes, including protonation, vacancy formation, and ion formation, were found to be closely related to the Mn oxidation states in Mn-based oxide structures.

Mn-based oxides with lower oxidation state (+2 or +3) are typically associated with higher OER activity than MnO_2 (+4) and the instability of Mn-based catalysts is derived from the phase change from MnO_2 to MnO_4^- at a high anodic potential.[152,153] In practice, Huynh *et al.* reported the minimal activity of electrodeposited MnO_x with various phase structure (δ-MnO_2, $Mn(OH)_2$, α-Mn_3O_4), achieving solely 2 mA cm^{-2} at an overpotential of 600 mV and limited stability at a modest current density of 0.1 mA cm^{-2} for over 8 hours.[152] Therefore, concerted efforts in material design are imperative to stabilize Mn-based oxide systems and further enhance their catalytic activity.

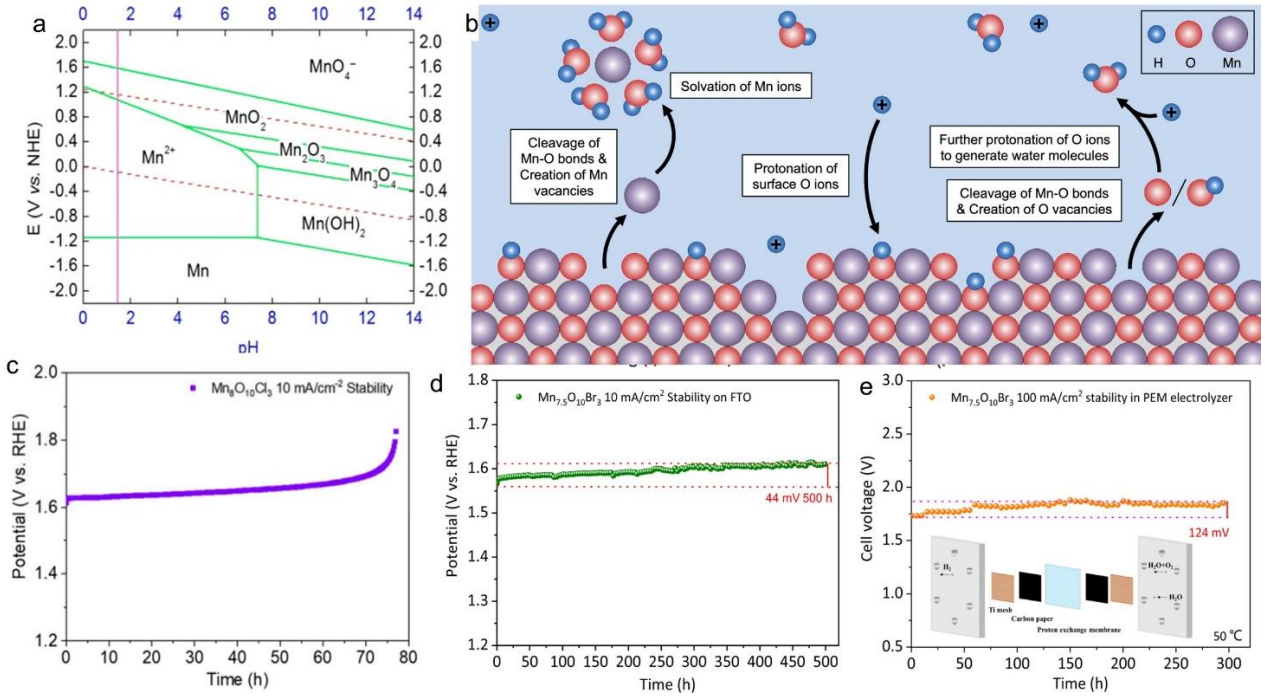

Figure 2.11 a) Simplified Pourbaix diagram for manganese oxide in aqueous solution. Reproduced with permission from J. Am. Chem. Soc. 136, 8 (2014).[148] Copyright 2014 American Chemical Society. b) Proposed the dissolution of Mn-based oxides in acid. Reproduced with permission from Chem. Mater. 34, 17, (2022).[151] Copyright 2022 American Chemical Society. c–e) Chronopotentiometry curves of c) $Mn_8O_{10}Cl_3$ and d–e) $Mn_{7.5}O_{10}Br_3$ oxide catalysts d) on a FTO substrate and e) in a PEM electrolyzer operated with a current density of 10 mA cm^{-2} at ambient

temperature and 100 mA cm^{-2} at 50 ºC, respectively. Reproduced with permission from Nat Commun 13, 2294 (2022).[117] Copyright 2022 Springer Nature.

The design of active and stable Mn-based oxides for acidic OER has predominantly relied on cation/anion substitution into MnO_x to modulate the electronic and crystal structure. For instance, Frydendal *et al.* demonstrated that the incorporation of a small amount of Ti into the MnO_2 structure could stabilize the structure in 0.05 M H_2SO_4 electrolyte, as confirmed by a decreased mass loss using EQCM and ICP.[154] The selection of Ti was informed by the DFT calculations on surface formation energy. The results indicated that TiO_2 is a cost-effective and acid-stable material with the ability to selectively block undercoordinated sites, which are particularly prone to dissolution. Likewise, Huynh *et al.* incorporated Co as a catalytically active element into MnO_x matrix to form $CoMnO_x$ structure.[118] This OEC enhanced acidic OER kinetics with approximately Tafel slope of 82 mV per decade in pH 2.5 and maintained a stable activity of 0.1 mA cm^{-2} for over 12 hours. However, the stability diminished at a higher current density due to the oxidation of Mn^{3+} to MnO_4^- following by the dissolution into electrolyte, turning the electrolyte solution into slightly pink.[118,152] To address this challenge, Sb was proposed to be incorporated into MnO_x.[124,155,156] The Mn-Sb-O system can maintain the valence state of Mn species between +2 and +3 based on the existence of Sb, thereby stabilizing Mn-based structures.[124] As a result, this OEC exhibited significantly higher activity, achieving a current density of ~50 mA cm^{-2} at 0.58 V overpotential in pH 0 with a gradual degradation observed over 4000 CV cycles.

In addition to metal cations, several research endeavors have explored the substitution of anion ions (*e.g.,* F^-, Cl^-, Br^-) into oxygen sites of MnO_x system to tune the electrocatalytic activity and stability. For example, substituting electronegative F^- in lieu of oxygen sites in oxide structures may render the neighboring sites more electron deficient and create relatively electron-poor active sites, thereby improving OER performance.[119,157,158] The synergistic interplay between Mn and guest metal species could facilitate OER activity based on the abundance of Mn^{3+} active species in surface, and prolong stability by tuning the bonding strength between metal and oxygen in structure. For instance, an Fe-Mn-based fluorinated oxide $MnFe_2F_{5.8}O_{1.1}$ exhibited sustained OER performance of 10 mA cm^{-2} at 515 mV overpotential over 20 hours in 0.5 M H_2SO_4.[157] Similarly, Patel *et al.* reported F-doped $Cu_{1.5}Mn_{1.5}O_4$ electrocatalysts, displaying a current density ~ 9 mA cm^{-2} at 1.55 V potential and the long-term stability for 6000 cycles with only negligible loss of performance in 0.5 M H_2SO_4 for 24 hours.[121] Subsequent work of this group demonstrated the influence of 10 wt% F on the activity in the $(Mn–Nb)O_2$ structure, reporting an enhancement on

electrocatalytic with a lower overpotential (0.68 V) to achieve a current density of 10 mA cm^{-2}, compared to that value recorded for undoped sample (0.87 V).[158] In terms of the stability, the current density gradually decayed from 8 to 6 mA cm^{-2} at a constant potential of 1.9 V in 1 N H_2SO_4 at 40 °C through 24-hour chronoamperograms.[158] Beyond fluorine, Pan *et al.* investigated the impact of Br and Cl on the OER activity and stability when introducing in MnO_x structure.[117] Between Br- and Cl-doped materials, Br-based materials were determined to have higher catalytic activity and better stability at 10 mA cm^{-2}. In specific, it required an overpotential of 295 mV for $Mn_{7.5}O_{10}Br_3$ OEC to generate a stable current density of 10 mA cm^{-2}, while the overpotential increased to 365 mV when $Mn_9O_{10}Cl_3$ catalyst was used. Regarding stability, the applied potential increased sharply after 75 hours with the $Mn_9O_{10}Cl_3$ catalyst (**Figure 2.11c**), whereas $Mn_{7.5}O_{10}Br_3$ demonstrated the ability to maintain a constant current density of 10 mA cm^{-2} over 500 hours in 0.5 M H_2SO_4, with only a 44 mV increase in applied potential (**Figure 2.11d**). When applied in a PEM electrolyzer, $Mn_{7.5}O_{10}Br_3$ could sustain a current of 100 mA cm^{-2} at 50 °C, experiencing a 124 mV increase in cell voltage after 300 hours electrolysis (**Figure 2.11e**). Characterization analysis elucidated the excellent stability arising from the self-oxidation process, resulting in the formation of a stable close-packed oxide to passivate MnO_x surface. This passivation layer acts as a protective shield for the catalyst structure under the anodic oxidation. Regarding OER activity, the superior performance was attributed to the Mn-halogen interaction, which enhances the electron transport capacity, along with the more favorable adsorption energy derived from Mn-O-Br.

2.3.4. Cobalt-based catalysts

Among various non-precious metal oxides, spinel Co_3O_4 stands out as the most renowned and extensively investigated oxide in acidic media.[136] The catalytic activity of Co_3O_4 is theoretically depicted by a volcano plot, illustrating the correlation between catalytic activity and calculated oxygen absorption energy based on the free energy diagram. This plot reflects the notably high activity of Co_3O_4, comparable to those of noble oxides such as IrO_2 and RuO_2 (**Figure 2.12a**).[159] Despite its commendable OER activity, the practical utilization of Co_3O_4 is constrained by its relatively low stability presented in Pourbaix diagram (**Figure 2.12b**).[148]

The degradation mechanism of Co_3O_4 in acidic OER is succinctly outlined in (**Figure 2.12c−d)** by *operando* Raman spectroscopy investigation.[160] Under the applied anodic oxidation potential, an atomically thin hydrous oxide layer (HOL) $CoO(OH)_x$ forms on the surface of Co_3O_4 and gradually grow into the bulk over the course of electrolysis (**Figure 2.12c**). The three-dimensional (3D) layer exhibits an electronically conductive and porous structure, facilitating the flow of electrons and

electrolytes. Nevertheless, when HOL becomes excessively thick and distant from the anhydrous oxide support underlayer, Co_3O_4 undergoes complete degradation into dissoluble CoO_x ions. HOL formation is attributed to the generation of oxygen vacancies in LOER cycle, exposing the metal-oxygen network to increase water attack and susceptibility to degradation (**Figure 2.12d**). Consequently, the authors proposed that the key stabilization strategy for Co_3O_4 catalysts is promoting the formation of Co^{3+} and Co^{4+} to enhance the active sites and reduce corrosion attack. Nevertheless, the existent of $Co^{>3+}$ species during OER remains controversial due to its transient nature, making it challenging to be detected by *in situ* X-ray absorption spectroscopy.[161–164]

Acidic-stable matrix of spinel Co_3O_4 were attained by integrating foreign metal elements (*e.g.,* Fe, Ag, Ba, Zn, Pd, Ce, *etc*.) into its structure.[136] These exotic integrated elements improve the OER activity, optimize the electronic structures, and expedite electron transfer between the heterointerfaces.[165] Therefore, they can modify the local bonding environment of Co_3O_4 to facilitate the oxidation of Co^{3+} surface species to Co^{4+}, resulting in the substantial enhancement of OER activity. For example, Anantharaj *et al.* synthesized Co_2TiO_4 by incorporating Ti^{4+} ions into the spinel lattices of Co_3O_4 at octahedral sites. The catalyst significantly boost OER activity, requiring a 513 mV overpotential to sustain a current density of 10 mA cm^{-2}, a reduction of 336 mV as compared to a bare Co_3O_4 anode.[166] Nevertheless, the stability of Co_2TiO_4 structure during OER tests was compromised, leading to its reconstruction into Co_3O_4 on the surface and a notable decline in activity. Similarly, the incorporation of Zn to form $ZnCo_2O_4$ spinel-type structure was reported, resulting in a three-fold increase in OER activity.[167] It was explained by the redox inert Zn^{2+} at the tetrahedral site of $ZnCo_2O_4$, stabilizing a high-valent Co^{4+} intermediate via oxidation of Co^{3+} and promoting more active sites for the water oxidation reaction. Nevertheless, its influence on extending acidic OER stability was not clarified. Wang *et al.* reported Ba-doped $Co_{3-x}Ba_xO_4$ on carbon paper, and the catalyst displays superior activity, requiring an overpotential of 278 mV for 10 mA cm^{-2}, and stability (110 hours) in 0.5 M H_2SO_4.[168] The doping of Ba was believed to trigger the adsorption of OH^- groups on the surface and promote the oxide path mechanism (OPM) pathway for O-O coupling, thereby expediting OER kinetics. Instead of substituting Co sites by foreign cations, nanocrystalline CeO_2 was incorporated with Co_3O_4 to form a heterogeneous Co_3O_4/CeO_2 nanocomposite.[169] The composite structure was proposed to modify the local bonding environment of Co_3O_4, facilitating the Co^{3+} to Co^{4+} oxidation, bypassing the potential-determining surface reconstruction process. Consequently, the Co_3O_4/CeO_2 composite exhibited enhances OER activity and stability for over 100 hours in 0.05 M H_2SO_4 at a current density of 10 mA cm^{-2}.

To date, the most durable Co-based OEC is Co_2MnO_4, synthesized by incorporating Mn into the Co_3O_4 spinel using thermal decomposition method.[114] It achieved a lifetime of over two months (1,500 hours) at 200 mA cm^{-2} in H_3PO_4 pH 1 electrolyte (**Figure 2.12e**). Moreover, Co_2MnO_4 could produce an outstanding OER activity of 1,000 mA cm^{-2} with applied potential below 2 V, a remarkable performance of non-noble metal electrocatalysts in acidic media. This is ascribed to the robust bonding between the lattice oxygen and Mn in the Co_2MnO_4 structure, the critical factor of the dissolution process. Additionally, the relatively high mass loading of ~5 mg cm^{-2} could, to a certain extent, contribute to the record durability of this OEC.

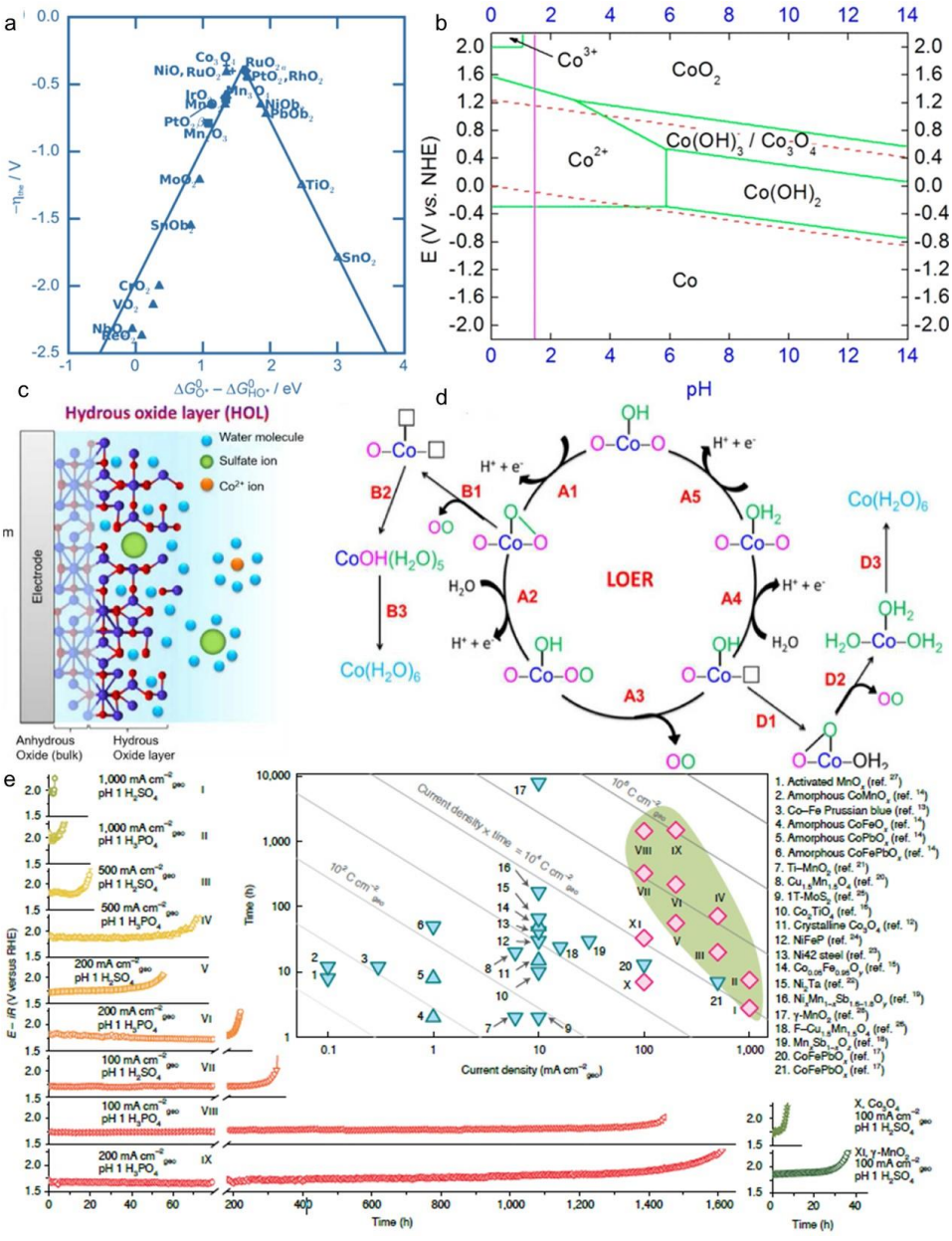

Figure 2.12 a) Activity trends toward oxygen evolution. The negative values of theoretical overpotential of transition metal oxides were plotted against the standard free energy. Reproduced

with permission from ChemCatChem 3, 7 (2011).[159] Copyright 2011, Wiley-VCH. b) Simplified Pourbaix diagram for cobalt oxide in aqueous solution. Reproduced with permission from J. Am. Chem. Soc. 136, 8 (2014).[148] Copyright 2014 American Chemical Society. c) Illustration of hydrous oxide layer, d) Proposed LOER mechanism and the degradation route of Co_3O_4 during LOER. Reproduced with permission from ACS Appl. Mater. Interfaces 13, 23 (2021).[160] Copyright 2021 American Chemical Society. e) Long-term stability of Co_2MnO_4. Time dependence of the electrochemical potential necessary to perform OER at 100, 200, 500 and 1,000 mA cm^{-2}_{geo} in H_2SO_4 (pH 1) and H_3PO_4 (pH 1), respectively. Reproduced with permission from Nat Catal **5**, 109–118 (2022).[114] Copyright 2022 Springer Nature.

Table 2.2 Summary recent acidic "stable matrix" OECs based on earth-abundant materials.

Electrocatalyst	Substrate	Mass loading ($mg\ cm^{-2}$)	Electrolyte	Overpotential (mV)	Stability (h) at j ($mA\ cm^{-2}$)	Decay (r_{decay} / $mV\ h^{-1}$) or Dissolution rate ($r_{dissolution}$ / ($\mu g\ cm^{-2}\ h^{-1}$)	Ref.
Pb, Sb-based OECs							
$CoSb_2O_x$	Ti grade	10	0.5 M H_2SO_4	561	200 at 10 650 at 100[f]	n/a $r_{dissolution}$ ~ 15	[145]
$Ni_{0.5}Mn_{0.5}Sb_yO_x$	Ti substrate	5	0.5 M H_2SO_4	598	168 at 10	n/a	[142]
$[MnPb+Sb]O_x$	FTO	0.23	0.5 M H_2SO_4	600	24 at 10	n/a	[147]
$CoSb_2O_7$	GCE	0.28	0.5 M H_2SO_4	288	40 at 1	n/a	[170]
$FeCoSbO_x$	Ti foam	n/a	0.05 M H_2SO_4	599	70 at 5	n/a	[146]
$[Ru-Sb]O_y$	FTO	0.3	0.5 M H_2SO_4	340	193 at 10	n/a	[144]
$[Mn-Sb]O_y$	FTO	0.3	0.5 M H_2SO_4	710	96 at 10	n/a	
$CoSb_2O_6$	FTO	0.6[a]	0.5 M H_2SO_4	760	24 at 10	n/a	[143]
$NiFePbO_x$	FTO	> 0.08	0.1 M KPi + 1 M KNO_3 pH 2.5	470[b]	25 at 1[f]	n/a	[139]
$Ni_{0.5}Mn_{0.5}Sb_{1.7}O_y$	ATO	> 0.13	0.5 M H_2SO_4	730	168 at 10	n/a	[123]
$CoFePbO_x$	FTO	43.3	1 M H_2SO_4	220[b]	50 at 1	n/a	[118]
Co, Mn-based OECs							
La, Mn-doped Co_3O_4	GCE	0.9	0.1 M $HClO_4$	353	353 at 10	r_{decay} ~ 0.28	[171]
$Mn_{7.5}O_{10}Br_3$	Carbon cloth	7.18	0.5 M H_2SO_4	295	500 at 10	r_{decay} ~ 0.09	[117]
$Co_{3-x}Ba_xO_4$	Carbon paper	1.6	0.5 M H_2SO_4	278	110 at 10	n/a	[168]
Co_2MnO_4	FTO	5	0.1 M H_2SO_4	400 520[c]	300 at 100[f]	$r_{dissolution}$ ~ 17	[114]

Co_2MnO_4	Pt/Ti mesh	n/a	0.1 M H_3PO_4	600[d]	1500 at 200[f]	n/a	
Fe-doped Co_3O_4@C	FTO	1.1	0.5 M H_2SO_4	396	50 at 10[f]	$r_{dissolution}$ ~ 22	172
$MnFe_2F_{5.8}O_{1.1}$	Carbon paper	1	0.5 M H_2SO_4	515	20 at 10[f]	$r_{dissolution}$ ~ 50	157
PdO@Co_3O_4	GCE	0.05	HNO_3 pH 1	523	1 at 10[f]	$r_{dissolution}$ ~ 50	173
Co_3O_4/CeO_2	carbon paper	n/a	0.05 M H_2SO_4	347	100 at 10	r_{decay} ~ 0.55	169
$Mn_{0.8}Nb_{0.2}O_2$:10F	Ti foil	0.3	1 M H_2SO_4	680	25 at 7[e]	n/a	158
$Cu_{1.5}Mn_{1.5}O_4$	n/a	n/a	0.5 M H_2SO_4	324	24 at 3[e]	n/a	119
$Co_{0.05}Fe_{0.95}O_y$	Ti foil	1	0.5 M H_2SO_4	650	50 at 10[f]	$r_{dissolution}$ ~ 20	174
Co_3O_4	FTO	n/a	0.05 M H_2SO_4	500[e]	16 at 1	n/a	83
Co_2TiO_4	Carbon cloth	0.16	0.5 M H_2SO_4	513	10 at 5[e]	n/a	166
Ag-doped Co_3O_4	FTO	n/a	0.5 M H_2SO_4	680	10 at 6[e]	n/a	175
Co_3O_4	FTO	n/a	H_2SO_4 pH 2.5	570	12 at 10	n/a	176
F doped $Cu_{1.5}Mn_{1.5}O_4$	Ti foil	1	H_2SO_4 pH 2.5	> 320	24 at 16[f]	$r_{dissolution}$ ~ 41.67	121
Ti–MnO_2	Au electrode	n/a	0.05 M H_2SO_4	> 670	n/a	n/a	154

Mass loading (mg cm^{-2}) is the mass of total catalyst loaded on substrate, except for ([a]) thickness of catalyst layer on flat substrate (μm).

Overpotential (mV) is recorded at the current density 10 mA cm^{-2}, except for ([b]), ([c]), ([d]), and (e) are reported at 1, 100, 1000, and 5 mA cm^{-2}, respectively.

Stability (hours) is a duration length of stability test measured at j (mA cm^{-2}) current density through chronoamperometric measurement, except for (e) tested by amperometry. Most of the catalysts can remain stable activity throughout the stability test, except for (f) shown the degradation sign when the potential starts to abruptly increase during extended OER test.

Decay rate, r_{decay}, (mV h^{-1}) is calculated by the decreased potential of catalysts reported after stability test.

Dissolution rate, $r_{dissolution}$, (μg cm^{-2} h^{-1}) is calculated by the total mass loading of catalyst divided the stability with the sign of degradation.

2.4. Self-healing OECs

Despite the strategies mentioned earlier that significantly enhance the acidic stability of earth-abundant OECs, their susceptibility to dissolution under anodic conditions remains a limiting factor for their durability. Another approach to address this challenge involves employing the self-healing concept, which relies on the dynamic equilibrium between dissolution and redeposition processes during OER operation. In this manner, the dissolved metal ions can be deposited into the catalyst structure and continued to function as active centers, allowing for a stable reaction without loss of activity.

Indeed, the self-healing concept has been extensively explored across various applications (*e.g.,* bio-inspired synthetic materials, metallic system, *etc*.) and used to describe materials that can autonomously self-assemble and regenerate *in situ*, thereby prolonging the stability and enabling long-term performance at a steady state.[177–179] These regeneration processes are typically initiated under the aid of an external force (*e.g.,* energy, pressure, light, or chemical healing agents).[177–182] Nevertheless, Thorarinsdottir et al. refined the definition of 'self-healing' for OECs to describe materials with regeneration through a dynamic equilibrium under specific OER operating conditions such as pH and applied bias potential.[180] The mechanism of self-healing OECs involves continuous reorganization of electrocatalyst structures through the deposition-dissolution of metal oxides, followed by the water oxidation reaction facilitated by *in situ* generated oxides (**Figure 2.13**).

A critical requirement for self-healing OECs is that the rate of the repair process (deposition) must be equal to or less than the rate of damage (dissolution). Historically, self-healing OECs have been predominantly employed in neutral and alkaline conditions (pH > 3.5) due to more favorable thermodynamic conditions for regeneration process. Nevertheless, in acidic conditions, they have shown exhibited challenges in performing simultaneous OER and self-healing processes.[180,182–185] Noticeably, in the absence of an applied bias potential, the self-healing catalysts dissolve. However, when an appropriate potential is applied, the dissolved cations are redeposited onto the catalyst film, highlighting the importance of optimizing operating conditions.[88,148] In the scope of this work, we reviewed the efforts to improve self-healing materials in acidic OER and summarized representative publications in (**Table 2.3)**.

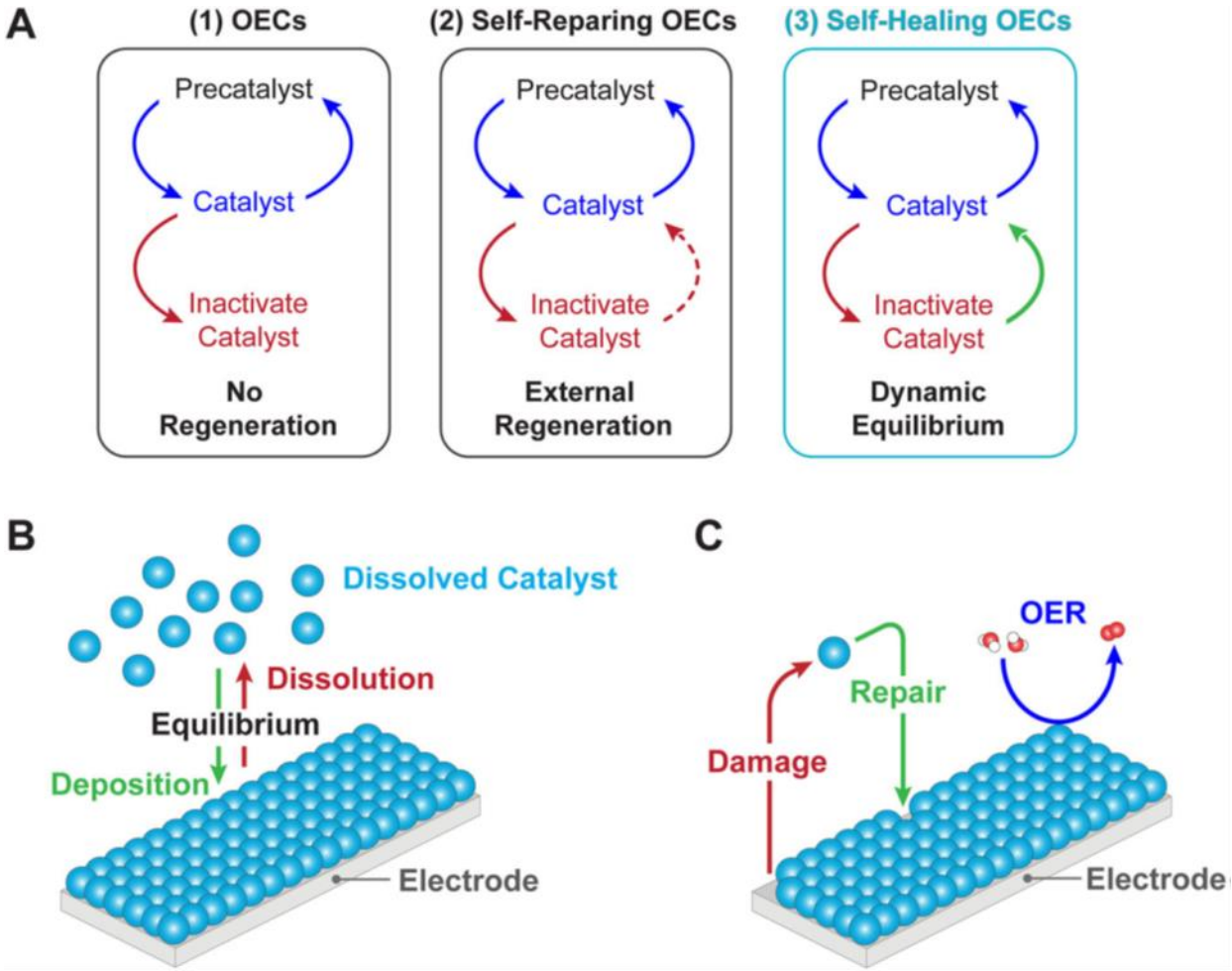

Figure 2.13 Schematic diagram of self-healing OECs. a) Self-repairing materials (center) can overcome the dissolution challenges of conventional OECs (left) and perform sustainable operation as they are regenerated with the aid of external factors. Self-healing OEC is a specific type of self-repairing materials which can continually regenerate through an equilibrium process under OER condition. b) Graphical representing two competitive processes of catalysts, deposition and dissolution that give rise to the equilibrium implicit for self-healing OECs, and c) Damage sites in self-healing OECs are continuously repaired during OER operation, thanks to the equal or greater rate of repairing than damaging processes. Reproduced with permission.[180] Copyright 2022, Springer Nature.

2.4.1. Self-healing Cobalt-based system

Initially, the concept of self-healing cobalt-based catalysts was introduced by Nocera's research group, exemplified by a self-healing Co-Pi OEC in an electrolyte containing cobalt ions and phosphate or methyl phosphonate buffer.[186–189] The researcher described that the self-healing process of Co-Pi catalyst occurs through the oxidation of dissolved Co^{2+} ions to Co^{3+} species and

then be redeposited on catalyst film, resulting in an initial catalyst film in neutral to mildly basic conditions.[180,187]

Instead of phosphate buffer, a subsequent study explored fluoride buffer (F^-/HF), which could meditate the electrochemical water oxidation and support to the self-healing mechanism under mildly acidic conditions (pH 3).[190] Fluoride, with a pK_a of ~3.2, was identified as an effective proton acceptor for water oxidation, facilitating the redeposition of cobalt irons near the acidic-pH limit. These studies underscore the crucial influence of electrolyte compositions on the self-healing functionality of cobalt-based materials. Another factor governs the self-healing process of cobalt-based catalysts is the concentration of dissolved cations.[162,180] For instance, while cobalt-based catalysts exhibit a lack of self-healing capability in phosphate buffer at pH < 5, the introduction of 0.1 – 1 mM Co^{2+} into fluoride electrolyte serves to functionally stabilize the catalyst within the pH range of 3 – 5.[162,190,191] This observed effect is attributed to the increased amount of Co^{2+}, which induces a dynamic equilibrium toward the redeposition process. Nevertheless, there are limited studies focusing on the self-healing cobalt-based catalysts operated at pH < 3. It is likely due to the insufficient redeposition of citations which fails to counterbalance catalyst damage under such rigorous conditions, necessitating substantial cobalt dissolution in the electrolyte and the application of high potentials. For example, Bloor et al. determined that the sustained operation of self-healing cobalt-based catalysts at pH 1.6 required more than 0.6 M Co^{2+} in phosphate or sulfate electrolyte.[148] However, they required a significantly high applied potential, above 2.05 V *vs* NHE, to drive the redeposition of cobalt compounds together with oxidation reaction at a minimal current density 1.8 mA cm^{-2}. It indicated that the self-healing catalysts consisting of only cobalt do not effectively catalyze acidic OER.

Therefore, other OER active metals have been incorporated to tailor catalytic activity and stability at low pH conditions. Chatti et al. introduced the self-healing CoFePb catalysts which could exhibit stable activity during acidic electrooxidation reaction.[87] This robust electrocatalyst could achieve a current density of 20 mA cm^{-2} at ~2.03 V and remain the stable performance for up to 12 hours without a significant loss of activity. The increase in reaction temperatures (60 °C, 80 °C) resulted in the improvement of current densities with no obviously identified loss of performance within 12 hours. Specially, at 80 °C, this OEC could drive a stable oxygen-evolving current density of 500 mA cm^{-2} at an overpotential < 0.7 V. However, the presence of Pb^{2+} and Fe^{3+} has a detrimental effect on electrolyzer components such as the proton-exchange membrane or even the cathode catalysts.[192,193] For this reason, Simondson *et al.* developed a self-healing catalytic system [Co-Fe-

Pb]O_x without the need of such cation ions, but only a 0.05 mM Co^{2+}, in the acidic electrolyte.[194] This OEC showcased the steady and outstanding water electrooxidation, sustaining a current density of 10 mA cm^{-2} over one-week of continuous electrolysis with an overpotential ~0.56 V at 80 ºC.

2.4.2. Self-healing Manganese-based system

In addition to cobalt-based OECs, MnO_x also exhibits functional stability through a self-healing mechanism.[195] The self-healing mechanism of MnO_x was extensively studied across a broad pH range through the electrochemical characterization (**Figure 2.14a**).[196] At pH < 2.5, Huynh et al. identified the most important stage to control Mn-based self-healing is an Mn^{3+} disproportionation process to form MnO_4^- ions at high potentials, preventing reassembling of Mn^{3+}. Consequently, the stability of Mn-OECs in acidic electrolytes is solely maintained at the relatively low applied potential, resulting in minimal OER rate (< 1 mA cm^{-2}).

Further study revealed a more stable phase, γ-MnO_2, capable of maintaining oxygen-evolving current density of 10 mA cm^{-2} over 8000 hours with no noticeable loss of activity in pH 2 electrolytes (**Figure 2.14b**).[197] It presents an exceptionally acid-tolerant performance of pure single metal oxide from earth-abundant materials. However, the sustainable catalytic activity of this material is confined to a narrow potential window of 1.6 – 1.75 V to prevent the MnO_4^- formation (indicated by the appearance of pink color in the electrolyte). Indeed, MnO_2 was deactivated completely within 120 hours at 100 mA cm^{-2} under a potential higher than 1.8 V.

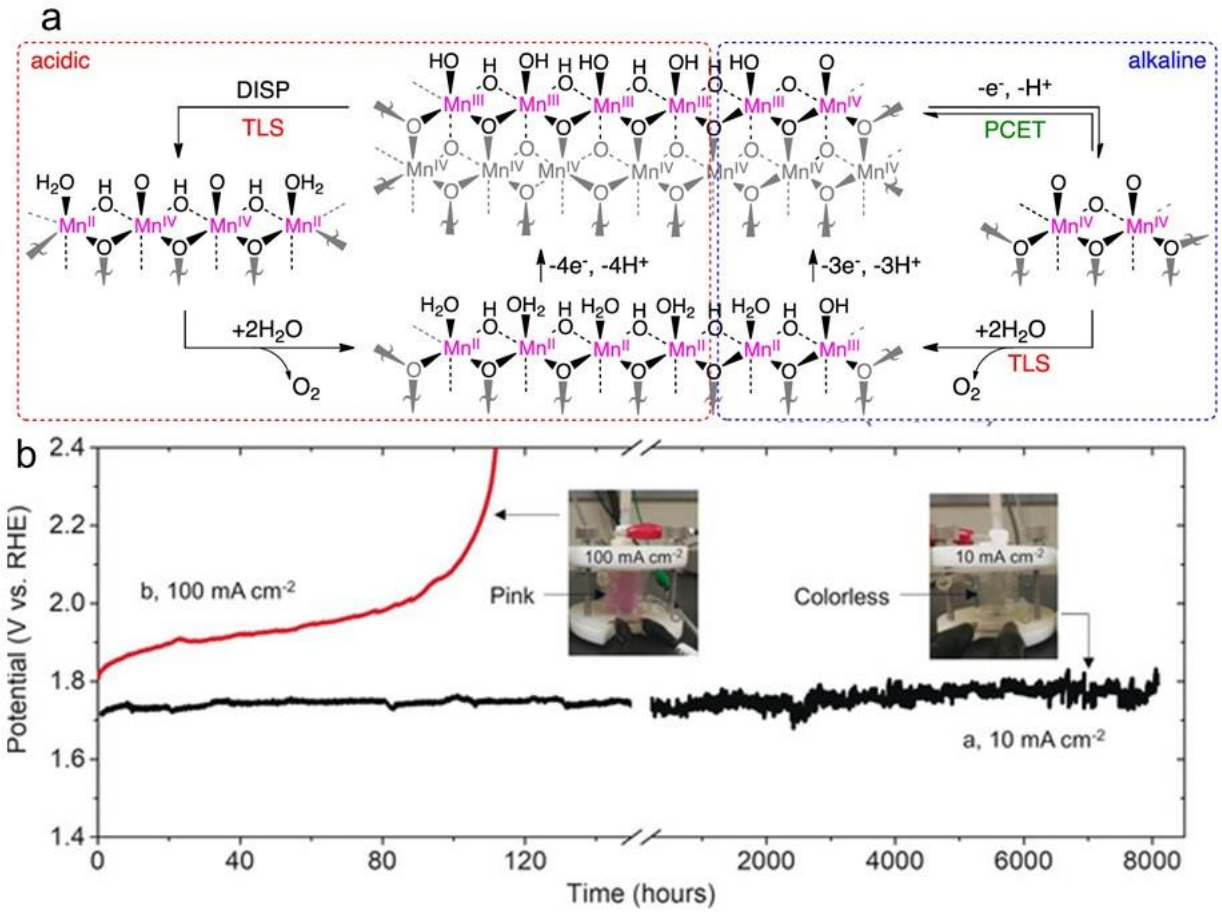

Figure 2.14 a) Proposed mechanism for the OER on MnO_x in (left) acidic and (right) alkaline pH conditions. In the acidic regime, the resting state composed of Mn^{3+} edge sites undergo turnover-limiting cross-site proton-coupled disproportionation to produce adjacent Mn^{4+} sites with terminal oxos. These terminal oxos couple to release O_2. Reproduced with permission.[196] Copyright 2014, American Chemical Society. b) Time dependence of the anode potential during electrolysis operated at a constant current density of 10 mA cm^{-2} and 100 mA cm^{-2}. Reproduced with permission.[197] Copyright 2019, Wiley-VCH.

2.4.3. Self-healing Bismuth-based system

Recently, bismuth (Bi) has emerged as a promising candidate for the structural component of self-healing OECs in acidic media. Thorarinsdottir et al. demonstrated the use of *p*-block bismuth oxide (BiO_x) catalyst to facilitate the long-term OER activity for an extended period of operation (110 hours) in highly acidic electrolyte (pH 1 – 2.25).[183] However, the required potential of 2.4 V to maintain a current density of 5 mA cm^{-2} is considered too high for practical operation as BiO_x is well-known an inactive OEC. Therefore, integration with active elements in BiO_x matrix is necessary to improve OER for realistic performance. Hence, Sn and Co were introduced to generate

Co-Bi-Sn based OECs, resulting in improvement in both activity and stability. In 0.1 M H_2SO_4, the OEC maintains persistent activity at 10 mA cm^{-2} for 9-day-long galvanostatic tests with a required potential of 1.9 V.[198] The study also unveiled the substantial influence of Sn, whether leached from the FTO substrate or intentionally added to the electrodeposition solution, in shaping and stabilizing catalytically active surface species. Likewise, Simondson et al. developed a self-healing [Ag + Bi]O_x OEC that exhibits stability acidic water oxidation conditions (pH ~ 1) at 1.93 V, driving a current density of 10 mA cm^{-2} over 400 hours.[88] Nonetheless, as previously noted, further exploration is needed to understand the impacts of dissolved cations on a membrane and cathode components in PEM cells.

Table 2.3 Summary of recent self-healing OECs in acidic electrolyte.

Electrocatalyst	Self-healing species	Substrate	Electrolyte	Overpotential (mV)	Stability (hours)	Ref.
Co-MnO_2	Co, Mn	Carbon fiber	0.1 M $HClO_4$ containing 2.4 mg mL^{-1} Co^{2+}	770	260	[199]
γ-MnO_2	Mn	FTO	1 M H_2SO_4	489	8000	[197]
[Co–Fe–Pb]O_x	Co	FTO	0.1 M H_2SO_4 containing 0.05 mM Co^{2+} + 80 ºC	570	168	[194]
[Co–Fe–Pb]O_x	Co, Fe, Pb	FTO	0.1 M H_2SO_4 containing 5 mM Co^{2+}, 1 mM Fe^{3+} and 0.5 mM Pb^{2+} + 80 ºC	< 700[a]	160	[87]
CoO_x	Co	FTO	1 M H_3PO_4 (pH 1.6)	1000	30	[148]
[Ag-Bi]O_x	Ag, Bi	FTO	0.1 M H_2SO_4	700	400	[88]
[Co-Bi-Sn]O_x	Co, Bi, Sn	FTO	0.1 M H_2SO_4	670	210	[198]
BiO_x	Bi	FTO	0.01 M H_2SO_4	~ 1170[b]	110[b]	[183]

Overpotential (mV) is recorded at the current density 10 mA cm^{-2}, except for ([a]) and ([b]) reported at 500 and 5 mA cm^{-2}, respectively.

Stability (hours) measured at 10 mA cm^{-2} current density is the duration of the stability test, except for ([b]) reported at 5 mA cm^{-2}.

2.4.4. Passivation layers

Of the abovementioned approaches, many require extensive efforts in material design to precisely tailor OECs structures and composition, impeding efficient utilization of existing catalysts. Applying corrosion-resistant overlayers offers a promising pathway to sustain catalytic performance of OECs without altering their intrinsic structures. While passivation layers are expected to bare the anodic oxidation in acid and physically shield underlying OECs from direct contact with corrosive electrolytes, it should not impede the electron transport between catalyst surface and an electrolyte. Indeed, protective overlayers have been extensively explored in various fields, including photoelectrochemistry, anti-corrosion coatings, or semiconductors, where they can also mitigate surface trapping sites to enhance performance and stability.[200–204] In the scope of this work, we focus only on the utilization of passivation layers in acidic OER and a summary of recent related studies is shown in (**Table 2.4)**.

TiO_2 is one of the most well-known protective overlayers and have been examined for its application on Si, GaAs, GaP, or CdS.[205] Although the crack- and hole-free TiO_2 layer with 1 mm thick, deposited by chemical vapor deposition, exhibited well protective effect for *n*-Si, *n*-GaAs, and *n*-GaP in 0.5 M Na_2SO_4 electrolyte, the thick coating (1 mm) negatively suppressed the interfacial charge transfer and reduced the electrocatalytic activity. It provoked the need for high-quality and precise preparation methods to deposit conformal coatings at nanometer scale.[202,206,207] Atomic layer deposition (ALD) involves depositing reactants atom by atom onto a substrate or surface. This process enables the creation of an exceptionally conformal and high-quality thin film with minimal pin-hole defects, meeting such stringent requirements. Utilizing ALD, Chen et al. fabricated ultrathin TiO_2 layer (2 nm) to protect Ir-catalyst during continuous water electrolysis in 1 M H_2SO_4.[208] The coated catalyst exhibited stability for 8 hours, contrasting to less than half an hour without the TiO_2 coating. Additionally, the TiO_2 layer was also reported to slightly enhance OER activity of underlying OECs. For instance, Finke et al. reported ALD of ~5 nm TiO_2, coated on IrO_2 electrocatalyst, to drive OER at 10 mA cm^{-2} in 1 M H_2SO_4 with a lower potential of 520 mV as compared to 710 mV from unmodified samples.[209] In terms of the longevity, the uncoated samples exhibited a rapid performance degradation within less than 1 hour at 10 mA cm^{-2}, while the thin TiO_2 overlayer (1.5 – 5 nm) enhanced durability to 4 hours and the thick layer (> 15 nm) prolonged stability to 9 hours at the same current density. However, the increased stability from the thick TiO_2 overlayer was accompanied by a decrease in performance, reflected by a rise of 100 mV overpotential compared with uncoated electrodes.[209] In another study, TiO_2 overlayer (7.5 nm) was

utilized to efficiently reduced the dissolution rate of Sn-doped hematite photoelectrocatalyst in 1 M H_2SO_4 electrolyte with a photocurrent density of 0.5 mA cm^{-2} at 1.5 V for 6 hours.[210] Further investigation into the trade-offs between TiO_2 thickness and OER performance revealed promising details.[211,212] The TiO_2 layer as thin as 2 nm showed the thickness-independent overpotential in a wide pH range of pH 0 – 14: in either acidic (1 M H_2SO_4), neutral (1 M phosphate-buffered), or basic (1 M NaOH) solutions, indicating reliable interfacial charge transport.[211] Thicker coating layers demonstrated a linear correlation between coating thicknesses and increased overpotentials.[211] Experimental results indicated that a TiO_2 thickness between 40-60 nm was sufficient to 'complete blocking' semiconductor materials to the electrolyte corrosion, although it compromised the electrocatalytic activity of underlaying catalysts.[212] Therefore, optimization is essential to define the most suitable overlayer thickness for each OEC. For example, in our study, we reported the process to optimize TiO_2 overlayer thicknesses on exemplified Co_3O_4 anode.[116] We found the trade-off relationship between the TiO_2 coating thickness and the OER activity. The thicker TiO_2 layer on Co_3O_4 would result in significantly increased overpotential drive to OER and more aggressive attack to shorten the stability time (**Figure 2.15a−b**). As a result, 4.4 nm was determined the best optimized TiO_2 thickness on Co_3O_4 as it could retain the stable EC performance within the longest operation time of 75 hours at 10 mA cm^{-2}, which was three times higher than the unmodified electrodes. TEM images revealed the progressive degradation of TiO_2 layers, leading to the formation of "pinholes" and ultimately resulting in the complete disappearance of this coating after 40 hours (**Figure 2.15c−e**).

In addition to TiO_2, other group IV metal oxides including HfO_2 and ZrO_2, have recently investigated as corrosion resistant layer in acidic condition.[213] Notably, HfO_2 showed the best chemical stability, without changes in thickness, after 20 days immersed in an acidic solution (1 mol L^{-1} H_2SO_4, 1 mol L^{-1} HCl) as compared to ZrO_2 and TiO_2, which displayed the etched rate of 1.06 and 0.5 – 1.5 nm per day, respectively.[213] However, the durability of HfO_2 under anodic oxidation in acid was not demonstrated. Recently, we studied the role of various oxides, such as TiO_2, Al_2O_3, SnO_2, SiO_2, and HfO_2, in the catalytic activity and durability of sputtered Co_3O_4 catalysts in 1 M H_2SO_4 electrolyte.[214] The experiments revealed that HfO_2 was the most effective protective for Co_3O_4 (**Figure 2.15f**), and an optimal coating of 12 nm increased the durability of Co_3O_4 anode by over threefold, reaching 42 h of continuous electrolysis at 10 mA cm^{-2}. DFT calculations indicated that the bonding energy between underlayer catalysts and overlayer materials plays a significant role in the protective effect, offering valuable information for further studies on ALD protective coating layers for acidic OER applications.

In addition to these oxides, carbon-based materials have recently been studied as protective coatings for noble metal-free OECs.[215,216] Yang et al. introduced a 3.6 nm layer of amorphous carbon on top of Co_3O_4 nanoarrays (Co_3O_4@C), prepared from the calcination carbon paper.[217] In 0.5 M H_2SO_4 electrolyte, Co_3O_4@C displayed a current density of 10 mA cm^{-2} at an overpotential of 0.37 V. Moreover, it exhibited a stable current density of 100 mA cm^{-2} for 86.8 hours with an applied potential lower than 2 V, demonstrating a 20-hour improvement as compared to the sample without carbon coating. Another study presented an amorphous carbon layer on Co_3O_4 catalysts by the direct decomposition of cobalt precursor on a commercial hydrophobic carbon paper, resulting in a robust carbon protection layer with strong adhesion between the catalyst and substrates.[218] This provided the good stability of > 50 hours at a minimal overpotential of 0.35 V to generate a current density of 10 mA cm^{-2} in 0.5 M H_2SO_4 electrolyte. Beyond bare carbon layer, the study has presented nitrogen-doped carbon layers on top of Co_3O_4 powder through ball-milling Co_3O_4 catalysts with a mixture of paraffin oil and graphite powder.[115] The Co_3O_4@C OEC maintained stability for over 40 hours at a low overpotential of ~ 0.4 V to drive 10 mA cm^{-2} current density without experiencing performance fatigue in 1 M H_2SO_4 electrolyte. Despite advancements in the stability of carbon coating, it is important to acknowledge that carbon tends to be oxidized due to its intrinsic thermodynamic and operational instability during anodic oxidation reactions.[215,216]

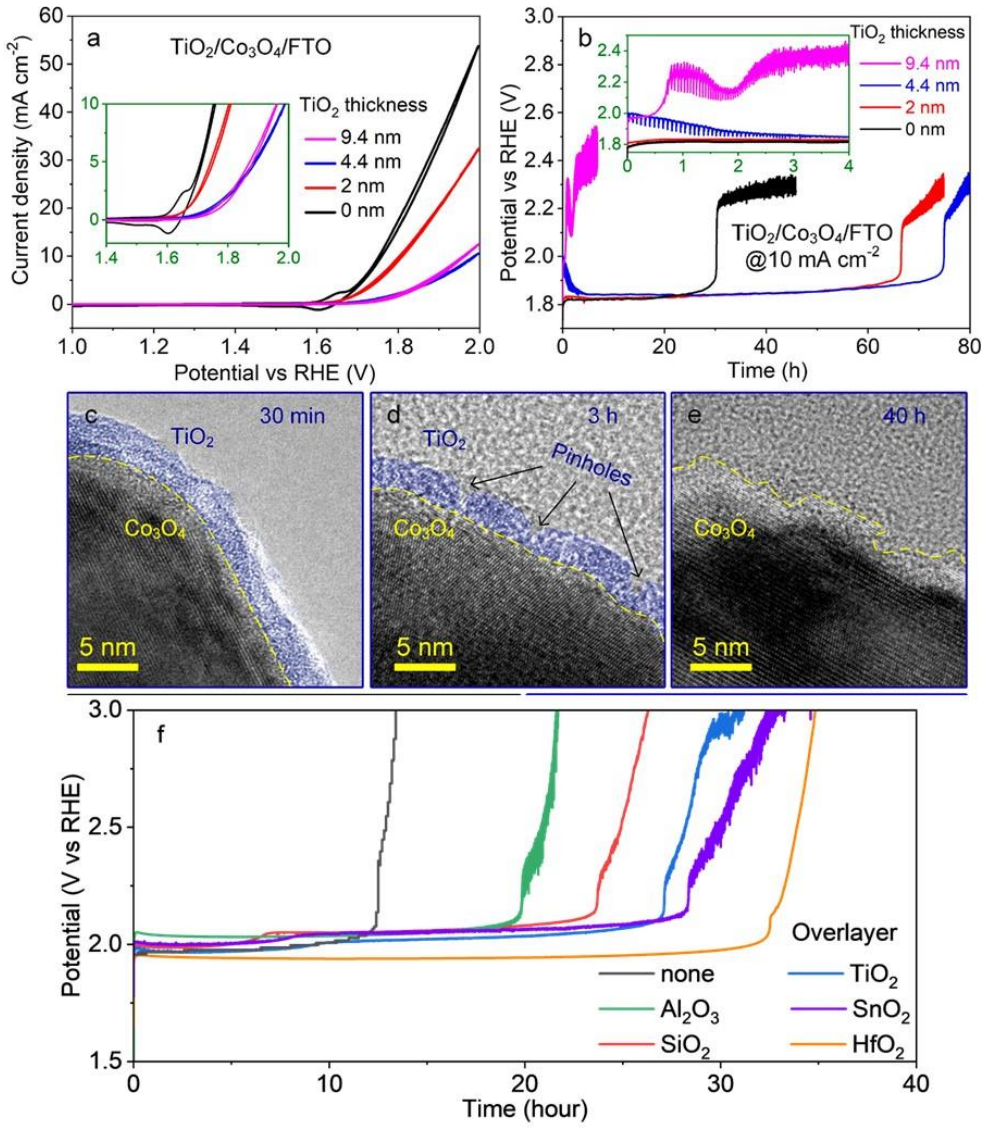

Figure 2.15 OER performance of Co_3O_4 as a function of various overcoating layers on FTO substrates: a) cyclic voltammetry (scan rate, v = 0.005 V s^{-1}; 5th scans) recorded for as-prepared Co_3O_4 (black line) and with various TiO_2 thickness (inset shows magnified plot of precatalytic region) and b) corresponding chronopotentiometric curves (inset displaying a magnified plot of initial 4 h of testing). c–e) TEM images of 4.4 nm-TiO_2/Co_3O_4/FTO after c) 30 min, d) 3 h, and e) 40 h of chronopotentiometric measurements. Reproduced with permission from ACS Appl. Mater. Interfaces 14, 29 (2022).[116] Copyright 2022 American Chemical Society. f) Chronopotentiometric curves of the Co_3O_4/FTO electrodes without (black) and with a 3–4 nm thick overlayer of Al_2O_3 (green), SiO_2 (green), TiO_2 (blue), SnO_2 (purple), and HfO_2 (orange) recorded at 10 mA cm^{-2} in 1 M H_2SO_4 electrolyte. Reproduced with permission from Small 2304650 (2023).[214] Copyright 2023 Wiley-VCH.

Table 2.4 Summary of recent studies on protective coating layers for acidic OER.

Electrocatalyst	Protective layer	Thickness (μm)	Substrate	Mas loading (mg cm^{-2})	Electrolyte	Overpotential (mV)	Stability (hours)	Dissolution rate (μg cm^{-2} h^{-1})	Ref.
Oxide-coated layers									
Co_3O_4	TiO_2 (4.4 nm)	1	FTO	n/a	1 M H_2SO_4	570[a]	75	n/a	116
Co_3O_4	HfO_2 (12 nm)	0.37	FTO	0.22	1 M H_2SO_4	540[a]	42	5.24	214
Carbon-coated layers									
Co_3O_4	Supported carbon	n/a	Carbon paper	12.6	0.5 M H_2SO_4	370	86.8[b]	n/a	217
Co_3O_4	Supported carbon	1	Hydrophobic carbon paper	n/a	0.5 M H_2SO_4	450	50	n/a	218
Co_3O_4	Supported carbon	n/a	GCE	20	1 M H_2SO_4	356	43	465.1	115
Co_3O_4	Supported carbon	n/a	Carbon paper	1.2	1 M H_2SO_4	225	80	15	219

Overpotential (mV) is recorded at the current density 10 mA cm^{-2} and corrected by iR-correction, except for ([a]).

Stability is measured at 10 mA cm^{-2} current density when potential starts to abruptly increase during extended OER test, except for ([b]) measured at 100 mA cm^{-2}.

Dissolution rate (μg cm^{-2} h^{-1}) is calculated by the total mass loading of catalyst divided the stability measured at 10 mA cm^{-2}.

2.5. Challenges and Opportunities

2.5.1. Prediction of stable acidic OECs

Considering the multitude of potential OEC compounds, computational high-throughput screening is essential to identify the most suitable compounds prior to experimental synthesis and characterization. This has been greatly facilitated by the adoption of theoretical calculations tools in the mechanistic understanding of various reactions including activity and instability of OER in acid.[70,124,151,220–229] For instance, Nørskov *et al.* implemented a high-throughput screening for more than 11000 kinds of two-dimensional materials by density functional theory, and filtered out 35 candidates with thermodynamically stable under the anodic conditions in acid with respect to the convex hull, the aqueous decomposition energy, and the electronic bandgaps.[230] Similarly, Wang *et al.* conducted a high-throughput screening with the support from large data collected from the Materials Project to assess 47814 binary metal oxides as active and stable OECs in acid.[70,221,222] They identified 68 likely acid-stable candidates and proposed an 'acid-stable periodic table' to support the new search of materials.[221,222] Other studies screened thousands of combinations, providing valuable insights into constructing active and stable matrix materials for acidic OECs.[124,155,231–233]

Nonetheless, conventional computational approaches often oversimplify the complexities of catalyst properties and testing conditions. For example, catalysts are generally assumed to be single crystals and unchanged during tests. In reality, pre-catalysts are imperfect crystallization, often exhibiting multiple phases with local defects or amorphization that undergo substantial evolution during the reaction. Moreover, it is challenging to comprehensively consider the impacts of operating parameters such as pH gradient, ionomers, or back pressure in these computational models.[221] As such, combining theoretical modeling and experimental validation has been the best approach to identifying and determining the suitable catalytic materials for acidic OER as demonstrated in (**Figure 2.16)**.[230]

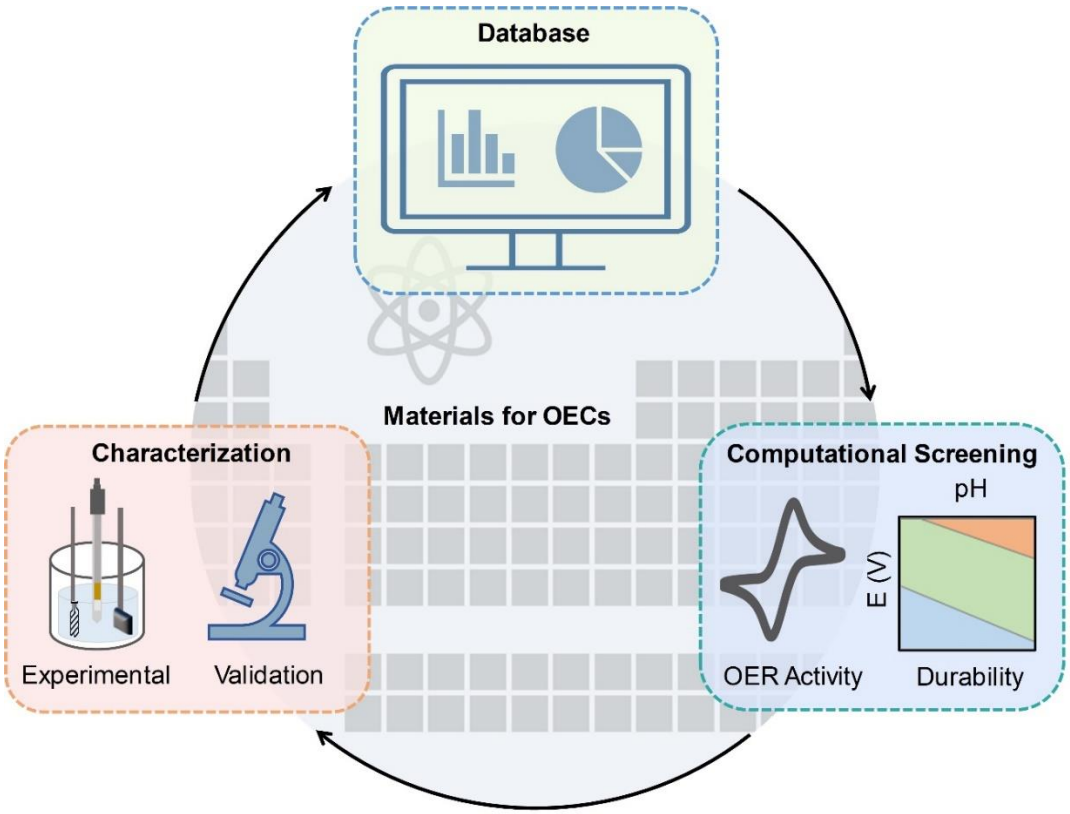

Figure 2.16 A schematic diagram outlines the integration of theoretical calculations supported by experimental tests to identify potential acidic OECs. Material properties sourced from an existing database are input into proposed models. The theoretical calculations yield selected compounds, subsequently validated through experimental studies. Data from these experiments serve as feedstocks to refine the theoretical models.

2.5.2. Performing acidic OECs at industry-relevant conditions

Despite the extensive foundational knowledge on acidic stability obtained from aqueous model system (AMS) in lab-scale studies, the practical applicability of OECs in real water electrolyzer systems should be widely investigated. It is due to a distinct discrepancy of the stability results between the AMS and the real-world membrane electrode assembly (MEA) cell for PEMWE or AEMWE devices in practical applications.[234–236] For example, the operating parameters such as local pH of the electrolyte, the mass transportation conditions, or the dissolution of catalysts can affect the degradation behavior of OECs very differently in AMS and PEMWE.[55] Some notable low-cost and acidic-stable OECs investigated in PEMWE were summarized in (**Table 2.5)**.

Some instability issues of PEMWE components were summarized in (**Figure 2.17)**. Particularly, the acidic corrosive environment of PEMWE does not originate from the aqueous electrolyte but is induced by the local environment at a triple phase boundary, where OECs contact with or are in

close proximity to the electrolyte and Nafion membrane. While the majority of AMS tests involve $HClO_4$ or H_2SO_4 electrolytes in pH ~ 1, MEA-representative pH is slightly higher, around 2.[131] Another different factor between the two setups is local metal ion concentration under the influence of electrolyte flow. For instance, a high-flow electrolyte could reduce the ohmic resistance in a stationary system by eliminating the bubble formation in the electrode|electrolyte interface and enhance activity by promoting the product outgassing from the electrode.[237–239]

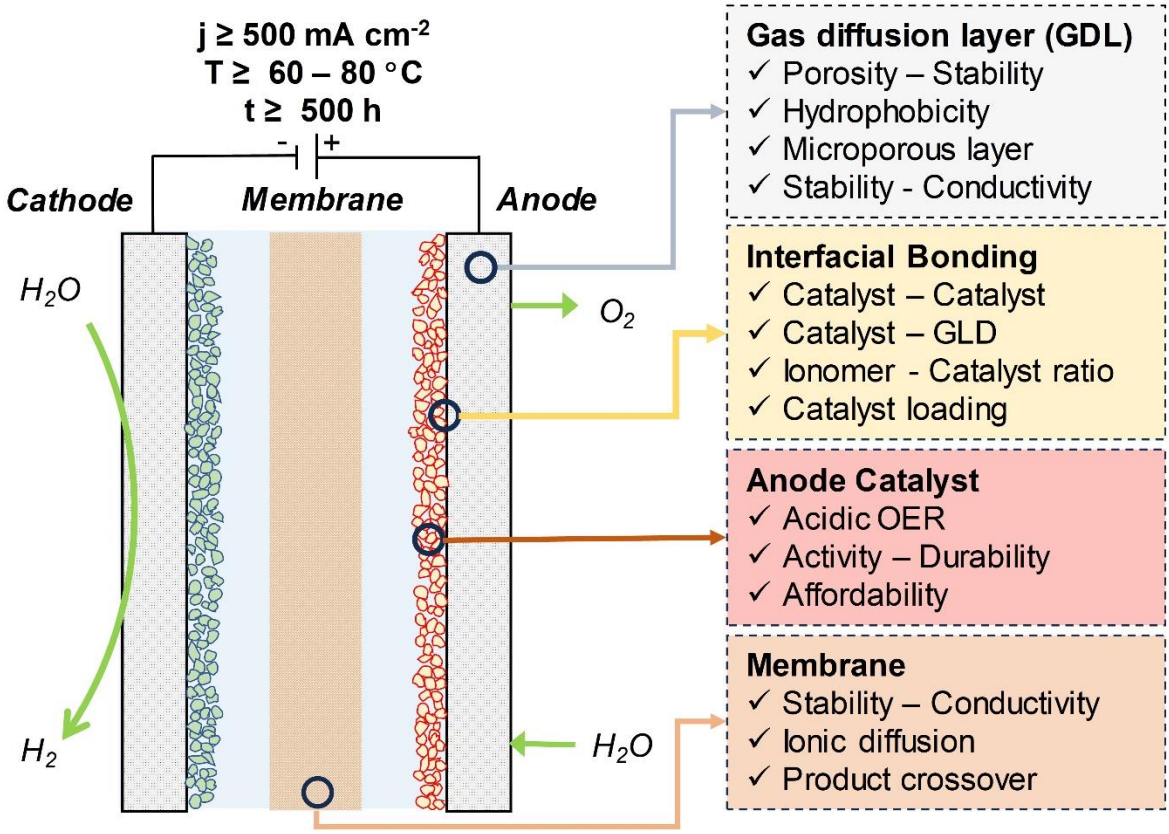

Figure 2.17 Simplified schematic of a proton exchange membrane water electrolyzer (PEMWE). From left to right, the components include gas diffusion layer (GDL), cathode catalyst, membrane, anode catalyst, and GDL. Both cathode and anode are continuously supplied with deionized water for water reduction to hydrogen and water oxidation to oxygen, respectively. For anodic durability, it is essential to consider not only OECs but other electrolyzer components including membrane, interfacial bonding, and GDL as illustrated in the figure.

Additionally, the instability in PEMWE can arise from the electrolyzer components including the membrane, flow fields, or gas diffusion layers.[55,192] For example, membrane degradation can occur via membrane thinning by radical attacks and metal poisons from catalyst corrosion.[240] Besides, the F^- ions formed from the radical attack on the perfluorosulfonic acid (PFSA) backbones during the membrane thinning can induce the TiO_2 passivation layer in the Ti-made components of flow fields

or gas diffusion layers. This degradation can make such components more susceptible to H_2 embrittlement and be corroded over the course of cell operation. Therefore, despite the higher costs and complexity of operating PEMWE at the lab scale to AMS systems, it is essential to accurately evaluate the same OECs in the realistic operating conditions such as elevated temperature (60 to 80 ºC), high current densities (>500 mA cm^{-2}), and long-term tests (> 500 h).

Table 2.5 Summary of noticeable low-cost acidic-stable OECs investigated in a PEMWE.

Electrocatalyst	Gas diffusion layer	Mass loading *(mg cm^{-2})*	Working area *(cm^2)*	Temperature *(^{o} C)*	Cell voltage *(V)* at *j (A cm^{-2})*	Stability (*h*) at *j (A cm^{-2})*	Ref.
Low-content-noble metal-based OECs							
IrO_x-MoO_3	Ti mesh	0.03*	1	80	1.85 at 1	24 at 0.5	241
$IrCoO_x$	Carbon fiber	0.25*	5	60	1.76 at 2	246 at 2	242
$RuCoO_x$	Carbon fiber	0.25*	5	60	1.76 at 2.1	253 at 2	
CrO_2–0.16IrO_2	Ti mesh	3	2	80	1.63 at 1 1.73 at 2	100 at 1	243
$SnRuO_x$	Ti felt	2*	4	50	1.57 at 1 1.66 at 2 1.74 at 3	1300 at 1	244
Ir-Doped $W_{18}O_{49}$	Ti fiber felt	2	n/a	60	2.27 at 1	90 at 0.5	245
Ni-RuO_2	Pt-Ti fiber felt	3.1	n/a	RT	1.95 at 1	1000 at 0.2	246
DNP-IrNi	Carbon paper/ Ti felt	0.7*	1	90	1.70 at 1.6	100 at 2	247
Ir/Nb_2O_{5-x}	Pt-Ti felt	3	3.4	80	1.84 at 3	2000 at 2	248
Sr_2CaIrO_6	Ti PSL/mesh-PTL	0.4*	4	80	1.81 at 2 2.40 at 6	450 at 2	96
Noble metal-free OECs							
La,Mn-doped Co_3O_4	PTL	1−2	5	60-80	2.2 at 2	90 at 0.3	171
$Mn_{7.5}O_{10}Br_3$	Carbon paper	3.2	4	50	1.75 at 0.1	300 at 0.1	117
γ-MnO_2	Carbon paper	3.5	4	RT	2.1 at 0.1	12 at 0.1	197

Mass loading (mg cm^{-2}) is the mass of total catalyst loaded on substrate, except for (*) calculated by the content of noble metal (Ir/Ru).

Stability at j is the stable operating hours measured at certain current for extended OER test. RT is room temperature.

2.5.3. Versatile applications of acidic OECs

Beyond the application in water electrolyzers, OECs play a crucial role in diverse electrochemical processes including CO/CO_2, O_2, or NO_x conversion in acidic conditions.[249–253] CO_2 reduction in acidic environment not only enhances the electronic conductivity but also mitigates the gradual formation of bicarbonate, a phenomenon observed in alkaline and neutral electrolytes.[249,250] An illustrative example by Monteiro *et al.* showcased that the Au gas diffusion electrode could achieve the FE of CO up to 80 – 90 % at 100 – 200 mA cm^{-2} in sulfate electrolyte at pH 2 – 4 by a considerably lower cell potentials, which was a 30 % improvement of the overall energy efficiency of neutral media.[254] The main issue of CO_2 reduction at low pH or high proton concentration is the competitive HER. However, HER in acidic electrolytes can be mitigated through adjustments to the electrolyte microenvironment, surface/interface modifications, and engineering efforts in electrolyzer design.[249–253] For instance, Xie *et al.* introduced a strategy to suppress the HER activity and maximize the co-adsorption of CO_2 by a strong affinity towards CO* in the bimetallic Pd-Cu catalysts system at low pH.[255] This approach induced a pH gradient that facilitates the conversion of local carbonate back to CO_2, thereby enhancing carbon utilization. Consequently, a CO_2-to-C_{2+} FE approached 89 % at 500 mA cm^{-2} in 0.5 M K_2SO_4 electrolyte adjusted pH by H_2SO_4 (pH ~ 4). Within this context, the stability of the electrolyzer system, necessitating the robust support of acid-tolerant OECs, becomes crucial.[249,250] The degradation of the anode catalysts can diminish partial current densities for targeted products, introduce impurities in the downstream production, and decrease overall efficiency.

Another promising application of acidic OECs is hydrogen peroxide (H_2O_2) production from oxygen reduction reaction (ORR), expanding beyond the traditional anthraquinone process.[256] Due to the market prospects of PEM fuel cell, the strong oxidizing capacity, and the more favorable reaction kinetics, the H_2O_2 production via two-electron ORR pathways in acid with high concentration of protons has attracted increasing attention for further development of fuel cell technologies and green chemical synthesis.[257] Cobalt-based nanomaterials emerge as attractive candidates for ORR, exhibiting high selectivity, facile mass transport, and cost-effectiveness.[256–258] Furthermore, they are potential for co-generating H_2O_2 by coupling the anode side with two-electrons water oxidation reaction, potentially maximizing energy conversion efficiency.[259] Nevertheless, the widespread use of these non-noble electrocatalysts is impeded by their limited long-term stability,[256,257] sharing similar challenges with those from acidic water electrolysis. Leveraging insights from the understanding of acidic OECs and employing design strategies for

stable water oxidation catalysts can be instrumental in addressing the stability issues inherent in this research domain.

2.5.4. Diverse applications beyond OER

Replacement of acidic OER by alternative reaction allows us to explore diverse applications such as coupling hydrogen production with higher value-added chemical synthesis. An intriguing example involves the oxidation of halides (Cl^-, Br^-) through the addition of halide-containing salts (NaCl, KBr), laying the fundamental concept of seawater electrolysis although the economic viability of using direct compared to purified seawater is still under debate.[260–264] In fact, the low reaction kinetics of the halide oxidation is beneficial to reduce the cell voltage and energy consumption for hydrogen production.[260–264] Studies have delved into the feasibility of chlorine production in acidic media, comparing the corrosion behavior of water oxidation and chloride evolution reactions.[143,265] Interestingly, the presence of Cl^- ions in electrolytes can stabilize transition-metal-based OECs, substantially enhancing their durability. Noticeably, Moreno-Hernandez *et al.* investigated the activity of Sb-based OEC in water oxidation and chlorine evolution.[265] The $CoSb_2O_6$ catalyst exhibited superior activity and prolonged stability in over 250 hours at a current density of 100 mA cm^{-2} in 4 M NaCl electrolyte adjusted to pH 2 by 1 mol L^{-1} HCl solution.

In a similar manner, the electrochemical conversion of organic compounds offers a promising alternative to OER.[266–269] Alcohols, an representative example, have been investigated in anodic oxidation reactions, revealing unexpected and prolonged performance of MnO_x in acidic conditions.[267] Notably, the presence of glycerol fueled a sustained 10 mA cm^{-2} at a low overpotential of 1.36 V for over 865 hours. This research showcased the possibility of value-added formic acid produced from glycerol oxidation. From an economic perspective, this concept facilitates the utilization of biomass feedstock, a by-product of various manufacturing processes, as a viable source of hydrogen.[266,270–272]

In summary, this review highlighted the recent development of acidic OECs though four main effective strategies, namely lowering precious metal content in catalysts, designing stable oxide systems, applying self-healing materials, and utilizing passivation layers. Amongst them, low-content noble-metal based materials have advantages relating to the high activity, whereas the acidic-stable matrices are highly considered due to the economic availability stemming from the low-cost and abundant elements. Although there have been a few acidic OECs performing good activity and durability at laboratory scale, their application at industry-relevant conditions is still

limited. For this reason, performing OECs at more industry-relevant conditions such as at high current densities, elevated temperature, and longer durability in a water electrolyzer is required. Moreover, employing novel theoretical calculation tools and machine learning in preliminary scans for stable OECs is expected to provide more accurate prediction of catalytic behavior during acidic OER, facilitating catalyst designing and preparation. In addition to water electrolysis, efficient acidic OECs can be utilized in various electrochemical systems such as CO_2 reduction in acid, H_2O_2 production, or halides/organic oxidation reactions, which can extend to various aspects following sustainable development goals.

2.6. References

[1] S.A.R. Khan, H.M. Zia-Ul-Haq, P. Ponce, and L. Janjua, "Re-investigating the impact of non-renewable and renewable energy on environmental quality: A roadmap towards sustainable development," Resour. Policy **81**(March), 103411 (2023).

[2] J. Wang, and W. Azam, "Natural resource scarcity, fossil fuel energy consumption, and total greenhouse gas emissions in top emitting countries," Geosci. Front. **15**(2), 101757 (2024).

[3] C. Yu, M. Moslehpour, T.K. Tran, L.M. Trung, J.P. Ou, and N.H. Tien, "Impact of non-renewable energy and natural resources on economic recovery: Empirical evidence from selected developing economies," Resour. Policy **80**(December 2022), 103221 (2023).

[4] Y. Xu, and F. Zhao, "Impact of energy depletion, human development, and income distribution on natural resource sustainability," Resour. Policy **83**(April), (2023).

[5] J. Chi, and H. Yu, "Water electrolysis based on renewable energy for hydrogen production," Chinese J. Catal. **39**(3), 390–394 (2018).

[6] S.J. Davis, N.S. Lewis, M. Shaner, S. Aggarwal, D. Arent, I.L. Azevedo, S.M. Benson, T. Bradley, J. Brouwer, Y. Chiang, C.T.M. Clack, A. Cohen, S. Doig, J. Edmonds, P. Fennell, C.B. Field, B. Hannegan, B. Hodge, M.I. Hoffert, E. Ingersoll, P. Jaramillo, K.S. Lackner, K.J. Mach, M. Mastrandrea, J. Ogden, P.F. Peterson, D.L. Sanchez, D. Sperling, J. Stagner, J.E. Trancik, C. Yang, and K. Caldeira, "Net-zero emissions energy systems," Science (80-.). **360**(6396), (2018).

[7] M.H. Nehrir, and C. Wang, in *Electr. Renew. Energy Syst.*, edited by M.H. Rashid (Academic Press, Boston, 2016), pp. 92–113.

[8] H. Nazir, C. Louis, S. Jose, J. Prakash, N. Muthuswamy, M.E.M. Buan, C. Flox, S. Chavan, X. Shi, P. Kauranen, T. Kallio, G. Maia, K. Tammeveski, N. Lymperopoulos, E. Carcadea, E. Veziroglu, A. Iranzo, and A.M. Kannan, "Is the H2 economy realizable in the foreseeable future? Part I: H2 production methods," Int. J. Hydrogen Energy **45**(27), 13777–13788 (2020).

[9] P. De Luna, C. Hahn, D. Higgins, S.A. Jaffer, T.F. Jaramillo, and E.H. Sargent, "What would it take for renewably powered electrosynthesis to displace petrochemical processes?," Science (80-.). **364**(6438), (2019).

[10] R.L. Germscheidt, D.E.B. Moreira, R.G. Yoshimura, N.P. Gasbarro, E. Datti, P.L. dos Santos, and J.A. Bonacin, "Hydrogen Environmental Benefits Depend on the Way of Production: An Overview of the Main Processes Production and Challenges by 2050," Adv. Energy Sustain. Res. **2**(10), 2100093 (2021).

[11] T.L. Levalley, A.R. Richard, and M. Fan, "The progress in water gas shift and steam reforming hydrogen production technologies - A review," Int. J. Hydrogen Energy **39**(30), 16983–17000 (2014).

[12] J. Chi, and H. Yu, "Water electrolysis based on renewable energy for hydrogen production," Chinese J. Catal. **39**(3), 390–394 (2018).

[13] A. Ajanovic, M. Sayer, and R. Haas, "The economics and the environmental benignity of different colors of hydrogen," Int. J. Hydrogen Energy **47**(57), 24136–24154 (2022).

[14] O. Bičáková, and P. Straka, "Production of hydrogen from renewable resources and its effectiveness," Int. J. Hydrogen Energy **37**(16), 11563–11578 (2012).

[15] J. Yang, W. Zhao, F. Xu, X. Hu, and B. Weng, "Nanoelectrocatalysts for Anodic Oxygen Evolution in Acid : A Review," (2023).

[16] J. Gao, H. Tao, and B. Liu, "Progress of Nonprecious-Metal-Based Electrocatalysts for Oxygen Evolution in Acidic Media," Adv. Mater. **33**(31), 1–18 (2021).

[17] Z. Lei, T. Wang, B. Zhao, W. Cai, Y. Liu, S. Jiao, Q. Li, R. Cao, and M. Liu, "Recent Progress in Electrocatalysts for Acidic Water Oxidation," Adv. Energy Mater. **10**(23), 1–18 (2020).

[18] Z. Chen, X. Duan, W. Wei, S. Wang, and B.J. Ni, "Electrocatalysts for acidic oxygen evolution reaction: Achievements and perspectives," Nano Energy **78**(August), 105392 (2020).

[19] Y. Lin, Y. Dong, X. Wang, and L. Chen, "Electrocatalysts for the Oxygen Evolution Reaction in Acidic Media," Adv. Mater. **35**(22), 1–38 (2023).

[20] F.Y. Chen, Z.Y. Wu, Z. Adler, and H. Wang, "Stability challenges of electrocatalytic oxygen evolution reaction: From mechanistic understanding to reactor design," Joule **5**(7), 1704–1731 (2021).

[21] S. Cherevko, "Stabilization of non-noble metal electrocatalysts for acidic oxygen evolution reaction," Curr. Opin. Electrochem. **38**(February), 101213 (2023).

[22] Q. Wang, Y. Cheng, H.B. Tao, Y. Liu, X. Ma, D. Li, H. Bin Yang, and B. Liu, "Long-Term Stability Challenges and Opportunities in Acidic Oxygen Evolution Electrocatalysis," Angew. Chemie Int. Ed., (2023).

[23] M. Carmo, D.L. Fritz, J. Mergel, and D. Stolten, "A comprehensive review on PEM water electrolysis," Int. J. Hydrogen Energy **38**(12), 4901–4934 (2013).

[24] S. Shiva Kumar, and V. Himabindu, "Hydrogen production by PEM water electrolysis – A review," Mater. Sci. Energy Technol. **2**(3), 442–454 (2019).

[25] N. Du, C. Roy, R. Peach, M. Turnbull, S. Thiele, and C. Bock, "Anion-Exchange Membrane Water Electrolyzers," Chem. Rev. **122**(13), 11830–11895 (2022).

[26] R.M. Navarro, R. Guil, and J.L.G. Fierro, in *Compend. Hydrog. Energy* (Elsevier, 2015), pp. 21–61.

[27] K. Zeng, and D. Zhang, "Recent progress in alkaline water electrolysis for hydrogen production and applications," Prog. Energy Combust. Sci. **36**(3), 307–326 (2010).

[28] T. Smolinka, H. Bergmann, J. Garche, and M. Kusnezoff, *The History of Water Electrolysis from Its Beginnings to the Present* (Elsevier B.V., 2021).

[29] S.A. Grigoriev, V.N. Fateev, D.G. Bessarabov, and P. Millet, "Current status, research trends, and challenges in water electrolysis science and technology," Int. J. Hydrogen Energy **45**(49),

26036–26058 (2020).

[30] S.E. Wolf, F.E. Winterhalder, V. Vibhu, L.G.J. (Bert) de Haart, O. Guillon, R.-A. Eichel, and N.H. Menzler, "Solid oxide electrolysis cells – current material development and industrial application," J. Mater. Chem. A **11**(34), 17977–18028 (2023).

[31] L. Zhang, X. Jie, Z.-G. Shao, Z.-M. Zhou, G. Xiao, and B. Yi, "The influence of sodium ion on the solid polymer electrolyte water electrolysis," Int. J. Hydrogen Energy **37**(2), 1321–1325 (2012).

[32] L. Ma, S. Sui, and Y. Zhai, "Investigations on high performance proton exchange membrane water electrolyzer," Int. J. Hydrogen Energy **34**(2), 678–684 (2009).

[33] H. Ito, N. Kawaguchi, S. Someya, and T. Munakata, "Pressurized operation of anion exchange membrane water electrolysis," Electrochim. Acta **297**, 188–196 (2019).

[34] A. Mayyas, M. Ruth, B. Pivovar, G. Bender, K. Wipke, A. Mayyas, M. Ruth, B. Pivovar, G. Bender, and K. Wipke, *Manufacturing Cost Analysis for Proton Exchange Membrane Water Electrolyzers* (2019).

[35] H. Yoon, B. Ju, and D. Kim, "Perspectives on the development of highly active, stable, and cost-effective OER electrocatalysts in acid," Batter. Energy **2**(5), (2023).

[36] Q. Ma, and S. Mu, "Acidic oxygen evolution reaction: Mechanism, catalyst classification, and enhancement strategies," Interdiscip. Mater. **2**(1), 53–90 (2023).

[37] Q. Wu, Y. Wang, K. Zhang, Z. Xie, K. Sun, W. An, X. Liang, and X. Zou, "Advances and status of anode catalysts for proton exchange membrane water electrolysis technology," Mater. Chem. Front. **7**(6), 1025–1045 (2023).

[38] A. Patonia, and R. Poudineh, "Cost-competitive green hydrogen: how to lower the cost of electrolysers?," Oxford Inst. Energy Stud. (January), (2022).

[39] E. Fabbri, and T.J. Schmidt, "Oxygen Evolution Reaction - The Enigma in Water Electrolysis," ACS Catal. **8**(10), 9765–9774 (2018).

[40] L. An, C. Wei, M. Lu, H. Liu, Y. Chen, G.G. Scherer, A.C. Fisher, P. Xi, Z.J. Xu, and C.H. Yan, "Recent Development of Oxygen Evolution Electrocatalysts in Acidic Environment," Adv. Mater. **33**(20), 1–31 (2021).

[41] T. Reier, H.N. Nong, D. Teschner, R. Schlögl, and P. Strasser, "Electrocatalytic Oxygen Evolution Reaction in Acidic Environments – Reaction Mechanisms and Catalysts," Adv. Energy Mater. **7**(1), (2017).

[42] Y. Hou, J. Lv, W. Quan, Y. Lin, Z. Hong, and Y. Huang, "Strategies for Electrochemically Sustainable H2 Production in Acid," Adv. Sci. **9**(7), 1–19 (2022).

[43] Z. Shi, X. Wang, J. Ge, C. Liu, and W. Xing, "Fundamental understanding of the acidic oxygen evolution reaction: Mechanism study and state-of-the-art catalysts," Nanoscale **12**(25), 13249–13275 (2020).

[44] A.R. Zeradjanin, J. Masa, I. Spanos, and R. Schlögl, "Activity and Stability of Oxides During Oxygen Evolution Reaction---From Mechanistic Controversies Toward Relevant Electrocatalytic Descriptors," Front. Energy Res. **8**(January), 1–17 (2021).

[45] F. Zeng, C. Mebrahtu, L. Liao, A.K. Beine, and R. Palkovits, "Stability and deactivation of OER electrocatalysts: A review," J. Energy Chem. **69**, 301–329 (2022).

[46] Y. Chen, Y. Liu, F. Wang, X. Guan, and L. Guo, "Toward practical photoelectrochemical water splitting and CO2 reduction using earth-abundant materials," J. Energy Chem. **61**, 469–488 (2021).

[47] J. Kibsgaard, Z. Chen, B.N. Reinecke, and T.F. Jaramillo, "Engineering the surface structure of MoS2 to preferentially expose active edge sites for electrocatalysis," Nat. Mater. **11**(11), 963–969 (2012).

[48] M. Chatti, T. Gengenbach, R. King, L. Spiccia, and A.N. Simonov, "Vertically Aligned Interlayer Expanded MoS2 Nanosheets on a Carbon Support for Hydrogen Evolution Electrocatalysis," Chem. Mater. **29**(7), 3092–3099 (2017).

[49] T.F. Jaramillo, K.P. Jørgensen, J. Bonde, J.H. Nielsen, S. Horch, and I. Chorkendorff, "Identification of active edge sites for electrochemical H2 evolution from MoS2 nanocatalysts," Science (80-.). **317**(5834), 100–102 (2007).

[50] L.A. King, M.K.A. Hubert, C. Capuano, J. Manco, N. Danilovic, E. Valle, T.R. Hellstern, K. Ayers, and T.F. Jaramillo, "A non-precious metal hydrogen catalyst in a commercial polymer electrolyte membrane electrolyser," Nat. Nanotechnol. **14**(11), 1071–1074 (2019).

[51] K. Macounova, M. Makarova, and P. Krtil, "Oxygen evolution on nanocrystalline RuO2 and Ru0.9Ni0.1O2−δ electrodes – DEMS approach to reaction mechanism determination," Electrochem. Commun. **11**(10), 1865–1868 (2009).

[52] X. Liu, Z. He, M. Ajmal, C. Shi, R. Gao, L. Pan, Z.F. Huang, X. Zhang, and J.J. Zou, "Recent Advances in the Comprehension and Regulation of Lattice Oxygen Oxidation Mechanism in Oxygen Evolution Reaction," Trans. Tianjin Univ. **29**(4), 247–253 (2023).

[53] S. Liu, Y. Chang, N. He, S. Zhu, L. Wang, and X. Liu, "Competition between Lattice Oxygen and Adsorbate Evolving Mechanisms in Rutile Ru-Based Oxide for the Oxygen Evolution Reaction," ACS Appl. Mater. Interfaces **15**(16), 20563–20570 (2023).

[54] C. Wei, Z. Wang, K. Otani, D. Hochfilzer, K. Zhang, R. Nielsen, I. Chorkendorff, and J. Kibsgaard, "Benchmarking Electrocatalyst Stability for Acidic Oxygen Evolution Reaction: The Crucial Role of Dissolved Ion Concentration," ACS Catal. **13**(21), 14058–14069 (2023).

[55] J. Edgington, and L.C. Seitz, "Advancing the Rigor and Reproducibility of Electrocatalyst Stability Benchmarking and Intrinsic Material Degradation Analysis for Water Oxidation," ACS Catal. **13**(5), 3379–3394 (2023).

[56] D.M. Morales, J. Villalobos, M.A. Kazakova, J. Xiao, and M. Risch, "Nafion-Induced Reduction of Manganese and its Impact on the Electrocatalytic Properties of a Highly Active MnFeNi Oxide for Bifunctional Oxygen Conversion," ChemElectroChem **8**(15), 2979–2983 (2021).

[57] D. Hochfilzer, I. Chorkendorff, and J. Kibsgaard, "Catalyst Stability Considerations for Electrochemical Energy Conversion with Non-Noble Metals: Do We Measure on What We Synthesized?," ACS Energy Lett. **8**(3), 1607–1612 (2023).

[58] Z. Wang, Y.-R. Zheng, J. Montoya, D. Hochfilzer, A. Cao, J. Kibsgaard, I. Chorkendorff, and J.K. Nørskov, "Origins of the Instability of Nonprecious Hydrogen Evolution Reaction Catalysts at Open-Circuit Potential," ACS Energy Lett. **6**(6), 2268–2274 (2021).

[59] G. Chen, C. Wei, Y. Zhu, and H. Huang, "Emerging chemical driving force in electrocatalytic water splitting," EcoMat **5**(2), (2023).

[60] D. Hochfilzer, J.E. Sørensen, E.L. Clark, S.B. Scott, I. Chorkendorff, and J. Kibsgaard, "The Importance of Potential Control for Accurate Studies of Electrochemical CO Reduction," ACS Energy Lett. **6**(5), 1879–1885 (2021).

[61] D. Hochfilzer, A. Xu, J.E. Sørensen, J.L. Needham, K. Krempl, K.K. Toudahl, G. Kastlunger, I. Chorkendorff, K. Chan, and J. Kibsgaard, "Transients in Electrochemical CO Reduction Explained

by Mass Transport of Buffers," ACS Catal. **12**(9), 5155–5161 (2022).

[62] S. Cherevko, A.R. Zeradjanin, A.A. Topalov, N. Kulyk, I. Katsounaros, and K.J.J. Mayrhofer, "Dissolution of noble metals during oxygen evolution in acidic media," ChemCatChem **6**(8), 2219–2223 (2014).

[63] H. Jin, S. Choi, G.J. Bang, T. Kwon, H.S. Kim, S.J. Lee, Y. Hong, D.W. Lee, H.S. Park, H. Baik, Y. Jung, S.J. Yoo, and K. Lee, "Safeguarding the RuO2 phase against lattice oxygen oxidation during acidic water electrooxidation," Energy Environ. Sci. **15**(3), 1119–1130 (2021).

[64] X. Ping, Y. Liu, L. Zheng, Y. Song, L. Guo, S. Chen, and Z. Wei, "Locking the lattice oxygen in RuO2 to stabilize highly active Ru sites in acidic water oxidation," Nat. Commun. **15**(1), 2501 (2024).

[65] Y. Ding, W. Liu, Z. Xu, and Z. Duan, "The origin of high electrochemical stability of iridium oxides for oxygen evolution," J. Mater. Chem. A **12**(31), 20317–20326 (2024).

[66] R. V. Mom, L.J. Falling, O. Kasian, G. Algara-Siller, D. Teschner, R.H. Crabtree, A. Knop-Gericke, K.J.J. Mayrhofer, J.J. Velasco-Vélez, and T.E. Jones, "Operando Structure-Activity-Stability Relationship of Iridium Oxides during the Oxygen Evolution Reaction," ACS Catal. **12**(9), 5174–5184 (2022).

[67] C. Liang, R.R. Rao, K.L. Svane, J.H.L. Hadden, B. Moss, S.B. Scott, M. Sachs, J. Murawski, A.M. Frandsen, D.J. Riley, M.P. Ryan, J. Rossmeisl, J.R. Durrant, and I.E.L. Stephens, "Unravelling the effects of active site density and energetics on the water oxidation activity of iridium oxides," Nat. Catal. **7**(7), 763–775 (2024).

[68] T. Priamushko, E. Franz, A. Logar, L. Bijelić, P. Guggenberger, D. Escalera-López, M. Zlatar, J. Libuda, F. Kleitz, N. Hodnik, O. Brummel, and S. Cherevko, "Be Aware of Transient Dissolution Processes in Co3O4 Acidic Oxygen Evolution Reaction Electrocatalysts," J. Am. Chem. Soc. **147**(4), 3517–3528 (2025).

[69] M. Pourbaix, *Atlas of Chemical and Electrochemical Equilibria in the Precence of a Gaseous Phase*, 2nd ed. (Houston, Tex., 1997).

[70] Z. Wang, X. Guo, J. Montoya, and J.K. Nørskov, "Predicting aqueous stability of solid with computed Pourbaix diagram using SCAN functional," Npj Comput. Mater. **6**(1), (2020).

[71] L. Tang, B. Han, K. Persson, C. Friesen, T. He, K. Sieradzki, and G. Ceder, "Electrochemical Stability of Nanometer-Scale Pt Particles in Acidic Environments," J. Am. Chem. Soc. **132**(2), 596–600 (2010).

[72] N. Hodnik, P. Jovanovič, A. Pavlišič, B. Jozinović, M. Zorko, M. Bele, V.S. Šelih, M. Šala, S. Hočevar, and M. Gaberšček, "New insights into corrosion of ruthenium and ruthenium oxide nanoparticles in acidic media," J. Phys. Chem. C **119**(18), 10140–10147 (2015).

[73] D.F. Abbott, D. Lebedev, K. Waltar, M. Povia, M. Nachtegaal, E. Fabbri, C. Copéret, and T.J. Schmidt, "Iridium oxide for the oxygen evolution reaction: Correlation between particle size, morphology, and the surface hydroxo layer from operando XAS," Chem. Mater. **28**(18), 6591–6604 (2016).

[74] J. Park, Y.J. Sa, H. Baik, T. Kwon, S.H. Joo, and K. Lee, "Iridium-Based Multimetallic Nanoframe@Nanoframe Structure: An Efficient and Robust Electrocatalyst toward Oxygen Evolution Reaction," ACS Nano **11**(6), 5500–5509 (2017).

[75] S. Cherevko, T. Reier, A.R. Zeradjanin, Z. Pawolek, P. Strasser, and K.J.J. Mayrhofer, "Stability of nanostructured iridium oxide electrocatalysts during oxygen evolution reaction in acidic

environment," Electrochem. Commun. **48**, 81–85 (2014).

[76] S. Cherevko, S. Geiger, O. Kasian, N. Kulyk, J.-P. Grote, A. Savan, B.R. Shrestha, S. Merzlikin, B. Breitbach, A. Ludwig, and K.J.J. Mayrhofer, "Oxygen and hydrogen evolution reactions on Ru, RuO2 , Ir, and IrO2 thin film electrodes in acidic and alkaline electrolytes: A comparative study on activity and stability," Catal. Today **262**, 170–180 (2016).

[77] Z. Kou, X. Li, L. Zhang, W. Zang, X. Gao, and J. Wang, "Dynamic Surface Chemistry of Catalysts in Oxygen Evolution Reaction," Small Sci. **1**(7), 2100011 (2021).

[78] L. Yang, K. Zhang, H. Chen, L. Shi, X. Liang, X. Wang, Y. Liu, Q. Feng, M. Liu, and X. Zou, "An ultrathin two-dimensional iridium-based perovskite oxide electrocatalyst with highly efficient {001} facets for acidic water oxidation," J. Energy Chem. **66**, 619–627 (2022).

[79] C.W. Song, J. Lim, H. Bin Bae, and S.Y. Chung, "Discovery of crystal structure-stability correlation in iridates for oxygen evolution electrocatalysis in acid," Energy Environ. Sci. **13**(11), 4178–4188 (2020).

[80] O. Kasian, J.P. Grote, S. Geiger, S. Cherevko, and K.J.J. Mayrhofer, "The Common Intermediates of Oxygen Evolution and Dissolution Reactions during Water Electrolysis on Iridium," Angew. Chemie - Int. Ed. **57**(9), 2488–2491 (2018).

[81] O. Kasian, S. Geiger, T. Li, J.P. Grote, K. Schweinar, S. Zhang, C. Scheu, D. Raabe, S. Cherevko, B. Gault, and K.J.J. Mayrhofer, "Degradation of iridium oxides via oxygen evolution from the lattice: Correlating atomic scale structure with reaction mechanisms," Energy Environ. Sci. **12**(12), 3548–3555 (2019).

[82] S. Geiger, O. Kasian, M. Ledendecker, E. Pizzutilo, A.M. Mingers, W.T. Fu, O. Diaz-Morales, Z. Li, T. Oellers, L. Fruchter, A. Ludwig, K.J.J. Mayrhofer, M.T.M. Koper, and S. Cherevko, "The stability number as a metric for electrocatalyst stability benchmarking," Nat. Catal. **1**(7), 508–515 (2018).

[83] M. Etzi Coller Pascuzzi, M. van Velzen, J.P. Hofmann, and E.J.M. Hensen, "On the Stability of Co3O4 Oxygen Evolution Electrocatalysts in Acid," ChemCatChem **13**(1), 459–467 (2021).

[84] H. Jang, S. Chung, and J. Lee, "In situ demonstration of anodic interface degradation during water electrolysis: Corrosion and passivation," Electrochim. Acta **365**, 137276 (2021).

[85] J.D. Benck, B.A. Pinaud, Y. Gorlin, and T.F. Jaramillo, "Substrate Selection for Fundamental Studies of Electrocatalysts and Photoelectrodes: Inert Potential Windows in Acidic, Neutral, and Basic Electrolyte," PLoS One **9**(10), e107942 (2014).

[86] L.F. Arenas, C. Ponce de León, and F.C. Walsh, "Three-dimensional porous metal electrodes: Fabrication, characterisation and use," Curr. Opin. Electrochem. **16**, 1–9 (2019).

[87] M. Chatti, J.L. Gardiner, M. Fournier, B. Johannessen, T. Williams, T.R. Gengenbach, N. Pai, C. Nguyen, D.R. MacFarlane, R.K. Hocking, and A.N. Simonov, "Intrinsically stable in situ generated electrocatalyst for long-term oxidation of acidic water at up to 80 °C," Nat. Catal. **2**(5), 457–465 (2019).

[88] D. Simondson, M. Chatti, J.L. Gardiner, B. V. Kerr, D.A. Hoogeveen, P. V. Cherepanov, I.C. Kuschnerus, T.D. Nguyen, B. Johannessen, S.L.Y. Chang, D.R. Macfarlane, R.K. Hocking, and A.N. Simonov, "Mixed Silver-Bismuth Oxides: A Robust Oxygen Evolution Catalyst Operating at Low pH and Elevated Temperatures," ACS Catal. **12**(20), 12912–12926 (2022).

[89] A. Angulo, P. van der Linde, H. Gardeniers, M. Modestino, and D. Fernández Rivas, "Influence of Bubbles on the Energy Conversion Efficiency of Electrochemical Reactors," Joule **4**(3), 555–

579 (2020).

[90] A. Hartig-Weiss, M.F. Tovini, H.A. Gasteiger, and H.A. El-Sayed, "OER Catalyst Durability Tests Using the Rotating Disk Electrode Technique: The Reason Why This Leads to Erroneous Conclusions," ACS Appl. Energy Mater. **3**(11), 10323–10327 (2020).

[91] H.A. El-Sayed, A. Weiß, L.F. Olbrich, G.P. Putro, and H.A. Gasteiger, "OER Catalyst Stability Investigation Using RDE Technique: A Stability Measure or an Artifact?," J. Electrochem. Soc. **166**(8), F458–F464 (2019).

[92] G.N. Martelli, R. Ornelas, and G. Faita, "Deactivation mechanisms of oxygen evolving anodes at high current densities," Electrochim. Acta **39**(11–12), 1551–1558 (1994).

[93] E.J. Park, C.G. Arges, H. Xu, and Y.S. Kim, "Membrane Strategies for Water Electrolysis," ACS Energy Lett. **7**(10), 3447–3457 (2022).

[94] M. Bernt, A. Siebel, and H.A. Gasteiger, "Analysis of Voltage Losses in PEM Water Electrolyzers with Low Platinum Group Metal Loadings," J. Electrochem. Soc. **165**(5), F305 (2018).

[95] C. Daiane Ferreira da Silva, F. Claudel, V. Martin, R. Chattot, S. Abbou, K. Kumar, I. Jiménez-Morales, S. Cavaliere, D. Jones, J. Rozière, L. Solà-Hernandez, C. Beauger, M. Faustini, J. Peron, B. Gilles, T. Encinas, L. Piccolo, F.H. Barros de Lima, L. Dubau, and F. Maillard, "Oxygen Evolution Reaction Activity and Stability Benchmarks for Supported and Unsupported IrOx Electrocatalysts," ACS Catal. **11**(7), 4107–4116 (2021).

[96] M. Retuerto, L. Pascual, J. Torrero, M.A. Salam, Á. Tolosana-Moranchel, D. Gianolio, P. Ferrer, P. Kayser, V. Wilke, S. Stiber, V. Celorrio, M. Mokthar, D.G. Sanchez, A.S. Gago, K.A. Friedrich, M.A. Peña, J.A. Alonso, and S. Rojas, "Highly active and stable OER electrocatalysts derived from Sr2MIrO6 for proton exchange membrane water electrolyzers," Nat. Commun. **13**(1), (2022).

[97] Y. Yang, Y. Yang, Z. Pei, K.-H. Wu, C. Tan, H. Wang, L. Wei, A. Mahmood, C. Yan, J. Dong, S. Zhao, and Y. Chen, "Recent Progress of Carbon-Supported Single-Atom Catalysts for Energy Conversion and Storage," Matter **3**(5), 1442–1476 (2020).

[98] E.J. Askins, M.R. Zoric, M. Li, Z. Luo, K. Amine, and K.D. Glusac, "Toward a mechanistic understanding of electrocatalytic nanocarbon," Nat. Commun. **12**(1), 3288 (2021).

[99] Y. Yi, J. Tornow, E. Willinger, M.G. Willinger, C. Ranjan, and R. Schlögl, "Electrochemical Degradation of Multiwall Carbon Nanotubes at High Anodic Potential for Oxygen Evolution in Acidic Media," ChemElectroChem **2**(12), 1929–1937 (2015).

[100] S.J. Ashton, and M. Arenz, "A DEMS study on the electrochemical oxidation of a high surface area carbon black," Electrochem. Commun. **13**(12), 1473–1475 (2011).

[101] S. Anantharaj, S. Kundu, and S. Noda, "Worrisome Exaggeration of Activity of Electrocatalysts Destined for Steady-State Water Electrolysis by Polarization Curves from Transient Techniques," J. Electrochem. Soc. **169**(1), 014508 (2022).

[102] S. Anantharaj, and S. Noda, "iR drop correction in electrocatalysis: everything one needs to know!," J. Mater. Chem. A **10**(17), 9348–9354 (2022).

[103] S. Anantharaj, P.E. Karthik, and S. Noda, "The Significance of Properly Reporting Turnover Frequency in Electrocatalysis Research," Angew. Chemie Int. Ed. **60**(43), 23051–23067 (2021).

[104] S. Anantharaj, S. Noda, M. Driess, and P.W. Menezes, "The Pitfalls of Using Potentiodynamic Polarization Curves for Tafel Analysis in Electrocatalytic Water Splitting," ACS Energy Lett. **6**(4), 1607–1611 (2021).

[105] K. Sivula, "Mott-schottky analysis of photoelectrodes: Sanity checks are needed," ACS Energy Lett. **6**(7), 2549–2551 (2021).

[106] L. Yu, and Z. Ren, "Systematic study of the influence of iR compensation on water electrolysis," Mater. Today Phys. **14**, 100253 (2020).

[107] S. Niu, S. Li, Y. Du, X. Han, and P. Xu, "How to Reliably Report the Overpotential of an Electrocatalyst," ACS Energy Lett. **5**(4), 1083–1087 (2020).

[108] W. Zheng, M. Liu, and L.Y.S. Lee, "Best Practices in Using Foam-Type Electrodes for Electrocatalytic Performance Benchmark," ACS Energy Lett. **5**(10), 3260–3264 (2020).

[109] S. Anantharaj, and S. Kundu, "Do the Evaluation Parameters Reflect Intrinsic Activity of Electrocatalysts in Electrochemical Water Splitting?," ACS Energy Lett. **4**(6), 1260–1264 (2019).

[110] C. Wei, R.R. Rao, J. Peng, B. Huang, I.E.L. Stephens, M. Risch, Z.J. Xu, and Y. Shao-Horn, "Recommended Practices and Benchmark Activity for Hydrogen and Oxygen Electrocatalysis in Water Splitting and Fuel Cells," Adv. Mater. **31**(31), 1–24 (2019).

[111] S. Anantharaj, S.R. Ede, K. Karthick, S. Sam Sankar, K. Sangeetha, P.E. Karthik, and S. Kundu, "Precision and correctness in the evaluation of electrocatalytic water splitting: Revisiting activity parameters with a critical assessment," Energy Environ. Sci. **11**(4), 744–771 (2018).

[112] C.C.L. McCrory, S. Jung, J.C. Peters, and T.F. Jaramillo, "Benchmarking Heterogeneous Electrocatalysts for the Oxygen Evolution Reaction," J. Am. Chem. Soc. **135**(45), 16977–16987 (2013).

[113] C.C.L. McCrory, S. Jung, I.M. Ferrer, S.M. Chatman, J.C. Peters, and T.F. Jaramillo, "Benchmarking Hydrogen Evolving Reaction and Oxygen Evolving Reaction Electrocatalysts for Solar Water Splitting Devices," J. Am. Chem. Soc. **137**(13), 4347–4357 (2015).

[114] A. Li, S. Kong, C. Guo, H. Ooka, K. Adachi, D. Hashizume, Q. Jiang, H. Han, J. Xiao, and R. Nakamura, "Enhancing the stability of cobalt spinel oxide towards sustainable oxygen evolution in acid," Nat. Catal. **5**(2), 109–118 (2022).

[115] J. Yu, F.A. Garcés-Pineda, J. González-Cobos, M. Peña-Díaz, C. Rogero, S. Giménez, M.C. Spadaro, J. Arbiol, S. Barja, and J.R. Galán-Mascarós, "Sustainable oxygen evolution electrocatalysis in aqueous 1 M H2SO4 with earth abundant nanostructured Co3O4," Nat. Commun. **13**(1), 4341 (2022).

[116] T. Tran-Phu, H. Chen, R. Daiyan, M. Chatti, B. Liu, R. Amal, Y. Liu, D.R. Macfarlane, A.N. Simonov, and A. Tricoli, "Nanoscale TiO2 Coatings Improve the Stability of an Earth-Abundant Cobalt Oxide Catalyst during Acidic Water Oxidation," ACS Appl. Mater. Interfaces **14**(29), 33130–33140 (2022).

[117] S. Pan, H. Li, D. Liu, R. Huang, X. Pan, D. Ren, J. Li, M. Shakouri, Q. Zhang, M. Wang, C. Wei, L. Mai, B. Zhang, Y. Zhao, Z. Wang, M. Graetzel, and X. Zhang, "Efficient and stable noble-metal-free catalyst for acidic water oxidation," Nat. Commun. **13**(1), 2294 (2022).

[118] M. Huynh, T. Ozel, C. Liu, E.C. Lau, and D.G. Nocera, "Design of template-stabilized active and earth-abundant oxygen evolution catalysts in acid," Chem. Sci. **8**(7), 4779–4794 (2017).

[119] S.D. Ghadge, M.K. Datta, O.I. Velikokhatnyi, R. Kuruba, P.M. Shanthi, and P.N. Kumta, "Influence of Defects on Activity-Stability of Cu1.5Mn1.5O4 for Acid-Mediated Oxygen Evolution Reaction," J. Electrochem. Soc. **167**(14), 144511 (2020).

[120] I.A. Moreno-Hernandez, B.S. Brunschwig, and N.S. Lewis, "Tin Oxide as a Protective

Heterojunction with Silicon for Efficient Photoelectrochemical Water Oxidation in Strongly Acidic or Alkaline Electrolytes," Adv. Energy Mater. **8**(24), 1801155 (2018).

[121] P.P. Patel, M.K. Datta, O.I. Velikokhatnyi, R. Kuruba, K. Damodaran, P. Jampani, B. Gattu, P.M. Shanthi, S.S. Damle, and P.N. Kumta, "Noble metal-free bifunctional oxygen evolution and oxygen reduction acidic media electro-catalysts," Sci. Rep. **6**(1), 28367 (2016).

[122] S.A. Bonke, K.L. Abel, D.A. Hoogeveen, M. Chatti, T. Gengenbach, M. Fournier, L. Spiccia, and A.N. Simonov, "Electrolysis of Natural Waters Contaminated with Transition-Metal Ions: Identification of A Metastable FePb-Based Oxygen-Evolution Catalyst Operating in Weakly Acidic Solutions," Chempluschem **83**(7), 704–710 (2018).

[123] I.A. Moreno-Hernandez, C.A. Macfarland, C.G. Read, K.M. Papadantonakis, B.S. Brunschwig, and N.S. Lewis, "Crystalline nickel manganese antimonate as a stable water-oxidation catalyst in aqueous 1.0 M H2SO4," Energy Environ. Sci. **10**(10), 2103–2108 (2017).

[124] L. Zhou, A. Shinde, J.H. Montoya, A. Singh, S. Gul, J. Yano, Y. Ye, E.J. Crumlin, M.H. Richter, J.K. Cooper, H.S. Stein, J.A. Haber, K.A. Persson, and J.M. Gregoire, "Rutile Alloys in the Mn-Sb-O System Stabilize Mn3+ to Enable Oxygen Evolution in Strong Acid," ACS Catal. **8**(12), 10938–10948 (2018).

[125] S. Chen, H. Huang, P. Jiang, K. Yang, J. Diao, S. Gong, S. Liu, M. Huang, H. Wang, and Q. Chen, "Mn-Doped RuO2 Nanocrystals as Highly Active Electrocatalysts for Enhanced Oxygen Evolution in Acidic Media," ACS Catal. **10**(2), 1152–1160 (2020).

[126] Z. Zhuang, Y. Wang, C.-Q. Xu, S. Liu, C. Chen, Q. Peng, Z. Zhuang, H. Xiao, Y. Pan, S. Lu, R. Yu, W.-C. Cheong, X. Cao, K. Wu, K. Sun, Y. Wang, D. Wang, J. Li, and Y. Li, "Three-dimensional open nano-netcage electrocatalysts for efficient pH-universal overall water splitting," Nat. Commun. **10**(1), 4875 (2019).

[127] R. Frydendal, E.A. Paoli, B.P. Knudsen, B. Wickman, P. Malacrida, I.E.L. Stephens, and I. Chorkendorff, "Benchmarking the Stability of Oxygen Evolution Reaction Catalysts: The Importance of Monitoring Mass Losses," ChemElectroChem **1**(12), 2075–2081 (2014).

[128] H.N. Nong, L. Gan, E. Willinger, D. Teschner, and P. Strasser, "IrOx core-shell nanocatalysts for cost- and energy-efficient electrochemical water splitting," Chem. Sci. **5**(8), 2955–2963 (2014).

[129] Y. Liu, Y. Chen, X. Mu, Z. Wu, X. Jin, J. Li, Y. Xu, L. Yang, X. Xi, H. Jang, Z. Lei, Q. Liu, S. Jiao, P. Yan, X. Li, and R. Cao, "Spinel-Anchored Iridium Single Atoms Enable Efficient Acidic Water Oxidation via Intermediate Stabilization Effect," ACS Catal. **13**(6), 3757–3767 (2023).

[130] X. Shi, H.-J. Peng, T.J.P. Hersbach, Y. Jiang, Y. Zeng, J. Baek, K.T. Winther, D. Sokaras, X. Zheng, and M. Bajdich, "Efficient and Stable Acidic Water Oxidation Enabled by Low-Concentration, High-Valence Iridium Sites," ACS Energy Lett. **7**(7), 2228–2235 (2022).

[131] J. Knöppel, M. Möckl, D. Escalera-López, K. Stojanovski, M. Bierling, T. Böhm, S. Thiele, M. Rzepka, and S. Cherevko, "On the limitations in assessing stability of oxygen evolution catalysts using aqueous model electrochemical cells," Nat. Commun. **12**(1), 1–9 (2021).

[132] Y.T. Kim, P.P. Lopes, S.A. Park, A.Y. Lee, J. Lim, H. Lee, S. Back, Y. Jung, N. Danilovic, V. Stamenkovic, J. Erlebacher, J. Snyder, and N.M. Markovic, "Balancing activity, stability and conductivity of nanoporous core-shell iridium/iridium oxide oxygen evolution catalysts," Nat. Commun. **8**(1), 1–8 (2017).

[133] L. She, G. Zhao, T. Ma, J. Chen, W. Sun, and H. Pan, "On the Durability of Iridium-Based Electrocatalysts toward the Oxygen Evolution Reaction under Acid Environment," Adv. Funct.

Mater. **32**(5), (2022).

[134] M.A. Hubert, A.M. Patel, A. Gallo, Y. Liu, E. Valle, M. Ben-Naim, J. Sanchez, D. Sokaras, R. Sinclair, J.K. Nørskov, L.A. King, M. Bajdich, and T.F. Jaramillo, "Acidic Oxygen Evolution Reaction Activity-Stability Relationships in Ru-Based Pyrochlores," ACS Catal. **10**(20), 12182–12196 (2020).

[135] G. Inzelt, B. Berkes, and Á. Kriston, "Temperature dependence of two types of dissolution of platinum in acid media. An electrochemical nanogravimetric study," Electrochim. Acta **55**(16), 4742–4749 (2010).

[136] C. Wang, R. Deng, M. Guo, and Q. Zhang, "Recent progress of advanced Co3O4-based materials for electrocatalytic oxygen evolution reaction in acid: from rational screening to efficient design," Int. J. Hydrogen Energy **48**(82), 31920–31942 (2023).

[137] X. Li, D. Pletcher, and F.C. Walsh, "Electrodeposited lead dioxide coatings," Chem. Soc. Rev. **40**(7), 3879–3894 (2011).

[138] Y. Li, L. Jiang, F. Liu, J. Li, and Y. Liu, "Novel phosphorus-doped PbO2–MnO2 bicontinuous electrodes for oxygen evolution reaction," RSC Adv. **4**(46), 24020 (2014).

[139] N. Li, T.P. Keane, S.S. Veroneau, R.G. Hadt, D. Hayes, L.X. Chen, and D.G. Nocera, "Template-stabilized oxidic nickel oxygen evolution catalysts," Proc. Natl. Acad. Sci. **117**(28), 16187–16192 (2020).

[140] A. Jain, G. Hautier, S.P. Ong, C.J. Moore, C.C. Fischer, K.A. Persson, and G. Ceder, "Formation enthalpies by mixing GGA and GGA + U calculation," Phys. Rev. B **84**(4), 045115 (2011).

[141] A. Jain, S.P. Ong, G. Hautier, W. Chen, W.D. Richards, S. Dacek, S. Cholia, D. Gunter, D. Skinner, G. Ceder, and K.A. Persson, "Commentary: The Materials Project: A materials genome approach to accelerating materials innovation," APL Mater. **1**(1), (2013).

[142] Z. Mahidashti, M. Rezaei, M. Borrelli, and A. Shaygan Nia, "Insight into the stability mechanism of nickel and manganese antimonate catalytic films during the oxygen evolution reaction in acidic media," J. Electroanal. Chem. **937**(March), 117404 (2023).

[143] T.A. Evans, and K.-S. Choi, "Electrochemical Synthesis and Investigation of Stoichiometric, Phase - Pure CoSb2O6 and MnSb2O6 Electrodes for the Oxygen Evolution Reaction in Acidic Media," ACS Appl. Energy Mater. **3**(6), 5563–5571 (2020).

[144] S. Luke, M. Chatti, A. Yadav, B. V. Kerr, J. Kangsabanik, T. Williams, P. V. Cherepanov, B. Johannessen, A. Tanksale, D.R. MacFarlane, R.K. Hocking, A. Alam, A. Yella, and A.N. Simonov, "Mixed metal-antimony oxide nanocomposites: low pH water oxidation electrocatalysts with outstanding durability at ambient and elevated temperatures," J. Mater. Chem. A **9**(48), 27468–27484 (2021).

[145] A. Babaei, and M. Rezaei, "Development of a highly stable and active non-precious anode electrocatalyst for oxygen evolution reaction in acidic medium based on nickel and cobalt-containing antimony oxide," J. Electroanal. Chem. **935**(October 2022), 117319 (2023).

[146] J. Wang, H. Kim, H. Lee, Y.-J. Ko, M.H. Han, W. Kim, J.M. Baik, J.-Y. Choi, H.-S. Oh, and W.H. Lee, "Sb incorporated into oxides enhances stability in acid during the oxygen evolution reaction by inhibiting structural distortion," Nano Energy **110**(March), 108355 (2023).

[147] S. Luke, M. Chatti, D. Simondson, K.N. Dinh, B. V. Kerr, T.D. Nguyen, G. Yilmaz, B. Johannessen, D.R. MacFarlane, A. Yella, R.K. Hocking, and A.N. Simonov, "High performance acidic water electrooxidation catalysed by manganese–antimony oxides promoted by secondary

metals," EES Catal., (2023).

[148] L.G. Bloor, P.I. Molina, M.D. Symes, and L. Cronin, "Low pH electrolytic water splitting using earth-abundant metastable catalysts that self-assemble in situ," J. Am. Chem. Soc. **136**(8), 3304–3311 (2014).

[149] J. Yu, S. Giancola, B. Khezri, D. Nieto-Castro, J. Redondo, F. Schiller, S. Barja, M.C. Spadaro, J. Arbiol, F.A. Garcés-Pineda, and J.R. Galán-Mascarós, "A survey of Earth-abundant metal oxides as oxygen evolution electrocatalysts in acidic media (pH < 1)," EES Catal. **1**(5), 765–773 (2023).

[150] Z. Wang, and L. Lu, "The rise of manganese as catalysts for acidic water oxidation: A mini review," Electrochem. Commun. **151**(February), 107505 (2023).

[151] J. Peng, L. Giordano, T.C. Davenport, and Y. Shao-Horn, "Stability Design Principles of Manganese-Based Oxides in Acid," Chem. Mater. **34**(17), 7774–7787 (2022).

[152] M. Huynh, C. Shi, S.J.L. Billinge, and D.G. Nocera, "Nature of Activated Manganese Oxide for Oxygen Evolution," J. Am. Chem. Soc. **137**(47), 14887–14904 (2015).

[153] D.M. Robinson, Y.B. Go, M. Mui, G. Gardner, Z. Zhang, D. Mastrogiovanni, E. Garfunkel, J. Li, M. Greenblatt, and G.C. Dismukes, "Photochemical Water Oxidation by Crystalline Polymorphs of Manganese Oxides: Structural Requirements for Catalysis," J. Am. Chem. Soc. **135**(9), 3494–3501 (2013).

[154] R. Frydendal, E.A. Paoli, I. Chorkendorff, J. Rossmeisl, and I.E.L. Stephens, "Toward an Active and Stable Catalyst for Oxygen Evolution in Acidic Media: Ti-Stabilized MnO2," Adv. Energy Mater. **5**(22), (2015).

[155] A. Shinde, R.J.R. Jones, D. Guevarra, S. Mitrovic, N. Becerra-Stasiewicz, J.A. Haber, J. Jin, and J.M. Gregoire, "High-Throughput Screening for Acid-Stable Oxygen Evolution Electrocatalysts in the (Mn–Co–Ta–Sb)Ox Composition Space," Electrocatalysis **6**(2), 229–236 (2015).

[156] Z.P. Ifkovits, J.M. Evans, P.A. Kempler, M.B. Morla, K.H. Pham, J.A. Dowling, A.I. Carim, and N.S. Lewis, "Powdered Mn y Sb 1– y O x Catalysts for Cerium-Mediated Oxygen Evolution in Acidic Environments," ACS Energy Lett. **7**(12), 4258–4264 (2022).

[157] K. Lemoine, Z. Gohari-Bajestani, R. Moury, A. Terry, A. Guiet, J.M. Grenèche, A. Hémon-Ribaud, N. Heidary, V. Maisonneuve, N. Kornienko, and J. Lhoste, "Amorphous Iron-Manganese Oxyfluorides, Promising Catalysts for Oxygen Evolution Reaction under Acidic Media," ACS Appl. Energy Mater. **4**(2), 1173–1181 (2021).

[158] S.D. Ghadge, O.I. Velikokhatnyi, M.K. Datta, P.M. Shanthi, S. Tan, and P.N. Kumta, "Computational and Experimental Study of Fluorine Doped (Mn 1– x Nb x)O 2 Nanorod Electrocatalysts for Acid-Mediated Oxygen Evolution Reaction," ACS Appl. Energy Mater. **3**(1), 541–557 (2020).

[159] I.C. Man, H. Su, F. Calle-Vallejo, H.A. Hansen, J.I. Martínez, N.G. Inoglu, J. Kitchin, T.F. Jaramillo, J.K. Nørskov, and J. Rossmeisl, "Universality in Oxygen Evolution Electrocatalysis on Oxide Surfaces," ChemCatChem **3**(7), 1159–1165 (2011).

[160] K. Natarajan, E. Munirathinam, and T.C.K. Yang, "Operando Investigation of Structural and Chemical Origin of Co3O4 Stability in Acid under Oxygen Evolution Reaction," ACS Appl. Mater. Interfaces **13**(23), 27140–27148 (2021).

[161] M. Zhang, M. de Respinis, and H. Frei, "Time-resolved observations of water oxidation intermediates on a cobalt oxide nanoparticle catalyst," Nat. Chem. **6**(4), 362–367 (2014).

[162] J.B. Gerken, J.G. McAlpin, J.Y.C. Chen, M.L. Rigsby, W.H. Casey, R.D. Britt, and S.S. Stahl, "Electrochemical water oxidation with cobalt-based electrocatalysts from pH 0-14: The thermodynamic basis for catalyst structure, stability, and activity," J. Am. Chem. Soc. **133**(36), 14431–14442 (2011).

[163] H.J. King, M. Fournier, S.A. Bonke, E. Seeman, M. Chatti, A.N. Jumabekov, B. Johannessen, P. Kappen, A.N. Simonov, and R.K. Hocking, "Photon-Induced, Timescale, and Electrode Effects Critical for the in Situ X-ray Spectroscopic Analysis of Electrocatalysts: The Water Oxidation Case," J. Phys. Chem. C **123**(47), 28533–28549 (2019).

[164] T. Tran-Phu, M. Chatti, J. Leverett, T.K.A. Nguyen, D. Simondson, D.A. Hoogeveen, A. Kiy, T. Duong, B. Johannessen, J. Meilak, P. Kluth, R. Amal, A.N. Simonov, R.K. Hocking, R. Daiyan, and A. Tricoli, "Understanding the Role of (W, Mo, Sb) Dopants in the Catalyst Evolution and Activity Enhancement of Co3O4 during Water Electrolysis via In Situ Spectroelectrochemical Techniques," Small **2208074**, 2208074 (2023).

[165] L. Lin, Q. Fu, R. Wang, T. Yao, X. Wang, and B. Song, "Spinel-Type Oxides for Acidic Oxygen Evolution Reaction: Mechanism, Modulation, and Perspective," Adv. Energy Sustain. Res. **4**(12), (2023).

[166] S. Anantharaj, K. Karthick, and S. Kundu, "Spinel Cobalt Titanium Binary Oxide as an All-Non-Precious Water Oxidation Electrocatalyst in Acid," Inorg. Chem. **58**(13), 8570–8576 (2019).

[167] B. Chakraborty, A. Indra, P.V. Menezes, M. Driess, and P.W. Menezes, "Improved chemical water oxidation with Zn in the tetrahedral site of spinel-type ZnCo2O4 nanostructure," Mater. Today Chem. **15**, 100226 (2020).

[168] N. Wang, P. Ou, R.K. Miao, Y. Chang, Z. Wang, S.-F. Hung, J. Abed, A. Ozden, H.-Y. Chen, H.-L. Wu, J.E. Huang, D. Zhou, W. Ni, L. Fan, Y. Yan, T. Peng, D. Sinton, Y. Liu, H. Liang, and E.H. Sargent, "Doping Shortens the Metal/Metal Distance and Promotes OH Coverage in Non-Noble Acidic Oxygen Evolution Reaction Catalysts," J. Am. Chem. Soc. **145**(14), 7829–7836 (2023).

[169] J. Huang, H. Sheng, R.D. Ross, J. Han, X. Wang, B. Song, and S. Jin, "Modifying redox properties and local bonding of Co3O4 by CeO2 enhances oxygen evolution catalysis in acid," Nat. Commun. **12**(1), 3036 (2021).

[170] Y. Wang, H. Zhao, Y. Guo, J. Wu, X. Lu, and X. Tang, "Pyrochlore-type cobalt and manganese antimonate electrocatalysts with excellent activity and stability for OER in acidic solution," Nanoscale **15**(21), 9413–9422 (2023).

[171] L. Chong, G. Gao, J. Wen, H. Li, H. Xu, Z. Green, J.D. Sugar, A.J. Kropf, W. Xu, X.-M. Lin, H. Xu, L.-W. Wang, and D.-J. Liu, "La- and Mn-doped cobalt spinel oxygen evolution catalyst for proton exchange membrane electrolysis," Science (80-.). **380**(6645), 609–616 (2023).

[172] D. Senthil Raja, P.Y. Cheng, C.C. Cheng, S.Q. Chang, C.L. Huang, and S.Y. Lu, "In-situ grown metal-organic framework-derived carbon-coated Fe-doped cobalt oxide nanocomposite on fluorine-doped tin oxide glass for acidic oxygen evolution reaction," Appl. Catal. B Environ. **303**(August 2021), 120899 (2022).

[173] G.S. Rocha, A.L. Silva, L.P.C. Silva, F.B. Passos, and N.M.F. Carvalho, "Improved Activity of PdO Supported over Co3O4 in the Electrocatalytic Oxygen Evolution Reaction in a Wide pH Range," Energy & Fuels **36**(20), 12719–12728 (2022).

[174] W.L. Kwong, C.C. Lee, A. Shchukarev, and J. Messinger, "Cobalt-doped hematite thin films for electrocatalytic water oxidation in highly acidic media," Chem. Commun. **55**(34), 5017–5020

(2019).

[175] K.-L. Yan, J.-Q. Chi, J.-Y. Xie, B. Dong, Z.-Z. Liu, W.-K. Gao, J.-H. Lin, Y.-M. Chai, and C.-G. Liu, "Mesoporous Ag-doped Co3O4 nanowire arrays supported on FTO as efficient electrocatalysts for oxygen evolution reaction in acidic media," Renew. Energy **119**, 54–61 (2018).

[176] J.S. Mondschein, J.F. Callejas, C.G. Read, J.Y.C. Chen, C.F. Holder, C.K. Badding, and R.E. Schaak, "Crystalline Cobalt Oxide Films for Sustained Electrocatalytic Oxygen Evolution under Strongly Acidic Conditions," Chem. Mater. **29**(3), 950–957 (2017).

[177] M.M. Najafpour, M. Fekete, D.J. Sedigh, E.M. Aro, R. Carpentier, J.J. Eaton-Rye, H. Nishihara, J.R. Shen, S.I. Allakhverdiev, and L. Spiccia, "Damage management in water-oxidizing catalysts: From photosystem II to nanosized metal oxides," ACS Catal. **5**(3), 1499–1512 (2015).

[178] V. Amendola, and M. Meneghetti, "Self-healing at the nanoscale," Nanoscale **1**(1), 74–88 (2009).

[179] Y. Yang, and M.W. Urban, "Self-healing polymeric materials," Chem. Soc. Rev. **42**(17), 7446–7467 (2013).

[180] A.E. Thorarinsdottir, S.S. Veroneau, and D.G. Nocera, "Self-healing oxygen evolution catalysts," Nat. Commun. **13**(1), 1–10 (2022).

[181] M.M. Najafpour, M. Khoshkam, D. Jafarian Sedigh, A. Zahraei, and M. Kompany-Zareh, "Self-healing for nanolayered manganese oxides in the presence of cerium(iv) ammonium nitrate: new findings," New J. Chem. **39**(4), 2547–2550 (2015).

[182] M.R. Mohammadi, S. Loos, P. Chernev, C. Pasquini, I. Zaharieva, D. González-Flores, P. Kubella, K. Klingan, R.D.L. Smith, and H. Dau, "Exploring the Limits of Self-Repair in Cobalt Oxide Films for Electrocatalytic Water Oxidation," ACS Catal. **10**(14), 7990–7999 (2020).

[183] A.E. Thorarinsdottir, C. Costentin, S.S. Veroneau, and D.G. Nocera, "P-Block Metal Oxide Noninnocence in the Oxygen Evolution Reaction in Acid: The Case of Bismuth Oxide," Chem. Mater. **34**(2), 826–835 (2022).

[184] J. Du, Z. Chen, S. Ye, B.J. Wiley, and T.J. Meyer, "Copper as a robust and transparent electrocatalyst for water oxidation," Angew. Chemie - Int. Ed. **54**(7), 2073–2080 (2015).

[185] D.K. Bediako, Y. Surendranath, and D.G. Nocera, "Mechanistic Studies of the Oxygen Evolution Reaction Mediated by a Nickel–Borate Thin Film Electrocatalyst," J. Am. Chem. Soc. **135**(9), 3662–3674 (2013).

[186] M.W. Kanan, and D.G. Nocera, "In situ formation of an oxygen-evolving catalyst in neutral water containing phosphate and Co2+," Science (80-.). **321**(5892), 1072–1075 (2008).

[187] D.A. Lutterman, Y. Surendranath, and D.G. Nocera, "A self-healing oxygen-evolving catalyst," J. Am. Chem. Soc. **131**(11), 3838–3839 (2009).

[188] C. Costentin, and D.G. Nocera, "Self-healing catalysis in water," Proc. Natl. Acad. Sci. U. S. A. **114**(51), 13380–13384 (2017).

[189] Y. Surendranath, M. Dincă, and D.G. Nocera, "Electrolyte-Dependent Electrosynthesis and Activity of Cobalt-Based Water Oxidation Catalysts," J. Am. Chem. Soc. **131**(7), 2615–2620 (2009).

[190] J.B. Gerken, E.C. Landis, R.J. Hamers, and S.S. Stahl, "Fluoride-modulated cobalt catalysts for electrochemical oxidation of water under non-alkaline conditions," ChemSusChem **3**(10), 1176–1179 (2010).

[191] Y. Surendranath, D.A. Lutterman, Y. Liu, and D.G. Nocera, "Nucleation, Growth, and Repair

of a Cobalt-Based Oxygen Evolving Catalyst," J. Am. Chem. Soc. **134**(14), 6326–6336 (2012).

[192] Q. Feng, X.Z. Yuan, G. Liu, B. Wei, Z. Zhang, H. Li, and H. Wang, "A review of proton exchange membrane water electrolysis on degradation mechanisms and mitigation strategies," J. Power Sources **366**, 33–55 (2017).

[193] M.H. Miles, E.A. Klaus, B.P. Gunn, J.R. Locker, W.E. Serafin, and S. Srinivasan, "The oxygen evolution reaction on platinum, iridium, ruthenium and their alloys at 80°C in acid solutions," Electrochim. Acta **23**(6), 521–526 (1978).

[194] D. Simondson, M. Chatti, S.A. Bonke, M.F. Tesch, R. Golnak, J. Xiao, D.A. Hoogeveen, P. V. Cherepanov, J.L. Gardiner, A. Tricoli, D.R. MacFarlane, and A.N. Simonov, "Stable Acidic Water Oxidation with a Cobalt–Iron–Lead Oxide Catalyst Operating via a Cobalt-Selective Self-Healing Mechanism," Angew. Chemie - Int. Ed. **60**(29), 15821–15826 (2021).

[195] M.M. Najafpour, M. Kompany-Zareh, A. Zahraei, D. Jafarian Sedigh, H. Jaccard, M. Khoshkam, R.D. Britt, and W.H. Casey, "Mechanism, decomposition pathway and new evidence for self-healing of manganese oxides as efficient water oxidizing catalysts: new insights," Dalt. Trans. **42**(40), 14603 (2013).

[196] M. Huynh, D.K. Bediako, and D.G. Nocera, "A Functionally Stable Manganese Oxide Oxygen Evolution Catalyst in Acid," J. Am. Chem. Soc. **136**(16), 6002–6010 (2014).

[197] A. Li, H. Ooka, N. Bonnet, T. Hayashi, Y. Sun, Q. Jiang, C. Li, H. Han, and R. Nakamura, "Stable Potential Windows for Long-Term Electrocatalysis by Manganese Oxides Under Acidic Conditions," Angew. Chemie **131**(15), 5108–5112 (2019).

[198] H. Du, M. Chatti, B. Kerr, C.K. Nguyen, T. Tran-Phu, D.A. Hoogeveen, P. V. Cherepanov, A.S.R. Chesman, B. Johannessen, A. Tricoli, R.K. Hocking, D.R. MacFarlane, and A.N. Simonov, "Durable Electrooxidation of Acidic Water Catalysed by a Cobalt-Bismuth-based Oxide Composite: An Unexpected Role of the F-doped SnO2 Substrate," ChemCatChem **14**(11), (2022).

[199] X. Zhang, C. Feng, B. Dong, C. Liu, and Y. Chai, "High-Voltage-Enabled Stable Cobalt Species Deposition on MnO2 for Water Oxidation in Acid," Adv. Mater. **35**(13), 1–12 (2023).

[200] L. Santinacci, "Atomic layer deposition: An efficient tool for corrosion protection," Curr. Opin. Colloid Interface Sci. **63**, 101674 (2023).

[201] F. Wang, G. Chen, N. Zhang, X. Liu, and R. Ma, "Engineering of carbon and other protective coating layers for stabilizing silicon anode materials," Carbon Energy **1**(2), 219–245 (2019).

[202] A.T. Sivagurunathan, S. Adhikari, and D.H. Kim, "Strategies and implications of atomic layer deposition in photoelectrochemical water splitting: Recent advances and prospects," Nano Energy **83**(January), 105802 (2021).

[203] N. Pastukhova, A. Mavrič, and Y. Li, "Atomic Layer Deposition for the Photoelectrochemical Applications," Adv. Mater. Interfaces **8**(7), 1–22 (2021).

[204] V. Dhaka, A. Perros, S. Naureen, N. Shahid, H. Jiang, J.P. Kakko, T. Haggren, E. Kauppinen, A. Srinivasan, and H. Lipsanen, "Protective capping and surface passivation of III-V nanowires by atomic layer deposition," AIP Adv. **6**(1), (2016).

[205] P.A. Kohl, S.N. Frank, and A.J. Bard, "Semiconductor Electrodes: XI . Behavior of n- and p-Type Single Crystal Semconductors Covered with Thin Films," J. Electrochem. Soc. **124**(2), 225–229 (1977).

[206] J. Su, Z. Li, Y. Yu, and X. Wang, "Atomic Layer Deposition for Advanced Electrode Design in

Photoelectrochemical and Triboelectric Systems," Adv. Mater. Interfaces **4**(4), 1600835 (2017).

[207] T. Wang, Z. Luo, C. Li, and J. Gong, "Controllable fabrication of nanostructured materials for photoelectrochemical water splitting via atomic layer deposition," Chem. Soc. Rev. **43**(22), 7469–7484 (2014).

[208] Y.W. Chen, J.D. Prange, S. Dühnen, Y. Park, M. Gunji, C.E.D. Chidsey, and P.C. McIntyre, "Atomic layer-deposited tunnel oxide stabilizes silicon photoanodes for water oxidation," Nat. Mater. **10**(7), 539–544 (2011).

[209] C.E. Finke, S.T. Omelchenko, J.T. Jasper, M.F. Lichterman, C.G. Read, N.S. Lewis, and M.R. Hoffmann, "Enhancing the activity of oxygen-evolution and chlorine-evolution electrocatalysts by atomic layer deposition of TiO2," Energy Environ. Sci. **12**(1), 358–365 (2019).

[210] T. Imrich, R. Zazpe, H. Krýsová, Paušová, F. Dvorak, J. Rodriguez-Pereira, J. Michalicka, O. Man, J.M. Macak, M. Neumann-Spallart, and J. Krýsa, "Protection of hematite photoelectrodes by ALD-TiO2 capping," J. Photochem. Photobiol. A Chem. **409**(December 2020), (2021).

[211] A.G. Scheuermann, J.D. Prange, M. Gunji, C.E.D. Chidsey, and P.C. McIntyre, "Effects of catalyst material and atomic layer deposited TiO2 oxide thickness on the water oxidation performance of metal-insulator-silicon anodes," Energy Environ. Sci. **6**(8), 2487–2496 (2013).

[212] T. Moehl, J. Suh, L. Sévery, R. Wick-Joliat, and S.D. Tilley, "Investigation of (Leaky) ALD TiO2 Protection Layers for Water-Splitting Photoelectrodes," ACS Appl. Mater. Interfaces **9**(50), 43614–43622 (2017).

[213] M. Li, Z.X. Jin, W. Zhang, Y.H. Bai, Y.Q. Cao, W.M. Li, D. Wu, and A.D. Li, "Comparison of chemical stability and corrosion resistance of group IV metal oxide films formed by thermal and plasma-enhanced atomic layer deposition," Sci. Rep. **9**(1), 1–12 (2019).

[214] X.M.C. Ta, T. Trần-Phú, J.A. Yuwono, T.K.A. Nguyen, A.D. Bui, T.N. Truong, L. Chang, E. Magnano, R. Daiyan, A.N. Simonov, and A. Tricoli, "Optimal Coatings of Co 3 O 4 Anodes for Acidic Water Electrooxidation," Small **2304650**, 1–11 (2023).

[215] Y. Yi, G. Weinberg, M. Prenzel, M. Greiner, S. Heumann, S. Becker, and R. Schlögl, "Electrochemical corrosion of a glassy carbon electrode," Catal. Today **295**(July), 32–40 (2017).

[216] S.H. Choudhury, Y. Ding, Y. Yi, C. Rohner, W. Frandsen, T. Lunkenbein, M. Greiner, R. Schlögl, and S. Heumann, "Oxidation Behavior of Glassy Carbon in Acidic Electrolyte," ChemElectroChem **9**(20), 1–7 (2022).

[217] X. Yang, H. Li, A.Y. Lu, S. Min, Z. Idriss, M.N. Hedhili, K.W. Huang, H. Idriss, and L.J. Li, "Highly acid-durable carbon coated Co3O4 nanoarrays as efficient oxygen evolution electrocatalysts," Nano Energy **25**, 42–50 (2016).

[218] Q. Lai, V. Vediyappan, K.-F. Aguey-Zinsou, and H. Matsumoto, "One-Step Synthesis of Carbon-Protected Co3O4 Nanoparticles toward Long-Term Water Oxidation in Acidic Media," Adv. Energy Sustain. Res. **2**(11), 2100086 (2021).

[219] X. Yang, J. Cheng, H. Li, Y. Xu, W. Tu, and J. Zhou, "Self-supported N-doped hierarchical Co3O4 electrocatalyst with abundant oxygen vacancies for acidic water oxidation," Chem. Eng. J. **465**(April), 142745 (2023).

[220] K.S. Exner, "Design criteria for oxygen evolution electrocatalysts from first principles: Introduction of a unifying material-screening approach," ACS Appl. Energy Mater. **2**(11), 7991–8001 (2019).

[221] G.T.K.K. Gunasooriya, and J.K. Nørskov, "Analysis of Acid-Stable and Active Oxides for the Oxygen Evolution Reaction," ACS Energy Lett. **5**(12), 3778–3787 (2020).

[222] Z. Wang, Y.R. Zheng, I. Chorkendorff, and J.K. Nørskov, "Acid-Stable Oxides for Oxygen Electrocatalysis," ACS Energy Lett. **5**(9), 2905–2908 (2020).

[223] W. Xiao, L. Zhang, D. Bukhvalov, Z. Chen, Z. Zou, L. Shang, X. Yang, D. Yan, F. Han, and T. Zhang, "Hierarchical ultrathin carbon encapsulating transition metal doped MoP electrocatalysts for efficient and pH-universal hydrogen evolution reaction," Nano Energy **70**(January), 104445 (2020).

[224] J. Resasco, F. Abild-Pedersen, C. Hahn, Z. Bao, M.T.M. Koper, and T.F. Jaramillo, "Enhancing the connection between computation and experiments in electrocatalysis," Nat. Catal. **5**(5), 374–381 (2022).

[225] Z. Fusco, M. Rahmani, T. Tran-Phu, C. Ricci, A. Kiy, P. Kluth, E. Della Gaspera, N. Motta, D. Neshev, and A. Tricoli, "Photonic Fractal Metamaterials: A Metal–Semiconductor Platform with Enhanced Volatile-Compound Sensing Performance," Adv. Mater. **32**(50), 1–10 (2020).

[226] H. Masood, C.Y. Toe, W.Y. Teoh, V. Sethu, and R. Amal, "Machine Learning for Accelerated Discovery of Solar Photocatalysts," ACS Catal. **9**(12), 11774–11787 (2019).

[227] J.A. Esterhuizen, B.R. Goldsmith, and S. Linic, "Interpretable machine learning for knowledge generation in heterogeneous catalysis," Nat. Catal. **5**(3), 175–184 (2022).

[228] K.T. Butler, D.W. Davies, H. Cartwright, O. Isayev, and A. Walsh, "Machine learning for molecular and materials science," Nature **559**(7715), 547–555 (2018).

[229] K.S. Exner, "Recent Progress in the Development of Screening Methods to Identify Electrode Materials for the Oxygen Evolution Reaction," Adv. Funct. Mater. **30**(42), (2020).

[230] A. Jain, Z. Wang, and J.K. Nørskov, "Stable Two-Dimensional Materials for Oxygen Reduction and Oxygen Evolution Reactions," ACS Energy Lett. **4**(6), 1410–1411 (2019).

[231] S. Back, K. Tran, and Z.W. Ulissi, "Discovery of Acid-Stable Oxygen Evolution Catalysts: High-Throughput Computational Screening of Equimolar Bimetallic Oxides," ACS Appl. Mater. Interfaces **12**(34), 38256–38265 (2020).

[232] W. Sun, S.T. Dacek, S.P. Ong, G. Hautier, A. Jain, W.D. Richards, A.C. Gamst, K.A. Persson, and G. Ceder, "The thermodynamic scale of inorganic crystalline metastability," Sci. Adv. **2**(11), (2016).

[233] X. Gao, H. Zhou, Z. Wang, G. Zhou, J. Wang, and Y. Wu, "Acid-stable antimonate based catalysts for the electrocatalytic oxygen evolution reaction," Nano Res. **16**(4), 4691–4697 (2023).

[234] S. Martens, L. Asen, G. Ercolano, F. Dionigi, C. Zalitis, A. Hawkins, A. Martinez Bonastre, L. Seidl, A.C. Knoll, J. Sharman, P. Strasser, D. Jones, and O. Schneider, "A comparison of rotating disc electrode, floating electrode technique and membrane electrode assembly measurements for catalyst testing," J. Power Sources **392**(January), 274–284 (2018).

[235] K. Ehelebe, N. Schmitt, G. Sievers, A.W. Jensen, A. Hrnjić, P. Collantes Jiménez, P. Kaiser, M. Geuß, Y.-P. Ku, P. Jovanovič, K.J.J. Mayrhofer, B. Etzold, N. Hodnik, M. Escudero-Escribano, M. Arenz, and S. Cherevko, "Benchmarking Fuel Cell Electrocatalysts Using Gas Diffusion Electrodes: Inter-lab Comparison and Best Practices," ACS Energy Lett. **7**(2), 816–826 (2022).

[236] T. Lazaridis, B.M. Stühmeier, H.A. Gasteiger, and H.A. El-Sayed, "Capabilities and limitations of rotating disk electrodes versus membrane electrode assemblies in the investigation of

electrocatalysts," Nat. Catal. **5**(5), 363–373 (2022).

[237] M.F. Kaya, N. Demir, N. V. Rees, and A. El-Kharouf, "Improving PEM water electrolyser's performance by magnetic field application," Appl. Energy **264**(October 2019), 114721 (2020).

[238] A.C. Olesen, C. Rømer, and S.K. Kær, "A numerical study of the gas-liquid, two-phase flow maldistribution in the anode of a high pressure PEM water electrolysis cell," Int. J. Hydrogen Energy **41**(1), 52–68 (2016).

[239] M.A. Hoeh, T. Arlt, I. Manke, J. Banhart, D.L. Fritz, W. Maier, and W. Lehnert, "In operando synchrotron X-ray radiography studies of polymer electrolyte membrane water electrolyzers," Electrochem. Commun. **55**, 55–59 (2015).

[240] S.A. Grigoriev, K.A. Dzhus, D.G. Bessarabov, and P. Millet, "Failure of PEM water electrolysis cells: Case study involving anode dissolution and membrane thinning," Int. J. Hydrogen Energy **39**(35), 20440–20446 (2014).

[241] Y. Chen, D. Liu, Q. Zhao, X. Long, J. Wang, J. Zhang, X.-Z. Fu, and J.-L. Luo, "IrOx-MoO3 nano-heterostructure electrocatalysts for efficient acidic water oxidation," Chem. Eng. J. **475**(September), 146255 (2023).

[242] L. Chong, J. Wen, E. Song, Z. Yang, I.D. Bloom, and W. Ding, "Synergistic Co─Ir/Ru Composite Electrocatalysts Impart Efficient and Durable Oxygen Evolution Catalysis in Acid," Adv. Energy Mater. **2302306**, 1–14 (2023).

[243] S. Ge, R. Xie, B. Huang, Z. Zhang, H. Liu, X. Kang, S. Hu, S. Li, Y. Luo, Q. Yu, J. Wang, G. Chai, L. Guan, H.-M. Cheng, and B. Liu, "A robust chromium–iridium oxide catalyst for high-current–density acidic oxygen evolution in proton exchange membrane electrolyzers," Energy Environ. Sci. **16**(9), 3734–3742 (2023).

[244] Z. Shi, J. Li, Y. Wang, S. Liu, J. Zhu, J. Yang, X. Wang, J. Ni, Z. Jiang, L. Zhang, Y. Wang, C. Liu, W. Xing, and J. Ge, "Customized reaction route for ruthenium oxide towards stabilized water oxidation in high-performance PEM electrolyzers," Nat. Commun. **14**(1), (2023).

[245] T. Yan, S. Chen, W. Sun, Y. Liu, L. Pan, C. Shi, X. Zhang, Z.-F. Huang, and J.-J. Zou, "IrO2 Nanoparticle-Decorated Ir-Doped W18O49 Nanowires with High Mass Specific OER Activity for Proton Exchange Membrane Electrolysis," ACS Appl. Mater. Interfaces **15**(5), 6912–6922 (2023).

[246] Z.Y. Wu, F.Y. Chen, B. Li, S.W. Yu, Y.Z. Finfrock, D.M. Meira, Q.Q. Yan, P. Zhu, M.X. Chen, T.W. Song, Z. Yin, H.W. Liang, S. Zhang, G. Wang, and H. Wang, "Non-iridium-based electrocatalyst for durable acidic oxygen evolution reaction in proton exchange membrane water electrolysis," Nat. Mater. **22**(1), 100–108 (2023).

[247] K.-R. Yeo, K.-S. Lee, H. Kim, J. Lee, and S.-K. Kim, "A highly active and stable 3D dandelion spore-structured self-supporting Ir-based electrocatalyst for proton exchange membrane water electrolysis fabricated using structural reconstruction," Energy Environ. Sci. **15**(8), 3449–3461 (2022).

[248] Z. Shi, J. Li, J. Jiang, Y. Wang, X. Wang, Y. Li, L. Yang, Y. Chu, J. Bai, J. Yang, J. Ni, Y. Wang, L. Zhang, Z. Jiang, C. Liu, J. Ge, and W. Xing, "Enhanced Acidic Water Oxidation by Dynamic Migration of Oxygen Species at the Ir/Nb2O5-x Catalyst/Support Interfaces," Angew. Chemie Int. Ed. **61**(52), (2022).

[249] T. Zhang, J. Zhou, T. Luo, J.Q. Lu, Z. Li, X. Weng, and F. Yang, "Acidic CO2 Electrolysis Addressing the 'Alkalinity Issue' and Achieving High CO2 Utilization," Chem. - A Eur. J. **29**(46), (2023).

[250] J. Li, and N. Kornienko, "Electrocatalytic carbon dioxide reduction in acid," Chem Catal. **2**(1), 29–38 (2022).

[251] Z. Ma, Z. Yang, W. Lai, Q. Wang, Y. Qiao, H. Tao, C. Lian, M. Liu, C. Ma, A. Pan, and H. Huang, "CO2 electroreduction to multicarbon products in strongly acidic electrolyte via synergistically modulating the local microenvironment," Nat. Commun. **13**(1), 1–11 (2022).

[252] Z. Xu, Y. Xie, and Y. Wang, "Pause electrolysis for acidic CO2 reduction on 3-dimensional Cu," Mater. Reports Energy **3**(1), 100173 (2023).

[253] C.J. Bondue, M. Graf, A. Goyal, and M.T.M. Koper, "Suppression of Hydrogen Evolution in Acidic Electrolytes by Electrochemical CO2Reduction," J. Am. Chem. Soc. **143**(1), 279–285 (2021).

[254] M.C.O. Monteiro, M.F. Philips, K.J.P. Schouten, and M.T.M. Koper, "Efficiency and selectivity of CO2 reduction to CO on gold gas diffusion electrodes in acidic media," Nat. Commun. **12**(1), 4943 (2021).

[255] Y. Xie, P. Ou, X. Wang, Z. Xu, Y.C. Li, Z. Wang, J.E. Huang, J. Wicks, C. McCallum, N. Wang, Y. Wang, T. Chen, B.T.W. Lo, D. Sinton, J.C. Yu, Y. Wang, and E.H. Sargent, "High carbon utilization in CO2 reduction to multi-carbon products in acidic media," Nat. Catal. **5**(6), 564–570 (2022).

[256] X. Ren, X. Dong, L. Liu, J. Hao, H. Zhu, A. Liu, and G. Wu, "Research progress of electrocatalysts for the preparation of H2O2 by electrocatalytic oxygen reduction reaction," SusMat **3**(4), 442–470 (2023).

[257] J.Y. Zhang, C. Xia, H.F. Wang, and C. Tang, "Recent advances in electrocatalytic oxygen reduction for on-site hydrogen peroxide synthesis in acidic media," J. Energy Chem. **67**, 432–450 (2022).

[258] Q. Zhang, X. Tan, N.M. Bedford, Z. Han, L. Thomsen, S. Smith, R. Amal, and X. Lu, "Direct insights into the role of epoxy groups on cobalt sites for acidic H2O2 production," Nat. Commun. **11**(1), (2020).

[259] K. Wang, J. Huang, H. Chen, Y. Wang, and S. Song, "Recent advances in electrochemical 2e oxygen reduction reaction for on-site hydrogen peroxide production and beyond," Chem. Commun. **56**(81), 12109–12121 (2020).

[260] H. Xie, Z. Zhao, T. Liu, Y. Wu, C. Lan, W. Jiang, L. Zhu, Y. Wang, D. Yang, and Z. Shao, "A membrane-based seawater electrolyser for hydrogen generation," Nature **612**(7941), 673–678 (2022).

[261] J. Guo, Y. Zheng, Z. Hu, C. Zheng, J. Mao, K. Du, M. Jaroniec, S.Z. Qiao, and T. Ling, "Direct seawater electrolysis by adjusting the local reaction environment of a catalyst," Nat. Energy **8**(3), 264–272 (2023).

[262] W. Tong, M. Forster, F. Dionigi, S. Dresp, R. Sadeghi Erami, P. Strasser, A.J. Cowan, and P. Farràs, "Electrolysis of low-grade and saline surface water," Nat. Energy **5**(5), 367–377 (2020).

[263] M.A. Khan, T. Al-Attas, S. Roy, M.M. Rahman, N. Ghaffour, V. Thangadurai, S. Larter, J. Hu, P.M. Ajayan, and M.G. Kibria, "Seawater electrolysis for hydrogen production: A solution looking for a problem?," Energy Environ. Sci. **14**(9), 4831–4839 (2021).

[264] J.N. Hausmann, R. Schlögl, P.W. Menezes, and M. Driess, "Is direct seawater splitting economically meaningful?," Energy Environ. Sci. **14**(7), 3679–3685 (2021).

[265] I.A. Moreno-Hernandez, B.S. Brunschwig, and N.S. Lewis, "Crystalline nickel, cobalt, and manganese antimonates as electrocatalysts for the chlorine evolution reaction," Energy Environ. Sci. **12**(4), 1241–1248 (2019).

[266] C. Coutanceau, and S. Baranton, "Electrochemical conversion of alcohols for hydrogen production: a short overview," Wiley Interdiscip. Rev. Energy Environ. **5**(4), 388–400 (2016).

[267] Y. Li, X. Wei, S. Han, L. Chen, and J. Shi, "MnO2 Electrocatalysts Coordinating Alcohol Oxidation for Ultra-Durable Hydrogen and Chemical Productions in Acidic Solutions," Angew. Chemie Int. Ed. **60**(39), 21464–21472 (2021).

[268] D. Bayer, S. Berenger, M. Joos, C. Cremers, and J. Tübke, "Electrochemical oxidation of C2 alcohols at platinum electrodes in acidic and alkaline environment," Int. J. Hydrogen Energy **35**(22), 12660–12667 (2010).

[269] C. Costentin, "Proton-Coupled Electron Transfer Catalyst: Homogeneous Catalysis. Application to the Catalysis of Electrochemical Alcohol Oxidation in Water," ACS Catal. **10**(12), 6716–6725 (2020).

[270] C.A. Martínez-Huitle, and S. Ferro, "Electrochemical oxidation of organic pollutants for the wastewater treatment: direct and indirect processes," Chem. Soc. Rev. **35**(12), 1324–1340 (2006).

[271] M.T. Bender, X. Yuan, and K.S. Choi, "Alcohol oxidation as alternative anode reactions paired with (photo)electrochemical fuel production reactions," Nat. Commun. **11**(1), (2020).

[272] N.P. Martínez, M. Isaacs, and K.K. Nanda, "Paired electrolysis for simultaneous generation of synthetic fuels and chemicals," New J. Chem. **44**(15), 5617–5637 (2020).

Chapter 3. Photoelectrochemical Water Splitting

This chapter is a literature review introducing about the photoelectrocatalysts to catalyze oxygen evolution reaction (OER) in photoelectrochemical (PEC) water splitting, a second electrolysis system investigated in this thesis. It gives an overview introduction about the PEC water splitting and semiconductor materials for photoanodes. The review also outlines the remaining issues limiting the efficiency of photoanodes; thus, it promotes the emerging promising materials, ternary metal oxides, and recent development strategies to enhance their performance. The reviews also highlight the flame spray pyrolysis (FSP) as a powerful deposition technique to synthesize and optimize photoelectrocatalysts, especially for ternary metal oxide materials. The conclusion is presented with the existing knowledge gaps in this space, offering the valuable scientific questions for the following research study.

Part of this chapter (section 3.1, 3.2, 3.3, and 3.4) was reprinted from the publication below with minor modifications. Ta, X. M. C., Daiyan, R., Nguyen, T. K. A., Amal, R., Tran-Phu, T., Tricoli, A., Alternatives to Water Photooxidation for Photoelectrochemical Solar Energy Conversion and Green H_2 Production. Adv. Energy Mater. 2022, 12, 2201358. 10.1002/aenm.202201358. Reproduced with permission. Copyright 2022, Wiley-VCH.

Authorship Attribution Statement

Xuan Minh Chau Ta is the principal author of this publication, which forms part of her thesis submitted for the examination for the Doctor of Philosophy degree. The corresponding author below provided the consent for inclusion of a part or whole of the following publication in this thesis and accept the following candidate statement of contribution for this publication.

Candidate contribution:

This study reviews the recent development of alternative anodic choices to OER when combined with the concurrent hydrogen evolution reaction. The manuscript was written, formatted, reviewed, and edited by Xuan Minh Chau Ta.

Corresponding author

Prof Dr Antonio Tricoli

3.1. Introduction

Over the past century, fossil fuels such as coal, oil, and natural gas have been the most popular energy resource due to their competitive price and availability.[1–3] However, these feedstocks are responsible for the majority of the anthropogenic carbon dioxide (CO_2) emission and are in depleting supply.[4–6] This is causing ever-growing problems to the environment including global warming, pollution, energy security, and consequent damage to our ecosystem.[7,8] Therefore, shifting to alternative resources, which are more sustainable and less harmful to the environment, is a strategic goal of the energy industry. As such, hydrogen (H_2) has received tremendous attention globally as a clean and promising energy carrier to gradually reduce our dependency on fossil fuels.[9–11] H_2 is the most abundant element on Earth, containing a high gravimetric energy density of 120 MJ kg^{-1} at a lower heating value compared to only 42 and 45.3 MJ Kg^{-1} of petrol and diesel, respectively.[12] Moreover, with the flexibility to be liquefied or converted to other hydrogen carriers, it can be employed in the existing infrastructure for different sectors such as transportation, agriculture, heat production, and electricity generation. Therefore, it is expected that H_2 will be a dominant energy carrier for a sustainable energy economy.[9,13]

At present, most of H_2 is produced industrially by coal gasification from fossil fuel such as natural gas or coal, due to its high energy efficiency (70 to 85%) and low operational production cost (1.25 to 3.50 USD kg^{-1} H_2).[14] However, CO_2 generated as a by-product of this process causes harmful effects on the environment. Meanwhile, water splitting driven by renewably sourced electricity, heat, or sunlight has emerged as the feasible solution toward the carbon-neutral H_2 resource.[9,15,16] Among these sources, solar light receives the greatest attention due to its abundance on the Earth. To date, there are three major solar-driven H_2 production methods namely photocatalysis (PC), photoelectrolysis (PEC), and photovoltaic-electrolysis (PV-EC), which are widely investigated.[16–19] The main difference between these technologies are the light-absorber components and catalysts of each system.[16,18–21]

In practice, PC and PEC required photo-active semiconductors, which can absorb photon energy from sunlight to generate photo-excited charge carriers and carry out two half-reactions of water splitting.[20,21] Of these approaches, PC is considered to be the simplest system because all processes such as light harvesting, charge transfer, OER, and HER occur at the photocatalyst, which is usually powder suspended in the electrolyte.[17,18] Particularly, a photocatalyst(s) first absorbs suitable illumination to generate photo-excited charge carriers, then transfer the carriers to the catalyst's surface to catalyze the OER and HER with the assistance of one or more co-catalysts in an aqueous

electrolyte. Thereby, it is promising to reduce costly components and produce H_2 at a competitive price.[22] However, since the overall water splitting efficiency primarily depends on the photocatalysts and uses illumination as single energy input, there are still many requirements to improve materials, in the aspect of the light absorber, charge carriers, stability.[17] Despite significant efforts, the solar-to-hydrogen (STH) efficiency of PC systems is still around 1%.[23,24]

Conversely, light harvesting and electrocatalytic processes are spatially decoupled in a PV-EC route.[19,25,26] This allows the combination of advances in each component to result in the most effective solar-driven H_2 pathway in terms of productivity. Given the PV device approaching theoretical maximal performance, the major attention in this method is paid to the improvement in the catalytic activity and stability of OER and HER electrocatalysts. Various methods including reducing mass loading, engineering active sites, introducing self-healing mechanism and protection layers, or exploiting activity of transition metals have been proposed.[27–39] For example, ultralow Ru loading transition metal phosphides demonstrated excellent water splitting electrocatalyst, reaching 20 mA cm^{-2} for OER and 10 mA cm^{-2} for HER in 1 M KOH with overpotentials of 191 and 35 mV, respectively.[32] Similar performance was reported by engineering the epitaxial heterointerface between Ru cluster and nickel nitrides, resulting in intrinsically higher catalytical activity.[33] In another example, with insights on theoretical predictions, cobalt-cobalt carbide (Co-Co_2C) electrocatalysts were engineered and showed excellent bifunctional overall water splitting performance.[34] PV-EC devices were also demonstrated by combining these active electrocatalysts with commercial solar cells, which can absorb and convert solar energy into electricity to drive the water splitting reactions using electrocatalysts; thus, they envisioned the large-scale implementation of this approach.[16,25,40] Up to now, the best performance of the PV-EC systems reaches *ca.* 30 % STH efficiency.[19,25,41,42] As such, PV-EC is a promising pathway towards the industrial-scale integration of PV power and electrolysis; however, the increased complexity of the total system may result in higher final H_2 production costs.[43,44]

In this scenario, a PEC system is considered as a more feasible approach as it straddles a middle ground between the simplicity of PC and the efficiency of PV-EC.[16,25] In the PEC approach, water molecules are dissociated to produce H_2 by photocatalysts, which can capture and utilize solar energy directly.[21,45–49] These photocatalysts are deposited separately as a thin photoanode or photocathode film onto supporting electrodes to drive each half-reaction independently.[21] The degree of system complexity, having a major effect on operation costs, is higher than that of PC system because it requires a supported electrode substrates and a separator in a two-compartment device. In comparison to PV-EC systems, PEC is relatively less complicated as the light absorption

and photocatalysts are combined in one component, *i.e.,* photoelectrodes. Moreover, the PEC system can also utilize low-cost photocatalysts in the PC system, which ensures a reasonable cost basis to compete with steam methane reforming.[22] In terms of efficiency, a PEC system shows a large variation of STH efficiency, depending on the PEC photocatalysts and configuration design. It is recorded from 3 %, in unassisted PEC systems with dual photoelectrodes,[50] up to *ca.* 19 % when PEC cell is integrated with monolithic PV device.[51,52] This performance is commensurate to commercial viability, but it still requires further improvements in efficiency and cost for widespread uptake.

Since the initial study from Fujishima and Honda in 1972 based on TiO_2 material,[53] PEC water splitting has drawn tremendous attention from researchers worldwide, proven by the rapid increase in the number of publications recently.[16,48] It suggests that a great deal of effort has been invested to increase PEC performance and the industrial viability of this approach. One of the prominent strategies is developing stable, non-toxic, and low-cost semiconductor materials as PEC photocatalysts that can achieve high STH efficiency.[26,47,54–56] Within this thesis, the review begins by introducing the fundamental principles of PEC water splitting, the experimental setup, and the key parameters that define PEC performance. It then delves into a detailed exploration of ternary metal oxide photoelectrocatalysts, which have garnered significant attention due to their advantages over binary counterparts in modifying band edge position and narrower band gap for the extended absorption range.[57] It also reviews some potential ternary metal oxides compounds for PEC application along with modification strategies to further improved their performance. Finally, the review highlights the potential of flame spray pyrolysis (FSP), a versatile and scalable technique for synthesizing and optimizing photoanodes, offering precise control over composition and morphology to enhance the performance of ternary metal oxide-based PEC catalysts. The integrated approach which fabricating ternary metal oxide photoelectrocatalysts by FSP provides an expectation to advance PEC technologies.

3.2. Principles of PEC Water Splitting

Generally, water splitting to produce two hydrogen and one oxygen molecules is a thermodynamically uphill reaction with a required free energy change (ΔG^0) of 237.2 kJ mol^{-1}, which is equivalent to 1.23 eV *vs.* the normal hydrogen electrode (NHE).[16,58] In a PEC device, water splitting relies on two half-reactions *viz.* the hydrogen evolution reaction (HER) and the oxygen evolution reaction (OER), which are driven on two separate electrodes.[59–61] Indeed, there are four holes joining in the photooxidation of water to generate O_2 in the anode (**Equation 3.2**),

while cathodic reaction generates H_2 via the water reduction, where four electrons are required (**Equation 3.3**). To accomplish overall PEC water splitting, light-driven energy equal to 1.23 eV per electron is required to convert liquid water molecules into gaseous oxygen and hydrogen (**Equation 3.4**).

$h\nu \rightarrow h^+ + e^-$ (**Equation 3.1**)

$2H_2O(l) + 4h^+ \rightarrow O_2(g) + 4H^+(aq)$ E_o = +1.23 V *vs.* NHE (**Equation 3.2**)

$4H^+(aq) + 4e^- \rightarrow 2H_2(g)$ E_o = 0 V *vs.* NHE (**Equation 3.3**)

$h\nu + 2H_2O(l) \rightarrow 2H_2(g) + O_2(g)$ ΔG^o = 237.2 kJ mol^{-1} (**Equation 3.4**)

The key components in the PEC processes are the photoelectrodes made of photoactive materials, which can simultaneously absorb and convert sunlight to create a photo-potential, a force to drive the PEC process. The photoelectrode usually consists of a layer of semiconductor materials on a transparent conductive substrate. A typical PEC cell can be composed of a single photoelectrode (photoanode or photocathode) and a counter electrode, or two photoelectrodes.[62] In the scope of this review, we focus on OER; thus, we further describe a PEC process occurring in a device with only the photoanode. Key principles to drive the PEC process are based on light absorption, photogeneration charge carriers formation, migration, and utilization to promote the surface reaction kinetics.[63] The schematic illustration of this process is presented in (**Figure 3.1**). When a photoanode absorbs photons with higher energy than its intrinsic bandgap energy (E_g), electrons are excited from valence bands (VB) to conduction bands (CB), leaving holes in the VB. Thus, these charge carriers migrate from the bulk to the surface to catalyze water splitting reactions. Holes diffuse to the photoanode's surface and assist the water oxidation reaction (**Equation 3.2**). Simultaneously, electrons migrate to the cathode through the external circuit to the interface of the cathode and promote cathodic water reduction to produce H_2 gas (**Equation 3.3**).

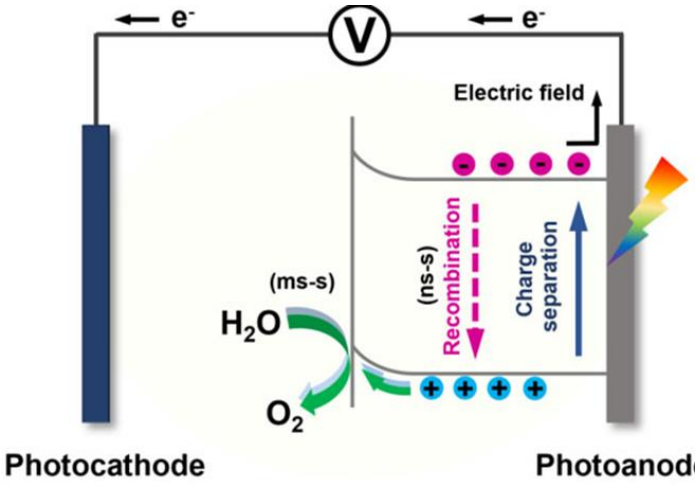

Figure 3.1. Schematic illustration of the processes of photogeneration, migration, and utilization in semiconductor-based photoanodes. Reproduced with permission.[63] Copyright 2023, The Author(s). Creative Commons Attribution 4.0 International License.

To successfully drive water splitting reactions, photoelectrodes must have a band alignment to satisfy the thermodynamic requirement (**Figure 3.2a**). In a configuration using a single photoanode, a semiconductor must have a valence band (VB) edge potential more positive than the O_2/H_2O redox potential, +1.23 V *vs.* reversible hydrogen electrode (RHE). Likewise, a photocathode is required the conduction band (CB) edge potential to be more negative than the $H^+|H_2$ redox potential, 0 V *vs.* RHE.[16] Secondly, the bandgap energy is an important factor to maximize the absorbed photon energy, which in turn will curb theoretical STH efficiency. In theory, the thermodynamic energy required to split water is 1.23 eV. However, the practical required energy to drive this reaction at a feasible rate and good performance commonly exceed 1.23 eV because of the energy loss from sluggish kinetics of the half-reactions, which primarily relates to OER.[58,64,65] This additional required energy is called "overpotential", and often in the range of several eV; thus, the bandgap energy requires incident photons to initiate water splitting with the energy around 1.4−1.8 eV.[58,66]

Bandgap energy also impacts the solar light absorption efficiency of photoelectrodes, which correlates with the energy of irradiation source. As a photoabsorber, desirable photoelectrode should have a narrow bandgap to absorb a wide range of illumination from the solar spectrum. Note that the solar spectrum is comprised of around 7 % of energy in ultraviolet (UV) (300−400 nm), 39 % in visible (VIS) (400−700 nm), and 54 % in near-infrared (NIR) (700−3000 nm) regions. The artificial solar spectrum is usually simulated by AM 1.5 G (*e.g.*, 1 sun condition, 100 mW cm^{-2}

power density) with the spectrum shown in (**Figure 3.2b)**. To date, the dominant light region of semiconductors is from UV to the start of VIS range. Therefore, semiconductors with bandgap energy between 1.9 eV and 3.2 eV (**Figure 3.2a**) can satisfy thermodynamic requirements to drive PEC system with only a single semiconductor photoelectrode. With a narrower bandgap, they are potential to generate higher STH efficiency because these materials can absorb more energy in solar spectrum (**Figure 3.2b**), consequently increase solar utilization. Therefore, lowering the bandgap of semiconductors to extend the absorption range into full UV-VIS or near infrared region by modulating bandgap structure has been extensively studied.[67,68]

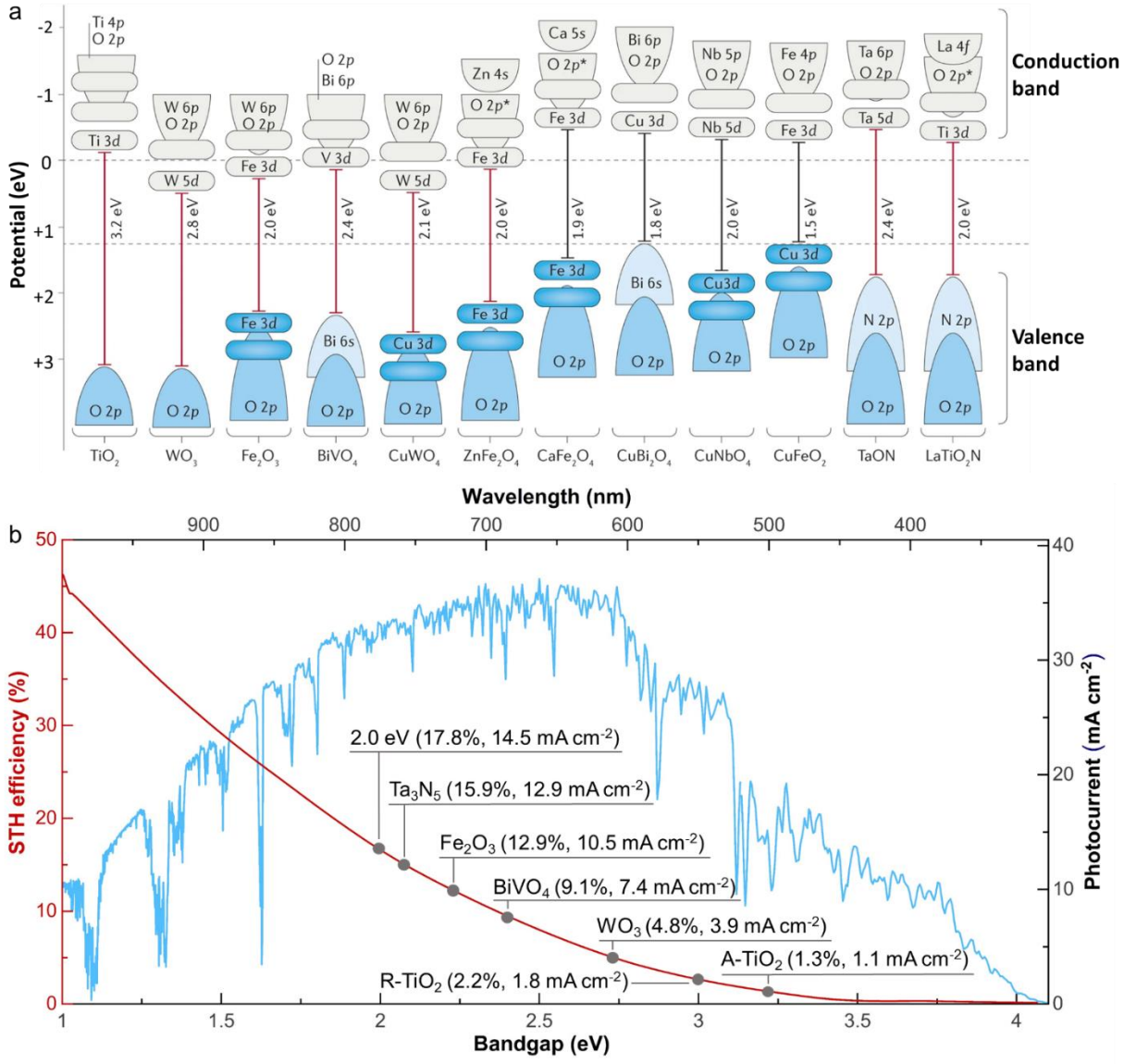

Figure 3.2 a) Bandgaps and band-edge positions with respect to the vacuum level and RHE for selected n-type (red) and p-type semiconductors. Reproduced with permission.[69] Copyright 2016, Nature Publishing Group. b) Dependence of the theoretical maximum solar-to-hydrogen (STH)

efficiency and the photocurrent density of photoelectrodes on the bandgap under AM 1.5 G irradiation. Reproduced with permission.[70] Copyright 2015, Royal Society of Chemistry.

In addition to the energy matching, the light intensity also can modulate various performance factors, such as photocurrent density, photogenerated charge carrier dynamic, light utilization efficiency, etc.[71–77] In the first stage of photoelectrolysis process, the light energy is utilized to generate the photogenerated charge carriers (electrons and holes) to promote the later water splitting. The increased light intensity directly leads to the higher production rate and the amount of photogenerated charge carriers, which is expected to enhance the photocurrent density.[72–74] For instance, the photocurrent density of CoPi/Mo-doped $BiVO_4$ enhanced about 6 times when the irradiation intensity increased from 1 to 9 suns.[74] However, the normalized value between the photocurrent density versus the light intensity showed the decrease, which determined the loss of photogenerated charge carriers due to the recombination process. Indeed, the photogenerated recombination is the competing process to targeted reaction. From low to moderate range (under 1 sun), the enhanced light intensity seems not considerably to trigger this process, proved by the near-linear relationship between the irradiation magnification and photocurrent density.[75] Nevertheless, at high regime (up to 1 sun), it is the sub-linear relationship between photocurrent density and light intensity due to the significant effect of recombination.[75–77] Noticeably, this behavior is material-dependent, especially for hematite (Fe_2O_3) photoanode with a linear relationship between photocurrent and light intensity throughout the investigated range (0.2 – 1.9 sun).[73] Besides, there is the photothermal effect, which is a result of the localized heating of the absorption of concentrated light energy.[72,74] In some cases, this effect is expected to promote the charge carrier transportation and mitigate the loss from recombination to enhance the surface reaction kinetic.[74] Nevertheless, the photo-induced heat generated from very concentrated light intensity may provoke the stability issue for the components of PEC reactor, such as rubber O-rings.[71]

Collectively, the performance of photoelectrocatalysts heavily rely on the band alignment and the light absorption capability, which are results from the specific PEC mechanism. They also cause differences in the active sites of PEC materials, compared with those in the conventional electrochemical system. In conventional electrochemistry, the active sites where the place to promote interfacial electron transfer and fuel OER process.[78,79] The key distinction of the active sites of photoelectrocatalysts is that they are required to balance light-driven charge carriers dynamic and catalytic function; hence, the active sites need to fuel the photogenerated charge carriers separation and catalyze OER concurrently.[80–83] Some detailed discussions about their

differences have been considered in (**Table 3.1)** below.[78–84] It is expected to reveal critical insights into how to control and improve the PEC processes and provide the rational design of more efficient photoelectrocatalysts for solar-driven water splitting.

Table 3.1 Comparison of the active sites of PEC and EC systems.

Aspects	Photoelectrochemistry	Electrochemistry
Origin	Surface defects/ heterojunction interfaces/ co-catalyst	Metal atoms/ cluster/ surface defects
Function	Integrate light absorption, charge separation, and promote OER	Interfacial electron transfer facilitation and promote OER
Driving force	Driven by illumination energy from light absorption	Driven by applied electrical potential (voltage) between electrodes
Charge dynamic	Photogenerated charge carriers migration and separation	Electron transfer at electrode-electrolyte interface
Influence factor	Recombination rate, defect concentration, and surface cocatalysts	Adsorption energetics and electronic structure
Stability	Photocorrosion	Catalyst degradation (dissolution, reconstruction)

3.3. PEC Cells

Generally, there are two main PEC configurations, three- and two-electrode systems, which are used for measuring the performance of single electrode or the efficiency of full-cell. The former system is often used to evaluate the performance of a single photoelectrode in a half-cell reaction, whereas the latter is more appropriate to evaluate the full-cell efficiency.[46,85]

In a lab-scale study, a three-electrode configuration is a feasible approach since it enables the characterization of PEC behaviors of an individual photoelectrode with minimal influence of the other half-cell reaction. Thereby, it provides useful insight into improving the PEC catalysts of each photoelectrode before coupling them together. There are three main components in a three-electrode system: an investigated photoelectrode as a working electrode (WE), a reference electrode (RE), and a counter electrode (CE). CE is the auxiliary electrode allowing the current flow, and RE is for

the reference of the potential and control over the potential applied at the WE. Thus, the applied potential on a WE is calculated with respect to that of a RE, along with some environmental parameters such as temperature and pH condition.[46,86–88]

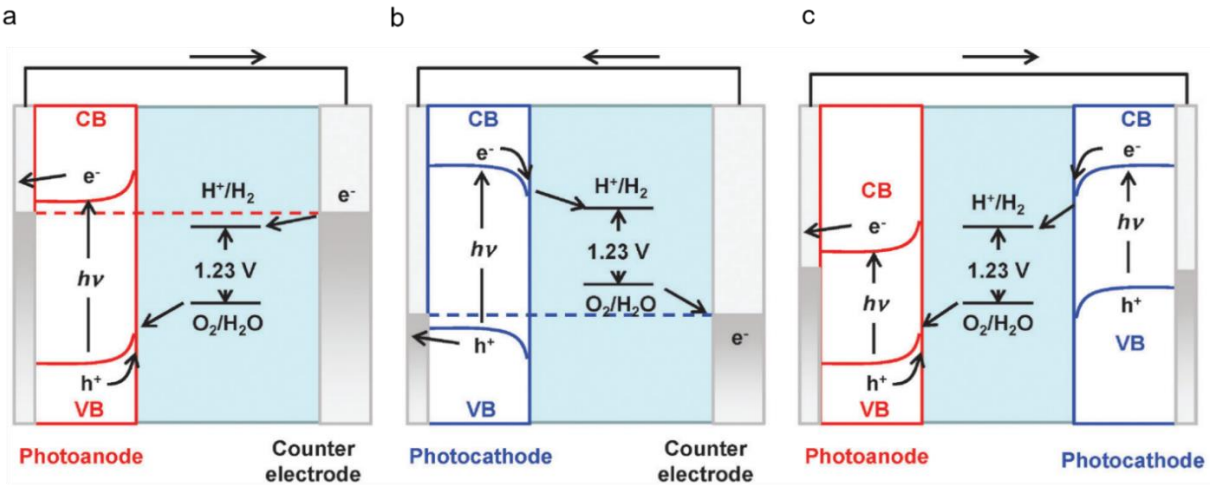

Figure 3.3 a–c) Energy diagrams and various configurations of PEC water splitting: a) a single photoanode, b) a single photocathode, and c) both photoanode and photocathode. Reproduced with permission.[46] Copyright 2014, Royal Society of Chemistry.

Regarding the two-electrode configuration, it only consists of two electrodes, (photo)anode and (photo)cathode, being integrated together in a full-cell device. However, it takes potential losses in both half-cell reactions and designed device, which is not appropriate to evaluate the single electrode performance. As a result, this approach is more comprehensive and necessary to assess overall cell efficiency and the possibility of practical implementation. For single-photoelectrode cell, the photoelectrode is chosen based on which half-cell reaction is the main subject of a study. For example, studies about OER kinetics would concentrate on photoanode and photocathode would be the main research subject of HER work. The other side of the two-electrode configuration would utilize a dark electrode, which plays a role as a counter electrode in the system. The schematics of these conditions are illustrated in **(Figure 3.3a–b).** However, some challenges limit the efficiency of the single-photoelectrode cell, including band-edge requirements and light absorption ability.[89,90] In comparison with the single-photoelectrode concept, a more advanced approach is utilizing photoanode and photocathode in a dual-absorber PEC tandem cell (**Figure 3.3c**) to increase the solar energy collected[91] and propose the possibility of an unassisted PEC device, which can drive the overall water splitting without an applied potential.[89,90] Nevertheless, it is of great challenge to engineer these efficient photoelectrodes to drive the water splitting reactions at a realistic reaction rate. Thus, most of them require an additional voltage as a chemical

or electrical bias to drive photogenerated carriers reaching the electrode|electrolyte interfaces for water splitting reactions.[62]

The primary apparatus is a single- or dual-compartment reactor, which is structured in various architectures depending on the goal of measurement. Most of them are fabricated with a transparent glass or equipped with a flat optical window to direct light into photoelectrode. Practically, a dual-compartment reactor allows to set up both three- and two-electrode configurations, whereas a single-compartment reactor is likely to suit a three-electrode system. Moreover, a dual-compartment reactor with an additional component, an ion-permeable separator/membrane, possesses several advantages over a single-compartment ones.[92] Particularly, the separator is dividing the reactor into two separated chambers but still allowing selective ion transportation. Therefore, it prevents chemical corrosion, contaminants, or performance degradation due to the gas crossover, in which H_2 can be re-oxidized back to protons at an anode and O_2 can be reduced at a cathode.[93] It is also critical when considering the explosive risk from the mixture of H_2 and O_2 gas evolved in each electrode and the gas evolution measurement step. Moreover, it enables to employ of different electrolytes as the function of catholyte and anolyte, the efficient strategy to optimize the working condition of HER and OER simultaneously. In a practical experiment, a H-shaped reactor is the most well-known system reported in the PEC measurement system.

3.4. Performance Indicators

When evaluating the PEC efficiency of water splitting reactions, there are several performance parameters that should be considered. One of the most important indicators is the photocurrent density, produced by the photoresponse of photoelectrodes divided by the surface area of a working electrode. For more accurate measurements of the photocurrent density, electrochemical surface area (ECSA) should be used, and the best practice for the ECSA or roughness factor is described in detail in previous reports.[94] Photocurrent density indicates PEC performance of a half-reaction and whole cell's activities. High photocurrent density can facilitate to faster evolution rate of value-added products at photoelectrodes.

Another important factor demonstrating PEC performance and energy efficiency of the PEC system is the required overpotential. It is the additional amount of energy required to overcome several system losses (*e.g.*, ohmic loss, mass transportation loss, losses caused by slow reaction kinetics) and to drive the expected anodic redox reactions at the desired rate.[58,95] Lowering overpotential is

beneficial to saving input energy and enhancing energy conversion efficiency. Thus, it is one of the critical parameters to be considered when evaluating alternative oxidation reactions.

Apart from photocurrent densities and overpotential, the efficiency of PEC cells should be assessed by quantifying product generation. One of the most considerable parameters is Faradaic efficiency (FE), which is defined as a ratio of the evolved gas divided by the theoretical maximum amount calculated at the observed current. It is a useful indicator to verify whether the generated photocurrent contributes to PEC conversion of expected product or photocorrosion or side reactions.[58]

If PEC processes involve reactions other than OER or HER (*e.g.,* alcohol oxidation or carbon dioxide reduction reactions) with multiple products, reporting the selectivity toward a particular product is a common practice. [96–98] It can be calculated by means of the yield of the targeted product divided by the total amount of obtained products. For further understanding of the product generation process, the production rate representing the amount of product generated in molar quantity within reaction time, based on specific electrode area, should be considered. It provides useful information relating to the reaction rate of each alternative reaction, which is necessary to assess its possibility to enhance H_2 production from the PEC water splitting system.

3.5. Photoelectrocatalyst materials - ternary metal oxides

As aforementioned, engineering efficient photoanodes with suitable band edge positions to drive water photooxidation, narrow bandgaps for wide light absorption range, and high charge separation efficiency are of key importance to PEC water splitting. Among various types of materials investigated for photoelectrodes, earth-abundant-based metal oxides have garnered a lot of attention thanks to their low cost and high stability in aqueous media. Since the pioneering PEC studies with TiO_2 photoanode, almost all possible binary metal oxide materials (Fe_2O_3, WO_3, ZnO, *etc*.) have been investigated as photoelectrocatalysts.[99–104] Despite the great efforts put into developing these materials, their performance is still not as good as expected due to their intrinsic wide bandgaps and the high recombination rate.[58,105,106] For this reason, PEC disciplines have considerably transitioned into ternary metal oxide semiconductors as an alternative class of materials for photoelectrocatalysts.

In general, ternary metal oxides are constructed by combining two metal cations and oxygen anions, enabling the obtaining thousands of formula compounds and providing greater flexibility to modify the optical and electronic properties.[107] In light of the hybridization of the O 2p orbital from two

metal element orbitals, most ternary metal oxides have the valence band pushed upward, resulting in the relative decrease in the band gap compared with their binary counterparts and better light absorption ability.[107] Indeed, some promising ternary metal oxides have demonstrated a band gap energy of 1.6 – 2.3 eV, which could achieve over 10 % STH efficiency in theory.[57,107–110]

Notwithstanding these several advantages, there are some challenges that affect the actual PEC performance of ternary metal oxide catalysts. Firstly, it requires the deposition method to achieve an accurate stoichiometry of metal cations, an important factor controlling the complex structure of mixed metal oxide phases. In the scope of this thesis, the proposed technique is FSP, which is an ultra-fast and facile synthesis process, enabling the control of the metal cations ratio and reducing the loss due to the difference of metal cation vapor in the calcination step.[111–113] A detailed review of flame-made photoelectrodes will be presented in the next section. The second challenge of ternary metal oxides relies on the low charge separation efficiency and the sluggish kinetics of PEC OER, which are also common weaknesses of PEC catalysts.[57,83,108,114–121] They require more effort put into the modification strategies to tackle these issues.

To tackle one of the most important issues relating charge separation efficiency, morphological control is the widely employed strategy. The key point in optimizing the nanostructure of photoanodes is achieving the thickness/dimension/particle size in the same range or smaller than carrier diffusion length, the average distance that excited charge/holes transfer before recombination.[115] Besides, photoelectrocatalysts with small nanoparticles sizes are also expected to have a high surface-active area, resulting in better PEC activity. Another method is utilizing the heterojunction structure by integrating with one or two semiconductors possessing the appropriate bandgap, which promotes the charge and hole traveling in two separated pathways and reduces the recombination rate.[116–118] Aside from the charge separation, the charge carrier mobility is also an important factor controlling the PEC activity that can be improved by incorporating suitable dopants or increasing the concentration of oxygen vacancies.[57,108,119] An optimal metal dopant level would enhance the carrier density and the electrical conductivity of ternary metal oxide photoanodes. Regarding the low OER kinetics, the rate of water oxidation can be promoted by coupling with co-catalysts, the active oxygen evolution catalysts (OECs) on the surface. In addition, OECs can play the role of a hole sink, affecting the band bending of the photoanode to decrease surface recombination.[83,108,114,120,121] The increased water oxidation rate based on co-catalysts is also favorable to suppressing the kinetics of photocorrosion and enhancing the stability of the photoanode. Utilizing these modification strategies, some current promising ternary oxide

photoanodes belonging to two attractive classes of photoanode materials, metal vanadate and tungstate, have been successfully developed and reviewed below.

3.5.1. $BiVO_4$ – metal vanadate photoanodes

Among various ternary metal oxides studied, the most successful material is bismuth vanadate ($BiVO_4$), a typical vanadate material constructed from Bi_2O_3 and V_2O_5. It is also one of the most popular photoanodes investigated for PEC applications in recent years.[101,108,122,123] Although $BiVO_4$ usually has three polymorphs in nature, the most prominent phase, which is usually achieved at a synthesis temperature higher than 400 ºC, is the monoclinic structure. $BiVO_4$ has a favorable optical feature with a reported bandgap of 2.4 – 2.5 eV, offering the theoretical maximum photocurrent that can be obtained at 1.23 V vs. RHE at ~ 7.5 mA cm^{-2}.[101,108,122,123]

To promote the activity of $BiVO_4$, Choi et al. engineer a high surface nanoporous structure with an average particle size of ~ 76 nm, which is similar to the calculated carrier diffusion length (~ 57 – 75 nm), by an electrodeposition BiOI, followed by drop-casting a V-containing solution and annealing process (**Figure 3.4a-b**).[124] It resulted in $BiVO_4$ photoanode achieving 90 % charge separation efficiency at 1.23 V vs. RHE without additional doping (**Figure 3.4a−c**). The post-treatment with N_2 and coupling with dual-layer FeOOH/NiOOH OECs could further enhance the PEC activity, achieving a photocurrent density of 4.7 mA cm^{-2} at 1.23 V *vs.* RHE and remarkable photostability up to 450 hours at 0.6 V vs. RHE.[125] Recently, one of the highest performance achieved from $BiVO_4$ photoanode was reported by Pihosh and co-workers.[126] They utilized the core-shell heterojunction $WO_3/BiVO_4$, in which the photoabsorb layer $BiVO_4$ was deposited at a much smaller thickness than hole diffusion length (25 nm) and promoted their PEC activity by CoPi co-catalysts (**Figure 3.4d−e**).[126] Consequently, $WO_3/BiVO_4$ – CoPi core-shell nanostructured photoanodes exhibit an impressive water oxidation photocurrent of 6.72 mA cm^{-2} at 1.23 vs RHE, which corresponds to ~ 90 % of the theoretically possible value for $BiVO_4$ (**Figure 3.4e**).

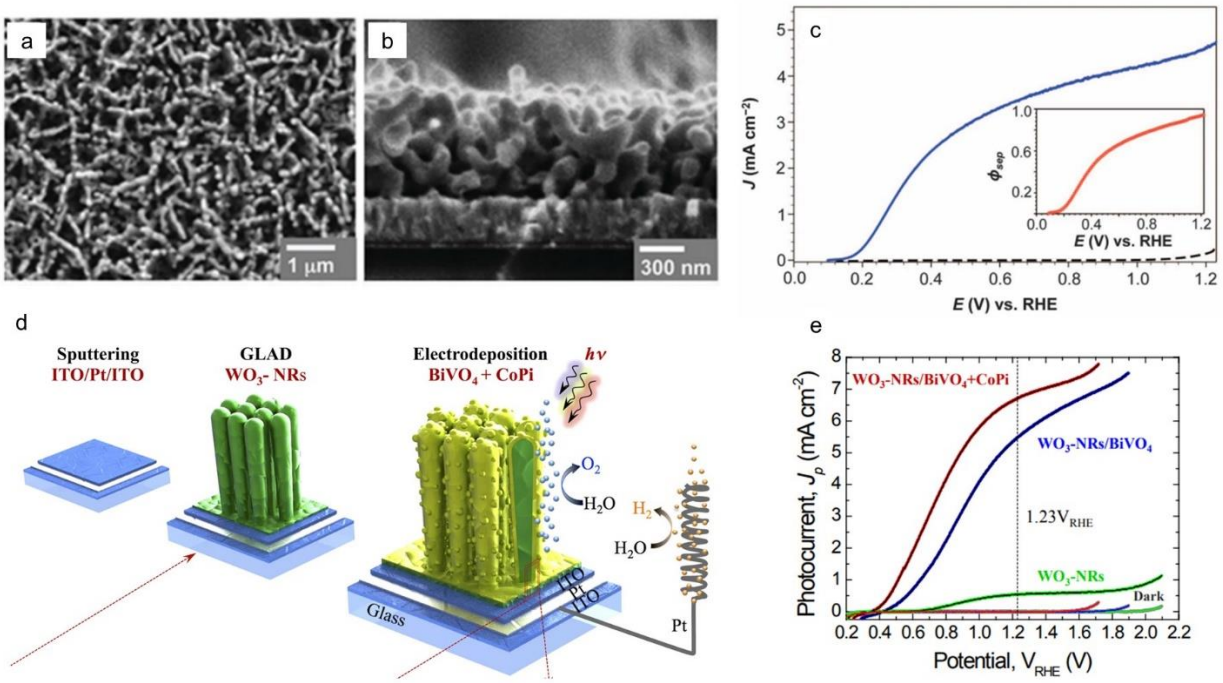

Figure 3.4 SEM images of a) Top and b) Side view images of a nanoporous $BiVO_4$ film, c) J-V curve of nanoporous $BiVO_4$ electrode measured in a 0.5 M phosphate buffer (pH 7) used to calculate the inset charge separation efficiency curve. Reproduced with permission from AAAS.[124] Copyright 2014, American Association for the Advancement of Science. d) Schematic illustration and e) J-V curve of a core-shell WO_3-NRs/$BiVO_4$ – CoPi photoanode. Reproduced with permission.[126] Copyright 2015, Springer Nature.

While $BiVO_4$ has been considered a leading photoanode for PEC applications, studies on this material are nearly saturated, making further significant improvements increasingly challenging. Thus, exploring alternative photoelectrocatalysts with narrower band gaps enabling extended light absorption range is necessary. Leveraging the advantages of ternary metal oxide structures, other metal vanadate materials such as copper vanadate and iron vanadate have recently received growing attention as promising alternatives.[127] There have been several copper vanadate phases explored ($Cu_2V_2O_7$, $Cu_5V_2O_{10}$, $Cu_{11}V_6O_{26}$, CuV_2O_6, γ-$Cu_3V_2O_8$, $Cu_{11}V_6O_{26}$).[127–133] Almost copper vanadate photoanodes showed a band gap of 1.8 – 2.0 eV, determining their favorable light absorption in the visible spectrum.[108,134,135] The most effective strategy to optimize the performance of copper vanadate is structural and morphological control during the preparation process.[127,136] The optimization of the stoichiometric Cu : V ratio can alter the photon absorption and charge separation properties, along with extending their photostability.[130,131,133,137] One of the potential materials is CuV_2O_6 with the calculated band edge position, which is feasible for water photooxidation reaction

and a slightly narrower bandgap for extended light absorption range (**Figure 3.5a**).[138] For further improvement of this photoanode, Khan et al. reported the pure CuV_2O_6 photoanode with the nanostructured peculiar platelets-shaped particles at 50 – 70 nm could achieve the photocurrent density of 0.68 mA cm^{-2} at 1.23 V *vs*. RHE.[130] In addition, doping is also a popular modification strategy employed to increase the carrier density and PEC activity of materials.[127,139–141] One of the promising results is the doping of Bi into the monoclinic CuV_2O_6 structure, causing an abrupt change to anorthic $Cu_3(VO_4)_2$ phase in the hierarchical nanoflower morphology.[141] The 20 % Bi dopants and the morphological change were beneficial to enhance the light absorption and increase the charge transport/separation efficiency, resulting in the remarkable performance at 1.29 mA cm^{-2} at 1.23 V *vs*. RHE.

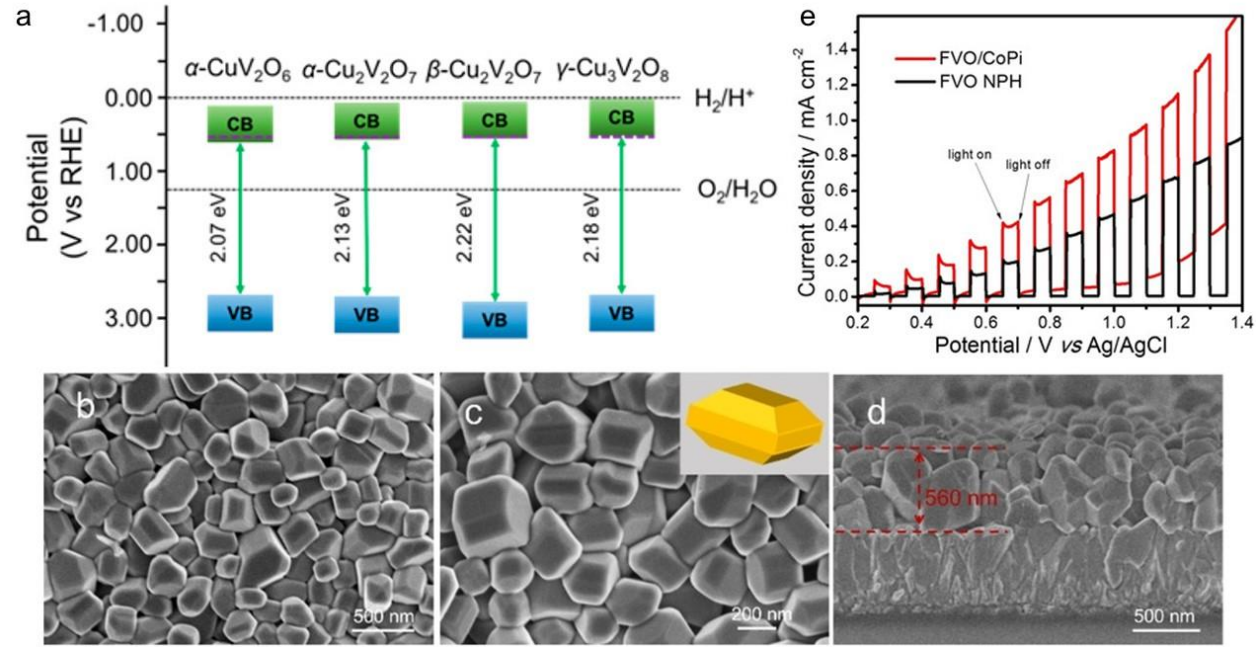

Figure 3.5 a) Calculated band edge positions of four copper vanadate materials for photoanodes. Reproduced with permission.[138] Copyright 2019, American Chemical Society. b–d) Cross- and sectional-view SEM images of $FeVO_4$, e) Chopped linear sweep voltametric curves of the $FeVO_4$ photoelectrodes. Reproduced with permission.[142] Copyright 2021, Wiley-VCH.

Another promising candidate in the class of vanadate compounds is iron vanadate, which represents the most active phase of $FeVO_4$.[108,143,144] Although $FeVO_4$ possesses the near-optimal bandgap of ~ 2 eV with the potential theoretical photocurrent and solar-to-hydrogen efficiency, early studies only reported the limited PEC activity due to its poor charge carrier transportation/separation properties.[108,145–150] Similar to copper vanadate materials discussed above, two effective modification methods employed to tackle the charge transportation/separation issues are

morphological control and doping.[110,136,145,148,150–153] Change et al. reported the pure crystalline $FeVO_4$ nanopolyhedron photoanode (**Figure 3.5b−d**) could achieve the photocurrent density of 0.4 mA cm^{-2} at 1.6V *vs*. RHE.[142] When decorating with a co-catalyst as CoPi, $FeVO_4$ photoanode achieved a photocurrent density of ~0.8 mA cm^{-2} at 1.6 V $_{vs}$. RHE, an increase of 74 % compared to the bare photoanode (**Figure 3.5e**). Besides, Zeng et al. reported the $FeVO_4$ film owning the ordered nanoblock morphology doped with Ti, demonstrating the remarkable photocurrent density of 1.47 mA cm^{-2} at 1.6V *vs*. RHE.[151]

3.5.2. Metal tungstate photoanodes

In addition to metal vanadate materials, metal tungstate semiconductors are a potential class of photoanodes that have attracted considerable attention in the role of photocatalysts/photoelectrocatalysts due to their advantages regarding the stability, band alignment, and optical properties.[154–156] The most investigated material in this class, copper tungstate ($CuWO_4$) in the triclinic phase, has a small band gap of 2.3 eV, enabling better visible-light absorption than WO_3 (**Figure 3.6a**). Moreover, $CuWO_4$ also has better photostability than WO_3 and a maximum theoretical photocurrent density up to ~9 mA cm^{-2}, comparable with $BiVO_4$.[155] Previous research reported that structural and morphological modifications can generate efficient $CuWO_4$ photoanodes without changing composition. For example, an optimized oriented $CuWO_4$ film with a high exposure ratio of the (100) crystal facet presented a photocurrent density of 0.38 mA cm^{-2} at 1.23V *vs*. RHE.[157] The flowerlike-nanostructure $CuWO_4$ exhibited a photocurrent density of 0.58 mA cm^{-2} at 0.8 V *vs*. RHE.[158] Furthermore, Mo-doping could replace W in the host structure and substantially narrow the band gap of 2 eV. Consequently, the optimized $CuWO_4$ with 32 at % Mo dopants achieved the highest photocurrent density of 0.62 mA cm^{-2} at 1.23 V *vs*. RHE.[159,160] Recently, the most remarkable performance of $CuWO_4$ was achieved when loading Ag to promote catalytic activity and enhance the charge transfer and separation efficiency. It could reach up to 1.5 mA cm^{-2} at 1.23 V *vs*. RHE.[160]

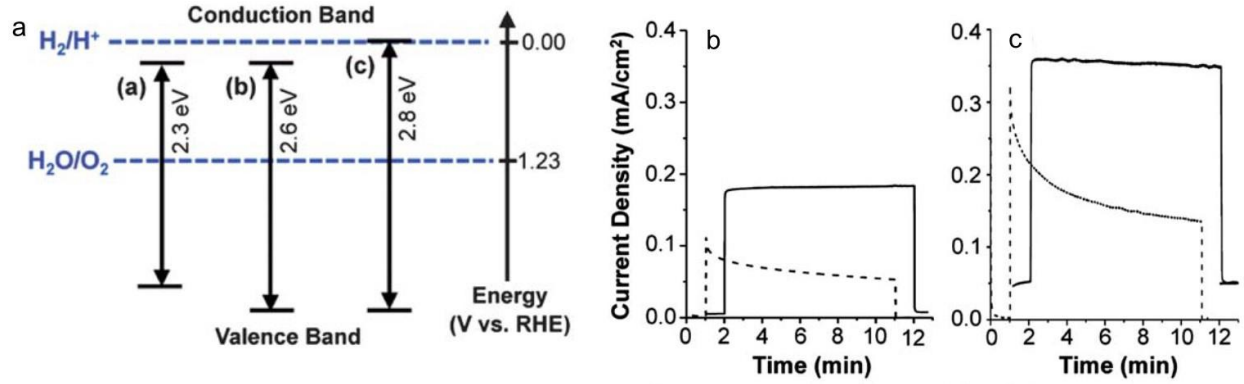

Figure 3.6 a) Schematic band diagrams of $CuWO_4$, WO_3, Bi_2WO_6, photocurrent of Bi_2WO_6 photoanode obtained at 1.03 V vs. RHE in b) 0.1 M borate buffer (pH 9) and c) 0.05 M H_2SO_4 (pH 1). Reproduced with permission.[161] Copyright 2013, The Royal Society of Chemistry.

Another metal tungstate material, bismuth tungstate (Bi_2WO_6), has been investigated as a potential photoanode. Although Bi_2WO_6 was reported with a larger bandgap than $CuWO_4$ (**Figure 3.6a**), its intrinsic PEC activity was considered to be higher than that of $CuWO_4$ in the same preparation and testing conditions.[161] It was attributed to the more favorable band alignment. Moreover, Bi_2WO_6 performed a considerable increase in photocurrent density from 0.2 mA cm^{-2} to 0.35 mA cm^{-2} in pH of 9 and 1, respectively, at 1 V *vs*. RHE, proposing a potential to apply for acidic electrolytes (**Figure 3.6b−c**).[161] For further enhancing the PEC performance of Bi_2WO_6, the well-known strategy, doping, was employed, which can increase the negligible photocurrent density up to 0.4 mA cm^{-2} at 1.2 V *vs*. RHE in 6 % Mo-doped sample, thanks to the beneficial impacts to the charge carrier density, separation efficiency, and possibly ion mobility.[162] Another method is utilizing a thin-layer $Co(OH)_x$ co-catalyst, providing more active sites to fuel OER and trap holes in the surface for decreased charge recombination. It achieved a remarkable photocurrent density of 0.94 mA cm^{-2} and a superior surface charge separation efficiency of 98 % at 1.23V *vs*. RHE.[163]

Iron tungstate materials are another class of catalyst studied for photoanode recently. They possess advantageous features, including a relatively narrow bandgap, 1.7−2.0 eV, making them effective for capturing a relatively large spectrum of solar energy in the ultraviolet to visible range. Besides, they are highly considered with a chemically and photoelectrochemically stable. Generally, there are two types of iron tungstate compounds, namely ferberite ($FeWO_4$) and wolframite (Fe_2WO_6). Although Fe_2WO_6 has been more extensively explored, the high synthesis temperature (750 – 800 ºC) limits the possibility of engineering tunable nanostructured morphologies and the direct deposition onto the substrate with low thermal resistance, for example, fluorine-doped tin oxide (FTO) glass. Meanwhile, $FeWO_4$ with a lower synthesis temperature has more opportunities to

control morphology during the fabrication process. $FeWO_4$ is a promising n-type direct semiconductor with a narrow band gap (~ 1.8 - 2.5 eV) and favorable energy band structure toward water photooxidation reaction. [110,164] Moreover, the stability in a wide range of pH, from 2 to 11, makes this material more promising for various applications, such as detectors, photocatalysts, sensors, *etc*.[110,164] However, there still remains a gap in the research on $FeWO_4$ photoanode in PEC water splitting, which has not been thoroughly explored in previous studies.[110,164] Despite its advantageous optical properties, $FeWO_4$ shares common drawbacks with other iron-based photoanodes, such as short hole diffusion lengths and low charge separation efficiency.[108,110,164] Further development of $FeWO_4$ in the role of photoanode in water photoelectrolysis is indeed more efforts in optimizing the composition and structure to address the charge recombination limitation and enhance their PEC activity.[164]

3.6. Flame-made photoelectrodes

Flame spray pyrolysis (FSP) is a powerful technique that allows nanostructured materials to be fabricated rapidly with a scalable opportunity.[111–113] A one-step FSP synthesis process is described in the schematic (**Figure 3.7a)**.[113] The synthesis process begins with mixing metal precursor in a flammable liquid fuel, then feeding into a nozzle by syringe pump and atomizing by CH_4/O_2 for a continuous spray flame. During combustion, the liquid precursors generate versatile vapor metal particles, which grow into nanoparticles and possibly agglomerate into fractal-like structures. The resulting materials can be collected as powder on a filter or solid film deposited directly on the substrate.

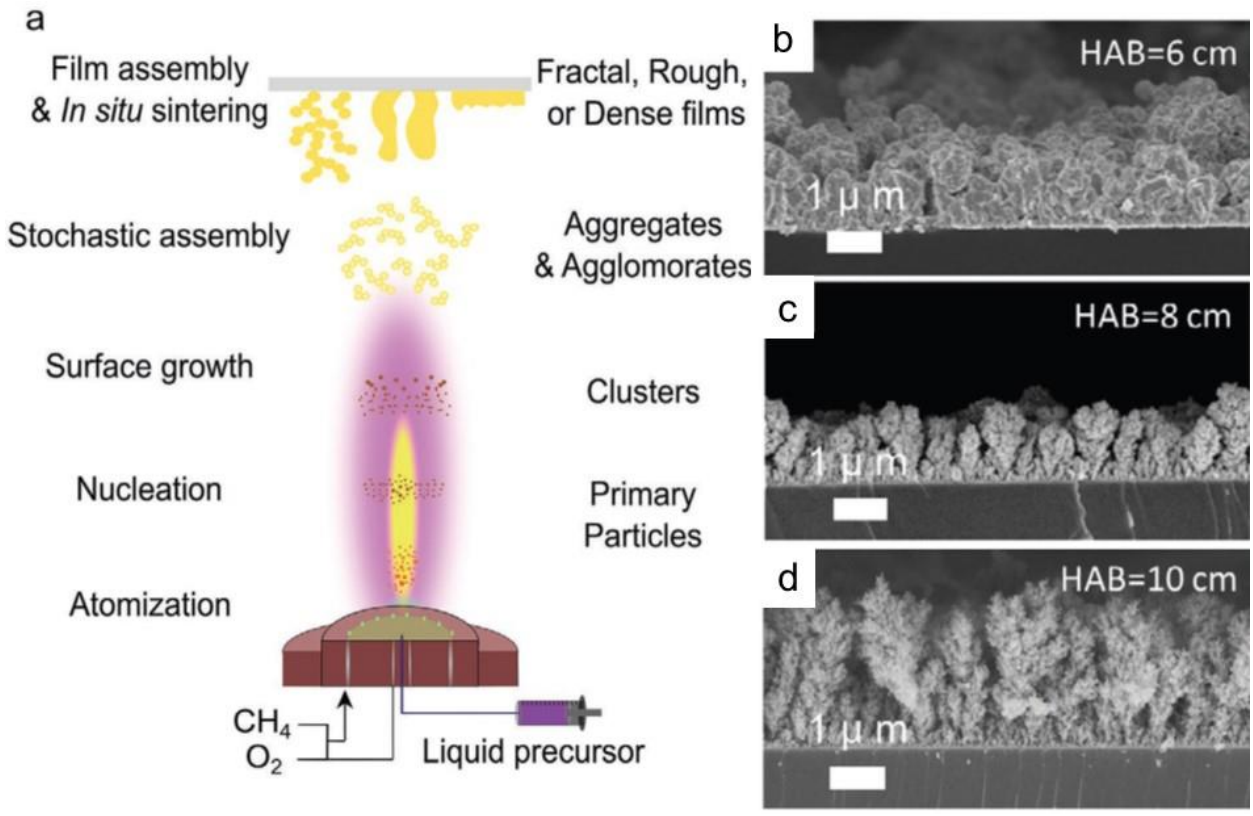

Figure 3.7 a) Schematic diagram of FSP process demonstrates the working principles of FSP and nanomaterial formation. Reproduced with permission.[113] Copyright 2022, Wiley-VCH. b–d) Direct synthesis of WO_3 photoanodes on FTO for PEC water splitting with different HAB. Reproduced with permission.[56] Copyright 2018, Wiley-VCH.

As a dry-phase synthesis method, the FSP method possesses an advantage over the wet-phase approach, which usually requires a multi-step and time-consuming procedure, which usually includes filtration, washing, drying, *etc*.[113] Moreover, modifying an optimal height above burner (HAB) and deposition time allows for control of the temperature and sintering of nanoparticles deposited onto the substrate.[111–113] Thus, it offers considerable potential for tunable porosity and controlled morphology, which are important factors in enhancing PEC activity.[111,113] As evidence, Chen et al. reported the direct fabrication of WO_3 photoanode on FTO glass by FSP, whose morphology could tune from cauliflower- to tree-like nanostructure (**Figure 3.7b**–**d**) when HAB changes from 6 to 10, respectively.[56] Simultaneously, the porosity of flame-made WO_3 also increased from 59 % to 78 %, with the enhanced HAB from 6 to 10.

As a well-established and efficient nanofabrication technology, FSP has been widely employed to synthesize transition metal oxides as PEC catalysts. Previously, this method has been mostly adopted to produce powder materials.[111,113,165] For example, Tantis et al. applied titania

nanoparticle paste made by FSP to prepare photoanodes on FTO glass by using a doctor-blading coating.[166] For the application to PEC water splitting and PhotoFuelCell, the FSP-made titania powder proved to have superior performance with respect to commercial P25 titania. Similarly, Chiang et al. prepared CuO photocathodes on ITO substrates using a spin coating method with FSP-made CuO powder.[167] It achieved the net photocurrent density at 1.20 mA cm^{-2} at an applied voltage of −0.55 V vs. Ag/AgCl in 1 M KOH electrolyte with one sun illumination, which was about 7.8 times higher than photoelectrodes made by CuO powder purchased from Sigma-Aldrich. The superior activity of FSP-made CuO powder could be explained by its relatively uniform CuO nanoparticles. Meanwhile, the commercial CuO powder didn't have a similar nanoparticle size, so the large particles might lead to an increased recombination rate.

Recent studies investigated the direct fabrication of semiconductor PEC materials onto conductive substrates to enhance mechanical adhesion and efficiently optimize the morphology of flame-made materials.[56,88,168,169] One of the pioneering studies is the synthesis of WO_3 photoanode with tunable porosity and morphology by adjusting the synthesis parameters such as position (HAB) and deposition time. The optimized WO_3 photoanode prepared at HAB 6 cm in 10 seconds displayed the best performance, achieved a photocurrent density of 0.91mA cm^{-2} at 1.23 V *vs.* reversible hydrogen electrode (RHE) under simulated one sun irradiation and good stability in 1 hour of PEC OER operation.[56] Flame-made WO_3 photoanode also performed 2–3 times higher activity than these samples fabricated by doctor-blader or sputtering. Likewise, the FSP-made nanostructured $BiVO_4$ photoanode optimized the optical density and porosity at different HABs in a time scale of seconds.[88] An optimized $BiVO_4$ photoanode prepared at HAB 10 cm had a porosity of 46 %. With a co-catalyst layer of FeOOH/NiOOH, this photoanode reached a photocurrent density of 1 mA cm^{-2} for water photooxidation at 1 V *vs.* RHE, which was up to 6 or 1.5 times higher than the counter samples with porosity of 80 % and 12 %, respectively. This study determined the important role of controlling porosity through HAB in FSP deposition, which can result in significant differences in the electrochemically active surface area, the hole diffusion length, and the recombination probability in improving PEC activity.

Despite the optimized performance of direct FSP-made photoelectrodes, the post-synthesis treatments can provide more opportunities to control various properties (morphology, crystallinity, preferential orientation, *etc*.) to further enhance their PEC activity.[111,113] For instance, Liu et al. employed the most physical- and chemical procedures to tune the structural and morphological properties of Sn-doped hematite photoanode directly fabricated by FSP for the enhanced

conductivity and charge carriers, a critical factor to overcome the intrinsic weakness of poor charge transportation.[168] As a result, an optimized hematite photoanode achieved a 24-fold enhancement in the performance toward water oxidation at 1.23 V *vs.* RHE compared with the as-prepared sample. For FSP-made $BiVO_4$ photoanode, the post-synthesis treatment with a vanadium source could be employed to re-introduce a small amount of vanadium in the surface to compensate for the vanadium loss in the as-prepared sample, increase the number of accessible sites for the OER, and enhances the photoluminescent lifetimes of photoexcited carriers.[45] As a result, a vanadium-treated $BiVO_4$ achieved 2 mA cm^{-2} for water oxidation at 1.23 V *vs.* RHE, nearly twice higher than those of the as-prepared vanadium-defective $BiVO_4$. In addition to $BiVO_4$, another ternary metal oxide, perovskite $BiFeO_3$ photoanode, was fabricated by FSP and investigated with two post-synthesis approaches to enhance the interfacial charge transfer, developing ultrathin TiO_2 overlayer or coupling with CoO_x co-catalyst.[169] It determined that the atomic layer deposition of TiO_2 overlayer and photo-assisted electrodeposition of a CoO_x co-catalyst could improve the surface charge transfer kinetics at the interface during water oxidation by $BiFeO_3$ photoanode. It resulted in a significant increase from negligible photocurrent of the pristine $BiFeO_3$ to 0.16 mA cm^{-2} at 1.23 V vs. RHE and the lower 0.7 V of water photooxidation onset potential.

3.7. Conclusions and Research Recommendations

Photoelectrochemical (PEC) water splitting presents a potential approach to sustainable H_2 production by solar-driven systems. The most important component in PEC electrolyzers is the photoanode, which plays a crucial role in controlling the energy conversion efficiency of the process. In the scope of this research, we introduced semiconductor metal vanadates and metal tungstate, two promising classes of ternary metal oxides. As discussed, despite several challenges remaining in these materials, there have been recent advances with encouraging results demonstrating their prospects in photoanodes of PEC water splitting. For the enhancement of ternary metal oxide photoanodes, aside from $BiVO_4$, the associated challenges and research opportunities are described below.

- While ternary metal oxide photoanodes have received significant attention for their advantages relating to band gaps and tunable optical/electronic properties, several challenges still limit their development. Specifically, this class of materials requires a suitable deposition method that can achieve well-mixing of different metal precursors and accurately control the stoichiometric ratio. Besides, more effort is required to resolve the low charge separation efficiency issue, which limits the overall PEC performance. The

crucial point to achieve this goal is optimizing the nanostructure/composition of material through the preparation process, post-synthesis treatment, or doping and utilizing co-catalysts to enhance the surface reaction kinetics further. Flame spray pyrolysis (FSP) is an efficient deposition technique that can tackle both aforementioned issues of ternary metal oxide photoanodes. Its prospect for controlling the stoichiometric ratio of mixed materials and optimizing morphology to enhance (photo)electrochemical activities is determined in previous studies. Further investigation into flame-made ternary metal oxide photoelectrocatalysts may unlock the efficient pathway to optimizing and enhancing photoanode materials.

- Among various semiconductor ternary metal oxides extensively investigated and discussed in this review, iron tungstate is a promising material. Theoretical calculation demonstrates an appropriate bandgap and band edge structure for water photooxidation under visible light, along with favorable electronic properties. Additionally, its application in a relevant field, photocatalysts, determines the possibility for effective charge transfer and reduced recombination rate under illumination. Nevertheless, the research about iron tungstate photoanode is currently limited, leaving an existing knowledge gap in the optimization process and its influence on all the functional properties and PEC activity. Addressing these questions is expected to promote and demonstrate iron tungstate as a potential photoanode material and provide valuable insights into optimizing and enhancing their efficiency.

3.8. References

[1] T. Kåberger, *Glob. Energy Interconnect.* **2018**, *1*, 48.

[2] D. Helm, *Oxford Rev. Econ. Policy* **2016**, *32*, 191.

[3] S. F. Lincoln, *Ambio* **2005**, *34*, 621.

[4] T. Covert, M. Greenstone, C. R. Knittel, *J. Econ. Perspect.* **2016**, *30*, 117.

[5] S. Shafiee, E. Topal, *Energy Policy* **2009**, *37*, 181.

[6] M. Höök, X. Tang, in *Energy Policy*, **2013**, pp. 797–809.

[7] K. O. Yoro, M. O. Daramola, in *Adv. Carbon Capture*, Elsevier, **2020**, pp. 3–28.

[8] Y. S. H. Najjar, *Innov. Energy Policies* **2011**, *1*, 1.

[9] H. Nazir, C. Louis, S. Jose, J. Prakash, N. Muthuswamy, M. E. M. Buan, C. Flox, S. Chavan, X. Shi, P. Kauranen, T. Kallio, G. Maia, K. Tammeveski, N. Lymperopoulos, E. Carcadea, E. Veziroglu, A. Iranzo, A. M. Kannan, *Int. J. Hydrogen Energy* **2020**, *45*, 13777.

[10] R. L. Germscheidt, D. E. B. Moreira, R. G. Yoshimura, N. P. Gasbarro, E. Datti, P. L. dos

Santos, J. A. Bonacin, *Adv. Energy Sustain. Res.* **2021**, *2*, 2100093.

[11] H. Nazir, N. Muthuswamy, C. Louis, S. Jose, J. Prakash, M. E. M. Buan, C. Flox, S. Chavan, X. Shi, P. Kauranen, T. Kallio, G. Maia, K. Tammeveski, N. Lymperopoulos, E. Carcadea, E. Veziroglu, A. Iranzo, A. M. Kannan, *Int. J. Hydrogen Energy* **2020**, *45*, 28217.

[12] A. Godula-Jopek, D. Stolten, C. Bourasseau, *Hydrogen Production by Electrolysis*, WILEY-VCH Verlag GmbH & Co. KGaA, Weinheim, Germany, **2015**.

[13] I. Staffell, D. Scamman, A. Velazquez Abad, P. Balcombe, P. E. Dodds, P. Ekins, N. Shah, K. R. Ward, *Energy Environ. Sci.* **2019**, *12*, 463.

[14] R. Yukesh Kannah, S. Kavitha, Preethi, O. Parthiba Karthikeyan, G. Kumar, N. V. Dai-Viet, J. Rajesh Banu, *Bioresour. Technol.* **2021**, *319*, 124175.

[15] M. R. Shaner, H. A. Atwater, N. S. Lewis, E. W. McFarland, *Energy Environ. Sci.* **2016**, *9*, 2354.

[16] J. H. Kim, D. Hansora, P. Sharma, J. W. Jang, J. S. Lee, *Chem. Soc. Rev.* **2019**, *48*, 1908.

[17] S. Chen, T. Takata, K. Domen, *Nat. Rev. Mater.* **2017**, *2*, 17050.

[18] I. Roger, M. A. Shipman, M. D. Symes, *Nat. Rev. Chem.* **2017**, *1*, 0003.

[19] Z. Wang, Y. Gu, L. Wang, *Front. Energy* **2021**, *15*, 596.

[20] M. Grätzel, *Nature* **2001**, *414*, 338.

[21] H. Wu, H. L. Tan, C. Y. Toe, J. Scott, L. Wang, R. Amal, Y. H. Ng, *Adv. Mater.* **2020**, *32*, 1904717.

[22] B. A. Pinaud, J. D. Benck, L. C. Seitz, A. J. Forman, Z. Chen, T. G. Deutsch, B. D. James, K. N. Baum, G. N. Baum, S. Ardo, H. Wang, E. Miller, T. F. Jaramillo, *Energy Environ. Sci.* **2013**, *6*, 1983.

[23] K. Maeda, T. Takata, M. Hara, N. Saito, Y. Inoue, H. Kobayashi, K. Domen, *J. Am. Chem. Soc.* **2005**, *127*, 8286.

[24] Q. Wang, T. Hisatomi, Q. Jia, H. Tokudome, M. Zhong, C. Wang, Z. Pan, T. Takata, M. Nakabayashi, N. Shibata, Y. Li, I. D. Sharp, A. Kudo, T. Yamada, K. Domen, *Nat. Mater.* **2016**, *15*, 611.

[25] B. Moss, O. Babacan, A. Kafizas, A. Hankin, *Adv. Energy Mater.* **2021**, *11*, 2003286.

[26] Y. Chen, Y. Liu, F. Wang, X. Guan, L. Guo, *J. Energy Chem.* **2021**, *61*, 469.

[27] L. An, C. Wei, M. Lu, H. Liu, Y. Chen, G. G. Scherer, A. C. Fisher, P. Xi, Z. J. Xu, C. H. Yan, *Adv. Mater.* **2021**, *33*, 1.

[28] S. Anantharaj, V. Aravindan, *Adv. Energy Mater.* **2020**, *10*, 1902666.

[29] A. E. Thorarinsdottir, S. S. Veroneau, D. G. Nocera, *Nat. Commun.* **2022**, *13*, 1.

[30] C. E. Finke, S. T. Omelchenko, J. T. Jasper, M. F. Lichterman, C. G. Read, N. S. Lewis, M. R. Hoffmann, *Energy Environ. Sci.* **2019**, *12*, 358.

[31] T. Tran-Phu, H. Chen, R. Daiyan, M. Chatti, B. Liu, R. Amal, Y. Liu, D. R. Macfarlane, A. N. Simonov, A. Tricoli, *ACS Appl. Mater. Interfaces* **2022**, *14*, 33130.

[32] D. Chen, Z. Pu, R. Lu, P. Ji, P. Wang, J. Zhu, C. Lin, H. Li, X. Zhou, Z. Hu, F. Xia, J. Wu, S. Mu, *Adv. Energy Mater.* **2020**, *10*, 2000814.

[33] J. Zhu, R. Lu, W. Shi, L. Gong, D. Chen, P. Wang, L. Chen, J. Wu, S. Mu, Y. Zhao, *ENERGY Environ. Mater.* **2022**, 1.

[34] P. Wang, J. Zhu, Z. Pu, R. Qin, C. Zhang, D. Chen, Q. Liu, D. Wu, W. Li, S. Liu, J. Xiao, S. Mu, *Appl. Catal. B Environ.* **2021**, *296*, 120334.

[35] X. Gao, I. Di Bernardo, P. Kreider, T. Tran-Phu, X. Cai, N. Wang, Y. Zhu, M. B. Venkataraman, J. Lipton-Duffin, A. Bayon, W. Lipiński, A. Tricoli, *ACS Catal.* **2019**, *9*, 9880.

[36] M. Chatti, J. L. Gardiner, M. Fournier, B. Johannessen, T. Williams, T. R. Gengenbach, N. Pai, C. Nguyen, D. R. MacFarlane, R. K. Hocking, A. N. Simonov, *Nat. Catal.* **2019**, *2*, 457.

[37] M. Chatti, T. Gengenbach, R. King, L. Spiccia, A. N. Simonov, *Chem. Mater.* **2017**, *29*, 3092.

[38] V. Stamenkovic, B. S. Mun, K. J. J. Mayrhofer, P. N. Ross, N. M. Markovic, J. Rossmeisl, J. Greeley, J. K. Nørskov, *Angew. Chemie* **2006**, *118*, 2963.

[39] S. Cherevko, *Curr. Opin. Electrochem.* **2018**, *8*, 118.

[40] G. Liu, Y. Sheng, J. W. Ager, M. Kraft, R. Xu, *EnergyChem* **2019**, *1*, 100014.

[41] J. Jia, L. C. Seitz, J. D. Benck, Y. Huo, Y. Chen, J. W. D. Ng, T. Bilir, J. S. Harris, T. F. Jaramillo, *Nat. Commun.* **2016**, *7*, 13237.

[42] H. Chen, M. Zhang, T. Tran-Phu, R. Bo, L. Shi, I. Di Bernardo, J. Bing, J. Pan, S. Singh, J. Lipton-Duffin, T. Wu, R. Amal, S. Huang, A. W. Y. Ho-Baillie, A. Tricoli, *Adv. Funct. Mater.* **2021**, *31*, 2008245.

[43] T. Hisatomi, K. Domen, *Faraday Discuss.* **2017**, *198*, 11.

[44] N. A. Burton, R. V. Padilla, A. Rose, H. Habibullah, *Renew. Sustain. Energy Rev.* **2021**, *135*, 110255.

[45] T. Tran-Phu, Z. Fusco, I. Di Bernardo, J. Lipton-Duffin, C. Y. Toe, R. Daiyan, T. Gengenbach, C.-H. Lin, R. Bo, H. T. Nguyen, G. M. J. Barca, T. Wu, H. Chen, R. Amal, A. Tricoli, *Chem. Mater.* **2021**, *33*, 3553.

[46] T. Hisatomi, J. Kubota, K. Domen, *Chem. Soc. Rev.* **2014**, *43*, 7520.

[47] J. Joy, J. Mathew, S. C. George, *Int. J. Hydrogen Energy* **2018**, *43*, 4804.

[48] Y.-H. Chiu, T.-H. Lai, M.-Y. Kuo, P.-Y. Hsieh, Y.-J. Hsu, *APL Mater.* **2019**, *7*, 080901.

[49] Z. Xing, X. Zong, J. Pan, L. Wang, *Chem. Eng. Sci.* **2013**, *104*, 125.

[50] L. Pan, J. H. Kim, M. T. Mayer, M.-K. Son, A. Ummadisingu, J. S. Lee, A. Hagfeldt, J. Luo, M. Grätzel, *Nat. Catal.* **2018**, *1*, 412.

[51] W. H. Cheng, M. H. Richter, M. M. May, J. Ohlmann, D. Lackner, F. Dimroth, T. Hannappel, H. A. Atwater, H. J. Lewerenz, *ACS Energy Lett.* **2018**, *3*, 1795.

[52] C. Moon, B. Shin, *Discov. Mater.* **2022**, *2*, 5.

[53] A. FUJISHIMA, K. HONDA, *Nature* **1972**, *238*, 37.

[54] W. Yang, J. Moon, *ChemSusChem* **2019**, *12*, 1889.

[55] W. Yang, R. R. Prabhakar, J. Tan, S. D. Tilley, J. Moon, *Chem. Soc. Rev.* **2019**, *48*, 4979.

[56] H. Chen, R. Bo, T. Tran-Phu, G. Liu, A. Tricoli, *Chempluschem* **2018**, *83*, 569.

[57] H. He, A. Liao, W. Guo, W. Luo, Y. Zhou, Z. Zou, *Nano Today* **2019**, *28*, 100763.

[58] C. Jiang, S. J. A. Moniz, A. Wang, T. Zhang, J. Tang, *Chem. Soc. Rev.* **2017**, *46*, 4645.

[59] T. Bak, J. Nowotny, M. Rekas, C. . Sorrell, *Int. J. Hydrogen Energy* **2002**, *27*, 991.

[60] M. G. Walter, E. L. Warren, J. R. McKone, S. W. Boettcher, Q. Mi, E. A. Santori, N. S. Lewis, *Chem. Rev.* **2010**, *110*, 6446.

[61] G. Wang, Y. Ling, H. Wang, L. Xihong, Y. Li, *J. Photochem. Photobiol. C Photochem. Rev.* **2014**, *18*, 35.

[62] L. J. Minggu, W. R. Wan Daud, M. B. Kassim, *Int. J. Hydrogen Energy* **2010**, *35*, 5233.

[63] N. Liu, Y. Liu, Y. Liu, Y. Li, Y. Cheng, H. Li, *Microstructures* **2022**, *3*, 2022022.

[64] N.-T. Suen, S.-F. Hung, Q. Quan, N. Zhang, Y.-J. Xu, H. M. Chen, *Chem. Soc. Rev.* **2017**, *46*, 337.

[65] S. Haussener, C. Xiang, J. M. Spurgeon, S. Ardo, N. S. Lewis, A. Z. Weber, *Energy Environ. Sci.* **2012**, *5*, 9922.

[66] M. A. Butler, D. S. Ginley, *J. Mater. Sci.* **1980**, *15*, 1.

[67] X. Chen, Z. Zhang, L. Chi, A. K. Nair, W. Shangguan, Z. Jiang, *Nano-Micro Lett.* **2016**, *8*, 1.

[68] P. Y. Hsieh, J. Y. Wu, T. F. M. Chang, C. Y. Chen, M. Sone, Y. J. Hsu, *Arab. J. Chem.* **2020**, *13*, 8372.

[69] K. Sivula, R. van de Krol, *Nat. Rev. Mater.* **2016**, *1*, 15010.

[70] J. Li, N. Wu, *Catal. Sci. Technol.* **2015**, *5*, 1360.

[71] K. Li, W. J. Dong, Z. Mi, *Front. Energy Res.* **2025**, *13*, 1.

[72] W. J. Dong, Z. Ye, S. Tang, I. A. Navid, Y. Xiao, B. Zhang, Y. Pan, Z. Mi, *Adv. Sci.* **2024**, *11*, DOI 10.1002/advs.202309548.

[73] Z. Wang, M. Lyu, P. Chen, S. Wang, L. Wang, *Phys. Chem. Chem. Phys.* **2018**, *20*, 22629.

[74] L. Pan, J. Wu, X. Xu, F. Lv, Y. Chen, L. Guo, *Int. J. Hydrogen Energy* **2023**, *48*, 13479.

[75] S. Bell, G. Will, J. Bell, *Int. J. Hydrogen Energy* **2013**, *38*, 6938.

[76] S. B. Patel, B. A. Thakar, *J. Emerg. Investig.* **2022**, *5*, 1.

[77] T. H. Lim, S. M. Jeong, S. D. Kim, J. Gyenis, *J. Photochem. Photobiol. A Chem.* **2000**, *134*, 209.

[78] Y. Tang, T. Zhang, X. Wu, S. Deng, *Front. Chem.* **2022**, *10*, 1.

[79] B. Garlyyev, J. Fichtner, O. Piqué, O. Schneider, A. S. Bandarenka, F. Calle-Vallejo, *Chem. Sci.* **2019**, *10*, 8060.

[80] K. H. Ly, I. M. Weidinger, *Chem. Commun.* **2021**, *57*, 2328.

[81] H. Zhang, L. Chen, F. Dong, Z. Lu, E. Lv, X. Dong, H. Li, Z. Yuan, X. Peng, S. Yang, J. Qiu, Z. Guo, Z. Wen, *Energy Environ. Sci.* **2024**, *17*, 6435.

[82] P. Zhang, T. Wang, X. Chang, J. Gong, *Acc. Chem. Res.* **2016**, *49*, 911.

[83] M. Kumar, B. Meena, P. Subramanyam, D. Suryakala, C. Subrahmanyam, *NPG Asia Mater.* **2022**, *14*, DOI 10.1038/s41427-022-00436-x.

[84] W. Qian, S. Xu, X. Zhang, C. Li, W. Yang, C. R. Bowen, Y. Yang, *Differences and Similarities of Photocatalysis and Electrocatalysis in Two-Dimensional Nanomaterials: Strategies, Traps, Applications and Challenges*, Springer Singapore, **2021**.

[85] G. Hodes, *J. Phys. Chem. Lett.* **2012**, *3*, 1208.

[86] X. Shi, L. Cai, M. Ma, X. Zheng, J. H. Park, *ChemSusChem* **2015**, *8*, 3192.

[87] T. Tran-Phu, R. Daiyan, J. Leverett, Z. Fusco, A. Tadich, I. Di Bernardo, A. Kiy, T. N. Truong, Q. Zhang, H. Chen, P. Kluth, R. Amal, A. Tricoli, *Chem. Eng. J.* **2022**, *429*, 132180.

[88] T. Tran-Phu, H. Chen, R. Bo, I. Di Bernardo, Z. Fusco, A. N. Simonov, A. Tricoli, *Energy Technol.* **2019**, *7*, 1801052.

[89] K. Zhang, M. Ma, P. Li, D. H. Wang, J. H. Park, *Adv. Energy Mater.* **2016**, *6*, 1600602.

[90] Q. Chen, G. Fan, H. Fu, Z. Li, Z. Zou, *Adv. Phys. X* **2018**, *3*, 863.

[91] Z. Li, W. Luo, M. Zhang, J. Feng, Z. Zou, *Energy Environ. Sci.* **2013**, *6*, 347.

[92] T. Bosserez, J. Rongé, J. van Humbeeck, S. Haussener, J. Martens, *Oil Gas Sci. Technol. – Rev. d'IFP Energies Nouv.* **2015**, *70*, 877.

[93] A. Berger, R. A. Segalman, J. Newman, *Energy Environ. Sci.* **2014**, *7*, 1468.

[94] D. Voiry, M. Chhowalla, Y. Gogotsi, N. A. Kotov, Y. Li, R. M. Penner, R. E. Schaak, P. S. Weiss, *ACS Nano* **2018**, *12*, 9635.

[95] F. F. Abdi, R. R. Gutierrez Perez, S. Haussener, *Sustain. Energy Fuels* **2020**, *4*, 2734.

[96] H. G. Cha, K. S. Choi, *Nat. Chem.* **2015**, *7*, 328.

[97] L. Luo, Z. Wang, X. Xiang, D. Yan, J. Ye, *ACS Catal.* **2020**, *10*, 4906.

[98] D. Liu, J.-C. Liu, W. Cai, J. Ma, H. Bin Yang, H. Xiao, J. Li, Y. Xiong, Y. Huang, B. Liu, *Nat. Commun.* **2019**, *10*, 1779.

[99] Y. Wang, W. Tian, C. Chen, W. Xu, L. Li, *Adv. Funct. Mater.* **2019**, *29*, 1809036.

[100] X. Yao, D. Wang, X. Zhao, S. Ma, P. S. Bassi, G. Yang, W. Chen, Z. Chen, T. Sritharan, *Energy Technol.* **2018**, *6*, 100.

[101] L. Wang, Y. Zhang, W. Li, L. Wang, *Mater. Reports Energy* **2023**, *3*, 100232.

[102] M. H. Sawal, A. A. Jalil, N. F. Khusnun, N. S. Hassan, M. B. Bahari, *Electrochim. Acta* **2023**, *467*, 143142.

[103] Z. Najaf, D. L. T. Nguyen, S. Y. Chae, O.-S. Joo, A. U. H. A. Shah, D.-V. N. Vo, V.-H. Nguyen, Q. Van Le, G. Rahman, *Int. J. Hydrogen Energy* **2021**, *46*, 23334.

[104] R. Abdullah, A. A. Jalil, M. Asmadi, N. S. Hassan, M. B. Bahari, M. Alhassan, N. M. Izzudin, M. H. Sawal, R. Saravanan, H. Karimi-Maleh, *Int. J. Hydrogen Energy* **2024**, DOI 10.1016/j.ijhydene.2024.05.461.

[105] C. W. Moon, M. J. Choi, J. K. Hyun, H. W. Jang, *Nanoscale Adv.* **2021**, *3*, 5981.

[106] L. M. Peter, K. G. Upul Wijayantha, *ChemPhysChem* **2014**, *15*, 1983.

[107] F. F. Abdi, S. P. Berglund, *J. Phys. D. Appl. Phys.* **2017**, *50*, 193002.

[108] D. K. Lee, D. Lee, M. A. Lumley, K.-S. Choi, *Chem. Soc. Rev.* **2019**, *48*, 2126.

[109] J. Ke, M. Adnan Younis, Y. Kong, H. Zhou, J. Liu, L. Lei, Y. Hou, *Nano-Micro Lett.* **2018**, *10*, 1.

[110] X. Wang, B. Liu, Y. Zhang, T. Butburee, K. (Ken) Ostrikov, S. Wang, W. Huang, *EcoEnergy* **2023**, *1*, 108.

[111] H. Chen, H. K. Mulmudi, A. Tricoli, *Chinese Chem. Lett.* **2020**, *31*, 601.

[112] W. Y. Teoh, R. Amal, L. Mädler, *Nanoscale* **2010**, *2*, 1324.

[113] T. Tran-Phu, R. Daiyan, X. M. C. Ta, R. Amal, A. Tricoli, *Adv. Funct. Mater.* **2022**, *32*, 1.

[114] D. Li, J. Shi, C. Li, *Small* **2018**, *14*, 1.

[115] G. Hodes, P. V. Kamat, *J. Phys. Chem. Lett.* **2015**, *6*, 4090.

[116] B. S. Kalanoor, H. Seo, S. S. Kalanur, *Mater. Sci. Energy Technol.* **2018**, *1*, 49.

[117] S. Li, W. Xu, L. Meng, W. Tian, L. Li, *Small Sci.* **2022**, *2*, DOI 10.1002/smsc.202100112.

[118] L. Shi, Y. Yin, L. C. Zhang, S. Wang, M. Sillanpää, H. Sun, *Appl. Catal. B Environ.* **2019**, *248*, 405.

[119] W. Lei, Y. Yu, H. Zhang, Q. Jia, S. Zhang, *Mater. Today* **2022**, *52*, 133.

[120] J. Yang, D. Wang, H. Han, C. Li, *Acc. Chem. Res.* **2013**, *46*, 1900.

[121] Z. Yu, Q. Huang, X. Jiang, X. Lv, X. Xiao, M. Wang, Y. Shen, G. Wittstock, *Anal. Chem.* **2021**, *93*, 12221.

[122] H. Shi, H. Guo, S. Wang, G. Zhang, Y. Hu, W. Jiang, G. Liu, *Energy and Fuels* **2022**, *36*, 11404.

[123] P. Luan, J. Zhang, *ChemElectroChem* **2019**, *6*, 3227.

[124] T. W. Kim, K. S. Choi, *Science (80-.).* **2014**, *343*, 990.

[125] D. K. Lee, K. S. Choi, *Nat. Energy* **2018**, *3*, 53.

[126] Y. Pihosh, I. Turkevych, K. Mawatari, J. Uemura, Y. Kazoe, S. Kosar, K. Makita, T. Sugaya, T. Matsui, D. Fujita, M. Tosa, M. Kondo, T. Kitamori, *Sci. Rep.* **2015**, *5*, 11141.

[127] S. S. Kalanur, J. Seetharamappa, Q. A. Sial, B. G. Pollet, *Nanomaterials* **2023**, *13*, 2599.

[128] M. Kim, B. Joshi, H. Yoon, T. Y. Ohm, K. Kim, S. S. Al-Deyab, S. S. Yoon, *J. Alloys Compd.* **2017**, *708*, 444.

[129] J. A. Seabold, N. R. Neale, *Chem. Mater.* **2015**, *27*, 1005.

[130] I. Khan, A. Qurashi, *Sci. Rep.* **2017**, *7*, 1.

[131] C. M. Jiang, G. Segev, L. H. Hess, G. Liu, G. Zaborski, F. M. Toma, J. K. Cooper, I. D. Sharp, *ACS Appl. Mater. Interfaces* **2018**, *10*, 10627.

[132] W. Guo, W. D. Chemelewski, O. Mabayoje, P. Xiao, Y. Zhang, C. B. Mullins, *J. Phys. Chem. C* **2015**, *119*, 27220.

[133] S. S. Kalanur, H. Seo, *Appl. Catal. B Environ.* **2019**, *249*, 235.

[134] P. F. Newhouse, D. A. Boyd, A. Shinde, D. Guevarra, L. Zhou, E. Soedarmadji, G. Li, J. B. Neaton, J. M. Gregoire, *J. Mater. Chem. A* **2016**, *4*, 7483.

[135] L. Zhou, Q. Yan, A. Shinde, D. Guevarra, P. F. Newhouse, N. Becerra-Stasiewicz, S. M. Chatman, J. A. Haber, J. B. Neaton, J. M. Gregoire, *Adv. Energy Mater.* **2015**, *5*, 1.

[136] I. Khan, Y. Gu, S. Wooh, *Chem. Rec.* **2024**, *24*, DOI 10.1002/tcr.202300127.

[137] C.-M. Jiang, M. Farmand, C. H. Wu, Y.-S. Liu, J. Guo, W. S. Drisdell, J. K. Cooper, I. D. Sharp, *Chem. Mater.* **2017**, *29*, 3334.

[138] M. K. Hossain, P. Sotelo, H. P. Sarker, M. T. Galante, A. Kormányos, C. Longo, R. T. Macaluso, M. N. Huda, C. Janáky, K. Rajeshwar, *ACS Appl. Energy Mater.* **2019**, *2*, 2837.

[139] D. Cardenas-Morcoso, A. Peiro-Franch, I. Herraiz-Cardona, S. Gimenez, *Catal. Today* **2017**, *290*, 65.

[140] M. A. Lumley, K. S. Choi, *Chem. Mater.* **2017**, *29*, 9472.

[141] B. Jansi Rani, G. Ravi, R. Yuvakkumar, M. Praveen Kumar, S. Ravichandran, D. Velauthapillai, M. Thambidurai, C. Dang, *Mater. Lett.* **2020**, *274*, 127996.

[142] S. Chang, M. Wang, C. C. Wang, X. Fu, H. Bi, Q. Zeng, *ChemSusChem* **2021**, *14*, 3010.

[143] D. Tang, A. J. E. Rettie, O. Mabayoje, B. R. Wygant, Y. Lai, Y. Liu, C. B. Mullins, *J. Mater. Chem. A* **2016**, *4*, 3034.

[144] H. Mandal, S. Shyamal, P. Hajra, A. Bera, D. Sariket, S. Kundu, C. Bhattacharya, *RSC Adv.* **2016**, *6*, 4992.

[145] M. Zhang, Y. Ma, D. Friedrich, R. van de Krol, L. H. Wong, F. F. Abdi, *J. Mater. Chem. A* **2018**, *6*, 548.

[146] W. Wang, Y. Zhang, L. Wang, Y. Bi, *J. Mater. Chem. A* **2017**, *5*, 2478.

[147] C. D. Morton, I. J. Slipper, M. J. K. Thomas, B. D. Alexander, *J. Photochem. Photobiol. A Chem.* **2010**, *216*, 209.

[148] S. K. Biswas, J. O. Baeg, *Int. J. Hydrogen Energy* **2013**, *38*, 14451.

[149] J. Feng, Z. Wang, X. Zhao, G. Yang, B. Zhang, Z. Chen, Y. Huang, *J. Phys. Chem. C* **2018**, *122*, 9773.

[150] S. Q.-A. Naqvi, J. R. Jennings, S. A. Raza, Y. W. Soon, Y. Liu, *ACS Appl. Energy Mater.* **2023**, *6*, 211.

[151] Q. Zeng, X. Fu, S. Chang, Q. Zhang, Z. Xiong, Y. Liu, G. Peng, M. Li, *J. Colloid Interface Sci.* **2021**, *604*, 562.

[152] S. Majumder, A. A. Yadav, L. A. M. Gomez, Y. M. Hunge, R. Srinivasan, K. H. Kim, *J. Alloys Compd.* **2024**, *1002*, 175391.

[153] T. H. Nguyen, M. G. Ahmed, M. Zhang, O. Halevi, F. F. Abdi, S. Magdassi, L. H. Wong, *ACS Appl. Energy Mater.* **2023**, *6*, 8297.

[154] I. Grigioni, A. Polo, C. Nomellini, L. Vigni, A. Poma, M. V. Dozzi, E. Selli, *ACS Appl. Energy Mater.* **2023**, *6*, 10020.

[155] C. R. Lhermitte, B. M. Bartlett, *Acc. Chem. Res.* **2016**, *49*, 1121.

[156] J. E. Yourey, K. J. Pyper, J. B. Kurtz, B. M. Bartlett, *J. Phys. Chem. C* **2013**, *117*, 8708.

[157] L. Chen, W. Li, W. Qiu, G. He, K. Wang, Y. Liu, Q. Wu, J. Li, *ACS Appl. Mater. Interfaces* **2022**, *14*, 47737.

[158] M. Zhou, Z. Liu, X. Li, Z. Liu, *Ind. Eng. Chem. Res.* **2018**, *57*, 6210.

[159] R. Wang, Z. Hao, H. Li, C. Xia, B. Dong, L. Cao, *Colloids Surfaces A Physicochem. Eng. Asp.* **2024**, *689*, 133647.

[160] H. Zhang, P. Yilmaz, J. O. Ansari, F. F. Khan, R. Binions, S. Krause, S. Dunn, *J. Mater. Chem. A* **2015**, *3*, 9638.

[161] J. C. Hill, K. S. Choi, *J. Mater. Chem. A* **2013**, *1*, 5006.

[162] S. Bera, S. Samajdar, S. Pal, P. S. Das, L. A. H. Jones, H. Finch, V. R. Dhanak, S. Ghosh, *Ceram. Int.* **2022**, *48*, 35814.

[163] G. Dong, H. Hu, L. Wang, Y. Zhang, Y. Bi, *J. Catal.* **2018**, *366*, 258.

[164] L. Zhou, A. Shinde, S. K. Suram, H. S. Stein, S. R. Bauers, A. Zakutayev, J. S. Duchene, G. Liu, E. A. Peterson, J. B. Neaton, J. M. Gregoire, *ACS Energy Lett.* **2018**, *3*, 2769.

[165] R. Strobel, S. E. Pratsinis, *J. Mater. Chem.* **2007**, *17*, 4743.

[166] I. Tantis, M. V. Dozzi, L. G. Bettini, G. L. Chiarello, V. Dracopoulos, E. Selli, P. Lianos, *Appl. Catal. B Environ.* **2016**, *182*, 369.

[167] C.-Y. Chiang, K. Aroh, N. Franson, V. R. Satsangi, S. Dass, S. Ehrman, *Int. J. Hydrogen Energy* **2011**, *36*, 15519.

[168] G. Liu, S. K. Karuturi, H. Chen, L. Spiccia, H. H. Tan, C. Jagadish, D. Wang, A. N. Simonov, A. Tricoli, *Nano Energy* **2018**, *53*, 745.

[169] G. Liu, S. K. Karuturi, H. Chen, D. Wang, J. W. Ager, A. N. Simonov, A. Tricoli, *Sol. Energy* **2020**, *202*, 198.

Chapter 4. Optimal coatings of Co_3O_4 anodes for acidic water electrooxidation

Proton-exchange membrane water electrolysis (PEMWE) is an emerging technology for large-scale green hydrogen (H_2) production. Stable low-cost electrocatalysts to catalyze acidic water electrooxidation play an important role in the efficient operation of PEMWE, which is detailed review in Chapter 2. One of the stabilization strategies promoted in this review is applying a passivation layer to enhance the stability of non-noble-based electrocatalysts, in which Co_3O_4 is the most extensive material studied. The following research in this chapter reveals the protective effects of the passivation layers based on different materials and thicknesses. Thus, it aims to provide the general guidelines for engineering protective coatings of non-noble-based anode catalysts for the acidic water electrolysis.

This chapter was reprinted from the publication below. X. M. C. Ta, T. Trần-Phú, J. A. Yuwono, T. K. A. Nguyen, A. D. Bui, T. N. Truong, L. Chang, E. Magnano, R. Daiyan, A. N. Simonov, A. Tricoli, Optimal Coatings of Co_3O_4 Anodes for Acidic Water Electrooxidation. Small 2024, 20, 2304650. https://doi.org/10.1002/smll.202304650. Reproduced with permission. Copyright 2024, Wiley-VCH.

Authorship Attribution Statement

Xuan Minh Chau Ta is the principal author of this publication, which forms part of her thesis submitted for the examination for the Doctor of Philosophy degree. The corresponding author below provide the consent for inclusion of a part or whole of the following publication in this thesis and accept the following candidate statement of contribution for this publication.

Candidate contribution:

This manuscript studied about the dielectric nanoscale-thin oxide layer to enhance the stability and catalytic activity of low-cost Co_3O_4 OER electrocatalyst. The manuscript was written, formatted, reviewed, and edited by Xuan Minh Chau Ta. This author was a main contributor, who was in charge designed and performed in the experiments and data analysis. The author also involved in the theoretical calculations part.

Corresponding author

Prof Dr Antonio Tricoli

Abstract

Implementation of proton-exchange membrane water electrolyzers for large-scale sustainable hydrogen production requires the replacement of scarce noble-metal anode electrocatalysts with low-cost alternatives. However, such earth-abundant materials often exhibit inadequate stability and/or catalytic activity at low pH, especially at high rates of the anodic oxygen evolution reaction (OER). Here, the authors explore the influence of a dielectric nanoscale-thin oxide layer, namely Al_2O_3, SiO_2, TiO_2, SnO_2, and HfO_2, prepared by atomic layer deposition, on the stability and catalytic activity of low-cost and active but insufficiently stable Co_3O_4 anodes. It is demonstrated that the ALD layers improve both the stability and activity of Co_3O_4 following the order of HfO_2 > SnO_2 > TiO_2 > Al_2O_3, SiO_2. An optimal HfO_2 layer thickness of 12 nm enhances the Co_3O_4 anode durability by more than threefold, achieving over 42 h of continuous electrolysis at 10 mA cm^{-2} in 1 M H_2SO_4 electrolyte. Density functional theory is used to investigate the superior performance of HfO_2, revealing a major role of the $HfO_2|Co_3O_4$ interlayer forces in the stabilization mechanism. These insights offer a potential strategy to engineer earth-abundant materials for low-pH OER catalysts with improved performance from earth-abundant materials for efficient hydrogen production.

Keywords: acidic water splitting, atomic layer deposition, Co_3O_4 anode, protection coating, HfO_2.

4.1. Introduction

Water electrolysis powered by renewable electricity to produce green hydrogen offers a promising route for achieving a carbon-neutral economy.[1–4] To date, there are four most developed water electrolysis technologies, namely alkaline water electrolysis (AWE), anion-exchange membrane water electrolysis (AEMWE), solid oxide electrolysis (SOE), and proton-exchange membrane water electrolysis (PEMWE), each coming with specific benefits and limitations.[5] While AWE and AEMWE can utilize low-cost electrocatalysts to promote water splitting at low to moderate temperatures under alkaline conditions, their overall efficiencies are limited by the low operating current densities.[6,7] SOE is a highly efficient method with low energy consumption and high purity hydrogen production, although operating at high temperatures (up to 1200 °C) and therefore requiring specialized materials and facilities.[5] Alternatively, PEMWE presents benefits of operation under mild temperature conditions using compact design cells with very high output current densities up to 10 A cm^{-2} and high energy efficiencies.[8–11]

Nonetheless, a key limitation of the PEMWE technology is the reliance on anode catalysts based on iridium, which prevents its large-scale implementation due to the scarcity of this noble metal.[12] To address this challenge, noble-metal-free electrocatalysts for the oxygen evolution reaction (OER) need to be developed. However, achieving both high stability and activity for the OER at low pH is problematic even for the most robust iridium-oxide-based catalysts.[13–19] Instability is even more of an issue for non-noble-metal-based catalysts.[20–24] For example, cobalt oxide (Co_3O_4) is relatively active towards the acidic OER, but its application is hindered by its low stability at low pH.[25,26]

One promising approach to improve the longevity of low-pH OER catalysts is to couple active elements with more thermodynamically stable or self-healing oxide matrixes, including PbO_2, TiO_2, BiO_x, SbO_x, and, to some extent, MnO_x.[22,23,27–31] Arguably, this catalyst design strategy has provided some of the best results in terms of balancing stability and activity. Recognizing that corrosion of non-noble metals during the operation of an OER catalyst is often unavoidable, the stability of some materials can be significantly improved through the intentional introduction of the metal precursors into the electrolyzed solutions, enabling operation at very high current densities and temperatures up to 80 °C.[31–35] However, operation of such systems in a practical electrolyzer device is yet to be demonstrated. Potential practical challenges include the poisoning of the proton-exchange membrane and the cathodes.

Another strategy to protect OER anodes against corrosion, while maintaining high catalytic activity, is to coat the electrocatalyst layer with a more stable passivation layer. Maintaining a nm- thickness of this layer allows for sufficiently high mass- and charge-transfer rates to sustain the electrocatalytic reactions, while significantly suppressing the dissolution of the catalyst.[36–39] Among thin-film deposition methods, atomic layer deposition (ALD) enables the formation of high-quality conformal layers with accurately controlled thickness.[36–39] A reasonably broad range of materials has been examined as protection layers for the OER catalysts with promising results demonstrated.[40–45] However, studies under acidic conditions are limited to TiO_2,[39–42] SiO_2,[46] or Al_2O_3[43] coatings on Co_3O_4, IrO_x, RuO_2, or WO_3 electrocatalysts, respectively. Besides, few studies have compared the chemical stability and corrosion resistance of some ultrathin oxide layers (Al_2O_3, TiO_2, ZnO, HfO_2, and ZrO_2) as protection layer in different electrolyte conditions, but they have not been comprehensively investigated in acidic anodic conditions.[44,45,47]

The present study aims to improve our understanding of the required properties for the passivation layer to improve the stability and electrochemical activity of earth-abundant OER catalysts for acidic electrolysis. To this end, we investigated the electrocatalytic activity of Co_3O_4 anodes modified with nanometer-thin conformal protective TiO_2, Al_2O_3, SnO_2, SiO_2, and HfO_2 layers, fabricated by ALD, for water electrooxidation in an H_2SO_4 electrolyte at pH 0. Through a combination of electrochemical, microscopic, spectroscopic, and theoretical studies, we reveal insights into the interrelation between the chemical nature and thickness of the coatings, electrocatalytic activity, and stability of the modified anodes.

4.2. Results and Discussion

4.2.1. Physical characterization

The water-oxidizing anodes examined herein were prepared by deposition of cobalt layers on fluorine-doped tin oxide (FTO) glass substrates by sputtering followed by the annealing process. This resulted in the formation of a dense uniform layer of Co_3O_4 particles, confirmed by scanning electron microscopy (SEM), X-ray diffraction (XRD), and Raman spectroscopy (**Figure 4.1a** and **Figure 4.2**). The uniformity of the Co_3O_4 layer, having a thickness of ≈360 nm, was confirmed by cross-sectional SEM images (**Figure 4.1b**) and energy-dispersive X-ray spectroscopic mapping (EDS) (**Figure 4.1c–f**).

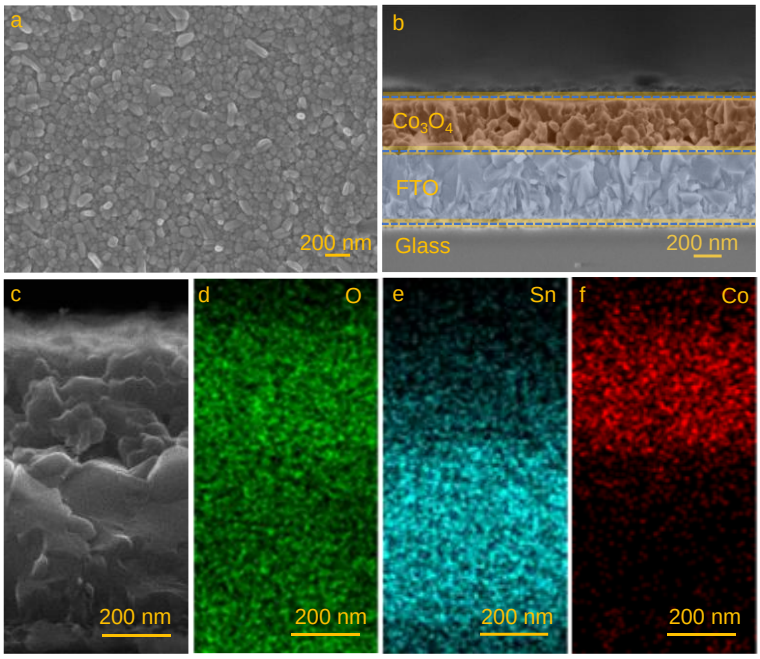

Figure 4.1 Microscopic characterization of a Co_3O_4/FTO electrode. a) Top and b) cross-sectional SEM images. Micrograph in panel (b) was colored post-analysis to assist the visualization of Co_3O_4 (orange), FTO (blue), and glass (grey); dashed lines highlight the boundaries between different layers. c) Higher magnification SEM and d−f) corresponding EDS elemental mapping of d) oxygen (green), e) tin (turquoise), and f) cobalt (red) for the Co_3O_4/FTO electrode.

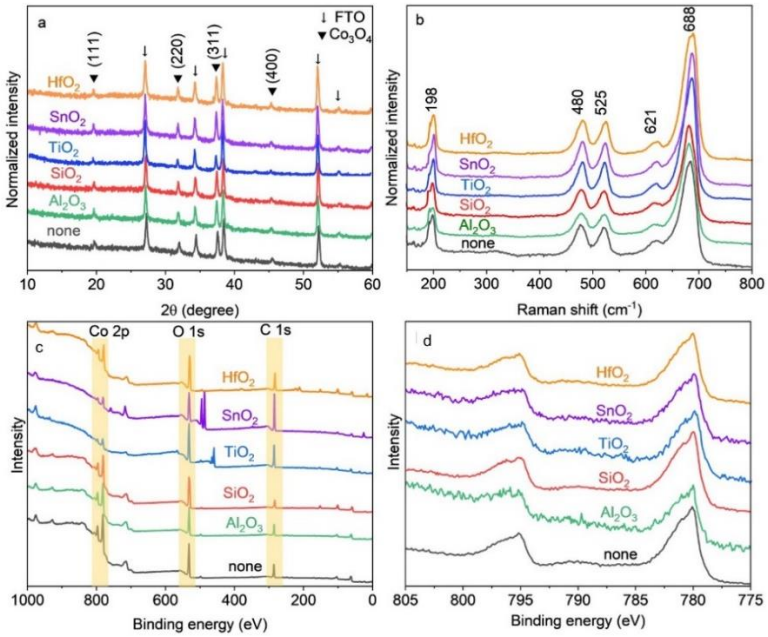

Figure 4.2 Structural characterization of (black) bare Co_3O_4 and Co_3O_4 electrocatalyst coated with, (green) Al_2O_3, (red) SiO_2, (blue) TiO_2, (purple) SnO_2, and (orange) HfO_2. a) XRD and b) Raman spectra.

Such planar Co_3O_4 anodes were coated by a thin Al_2O_3, SiO_2, TiO_2, SnO_2 and HfO_2 passivation layer by ALD, which were indiscernible in the SEM images and undetectable by XRD and Raman (**Figure 4.2**, **Figure 4.3** & **Figure 4.4**). However, the corresponding EDS data confirms the presence and uniform distribution of the coating elements over the Co_3O_4 films (**Figure 4.4**). For the initial screening studies, the thickness of the ALD layer was kept similar within 3−4 nm, as measured by ellipsometry (**Table 4.1**).

Table 4.1 Summary of the key properties of the investigated Co_3O_4/FTO electrodes.

Overlayer	ECSA [cm^2 $cm_{geom.}^{-2}$]	Overlayer thickness [nm]	$E_{10\ mA\ cm^{-2}}$ [V versus RHE]	Stability at 10 mA cm^{-2} [h][a)]
none	3.43	0	1.96	12
Al_2O_3	3.30	3.1	2.06	20
SiO_2	3.08	3.9	2.06	23
TiO_2	3.30	3.1	2.02	27
SnO_2	3.26	3.9	2.01	28
HfO_2	3.43	3.0	1.93	32

$E_{10\ mA\ cm^{-2}}$ – initial quasi-stabilized potential required to sustain the OER rate of 10 mA cm^{-2} derived from 30 min chronopotenitometric measurements; [a)] Stability at 10 mA cm^{-2} – point of time when potential starts to abruptly increase during extended OER tests at 10 mA cm^{-2}.

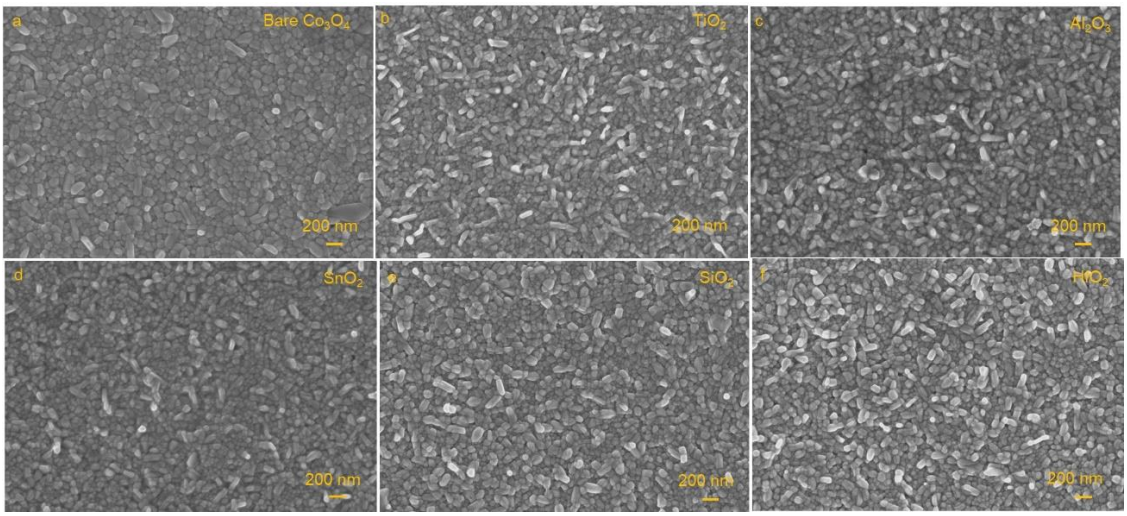

Figure 4.3 Top-view SEM images of a) bare Co_3O_4 and Co_3O_4 anodes coated b) Al_2O_3, c) SiO_2, d) TiO_2, e) SnO_2, and f) HfO_2.

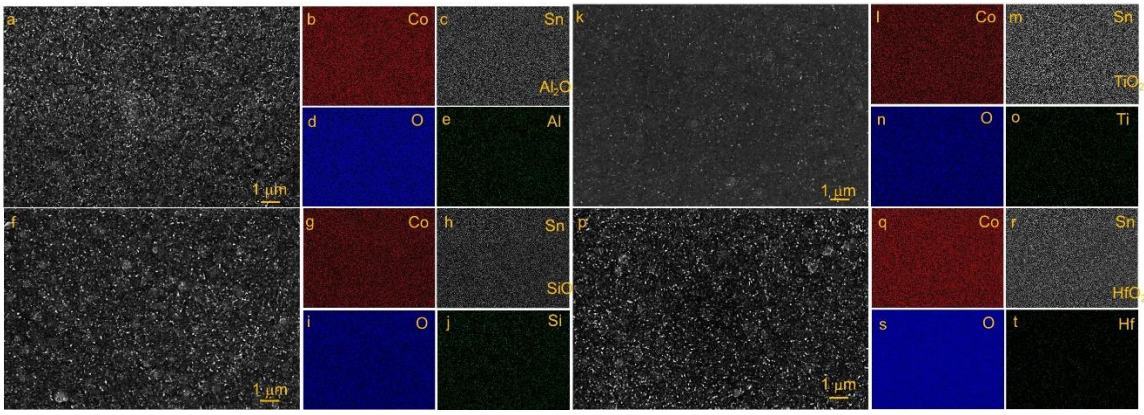

Figure 4.4 SEM-EDS elemental mapping of Co_3O_4/FTO coated with a−e) Al_2O_3, f−j) SiO_2, k−o) TiO_2, and q−t) HfO_2 layer.

To probe the chemical state of the elements in the produced electrodes, X-ray photoelectron spectroscopic (XPS) analysis was undertaken (**Figure 4.2** and **Figure 4.5**). The Co 2p spectrum of the unmodified Co_3O_4/FTO electrode is consistent with the published data for the cobalt(II, III) oxide (**Figure 4.5a**).[39,48–50] After deposition of the coating layer, the features of the Co 2p spectra remained unaltered although the intensity of the peaks was slightly reduced (**Figure 4.2**). Secondary elements forming the nanometer-thick overlayers were clearly detectable by XPS, with the peak positions corresponding to Al_2O_3 (74.4 eV; **Figure 4.5b**),[51,52] SiO_2 (Si^{4+} 103.5 and Si^{3+} 101.8 eV; **Figure 4.5c**),[53] TiO_2 (Ti^{4+} $2p_{3/2}$ 459.0 and Ti^{4+} $2p_{1/2}$ 465.0 eV; **Figure 4.5d**),[39,51,54,55] SnO_2 (Sn^{4+} $3d_{5/2}$ 486.8 and Sn^{4+} $3d_{3/2}$ 495.2 eV; **Figure 4.5e**),[51] and HfO_2 (Hf^{4+} $4f_{7/2}$ 17.5 and Hf^{4+} $4f_{5/2}$ 19.2 eV; **Figure 4.5f**).[51,56] Together, these physical characterization results indicate the successful deposition of nanoscale oxide coatings on the Co_3O_4/FTO surface and no detectable changes to the properties of the underlying Co_3O_4 layers induced by the ALD.

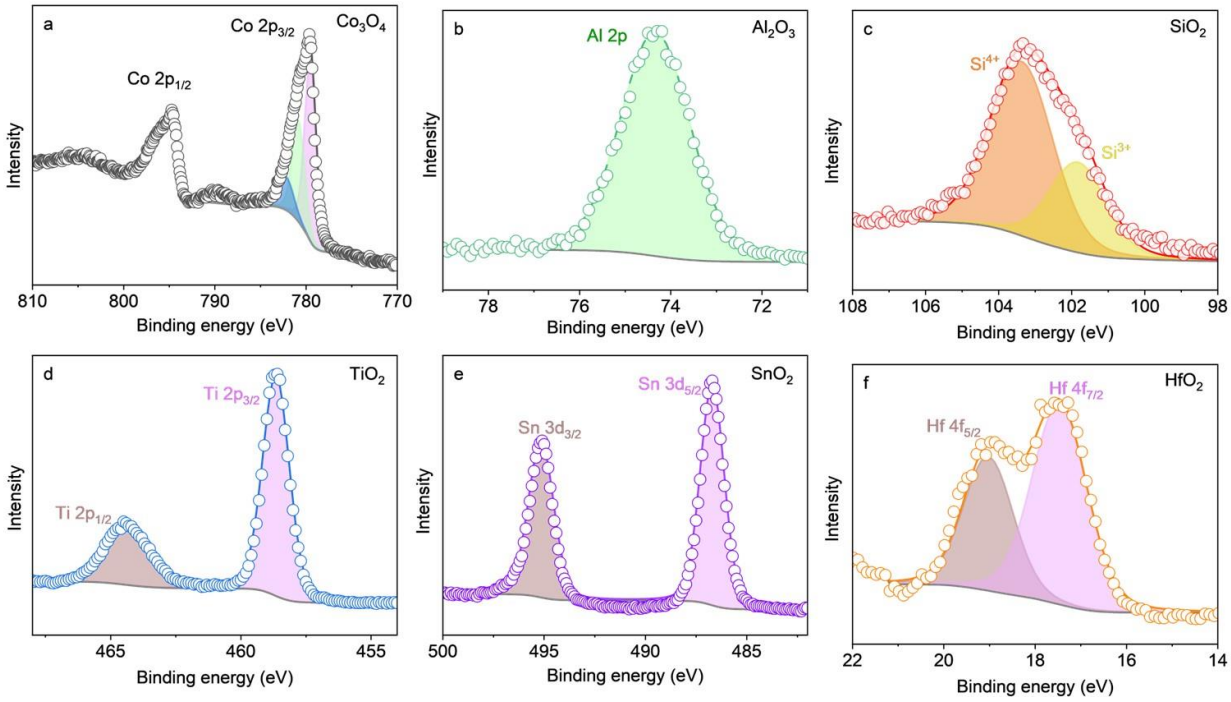

Figure 4.5 High-resolution XP spectra of a) Co 2p, b) Al 2p, c) Si 2p, d) Ti 2p, e) Sn 3d, and f) Hf 4f (colored dots) and corresponding fitting (solid lines – cumulative curve; filled areas – individual peak components; grey line – background) for a) unmodified Co_3O_4/FTO, and Co_3O_4/FTO electrodes coated 3−4 nm thick overlayers of b) Al_2O_3, c) SiO_2, d) TiO_2, e) SnO_2, and f) HfO_2.

The electrochemically active surface area (ECSA) of the catalytic surface was derived from the capacitance values measured by cyclic voltammetry in the potential range devoid of significant faradaic processes (**Figure 4.6**).[57,58] Deposition of the overlayers onto sputtered Co_3O_4/FTO electrodes did not change the ESCA values significantly, which resulted in relatively similar double layer capacitance values (**Figure 4.6h**), estimated from the slopes of the capacitive currents as a function of scan rates between bare and coated Co_3O_4 surfaces.[59–61] To estimate the ECSA values, a specific capacitance of a smooth surface such as a polished glassy carbon under identical pH and applied potential conditions might be used as an approximate reference;[61,62] however, one should recognize obvious differences in the chemical nature and double-layer structure between the metal oxides and carbon electrodes. In our study, a specific capacitance of 0.042 mF cm^{-2} at 0.81 V versus a reversible hydrogen electrode (RHE) was measured in 1 M H_2SO_4 for a polished glassy carbon surface. The approximate ECSA values of pristine and ALD-coated Co_3O_4 anodes were then obtained (**Table 4.1**).

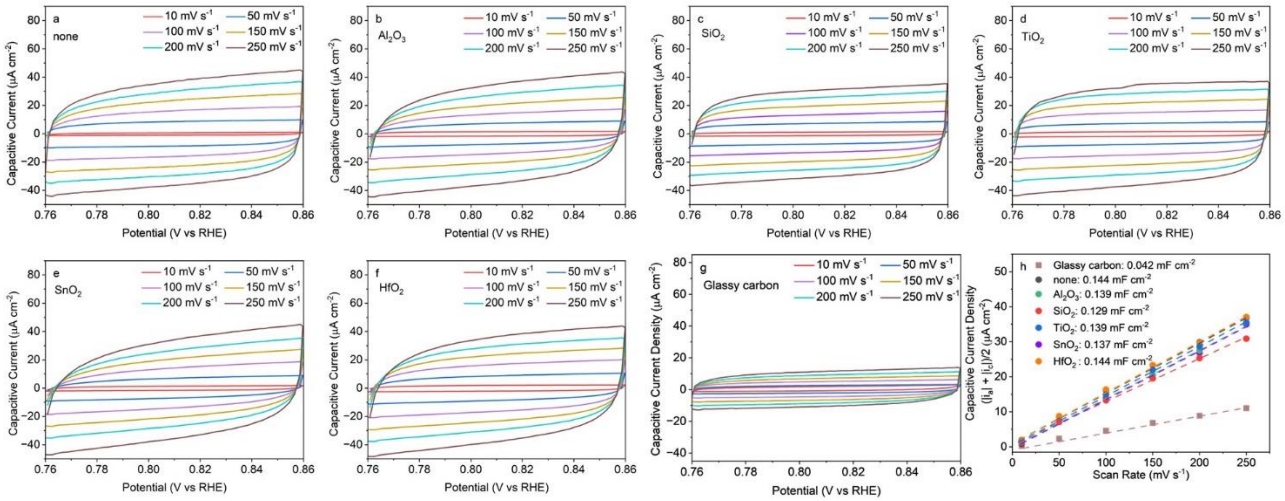

Figure 4.6 Capacitive current density versus applied potential at different scan rate plots for a) bare Co_3O_4 sample and samples coated with b) Al_2O_3, c) SiO_2, d) TiO_2, e) SnO_2, f) HfO_2, g) glassy carbon (Measurements were taken in H_2SO_4 electrolyte pH 0 within potential window of 0.76 and 0.86 V), and h) the capacitive current density as function of scan rates at 0.81 V versus RHE for electrochemical active surface area measurements.

4.2.2. Electrocatalytic performance

The OER electrocatalytic activity of the bare and coated Co_3O_4 anodes was studied in 1 M H_2SO_4 electrolyte with pH 0 at ambient temperature. First, the Co_3O_4 films were investigated using electrochemical impedance spectroscopy (EIS) at 0.3 V and 1.8 V versus RHE (**Figure 4.7**). The series resistance (R_s) and charge transfer resistance of the Co_3O_4/FTO with and without the protective oxide layers (R_{ct}) were determined by fitting a simplified circuit model (inset circuit in **Figure 4.7**), with the fitted values presented in **Table 4.2**. The results show that the electrical conductivity decreases upon deposition introduction of the dielectric coating, following the order of bare Co_3O_4 > HfO_2/Co_3O_4 > SnO_2/Co_3O_4 > TiO_2/Co_3O_4 > Al_2O_3/Co_3O_4 > SiO_2/Co_3O_4, indicating a reduction in the charge transfer kinetics of coated electrodes compared to the bare anodes, despite their small thickness of 3 to 4 nm (**Figure 4.7** and **Table 4.2**).[63–65]

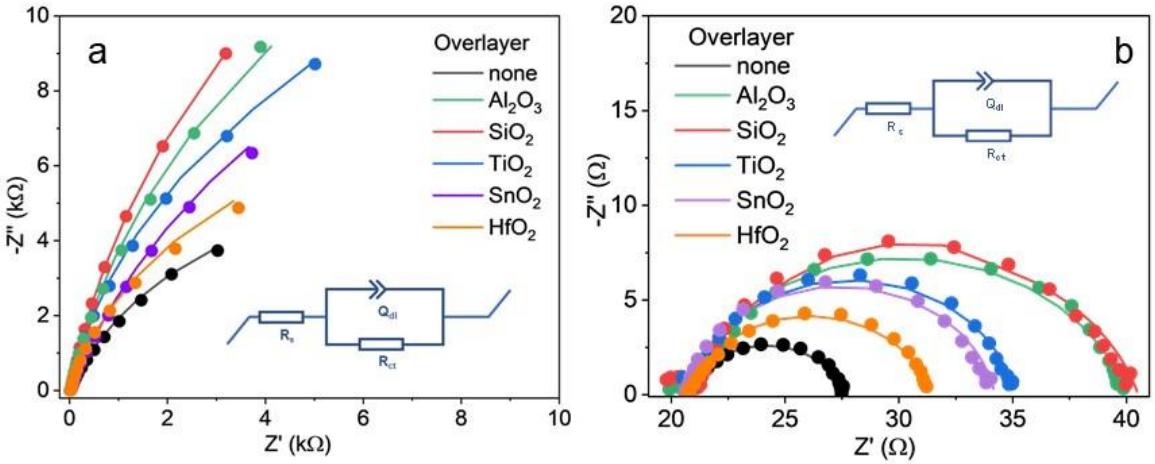

Figure 4.7 Nyquist plots of the electrochemical impedance spectroscopy (EIS) data collected at a) 0.3 V, b) 1.8 V *versus* RHE of Co_3O_4/FTO without and with 3 – 4 nm Al_2O_3, SiO_2, TiO_2, SnO_2, and HfO_2 coated layer (inset image: graph illustrating the Randle circuit used for EIS fitting): colored dots: raw EIS data; solid colored line: simulation curves after fitting with Randle circuit.

Table 4.2 Summary of electrochemical impedance spectroscopy fitting for bare Co_3O_4 and Co_3O_4 electrocatalysts coated with Al_2O_3, SiO_2, TiO_2, SnO_2, and HfO_2.

Overlayer	**R_s [Ω]**	**R_{ct} [Ω]**	**Q_{dl} [F cm^{-2} s$^{\alpha-1}$]**	**α_{dl}**
0.3 V *versus* RHE				
none	19.32	13445	0.252×10^{-3}	0.799
Al_2O_3	21.78	38118	0.139×10^{-3}	0.901
SiO_2	21.17	50185	0.075×10^{-3}	0.872
TiO_2	19.9	33466	0.130×10^{-3}	0.892
SnO_2	20.04	28155	0.167×10^{-3}	0.799
HfO_2	21.54	15251	0.115×10^{-3}	0.866
1.8 V *versus* RHE				
none	20.68	6.974	0.668×10^{-3}	0.816
Al_2O_3	20.42	19.62	1×10^{-3}	0.807
SiO_2	20.61	19.91	0.674×10^{-3}	0.821
TiO_2	20.69	14.39	2.97×10^{-3}	0.89
SnO_2	20.71	13.61	2.74×10^{-3}	0.89
HfO_2	20.76	10.67	0.699×10^{-3}	0.842

The water oxidation performance in 1 M H_2SO_4 of the Co_3O_4/FTO anodes with and without protective layers was further compared using voltammetric and chronopotentiometric data (**Figure 4.8a–c**). Linear sweep voltammetry (LSV) curves of unmodified samples showed an oxidation peak at ≈1.65 V versus RHE, which was attributed to the oxidation of the lattice Co species in

Co_3O_4 to a higher oxidation state during the anodic polarization. This oxidation peak could be observed more clearly when the scan rate was increased to 20 and 50 mV s^{-1}. (**Figure 4.9**).[39,66,67] Amongst the coating layers, only HfO_2 produced a slight increase in the electrocatalytic activity at potentials more positive than ≈1.8 V versus RHE as compared to unmodified Co_3O_4/FTO (**Figure 4.8d** and **Table 4.1**). All other oxide coatings (Al_2O_3, TiO_2, SnO_2, SiO_2) decreased electrocatalytic current but did not completely suppress it, indicating that the charge/mass transport through these very thin layers is sufficient to sustain the OER. These trends were confirmed by chronopotentiometric measurements at 10 mA cm^{-2}, showing that the HfO_2/Co_3O_4/FTO requires a potential of ≈1.93 V to sustain this OER rate, which is ≈0.03 V better than the bare Co_3O_4/FTO. All other coatings required a 0.05–0.1 V more positive potentials required to achieve 10 mA cm^{-2} (**Figure 4.8d** and **Table 4.1**). Additionally, the apparent Tafel slopes of these anodes were analyzed. **Figure 4.9** shows the slopes of the semilogarythmic dependencies of potential on current density are similar, suggesting similar reaction kinetics with and without coating layers.

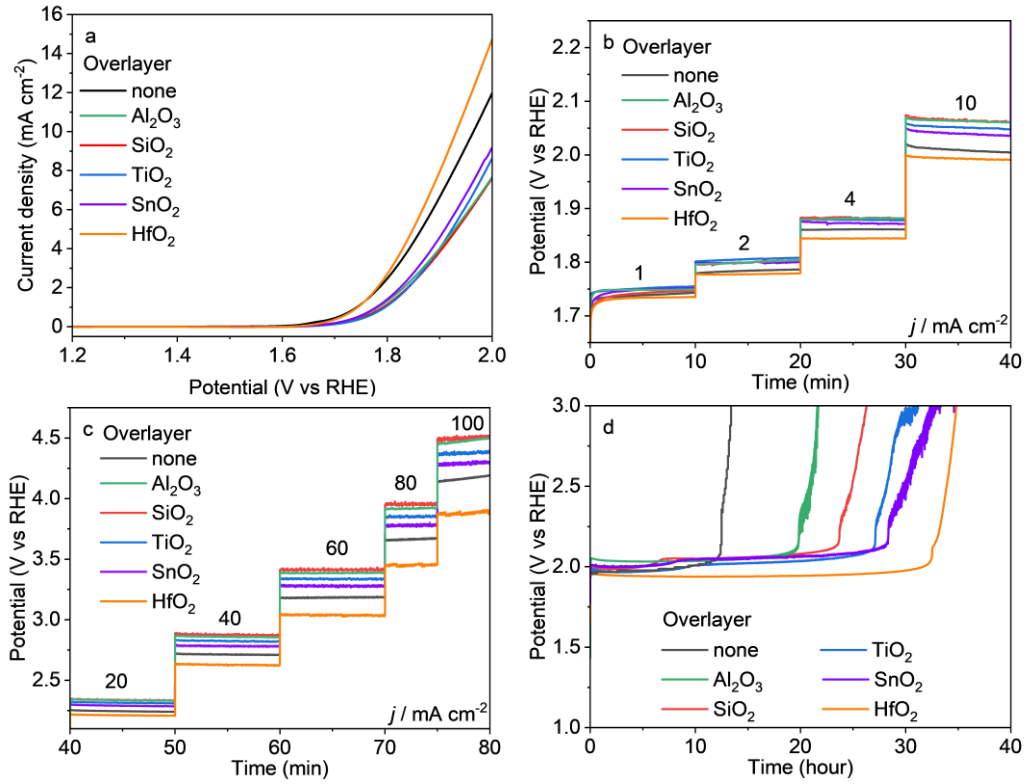

Figure 4.8 Electrochemical characterization of the Co_3O_4/FTO electrodes without (black) and with a 3−4 nm thick overlayer of Al_2O_3 (green), SiO_2 (green), TiO_2 (blue), SnO_2 (purple), and HfO_2 (orange). a) Quasi-stabilized linear sweep voltammetry curves (third scan, scan rate 0.005 V s^{-1}), b,c) chronopotentiograms at varied current densities b) 1 to 10 mA cm^{-2} and c) 20 to 100 mA cm^{-2},

and d) chronopotentiometric curves recorded at 10 mA cm^{-2} in 1 M H_2SO_4. Currents are normalized to the geometric surface area.

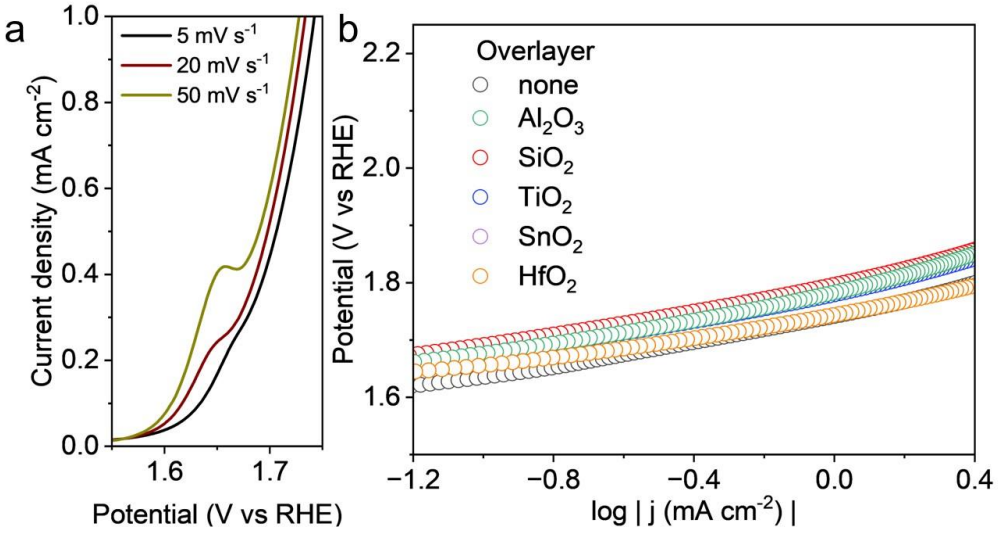

Figure 4.9 a) LSV curves of Co_3O_4/FTO electrodes obtained at different scan rates with potential window 1.55–1.75 V *versus* RHE and b) Steady-state Tafel plots for Co_3O_4/FTO electrodes without (black) and with a 3−4 nm thick overlayer of Al_2O_3 (green), SiO_2 (red), TiO_2 (blue), SnO_2 (purple), and HfO_2 (orange) in 1 M H_2SO_4 electrolyte (pH 0).

Importantly, a significant enhancement in the electrode stability was observed for all nanoscale coatings. The bare Co_3O_4 maintained a stable potential of ≈1.96 V versus RHE for a current of 10 mA cm^{-2} for less than 12 h before displaying a sharp increase in the potential, which indicates the loss of the catalytically active Co_3O_4 layer. The latter was confirmed by the inductively coupled plasma mass spectroscopy (ICP-MS) analysis (**Figure 4.10)**. The Al_2O_3 and SiO_2 layers prolonged the durability of the electrodes under the examined conditions to 20 and 23 h, respectively, while the TiO_2 and SnO_2 layers improved the stability to ≈27−28 h. Notably, the HfO_2 layer not only improved the electrocatalytic activity of the Co_3O_4 electrode but also enhanced its stability to 32 h, the best protective layer amongst the oxides examined herein.

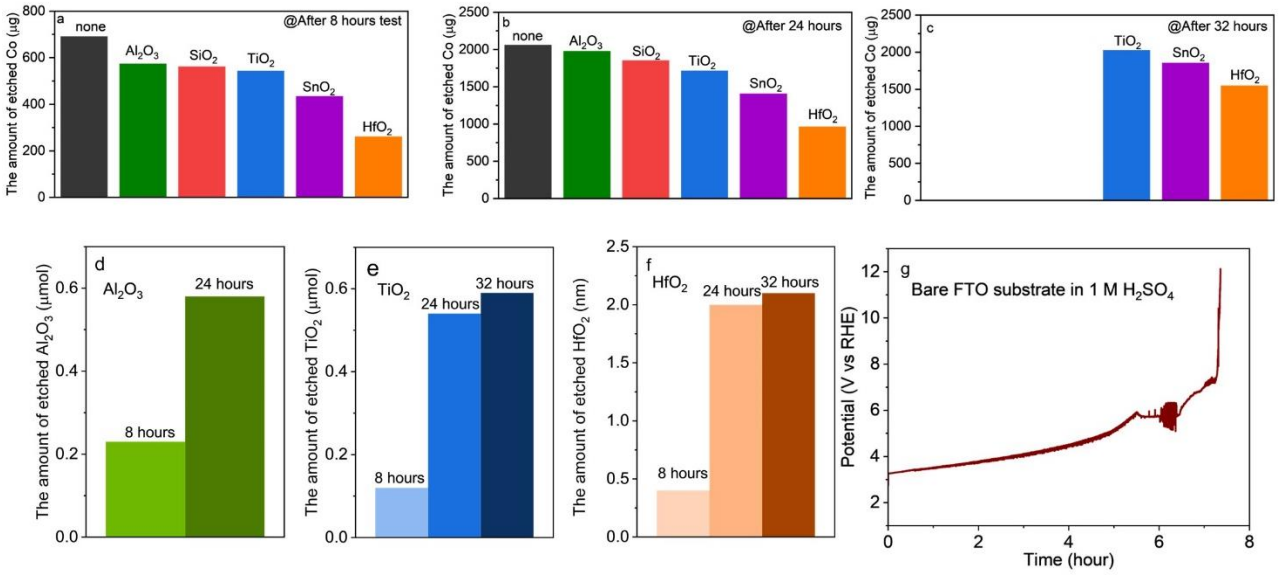

Figure 4.10 a–c) Metallic Co concentration and d – e) the amount of dissolved Al_2O_3, TiO_2, HfO_2 detected from the inductively coupled plasma mass spectrometry (ICP–MS) measurements of the electrolytes after 8, 24, 32 h of galvanostatic operation, g) Chronopotentiometric curves of bare FTO substrate recorded at 10 mA cm^{-2} in 1 M H_2SO_4.

To map the anode morphological changes during the OER, we carried out SEM analysis of the samples tested at 10 mA cm^{-2} for 8 and 24 h (**Figure 4.11** & **Figure 4.12**). Top-view images reveal pitting of the anode surface, with the size and density depending on the composition of the coating and the duration of the tests. For the unmodified Co_3O_4, large holes of hundreds of nm in size were already observed after 8 h and essentially no catalyst was detectable after 24 h (**Figure 4.11a**). This was corroborated by the side-view imaging and SEM-EDS elemental mapping, showing a significant reduction in the Co_3O_4 layer thickness from 360 to 200 nm after 8 h and its almost complete disappearance after 24 h (**Figure 4.12a**). These results are consistent with SEM-EDS mapping presented in (**Figure S 4.1)**, which revealed the disappearance of the Co element in unmodified samples after 24 h.

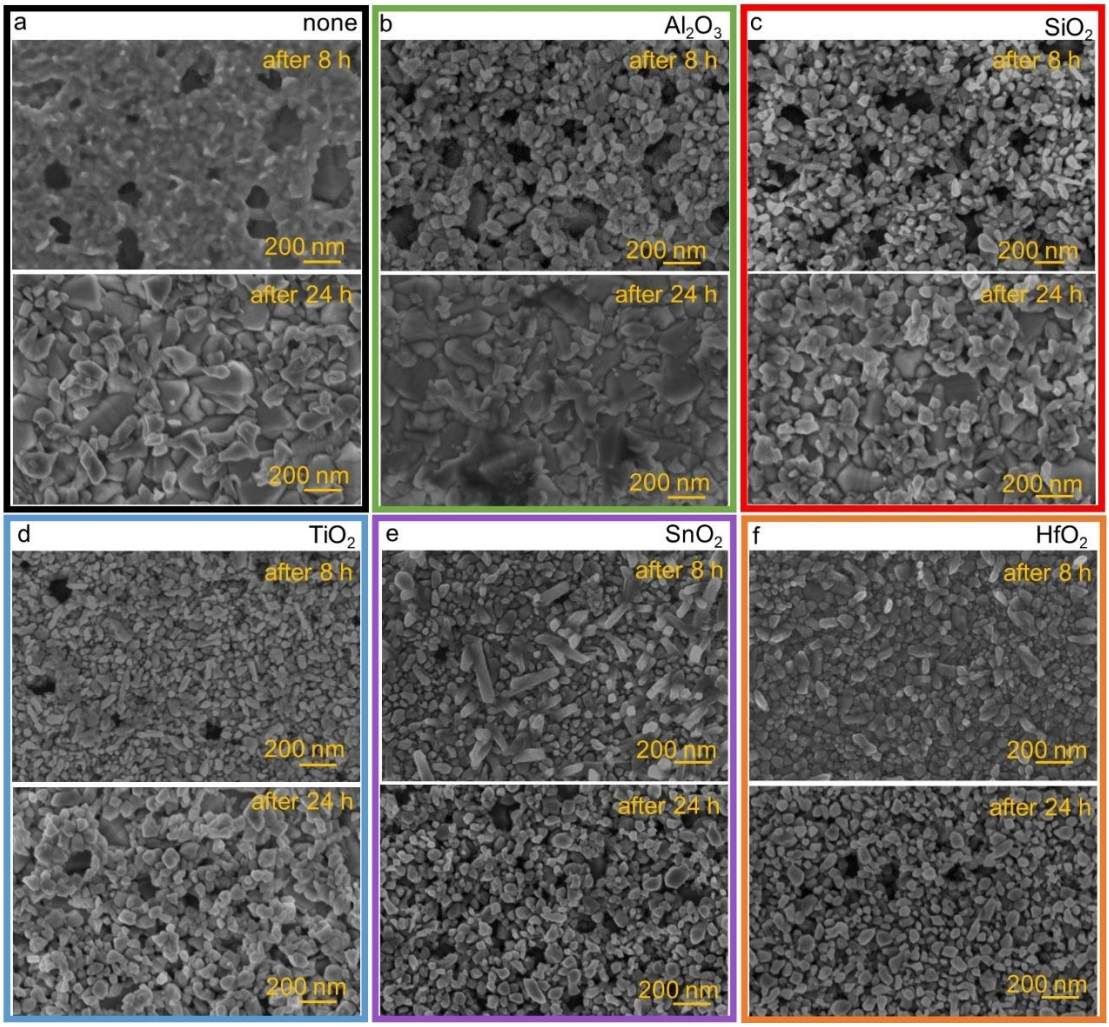

Figure 4.11 Top-view SEM images of a) unmodified Co_3O_4/FTO and Co_3O_4/FTO electrodes coated with 3−4 nm thick coating layers of b) Al_2O_3, c) SiO_2, d) TiO_2, e) SnO_2, and f) HfO_2 after 8 and 24 h of galvanostatic OER tests in H_2SO_4 electrolyte pH 0 at 10 mA cm^{-2}.

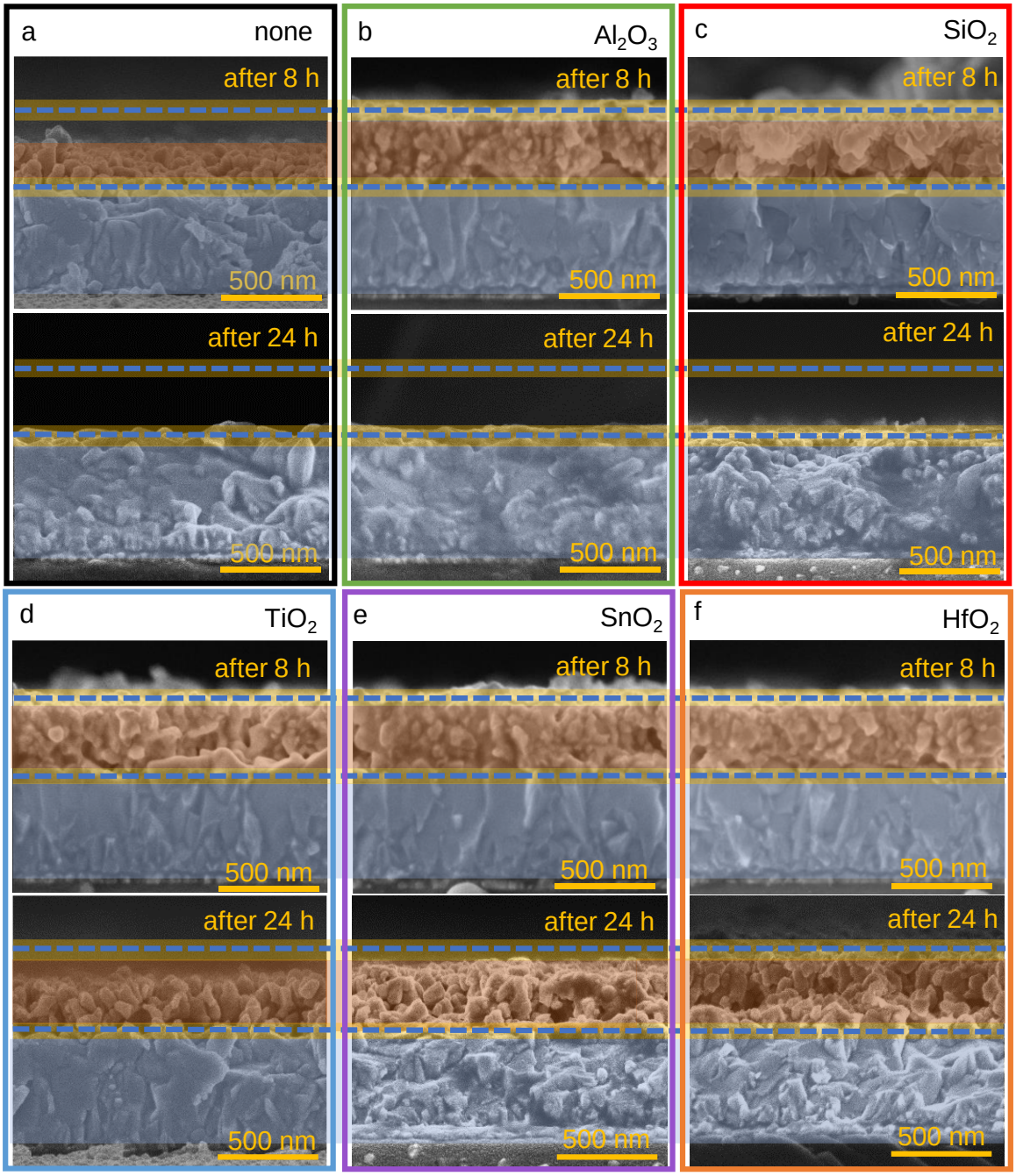

Figure 4.12 Cross-sectional SEM images of a) unmodified Co_3O_4/FTO and Co_3O_4/FTO anodes coated with 3−4 nm thick overlayers of b) Al_2O_3, c) SiO_2, d) TiO_2, e) SnO_2, and f) HfO_2 after 8 (top) and 24 h (bottom) of galvanostatic OER tests in a H_2SO_4 electrolyte with a pH 0 at 10 mA cm^{-2}. (orange: Co_3O_4 electrocatalyst, blue: FTO, and the blue dashed line: the boundary of pristine Co_3O_4 layer)

When coated with nanosized passivation layers, holes of varying sizes appeared on the surface for all electrodes after 8 h except those coated with HfO_2 (**Figure 4.11f**). The Al_2O_3/Co_3O_4 and SiO_2/Co_3O_4 anodes showed a similar morphology with hole diameters ranging from 200 to 400 nm

after 8 h (**Figure 4.11b, c**), while fewer and smaller holes were observed on the TiO_2/Co_3O_4 (**Figure 4.11d**) and SnO_2/Co_3O_4 anodes (**Figure 4.11e**). At the same time, the density of these pitting sites was low for the coated anodes, and no significant changes in the thickness of the underlying Co_3O_4 anode were detected after 8 h for all overlayers examined (**Figure 4.12b−f**). Increasing the electrolysis time to 24 h, resulted in a complete loss of the Co_3O_4 layer for the anodes coated with Al_2O_3 and SiO_2 (**Figure 4.11b, c** & **Figure 4.12b, c**). These observations are consistent with the results of the galvanostatic tests showing a sharp increase in the applied potential before 24 h (**Figure 4.8d**) and SEM-EDS mapping (**Figure S 4.2** & **Figure S 4.3**). The TiO_2, SnO_2, and HfO_2 coatings were able to preserve the Co_3O_4 anode for up to 24 h (**Figure 4.11d−f**) with the residual Co_3O_4 thickness following the order of HfO_2/Co_3O_4 > SnO_2/Co_3O_4 > TiO_2/Co_3O_4 (**Figure 4.12d−f**), consistently with the galvanostatic measurements (**Figure 4.8d** & **Table 4.1**) and SEM-EDS mapping (**Figure S 4.4**, **Figure S 4.5**, & **Figure S 4.6**).

As the most stable electrode, changes in the morphology of the HfO_2/Co_3O_4 anode were further investigated by TEM and EDS before and after 24 h tests. TEM images of the as-deposited sample (**Figure 4.13A**) revealed agglomerates of thick, crystalline Co_3O_4, covered with an amorphous HfO_2 layer, which was further evidenced by EDS elemental mapping. After 24 h of electrolysis, although we still observe the (220) lattice planes of crystalline Co_3O_4 (**Figure 4.13B b,d**), their grains become thinner with the appearance of new holes (**Figure 4.13B a,d**) with disappearance of HfO_2 coating layer (**Figure 4.13B b,e,f**).

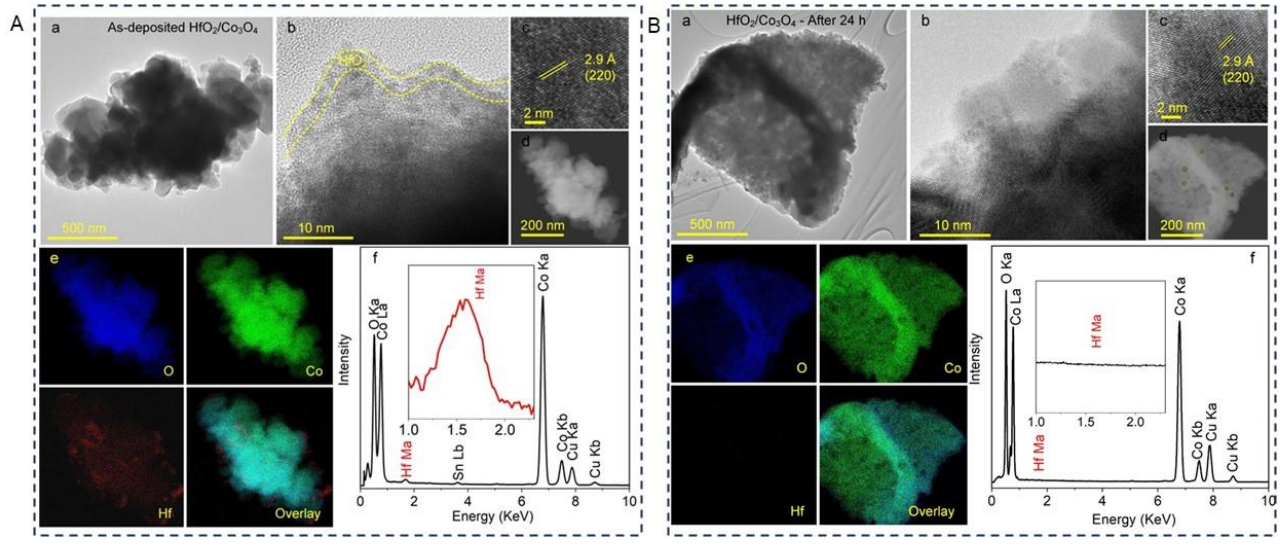

Figure 4.13 TEM analysis of as-prepared A) and B) after 24 h of water electrolysis HfO_2/Co_3O_4/FTO including a–d) TEM images, e) corresponding EDS elemental mapping, and f) EDS spectra.

Additionally, electrolytes derived from testing of the Co_3O_4 anodes without and with overcoating layers after 8, 24, and 32 h electrolysis were analyzed with ICP-MS (**Table 4.3** and **Figure 4.10a-c**). The corrosion rate after 8 h of the OER was the highest (0.49 μmol h^{-1}) for the unmodified electrodes, followed by the Al_2O_3 (0.43 μmol h^{-1}), SiO_2 (0.42 μmol h^{-1}) > TiO_2 (0.38 μmol h^{-1}) > SnO_2 (0.31 μmol h^{-1}) > HfO_2 (0.19 μmol h^{-1}) coated anodes (**Table 4.3** and **Figure 4.10a**). After 24 h electrolysis, the OER activity of the unmodified and Al_2O_3 coated anodes mostly come from the F-doped SnO_2 substrate, leading to an applied potential of over 3.2 V versus RHE to maintain a current density of 10 mA cm^{-2} (**Figure 4.10g**). However, the required potential in SiO_2 coated anode was still under 3.2 V versus RHE, indicating the existence of some Co_3O_4 catalyst on the FTO substrate to contribute to the OER activity. For this reason, the amount of dissolved Co in the electrolyte from the SiO_2-coated anode was slightly lower than those in the unmodified and Al_2O_3-coated anodes (**Figure 4.10b**). For TiO_2, SnO_2, and HfO_2 coated anodes, the corrosion rates of Co_3O_4 significantly increased during 24 h of electrolysis, consistent with more pin-holes appearing on the surface of the electrode after 8 h (**Figure 4.11**) and less catalyst materials remained on the substrate after 24 h (**Figure 4.12**). After 32 h, the amount of etched Co from TiO_2/Co_3O_4/FTO and SnO_2/Co_3O_4/FTO anodes was similar to that from the unmodified samples after 24 h (**Figure 4.10c**), indicating complete dissolution of Co_3O_4. For the HfO_2/Co_3O_4/FTO anode, the dissolution rate of Co_3O_4 detected within 24–32 h was lower compared to those from other electrodes, indicating the efficient protection effect of the HfO_2 layer on the Co_3O_4 electrodes. Additionally, the dissolution of the overlayers from Al, Ti, and Hf was investigated by ICP-MS analysis (**Figure 4.10d, e**). It revealed the dissolved amount of the overcoating layer significantly increased over time. Noticeably, after 24 h, the changes in the amount of TiO_2 and HfO_2 were negligible, indicating the nearly complete dissolution of the overlayers.

Table 4.3 Dissolution rate of Co_3O_4 into electrolytes from OER operation detected by ICP-MS.

Overlayer	Stability at 10 mA cm^{-2} [h[a)]]	Dissolution rate of Co_3O_4 [μmol h^{-1}]		
		8 h	24 h	32 h
none	12	0.49	n/a[b)]	n/a
Al_2O_3	20	0.43	n/a	n/a
SiO_2	23	0.42	n/a	n/a
TiO_2	27	0.38	0.41	n/a
SnO_2	28	0.31	0.34	n/a
HfO_2	32	0.19	0.27	0.39

[a)] Stability at 10 mA cm^{-2} – point of time when potential starts to abruptly increase during extended OER tests at 10 mA cm^{-2}. [b)]n/a: data is not available as the electrodes stop working before this time.

In short, our results determined the stability of our Co_3O_4 anode enhanced in the presence of the ALD-based passivation layer. The stability and corrosion of these Co_3O_4 films were evaluated by the surface morphology changes and the amount of dissolved Co ions through SEM, TEM, ICP analysis. The stability of Co_3O_4 anode followed this order HfO_2 > SnO_2 > TiO_2 > Al_2O_3, SiO_2 > uncoated films. The most serious corrosive film occurs in the undoped Co_3O_4 film with the observed significant pitting and large holes (hundreds of nm) appeared on the surface and a 44 % thickness reduction (360 nm → 200 nm) after 8 h OER, and the film almost completely disappeared after 24 h test. This substantial loss of material was confirmed by a very high rate of Co migration of 0.49 μmol/h. The enhanced stability of coated Co_3O_4 film was presented by the delayed corrosion process, i.e. significant decrease in the size and density of corrosive pitting holes, the slower film thickness degradation, and the reduced Co migration rate. Among them, HfO_2-coated Co_3O_4 electrodes reduced Co dissolution by 61 % (0.19 μmol/h) aligning with minimal pitting (<100 nm) and the relative retention of pristine thickness under identical conditions.

Collectively, our findings suggest that HfO_2 is the best passivation layer among the investigated dielectric materials. To determine the optimal thickness of HfO_2, we varied its thickness from 3 to 20 nm. Voltammetric and chronopotentiometric analysis of these electrodes indicate that increasing the HfO_2 thickness up to 12 nm does not significantly affect the OER activity of the electrode (**Figure 4.14**). The results suggest that the mass and charge transport in anodes coated with less than 12 nm HfO_2 thickness was still sufficient to catalyze the reaction. However, deposition of a 20 nm layer substantially deteriorated the OER performance, increasing the potential to ≈2.2 V versus RHE, ≈0.27 V higher than that of the unmodified Co_3O_4/FTO, to achieve an OER rate of 10 mA cm^{-2}. It is attributed to a strong decrease in the conductivity of the anodes, which is reflected by an increase of charge transfer resistance from 13.5 kΩ to 293.6 kΩ with increasing HfO_2 thickness from 0 to 20 nm in the EIS measurements (**Figure 4.14** and **Table 4.4**). Extended durability tests indicate that coating Co_3O_4 with a 12 nm thick HfO_2 can prolong the stability of the OER performance to 42 h (**Figure 4.14b**). This is 10 h more than that with the 3 nm HfO_2 coating and 3.5-time increase over that of the unmodified electrode. This is also considerably good stability in comparison to acidic water oxidation at low pH (**Table 4.5**). Notably, further increasing the thickness to 20 nm did not improve stability. This might be attributed to the more positive potential applied to the electrode during the test due to the lower electrocatalytic activity (**Figure 4.14b**). Likewise, the impact of the coating thicknesses (3, 6, 8, and 10 nm) of Al_2O_3 and TiO_2 on the catalytic activity and stability of the anodes was also investigated. The chronopotentiometric results

(**Figure 4.15**) indicate that the optimal Al_2O_3 and TiO_2 thicknesses are in the range of 3–6 nm. Thinner or thicker coating layers decrease the stability and activity of the electrodes as similarly observed from the HfO_2 coating and reported in the literature.[39,68] Importantly, their activity could not be retained after 27 h OER, which is by far shorter than 42 h obtained from the anode coated with an optimized HfO_2 layer.

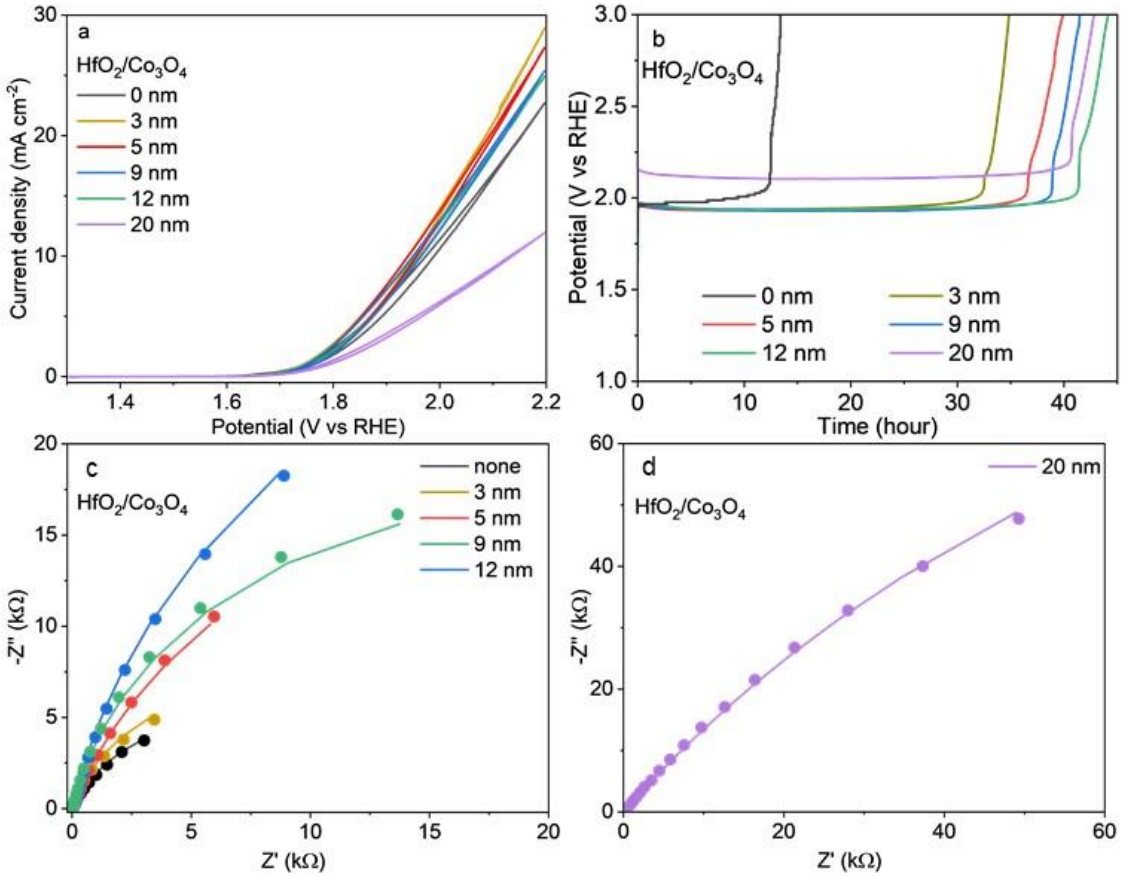

Figure 4.14 Electrochemical characterization of Co_3O_4/FTO electrodes coated with different HfO_2 thicknesses in H_2SO_4 electrolyte pH 0. (a) Quasi-stabilized linear sweep voltammetry curves (third scan with scan rate 0.005 V s^{-1}), and (b) chronopotentiometric curves recorded at 10 mA cm^{-2}. Currents are normalized to the geometric surface area; Nyquist plots of the EIS data with different HfO_2 thicknesses c) in a range from 0–12 nm and at d) at 20 nm: colored dots: raw EIS data; solid colored line: simulation curve after fitting with Randle circuit.

Table 4.4 Summary of electrochemical impedance spectroscopy fitting for HfO_2/Co_3O_4/FTO in a variation of HfO_2 thickness.

Overlayer	R_s [Ω]	R_{ct} [Ω]	Q_{dl} [F cm^{-2} s$^{\alpha-1}$]	α_{dl}
0 nm	19.32	13445	0.252×10^{-3}	0.799
3 nm	21.54	15251	0.115×10^{-3}	0.866
5 nm	22.33	35432	0.14×10^{-3}	0.782
9 nm	22.26	41547	0.039×10^{-3}	0.793
12 nm	21.31	87670	0.068×10^{-3}	0.824
20 nm	23.21	293622	0.078×10^{-3}	0.624

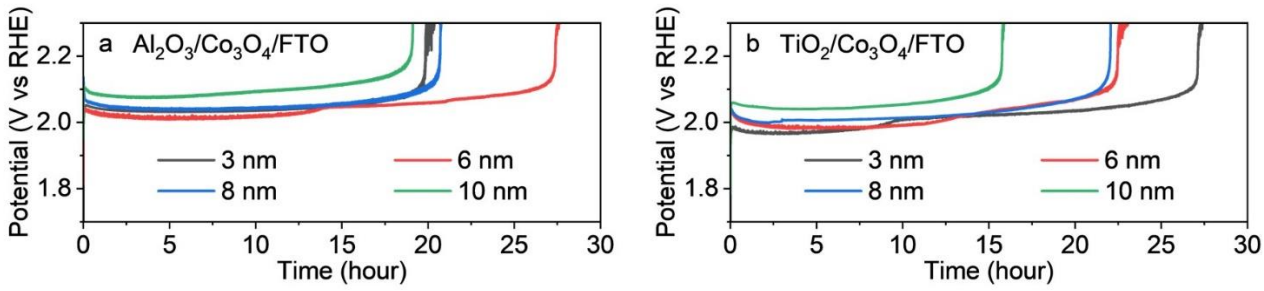

Figure 4.15 Chronopotentiometric curves of Co_3O_4/FTO electrodes coated with different thicknesses of a) Al_2O_3 and b) TiO_2 passivation layers recorded at 10 mA cm^{-2} in H_2SO_4 electrolyte pH 0. Currents are normalized to the geometric surface area.

The 12 nm thick HfO_2 coating had the best stability and activity and thus was further investigated with an extended durability test in 0.1 M H_2SO_4 solution with pH ≈1 (**Figure 4.16**). This anode required ≈2.05 V versus RHE to achieve an oxygen evolution rate of 10 mA cm^{-2} and remained stable for a duration of ≈70 h. However, the applied potential surged after 70 h of continuous electrolysis, which could be attributed to the significant loss of the active electrocatalysts, leaving the inactive FTO surface (**Figure 4.16b**). Though the (12 nm) HfO_2 layer can prolong the stability and maintain the OER activity of the electrode for nearly 70 h, the anode still dissolved under anodic OER in strong acid, which indeed can dissolve noble metal oxides, such as RuO_x or IrO_x, to a certain extent.[16,69,70] The OER performance and stability of the HfO_2/Co_3O_4/FTO anodes are compared with recent stable acidic OER catalysts in **Table 4.5**. Many of these anodes achieved a prolonged lifetime due to a higher mass loading or a thicker catalyst layer.[39,71–74] To compare the stability of different catalysts reported in various publications, the catalyst lifetime was normalized to its mass and thickness. The normalized stabilities of our HfO_2 coated anode are 262.5 h mg_{co}^{-1} and 113 h μm^{-1} at a pH of 0, and 500 h mg_{co}^{-1} and 215 h μm^{-1} at a pH of 1, respectively, for a current of 10 mA cm^{-2}. These outperform most of the recently reported acidic OER anodes made of earth-

abundant materials (**Table 4.5**).[39,71–74] Exclusively, the superior durability of Co_2MnO_4 and $Ni_{0.5}Mn_{0.5}Sb_{1.7}O_y$, achieving 208 h mg_{co}^{-1} for a current of 100 mA cm^{-2} and 1292.3 h mg^{-1} for a current of 10 mA cm^{-2}, respectively, can be attributed to the stability of the Mn and/or Sb matrix.[75,76] However, they require a more complex preparation process and a precise composition. The implementation of a surface protective layer shown in this study provides a promising direction for a wide range of catalyst materials for acidic OER.

Table 4.5 Summary of important numerical data for recent acid-stable OER catalysts reported.

Catalyst	Catalyst loading		pH of electrolytes	Overpotential [V versus RHE]	Mass stability [h mg^{-1}]	Stability versus thickness [h μm^{-1}]	Ref
	Mass [mg cm^{-2}_{geo}]	Thickness [μm]					
HfO_2/Co_3O_4/FTO	0.16[a)]	0.372	0.1	0.47	262.5	113	This work
	0.16[a)]	0.372	1.1	0.54	500	215.1	
	0.22	0.372	0.1	0.47	190.9	113	
	0.22	0.372	1.1	0.54	363.6	215.1	
Ir−Co_3O_4/CFP	2.75		0.3[c)]	0.225	47.27[f)]		[77]
$CoSb_2O_x$/Ti grade	10		0.29	0.561	21.6[f)] 65[e)]		[71]
TiO_2/Co_3O_4/FTO		7	0 [c)]	0.57 [d)]		10.7	[39]
Co_2MnO_4/FTO	5.0[a)]		1	0.395	64[e)]		[75]
	2.5[a)]		1	0.405	98[e)]		
	1.0[a)]		1	0.415	171[e)]		
	0.5[a)]		1	0.423	208[e)]		
	0.2[a)]		1	0.443	194[e)]		
	0.1[a)]		1	0.433	190[e)]		
Co_3O_4@C/GPO	20		0.1	0.42	2.26[f)]		[72]
Co_3O_4/Co/29BC		100	0.3	0.35		0.5	[73]
$CoSb_2O_6$/FTO		0.6	0.3	0.76		40[f)]	[78]
$Mn_{0.8}Nb_{0.2}O_2$:10F/Ti foil	0.3		0.3[c)]	0.68	83[f)]		[79]
Co_2TiO_4/carbon cloth	0.16[b)]		0.3[c)]	0.51	62.5[f)]		[80]
$Co_{0.05}Fe_{0.95}O_y$/Ti foil	1		0.3	0.65	50		[81]
c−Fe_2O_3/Ti foil	1		0.3	0.65	24		[82]

$Mn_{0.67}Sb_{0.33}O_z$/Pt/Ti	0.12		0.13	0.51	17		[83]
$Ni_{0.5}Mn_{0.5}Sb_{1.7}O_y$/ATO	> 0.134	0.3	0	0.73	< 1292.3	< 560	[76]
Co_3O_4/FTO		300	0.3	0.57		0.04	[84]
Co_3O_4@C/CP	12.6		0.3	0.37	6.89 [e)]		[74]

All electrolytes are acid sulfuric (H_2SO_4) solutions with concentration from 0.1–1 M. Overpotentials recorded at 10 mA cm^{-2} are corrected with iR compensation. Mass stability and thickness versus stability were recorded and calculated at 10 mA cm^{-2}.

a) mass loading calculated by mass of Co

b) mass loading value was estimated from Figure 2 of original publication.

c) pH was estimated from the concentration of H_2SO_4 electrolytes reported in publication.

d) overpotential is not corrected with iR compensation.

e) mass stability and thickness versus stability were recorded and calculated at 100 mA cm^{-2}.

f) the values were calculated by the operation time reported in publications.

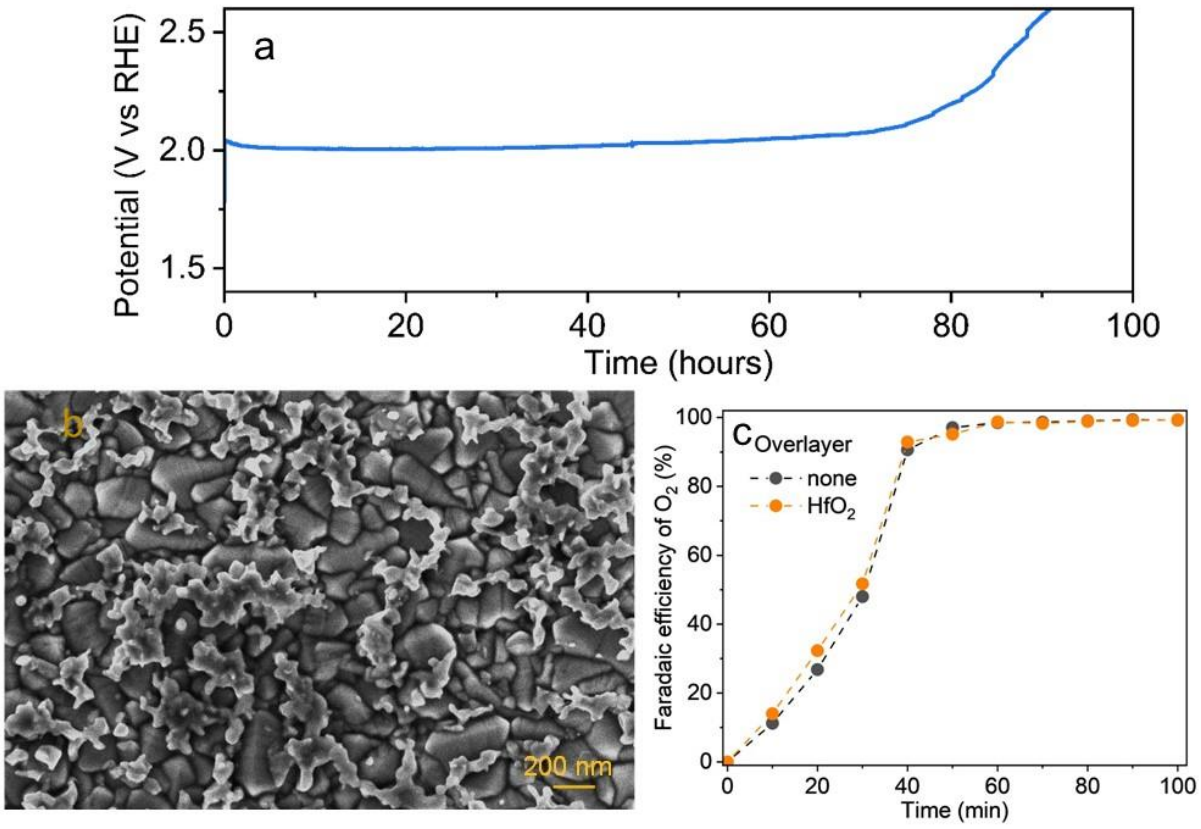

Figure 4.16 Extended stability test of HfO_2 (12 nm)/Co_3O_4/FTO: a) chronopotentiometric curve and b) SEM image after 80 h electrolysis, c) Faradaic efficiency for O_2 evolved from Co_3O_4/FTO and HfO_2/ Co_3O_4/FTO electrodes at 10 mA cm^{-2} in 1 M H_2SO_4 electrolyte.

To understand the production efficiency, the Faradaic efficiency (FE) of O_2 evolved from HfO_2/Co_3O_4/FTO and Co_3O_4/FTO anodes were measured (**Figure 4.16c**). Both samples reached stable FE efficiency at nearly 100 %, confirming the ALD coating layers have negligible impacts on the OER selectivity of the Co_3O_4 electrocatalyst.

Our electrochemical and spectroscopic characterization showed that ALD coating results in a slight difference in OER activity but a significant enhancement of the stability, following the order of HfO_2 > SnO_2 > TiO_2 > SiO_2, Al_2O_3. Since the difference in the thickness of the coating layers was minimal, the changes in stability can be attributed to the intrinsic material properties of the overlayers during the OER in an acidic environment. Such intrinsic properties can be determined by thermodynamic stability in connection with the underlying Co_3O_4 catalysts, which are further supplemented in the theoretical calculations below.

4.2.3. Theoretical Calculations

Our experimental results show that the stability of the coated anodes follows the order of HfO_2 > SnO_2 > TiO_2 > Al_2O_3, SiO_2. However, when deriving the thermodynamic stability of the oxide coatings from Pourbaix diagrams, SnO_2, SiO_2, and TiO_2 are expected to be more stable at low pH conditions (**Figure S 4.7**).[85] We hypothesize that in addition to the thermodynamic stability of the coating, the bonding strength between the Co_3O_4 surface and the overlayer also plays an important role. To further investigate and gain insights into such bonding strength, we carried out density functional theory (DFT) calculations (**Figure 4.17**).

By employing simplified models where the (110) surface of Co_3O_4 is bonded with the coating molecule via an oxygen atom, our finding reveals that the Co−O−Hf bonding energy (−3.48 eV) is the strongest, followed by Co−O−Sn (−3.44 eV), Co−O−Al (−3.34 eV), Co−O−Ti (−3.04 eV), and Co−O−Si (−2.89 eV). The (110) facet was used in modeling as it is one of the specific lattices of the Co_3O_4 spinel reflected in XRD patterns and high-resolution TEM analysis. It is worth noting that although Co−O−Al bonding energy is stronger than those of Ti and Si, Al_2O_3 is less thermodynamically stable according to the data shown in the Pourbaix diagram at low pH compared to TiO_2 and SiO_2 (**Figure S 4.7**). This indicates that both the thermodynamic stability of coating oxides and bonding strength between the underlying and coating layers should be considered when assessing the durability of oxygen evolution catalysts at low pH. This implies the effectiveness of combining theoretical and experimental studies, providing directions for acidic water electrolysis studies, including self-healing strategy.[29,31,33,34]

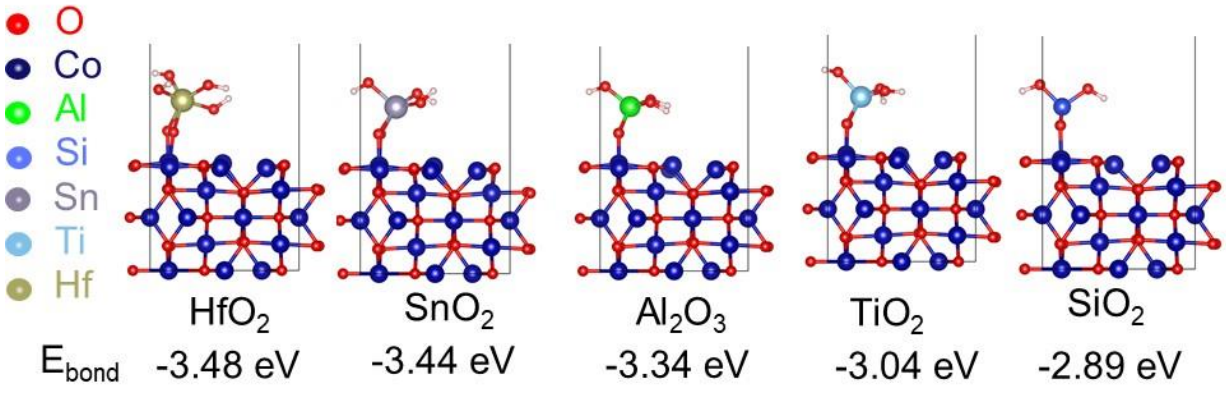

Figure 4.17 Theoretical calculations of the bonding energy (E_{bond}) between (110) facet of Co_3O_4 and the coating oxides using simplified models: from left to right, Co_3O_4−HfO_2, −SnO_2, −Al_2O_3, −TiO_2, and −SiO_2.

Noticeably, it is very limited studies reporting the quantified interfacial bonds between overlayer with Co_3O_4 system. Most literature did not explicitly quantify the bond energy by DFT, and they just assessed the bond strength with different elements (Ir, Bi, Ni, Fe, etc.) in Co_3O_4 system through electrochemical measurement or structural characterization (XAS, XPS, XRD).[86–89] Their main application was to enhance the absorption energies of intermediates, modulate the electronic/structural characteristics to enhance the OER activity. For comparison purpose, it is lack of the study with the quantify bonding value and the similar focus on the enhanced OER stability in acidic condition.

4.3. Conclusions

In this study, we presented a systematic investigation of the key properties of nanoscale dielectric layers to stabilize earth-abundant Co_3O_4 OER anode electrocatalysts in highly acidic conditions. Dielectric layers of Al_2O_3, SiO_2, TiO_2, SnO_2, and HfO_2 were conformally deposited on Co_3O_4 anodes by ALD. We reveal that though the nanoscale coatings cannot prevent the ultimate dissolution of the underlying Co_3O_4, they can significantly improve the anode long-term stability, while maintaining the Co_3O_4 catalytic activity with the order of $HfO_2 > SnO_2 > TiO_2 > Al_2O_3, SiO_2$. Our theoretical calculations suggest that this may be attributed to the stronger bonding energy of the $Co_3O_4|HfO_2$ interface as compared to other oxide coatings, highlighting the importance of the interfacial engineering between the coating and coated layers. The optimally coated anode with a HfO_2 thickness of 12 nm was able to retain a current density of 10 mA cm^{-2} at ≈1.95 V versus RHE for > 42 h in an H_2SO_4 electrolyte pH 0. These insights provide guidelines for engineering coatings of non-platinum group metal (non-PGM) anode catalysts for acidic electrolysis. While this study was conducted in conventional H-cell tests at pH 0, experiments in a PEMWE, where local pH, current densities, and temperature are higher, should be demonstrated to assess the activity and stability of the anode catalysts under practical conditions.

4.4. Experiment section

4.4.1. Material

All the chemical reagents and solvents for the material synthesis were used as received without any further purification. Ultrapure deionized water (resistivity 18.2 MΩ cm^{-1}) was used in preparing aqueous solutions in all experiments.

4.4.2. Substrate preparation

The fluorine-doped tin oxide (FTO) glass substrate 10 × 35 mm was purchased from OPV Tech. The substrate was first cleaned with ethanol and water and dried. The exposed geometric area of the substrate to the electrolyte solutions was 1 cm^2.

4.4.3. Fabrication of Co_3O_4 catalysts

Cobalt (Co) film was deposited onto FTO glass substrate by DC magnetron sputtering in 1200 seconds at an applied bias 600 W. Then, they were annealed at 550 ºC in 2 h with the ramp rate 2 ºC min^{-1} to obtain the cobalt oxide (Co_3O_4) layer. The mass loading of Co_3O_4 anode was estimated with the mass density extracted from The Materials Project for cubic Co_3O_4 materials (6.1 g/cm^3).[85]

Conformal TiO_2, Al_2O_3, SiO_2, SnO_2, and HfO_2 films were deposited onto the Co_3O_4|FTO anodes using plasma-assisted atomic layer deposition (PA-ALD) system (PicoSun-Sunale) with argon and oxygen plasma as the co-reactants. Al, Si, Ti, Sn, and Hf sources were trimethylaluminum ($AlCl_3$), silane (SiH_4), titanium tetrachloride ($TiCl_4$), tetrakis (dimethylamino) tin ($[(CH_3)_2N]_4Sn$), tetrakis (ethylmethylamido) hafnium ($[(CH_3)(C_2H_5)N]_4Hf$), respectively. SiO_2 and SnO_2 were deposited by PA-ALD system at 300 ºC and 83 °C, respectively. The vessels of three hot sources including SiO_2, SnO_2, and HfO_2 were heated at 45 °C, 55 °C, and 120 °C throughout the ALD deposition process. HfO_2, Al_2O_3, and TiO_2 were deposited at ambient temperature and the vessels of TiO_2 and Al_2O_3 sources were kept at room temperature. The thickness of ALD coating layer was precisely controlled by tuning the ALD deposition cycles.

4.4.4. Material characterisation

The morphology of the films was investigated using a field-emission scanning electron microscope (FESEM) Zeiss Ultra Plus operating at 3 kV without coating. Samples for SEM were prepared by fixing the cut pieces of the electrode on the specimen stubs using carbon tape.

X-ray diffraction (XRD) patterns were recorded by a D2 Phaser Bruker system with Cu Kα radiation of average wavelength 1.54056 Å at a scan rate of 1.17 deg min^{-1}. The XRD results were obtained by direct measurement of the samples on FTO substrates. Raman spectra were recorded at room temperature by LabRAM HR (Horiba) evolution CCD camera 532 delta diode laser, using grating 1800 (500 nm). The laser power was 22 mW with 100 percent intensity. The spectra were collected at 50 seconds of acquisition time.

X-ray photoelectron spectroscopy (XPS) analysis was performed using a calibrated ESCALAB250Xi spectrometer (Thermo Scientific, UK) with a monochromated Al Kα source at a power of 120 W (13.8 kV × 8.7 mA). The base pressure in the main vacuum chamber during analysis was typically between 10^{-9} and 10^{-8} mbar. Survey spectra were acquired at pass energy of 160 eV. To obtain more detailed information about the chemical structure, oxidation states, and so forth, high-resolution spectra were recorded at 20 eV pass energy (yielding a typical peak width for polymers of approximately 1.0 eV). Spectra were collected at normal emission. The data was analysed using CasaXPS software version 2.3.25 PR1.0. Adventitious C 1s (284.8 eV) peak was used to calibrate the spectra.

The coating thicknesses were measured using a JA Woollam M2000D ellipsometer. The measurements were conducted with the thin oxide layers on the double-side polished Si wafer.

The inductively coupled plasma mass spectroscopy (ICP-MS) performed by Nexion5000 from PerkinElmer, USA. Samples for ICP–MS measurements were prepared by using 3 mL electrolyte in the continuous flow. The amount of Co etched in the electrolyte was detected by Co-59 mass, Helium KED mode, internal standard-Rh-103.

4.4.5. Electrochemical characterisation

All electrochemical measurements in this study were carried out with a BioLogic electrochemical workstation using a customized two compartment separated by a Nafion@117 membrane (sourced from FuelCellStore). In the electrochemical tests, the ALD coating layer/Co_3O_4/FTO anodes, depicted as in **(Figure 4.18a)**, played as working electrodes. Both sides of anode–front-side coated with catalyst and the back-side with only glass–were totally immersed in the electrolyte. The area test of working electrode was 1 cm^2. Electrochemical performance of the electrodes was evaluated in a three-electrode configuration using a Pt wire as the counter electrode and a double-junction Ag|AgCl|KCl(sat.) (+0.197 V *vs*. SHE) as the reference electrode. The scheme of three-electrode cell setup for electrochemical measurement was illustrated in **(Figure 4.18b)**. 1 M and 0.1 M acid sulfuric (H_2SO_4) solution at pH 0.08 and 1.13, respectively, were employed as an electrolyte. The potentials were converted to the reversible hydrogen electrode (RHE) scale via the Nernst equation:

$$E_{RHE} = E_{Ag/AgCl} + 0.197 + 0.059 \times pH \qquad \textbf{(Equation 4.1)}$$

Electrochemical impedance spectra (EIS) were collected at 0.3 V versus RHE and 1.8 V versus RHE over a frequency range of 0.1 Hz – 200 kHz with a 5 mV amplitude. For comparison with previous publications, the overpotentials recorded in (**Table 4.5)** were corrected for the *i*R product,

using the uncompensated resistance values for FTO from EIS in pH 0 and pH 1. Electrochemically active surface area (ECSA) was investigated through the electrochemical capacitance current at 0.81 V *vs*. RHE, which was measured by scanning cyclic voltammetry curves at different rates at the potential window of 0.76 to 0.86 V *vs*. RHE. ECSA is calculated by comparing the double layer capacitance of the Co_3O_4 anode (C_{dl}) to the specific capacitance (C_s) that ECSA = C_{dl}/C_s, where C_s is the capacitance of an atomically smooth planar surface of the material per unit area under identical electrolyte conditions, meaning identical pH and applied potential range.[59–61,90] Here, a glassy carbon surface sourced from PINE research (AFE5T050GC with a disk diameter of 5 mm) was used to measure a specific capacitance of the planar electrode. Faradaic efficiency for the OER was measured in a continuous-flow set-up, in which an air-tight H-cell was connected to a gas chromatography (GC). The high-quality argon was used as a carrier gas to pass through the electrolyte solution and then to the GC with a flow rate of 10 mL min^{-1}.

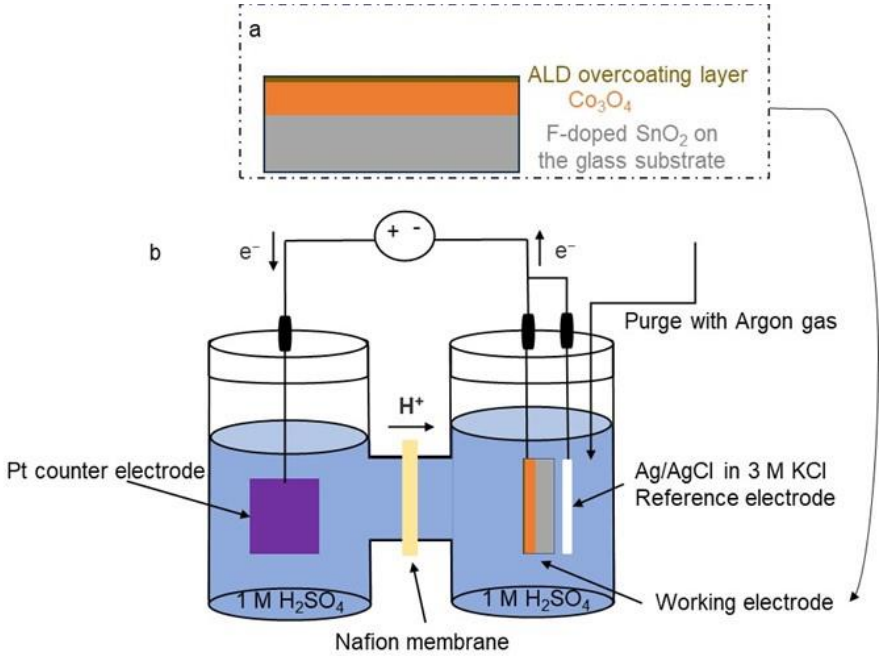

Figure 4.18 Graphical illustration of (a) ALD overcoating layers/Co_3O_4/FTO electrode and (b) a three-electrochemical system for electrochemical measurement.

4.4.6. Theoretical Calculations

Density functional theory (DFT) calculations were performed using the Projector Augmented Wave (PAW) method[91,92] as implemented in the Vienna Ab initio Simulation Package (VASP).[93,94] The calculations were completed with a plane-wave cut-off energy of 500 eV and Monkhorst-Pack k-points mesh of 3×3×1. The electronic self-consistent calculation was converged to 1×10^{-5} eV and

ionic relaxation steps were performed using the conjugate-gradient method (IBRION=2) and continued until the total force on each atom dropped below a tolerance of 3×10^{-2} eV/Å. The generalised gradient approximation (GGA) was used for the exchange-correlation functionals as parameterized by Perdew-Burke-Ernzerhof (PBE).[95] The adsorption energy is calculated using the following equation:

$$E_{ads} = E(slab*MO) - E(slab) - E(MO) \quad \textbf{(Equation 4.2)}$$

where E(slab*MO), E(slab) and E(MO) are the electronic energies of Co_3O_4 surface with adsorbed oxide (MO), clean Co_3O_4 surface and MO as adsorbate. Co_3O_4 surfaces of (011) was investigated in this study using the slab method with a vacuum thickness of 20 Å, along with different oxides of Al, Hf, Sn, Ti, and Si.

4.5. Supporting Information

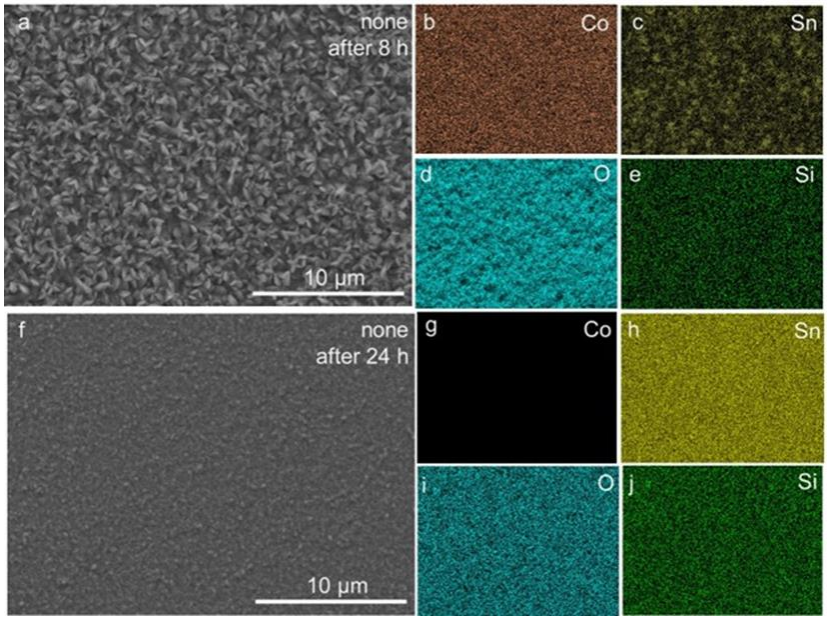

Figure S 4.1 SEM-EDS elemental mapping of unmodified Co_3O_4/FTO after a–e) 8 and f–i) 24 h of galvanostatic operation at 10 mA cm^{-2} in H_2SO_4 pH 0 electrolyte.

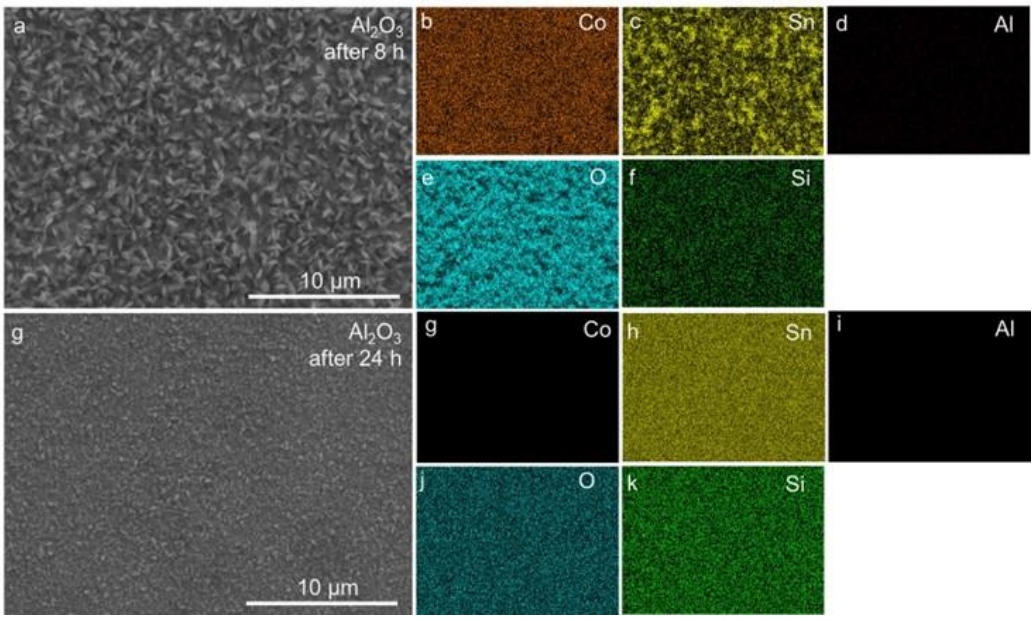

Figure S 4.2 SEM-EDS elemental mapping of Al_2O_3/Co_3O_4/FTO after a–f) 8 and g–j) 24 h of galvanostatic operation at 10 mA cm^{-2} in H_2SO_4 pH 0 electrolyte.

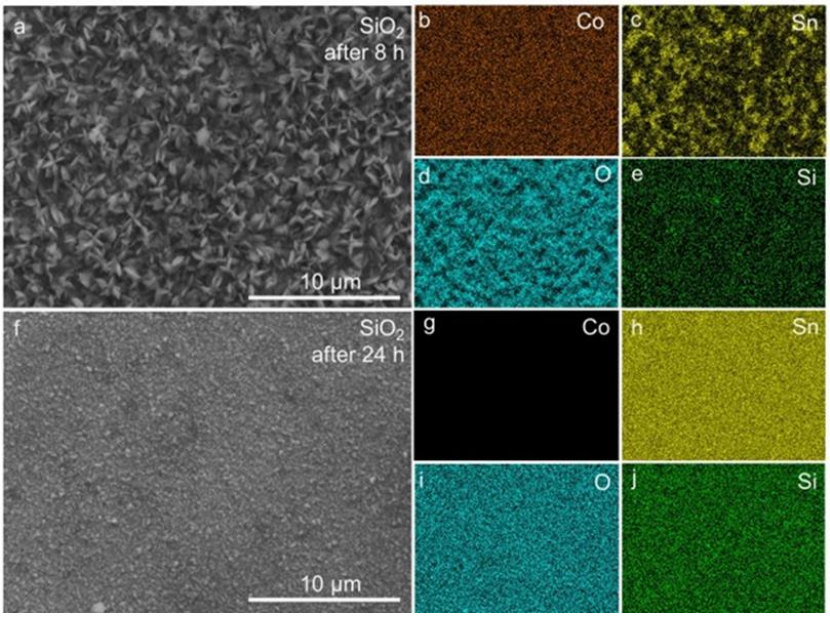

Figure S 4.3 SEM-EDS elemental mapping of SiO_2/Co_3O_4/FTO after a–e) 8 and f–i) 24 h of galvanostatic operation at 10 mA cm^{-2} in H_2SO_4 pH 0 electrolyte.

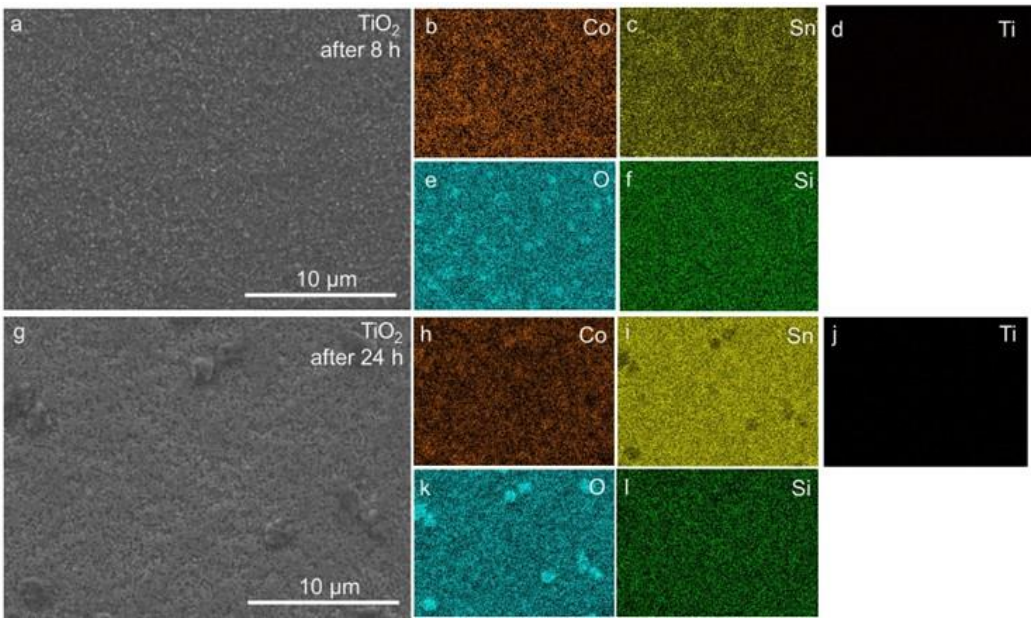

Figure S 4.4 SEM-EDS elemental mapping of TiO_2/Co_3O_4/FTO after a–f) 8 and g–l) 24 h of galvanostatic operation at 10 mA cm^{-2} in H_2SO_4 pH 0 electrolyte.

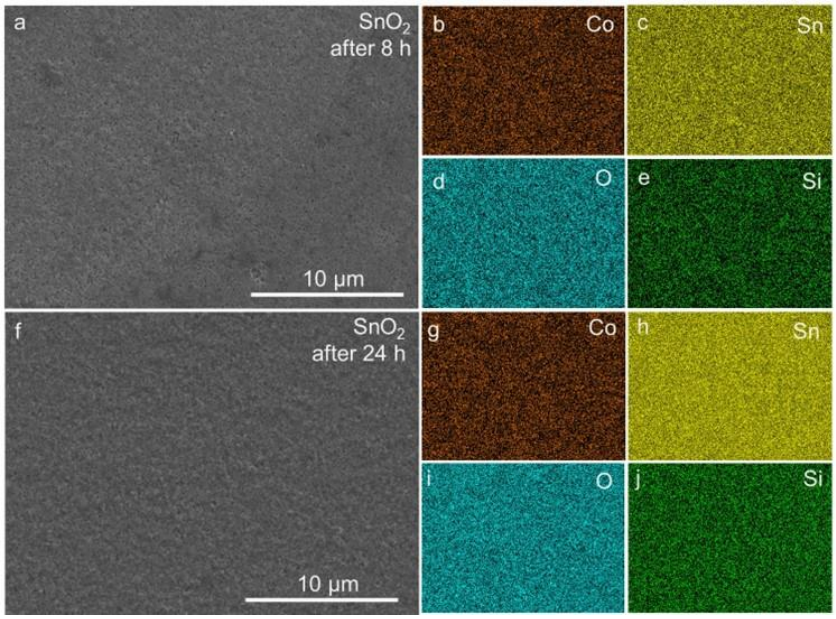

Figure S 4.5 SEM-EDS elemental mapping of SnO_2/Co_3O_4/FTO after a–e) 8 and f–j) 24 h of galvanostatic operation at 10 mA cm^{-2} in H_2SO_4 pH 0 electrolyte.

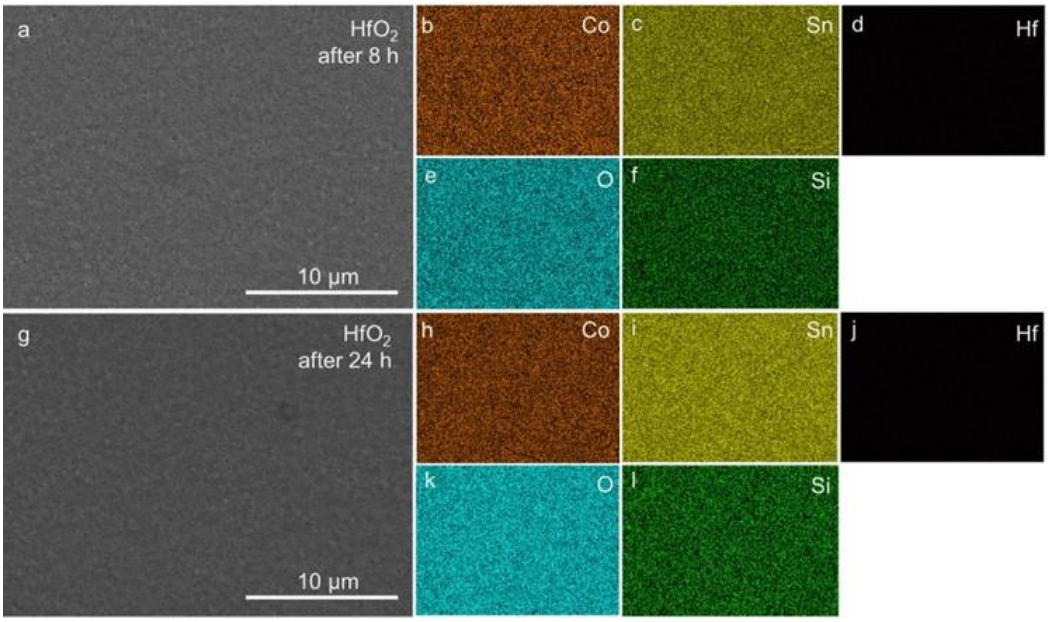

Figure S 4.6 SEM-EDS elemental mapping of HfO_2/Co_3O_4/FTO after a–f) 8 and g–l) 24 h of galvanostatic operation at 10 mA cm^{-2} in H_2SO_4 pH 0 electrolyte.

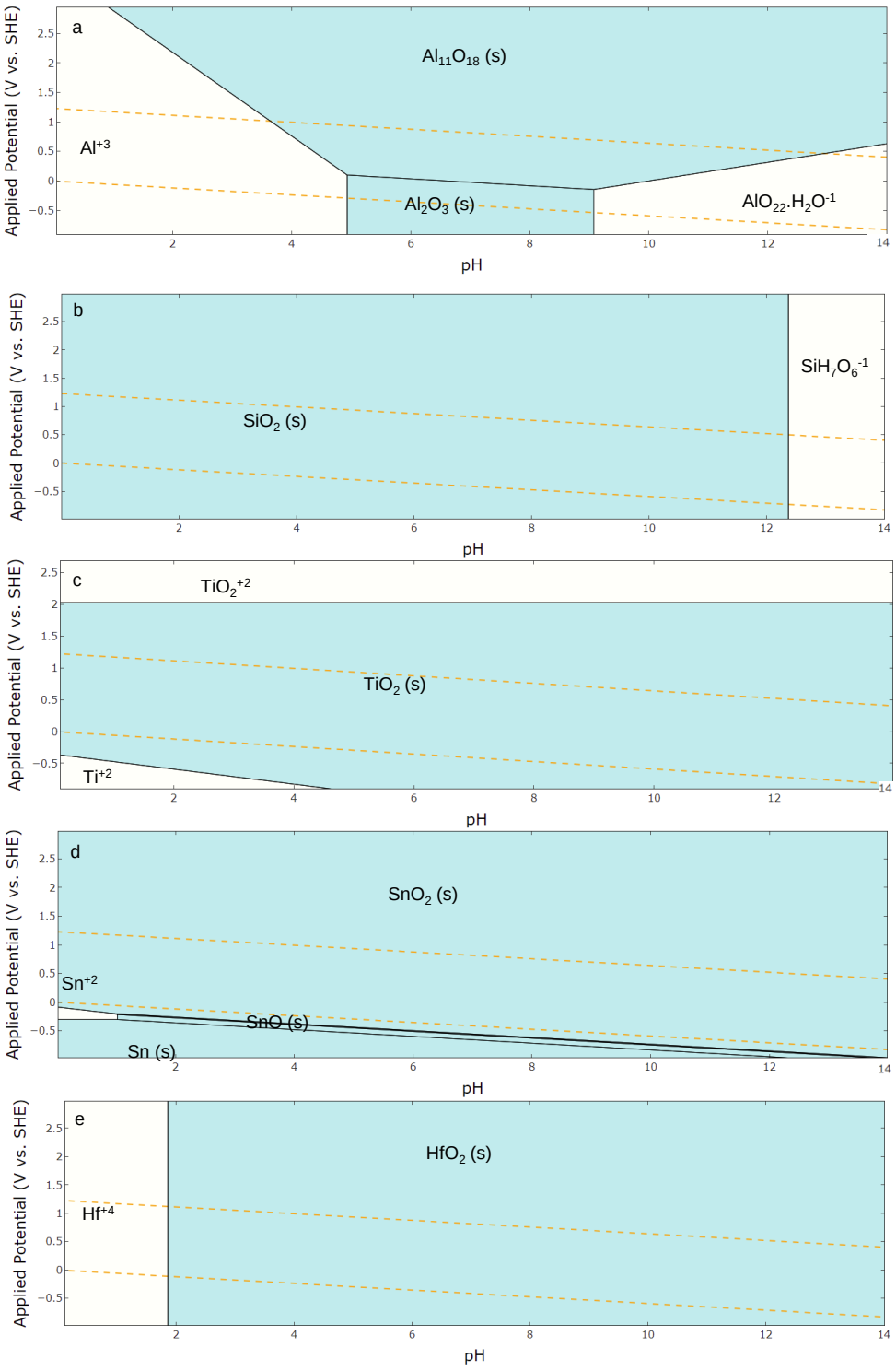

Figure S 4.7 Pourbaix diagram of invested oxides used as protective layers. Data extracted from The Materials Project.[85]

4.6. References

[1] O. Bičáková, P. Straka, *Int. J. Hydrogen Energy* **2012**, *37*, 11563.

[2] H. Ishaq, I. Dincer, C. Crawford, *Int. J. Hydrogen Energy* **2022**, *47*, 26238.

[3] P. J. Megia, A. J. Vizcaino, J. A. Calles, A. Carrero, *Energy and Fuels* **2021**, *35*, 16403.

[4] A. Godula-Jopek, D. Stolten, C. Bourasseau, *Hydrogen Production by Electrolysis*, WILEY-VCH Verlag GmbH & Co. KGaA, Weinheim, Germany, **2015**.

[5] S. Shiva Kumar, H. Lim, *Energy Reports* **2022**, *8*, 13793.

[6] Y. Leng, G. Chen, A. J. Mendoza, T. B. Tighe, M. A. Hickner, C. Y. Wang, *J. Am. Chem. Soc.* **2012**, *134*, 9054.

[7] K. Zeng, D. Zhang, *Prog. Energy Combust. Sci.* **2010**, *36*, 307.

[8] M. Carmo, D. L. Fritz, J. Mergel, D. Stolten, *Int. J. Hydrogen Energy* **2013**, *38*, 4901.

[9] L. Zhang, X. Jie, Z.-G. Shao, Z.-M. Zhou, G. Xiao, B. Yi, *Int. J. Hydrogen Energy* **2012**, *37*, 1321.

[10] L. Ma, S. Sui, Y. Zhai, *Int. J. Hydrogen Energy* **2009**, *34*, 678.

[11] S. Shiva Kumar, V. Himabindu, *Mater. Sci. Energy Technol.* **2019**, *2*, 442.

[12] J. Kibsgaard, I. Chorkendorff, *Nat. Energy* **2019**, *4*, 430.

[13] L. An, C. Wei, M. Lu, H. Liu, Y. Chen, G. G. Scherer, A. C. Fisher, P. Xi, Z. J. Xu, C. H. Yan, *Adv. Mater.* **2021**, *33*, 1.

[14] E. Fabbri, T. J. Schmidt, *ACS Catal.* **2018**, *8*, 9765.

[15] Q. Wang, Y. Cheng, H. B. Tao, Y. Liu, X. Ma, D. Li, H. Bin Yang, B. Liu, *Angew. Chemie Int. Ed.* **2023**, DOI 10.1002/anie.202216645.

[16] S. Cherevko, A. R. Zeradjanin, A. A. Topalov, N. Kulyk, I. Katsounaros, K. J. J. Mayrhofer, *ChemCatChem* **2014**, *6*, 2219.

[17] S. Cherevko, S. Geiger, O. Kasian, A. Mingers, K. J. J. Mayrhofer, *J. Electroanal. Chem.* **2016**, *773*, 69.

[18] S. Cherevko, S. Geiger, O. Kasian, N. Kulyk, J.-P. Grote, A. Savan, B. R. Shrestha, S. Merzlikin, B. Breitbach, A. Ludwig, K. J. J. Mayrhofer, *Catal. Today* **2016**, *262*, 170.

[19] M. A. Hubert, A. M. Patel, A. Gallo, Y. Liu, E. Valle, M. Ben-Naim, J. Sanchez, D. Sokaras, R. Sinclair, J. K. Nørskov, L. A. King, M. Bajdich, T. F. Jaramillo, *ACS Catal.* **2020**, *10*, 12182.

[20] C. C. L. McCrory, S. Jung, I. M. Ferrer, S. M. Chatman, J. C. Peters, T. F. Jaramillo, *J. Am. Chem. Soc.* **2015**, *137*, 4347.

[21] X. Sun, K. Xu, C. Fleischer, X. Liu, M. Grandcolas, R. Strandbakke, T. Bjørheim, T. Norby, A. Chatzitakis, *Catalysts* **2018**, *8*, 657.

[22] M. Huynh, T. Ozel, C. Liu, E. C. Lau, D. G. Nocera, *Chem. Sci.* **2017**, *8*, 4779.

[23] S. Cherevko, *Curr. Opin. Electrochem.* **2023**, *38*, 101213.

[24] Z. Wu, X. F. Lu, S. Zang, X. W. (David) Lou, *Adv. Funct. Mater.* **2020**, *30*, 1910274.

[25] R. Frydendal, E. A. Paoli, B. P. Knudsen, B. Wickman, P. Malacrida, I. E. L. Stephens, I.

Chorkendorff, *ChemElectroChem* **2014**, *1*, 2075.

[26] L. G. Bloor, P. I. Molina, M. D. Symes, L. Cronin, *J. Am. Chem. Soc.* **2014**, *136*, 3304.

[27] N. Li, T. P. Keane, S. S. Veroneau, R. G. Hadt, D. Hayes, L. X. Chen, D. G. Nocera, *Proc. Natl. Acad. Sci.* **2020**, *117*, 16187.

[28] S. Luke, M. Chatti, A. Yadav, B. V. Kerr, J. Kangsabanik, T. Williams, P. V. Cherepanov, B. Johannessen, A. Tanksale, D. R. MacFarlane, R. K. Hocking, A. Alam, A. Yella, A. N. Simonov, *J. Mater. Chem. A* **2021**, *9*, 27468.

[29] H. Du, M. Chatti, B. Kerr, C. K. Nguyen, T. Tran-Phu, D. A. Hoogeveen, P. V. Cherepanov, A. S. R. Chesman, B. Johannessen, A. Tricoli, R. K. Hocking, D. R. MacFarlane, A. N. Simonov, *ChemCatChem* **2022**, *14*, DOI 10.1002/cctc.202200013.

[30] A. E. Thorarinsdottir, C. Costentin, S. S. Veroneau, D. G. Nocera, *Chem. Mater.* **2022**, *34*, 826.

[31] D. Simondson, M. Chatti, J. L. Gardiner, B. V. Kerr, D. A. Hoogeveen, P. V. Cherepanov, I. C. Kuschnerus, T. D. Nguyen, B. Johannessen, S. L. Y. Chang, D. R. Macfarlane, R. K. Hocking, A. N. Simonov, *ACS Catal.* **2022**, *12*, 12912.

[32] C. Costentin, D. G. Nocera, *Proc. Natl. Acad. Sci. U. S. A.* **2017**, *114*, 13380.

[33] A. E. Thorarinsdottir, S. S. Veroneau, D. G. Nocera, *Nat. Commun.* **2022**, *13*, 1.

[34] M. Chatti, J. L. Gardiner, M. Fournier, B. Johannessen, T. Williams, T. R. Gengenbach, N. Pai, C. Nguyen, D. R. MacFarlane, R. K. Hocking, A. N. Simonov, *Nat. Catal.* **2019**, *2*, 457.

[35] D. Simondson, M. Chatti, S. A. Bonke, M. F. Tesch, R. Golnak, J. Xiao, D. A. Hoogeveen, P. V. Cherepanov, J. L. Gardiner, A. Tricoli, D. R. MacFarlane, A. N. Simonov, *Angew. Chemie - Int. Ed.* **2021**, *60*, 15821.

[36] J. Su, Z. Li, Y. Yu, X. Wang, *Adv. Mater. Interfaces* **2017**, *4*, 1600835.

[37] T. Wang, Z. Luo, C. Li, J. Gong, *Chem. Soc. Rev.* **2014**, *43*, 7469.

[38] A. T. Sivagurunathan, S. Adhikari, D. H. Kim, *Nano Energy* **2021**, *83*, 105802.

[39] T. Tran-Phu, H. Chen, R. Daiyan, M. Chatti, B. Liu, R. Amal, Y. Liu, D. R. Macfarlane, A. N. Simonov, A. Tricoli, *ACS Appl. Mater. Interfaces* **2022**, *14*, 33130.

[40] Y. W. Chen, J. D. Prange, S. Dühnen, Y. Park, M. Gunji, C. E. D. Chidsey, P. C. McIntyre, *Nat. Mater.* **2011**, *10*, 539.

[41] T. Moehl, J. Suh, L. Sévery, R. Wick-Joliat, S. D. Tilley, *ACS Appl. Mater. Interfaces* **2017**, *9*, 43614.

[42] L. Pan, J. H. Kim, M. T. Mayer, M. K. Son, A. Ummadisingu, J. S. Lee, A. Hagfeldt, J. Luo, M. Grätzel, *Nat. Catal.* **2018**, *1*, 412.

[43] W. Kim, T. Tachikawa, D. Monllor-Satoca, H. Il Kim, T. Majima, W. Choi, *Energy Environ. Sci.* **2013**, *6*, 3732.

[44] M. Li, Z. X. Jin, W. Zhang, Y. H. Bai, Y. Q. Cao, W. M. Li, D. Wu, A. D. Li, *Sci. Rep.* **2019**, *9*, 1.

[45] J. S. Daubert, G. T. Hill, H. N. Gotsch, A. P. Gremaud, J. S. Ovental, P. S. Williams, C. J. Oldham, G. N. Parsons, *ACS Appl. Mater. Interfaces* **2017**, *9*, 4192.

[46] A. F. Baxter, J. Abed, D. V. Fraga Alvarez, D. Zhou, D. Kuvar, E. H. Sargent, D. Esposito,

J. Electrochem. Soc. **2023**, DOI 10.1149/1945-7111/accfc1.

[47] Y. Liu, J. Li, W. Li, Q. Liu, Y. Yang, Y. Li, Q. Chen, *Int. J. Hydrogen Energy* **2015**, *40*, 8856.

[48] M. C. Biesinger, B. P. Payne, A. P. Grosvenor, L. W. M. Lau, A. R. Gerson, R. S. C. Smart, *Appl. Surf. Sci.* **2011**, *257*, 2717.

[49] T. Tran-Phu, R. Daiyan, J. Leverett, Z. Fusco, A. Tadich, I. Di Bernardo, A. Kiy, T. N. Truong, Q. Zhang, H. Chen, P. Kluth, R. Amal, A. Tricoli, *Chem. Eng. J.* **2022**, *429*, 132180.

[50] T. Tran-Phu, M. Chatti, J. Leverett, T. K. A. Nguyen, D. Simondson, D. A. Hoogeveen, A. Kiy, T. Duong, B. Johannessen, J. Meilak, P. Kluth, R. Amal, A. N. Simonov, R. K. Hocking, R. Daiyan, A. Tricoli, *Small* **2023**, *2208074*, 2208074.

[51] A. K.-V. S. W. G. and C. J. P. Alexander V. Naumkin, "NIST X-ray Photoelectron Spectroscopy Database," **n.d.**

[52] N. M. Figueiredo, N. J. M. Carvalho, A. Cavaleiro, *Appl. Surf. Sci.* **2011**, *257*, 5793.

[53] A. Dane, U. K. Demirok, A. Aydinli, S. Suzer, *J. Phys. Chem. B* **2006**, *110*, 1137.

[54] M. C. Biesinger, L. W. M. Lau, A. R. Gerson, R. S. C. Smart, *Appl. Surf. Sci.* **2010**, *257*, 887.

[55] M. C. Biesinger, B. P. Payne, B. R. Hart, A. P. Grosvenor, N. S. McIntryre, L. W. M. Lau, R. S. Smart, *J. Phys. Conf. Ser.* **2008**, *100*, 012025.

[56] J. F. Moulder, W. F. Stickle, W. M. Sobol, K. D. Bomben, **1992**.

[57] M. Chatti, T. Gengenbach, R. King, L. Spiccia, A. N. Simonov, *Chem. Mater.* **2017**, *29*, 3092.

[58] E. Charnetskaya, M. Chatti, B. V. Kerr, T. Tran-Phu, T. D. Nguyen, P. V. Cherepanov, D. A. Hoogeveen, B. Johannessen, A. Tricoli, D. R. Macfarlane, R. K. Hocking, A. N. Simonov, *ACS Sustain. Chem. Eng.* **2022**, *10*, 7117.

[59] P. Connor, J. Schuch, B. Kaiser, W. Jaegermann, *Zeitschrift für Phys. Chemie* **2020**, *234*, 979.

[60] S. Trasatti, O. A. Petrii, *J. Electroanal. Chem.* **1992**, *327*, 353.

[61] C. C. L. McCrory, S. Jung, J. C. Peters, T. F. Jaramillo, *J. Am. Chem. Soc.* **2013**, *135*, 16977.

[62] X. M. C. Ta, T. K. A. Nguyen, A. D. Bui, H. T. Nguyen, R. Daiyan, R. Amal, T. Tran-Phu, A. Tricoli, *Adv. Mater. Technol.* **2023**, *2201760*, 2201760.

[63] S. Anantharaj, S. Noda, *ChemElectroChem* **2020**, *7*, 2297.

[64] M. D. Obradović, B. D. Balanč, U. Č. Lačnjevac, S. L. Gojković, *J. Electroanal. Chem.* **2021**, *881*, 114944.

[65] X. Deng, S. Öztürk, C. Weidenthaler, H. Tüysüz, *ACS Appl. Mater. Interfaces* **2017**, *9*, 21225.

[66] M. Favaro, J. Yang, S. Nappini, E. Magnano, F. M. Toma, E. J. Crumlin, J. Yano, I. D. Sharp, *J. Am. Chem. Soc.* **2017**, *139*, 8960.

[67] A. Bergmann, E. Martinez-Moreno, D. Teschner, P. Chernev, M. Gliech, J. F. De Araújo, T. Reier, H. Dau, P. Strasser, *Nat. Commun.* **2015**, *6*, DOI 10.1038/ncomms9625.

[68] A. G. Scheuermann, J. D. Prange, M. Gunji, C. E. D. Chidsey, P. C. McIntyre, *Energy Environ. Sci.* **2013**, *6*, 2487.

[69] S. Wang, T. Shen, C. Yang, G. Luo, D. Wang, *ACS Catal.* **2023**, *13*, 8670.

[70] T. Reier, H. N. Nong, D. Teschner, R. Schlögl, P. Strasser, *Adv. Energy Mater.* **2017**, *7*, DOI 10.1002/aenm.201601275.

[71] A. Babaei, M. Rezaei, *J. Electroanal. Chem.* **2023**, *935*, 117319.

[72] J. Yu, F. A. Garcés-Pineda, J. González-Cobos, M. Peña-Díaz, C. Rogero, S. Giménez, M. C. Spadaro, J. Arbiol, S. Barja, J. R. Galán-Mascarós, *Nat. Commun.* **2022**, *13*, 4341.

[73] Q. Lai, V. Vediyappan, K.-F. Aguey-Zinsou, H. Matsumoto, *Adv. Energy Sustain. Res.* **2021**, *2*, 2100086.

[74] X. Yang, H. Li, A. Y. Lu, S. Min, Z. Idriss, M. N. Hedhili, K. W. Huang, H. Idriss, L. J. Li, *Nano Energy* **2016**, *25*, 42.

[75] A. Li, S. Kong, C. Guo, H. Ooka, K. Adachi, D. Hashizume, Q. Jiang, H. Han, J. Xiao, R. Nakamura, *Nat. Catal.* **2022**, *5*, 109.

[76] I. A. Moreno-Hernandez, C. A. Macfarland, C. G. Read, K. M. Papadantonakis, B. S. Brunschwig, N. S. Lewis, *Energy Environ. Sci.* **2017**, *10*, 2103.

[77] Y. Xie, Y. Su, H. Qin, Z. Cao, H. Wei, F. Wu, G. Ou, *Int. J. Hydrogen Energy* **2023**, *48*, 14642.

[78] T. A. Evans, K.-S. Choi, *ACS Appl. Energy Mater.* **2020**, *3*, 5563.

[79] S. D. Ghadge, O. I. Velikokhatnyi, M. K. Datta, P. M. Shanthi, S. Tan, P. N. Kumta, *ACS Appl. Energy Mater.* **2020**, *3*, 541.

[80] S. Anantharaj, K. Karthick, S. Kundu, *Inorg. Chem.* **2019**, *58*, 8570.

[81] W. L. Kwong, C. C. Lee, A. Shchukarev, J. Messinger, *Chem. Commun.* **2019**, *55*, 5017.

[82] W. L. Kwong, C. C. Lee, A. Shchukarev, E. Björn, J. Messinger, *J. Catal.* **2018**, *365*, 29.

[83] L. Zhou, A. Shinde, J. H. Montoya, A. Singh, S. Gul, J. Yano, Y. Ye, E. J. Crumlin, M. H. Richter, J. K. Cooper, H. S. Stein, J. A. Haber, K. A. Persson, J. M. Gregoire, *ACS Catal.* **2018**, *8*, 10938.

[84] J. S. Mondschein, J. F. Callejas, C. G. Read, J. Y. C. Chen, C. F. Holder, C. K. Badding, R. E. Schaak, *Chem. Mater.* **2017**, *29*, 950.

[85] "The Materials Project," can be found under https://materialsproject.org/, **n.d.**

[86] Y. Zhu, J. Wang, T. Koketsu, M. Kroschel, J. M. Chen, S. Y. Hsu, G. Henkelman, Z. Hu, P. Strasser, J. Ma, *Nat. Commun.* **2022**, *13*, 1.

[87] D. Gorylewski, F. Zasada, G. Słowik, M. Lofek, G. Grzybek, K. Tyszczuk-Rotko, A. Kotarba, P. Stelmachowski, *ACS Catal.* **2025**, *15*, 4746.

[88] R. T. M. van Limpt, C. A. A. van Helvoirt, M. Creatore, M. A. Verheijen, *Nanoscale* **2025**, *17*, 11037.

[89] X. Zhang, H. Xu, Q. Shi, W. Sun, X. Han, D. Jiang, Y. Cao, D. He, X. Cui, *J. Colloid Interface Sci.* **2024**, *670*, 142.

[90] T. Tran-Phu, Z. Fusco, I. Di Bernardo, J. Lipton-Duffin, C. Y. Toe, R. Daiyan, T. Gengenbach, C.-H. Lin, R. Bo, H. T. Nguyen, G. M. J. Barca, T. Wu, H. Chen, R. Amal, A. Tricoli, *Chem. Mater.* **2021**, *33*, 3553.

[91] P. E. Blöchl, *Phys. Rev. B* **1994**, *50*, 17953.

[92] G. Kresse, D. Joubert, *Phys. Rev. B* **1999**, *59*, 1758.

[93] G. Kresse, J. Furthmüller, *Phys. Rev. B* **1996**, *54*, 11169.

[94] G. Kresse, J. Furthmüller, *Comput. Mater. Sci.* **1996**, *6*, 15.

[95] J. P. Perdew, K. Burke, M. Ernzerhof, *Phys. Rev. Lett.* **1996**, *77*, 3865.

Chapter 5. Environmental-friendly and earth-abundant self-healing electrocatalyst systems for durable and efficient acidic water splitting

This chapter is the follow-up research from the literature review in Chapter 2 and acidic stable oxygen evolution catalysts (OECs) based on passivation layers in Chapter 4. The study in this chapter concentrates on another stabilization strategy, constructing the acidic stable matrix from non-noble-based self-healing materials. Herein, we develop the earth-abundant OECs by constructing the stable matrix of bismuth oxide based on its self-healing behavior and integrating with the active elements, which play the role of catalytic component. It is expected to achieve stable self-healing electrocatalyst systems, which can demonstrate sustainable long-term operation for efficient acidic water splitting.

This chapter was reprinted from the publication below. Ta, X. M. C., Trần-Phú, T., Nguyen, T. K. A., Wang, Q., Tricoli, A., Environmental-friendly and earth-abundant self-healing electrocatalyst systems for durable and efficient acidic water splitting. *ACS Applied Materials & Interfaces* **2025** *17* (17), 25327-25336 DOI: 10.1021/acsami.5c01637. Reprinted with permission.

Authorship Attribution Statement

Xuan Minh Chau Ta is the principal author of this publication, which forms part of her thesis submitted for the examination for the Doctor of Philosophy degree. The corresponding author below provided the consent for inclusion of a part or whole of the following publication in this thesis and accept the following candidate statement of contribution for this publication.

Candidate contribution:

This manuscript studied about the self-healing electrocatalysts for the stable acidic water electrolysis. The manuscript was written, formatted, reviewed, and edited by Xuan Minh Chau Ta. This author was a main contributor, who was in charge designed and performed in all the experiments and data analysis.

Corresponding author

Prof Dr Antonio Tricoli

Abstract

Electrochemical water splitting in acidic conditions is an efficient route for green hydrogen production from renewable electricity. Its implementation on a globally relevant scale is hindered by the lack of abundant and low-cost electrocatalysts for the oxygen evolution reaction that can operate stably and efficiently at highly acidic anodic conditions. Here, we report on the design of stable and efficient acidic OER electrocatalysts consisting of a self-healing bismuth (Bi)-based matrix hosting transition metal active site. Comprehensive structural-performance investigation of Co- and Ni-BiO_x electrodes provides insights into the role of the electrolyte composition and pH in the self-healing mechanism under anodic conditions. Our best performing [Co-Bi]O_x and [Ni-Bi]O_x anodes achieve over 200 hours of continuous electrolysis at a catalytic current of 10 mA cm^{-2} with an overpotential of 570 and 670 mV at a pH of 1 in a 0.1 M H_2SO_4 electrolyte. Our finding provides a promising strategy for the engineering of earth-abundant materials for efficient acidic water splitting, as an alternative to the use of poorly scalable and affordable noble metal catalysts.

Keywords: acidic electrolysis, electrocatalysts, earth-abundant, stability, self-healing.

5.1. Introduction

Water electrolysis stands as one of the most effective routes for the carbon-free production of hydrogen (H_2), offering a promising solution for the storage and transportation of renewable energy.[1–3] Proton-exchange-membrane water electrolysis (PEMWE) is amongst the most mature technologies for industrial H_2 production, offering high current density and efficiency.[4,5] However, designing catalysts for the anodic oxygen evolution reaction (OER) of the water splitting system is demanding, due to the requirement of four-electron transfers with an associated large kinetic barrier.[6] Furthermore, the large oxidation potential at the highly acidic conditions of PEMWE requires high material resistance to corrosion.[7–9] Current oxygen evolution electrocatalysts employed in industrial-scale PEMWE are based on noble metals, including iridium (Ir) and ruthenium (Ru).[7,10–12] Notwithstanding their remarkable catalytic activity, these materials still provide insufficient corrosion resistance at the highly acidic OER conditions. Furthermore, their high cost and scarcity negatively impact the economic feasibility and scalability of PEMWE.[5,13–16] The design of alternative non-noble metal OER electrocatalysts, which can display comparative activity to rare-earth metals under industry-relevant conditions, is the focus of broad research efforts.

To date, most extensively studied earth-abundant electrocatalysts are based on first-row transition elements, such as cobalt (Co), iron (Fe), manganese (Mn), nickel (Ni), in view of their relatively high OER activity.[17–20] Nevertheless, the application of these catalysts to PEMWE is limited by their low stability in acidic anodic conditions. One prominent approach to enhance the stability of non-noble metal OER electrocatalysts is incorporating the active sites into metal oxide lattices to modulate the electronic configuration and suppress dissolution kinetics.[18,21–24] Li et al. reported a $CoMn_2O_4$ spinel oxide OER catalyst that exhibited substantial stability, surpassing 1500 h at 200 mA cm^{-2} and a pH of 1.[25] Another strategy is to physically shield the electrocatalyst surface from direct contact with the electrolyte using acidic stable nano-thin coatings, such as TiO_2, Al_2O_3, SiO_2, SnO_2, HfO_2, and carbon-based layers.[26–28] We reported that a 4.4 nm amorphous TiO_2 layer extended the lifetime of bare Co_3O_4 anodes by over threefold from 25 to 75 h at 10 mA cm^{-2} and near-zero pH.[27] While promising, both strategies require multi-step, laborious catalyst preparation processes or high amount of catalyst loading, but they have not been able to completely inhibit the corrosion of materials during long-term acidic OER.

As an alternative to inhibiting the corrosion process, the exploration of self-healing electrocatalysts has gained increased interest as a potential route for long-lasting acidic OER materials.[29] This

strategy relies on the attainment of a quasi-equilibrium state between the solid and dissolved species of a catalyst in the electrolyte, where the loss of catalyst due to corrosion occurs at the same or slower rate than its re-electrodeposition.[29] Pioneering studies have been focusing on self-healing lead (Pb) and cobalt (Co) compounds, where Pb served as a structuring component offering a thermodynamically stable PbO_2 matrix, and Co acted as the catalytically active site with a dominant role on the OER activity.[30] Following studies attempted to combine the $CoPbO_x$ system with iron (Fe) to construct self-healing [Co-Fe-Pb]O_x mixed oxides.[31–33] The [Co-Fe-Pb]O_x OER electrocatalyst demonstrated stable current density at 10 mA cm^{-2} with an overpotential 0.56 V over one-week continuous operation at a pH of 1.[31] However, high concentrations of metal cations in the electrolyte causes detrimental effects on the commercial proton-exchange-membrane of PEMWE as well as poisoning the cathodic catalysts.[34,35] Moreover, PbO_x is highly toxic to both human and wildlife, bringing upon some challenges in its fabrication and use.

Recently, self-healing BiO_x was proposed as an environmentally friendly acidic stable host for OER electrocatalysts.[36–38] Thorarinsdottir et al. demonstrated the use of BiO_x catalyst for continuous OER operation for 110 h in a highly acidic electrolyte (pH 1 – 2.25).[36] However, BiO_x required a high potential required of over 2 V *vs.* RHE to drive a small current density of 1 – 5 mA cm^{-2}. Simondson et al. used BiO_x oxide as an acidic stable matrix and integrated Ag, as the catalytically active element [Ag-Bi]O_x.[38] The [Ag-Bi]O_x demonstrated an OER current of 100 mA cm^{-2} at an overpotential of 0.7 V *vs.* RHE over two weeks operation at pH 0.3. Nevertheless, the reliance on Ag makes it less economically attractive.

Here, we present a detailed investigation of the structural stability and activity of self-healing oxide-based earth-abundant compounds for acidic OER, identifying compositions that provide superior short and long-term performance. A survey of the electrochemical performance of seven promising non-noble metal electrocatalysts reveals two promising transition metals, namely cobalt and nickel, as highly OER active components and bismuth oxide as acidic stable matrix. Investigation and optimization of the self-healing mechanism of nanostructured [Co-Bi]O_x and [Ni-Bi]O_x anodes in a subset of representative electrolytes leads to the identification of ultra-stable and active compounds maintain a current of 10 mA cm^{-2} at an overpotential of 0.57 V for 200 h for [Ni-Bi]O_x at pH near zero. Measurement of the post-electrolysis catalysts provides insights into the potential impacts of the electrolyte's conditions on their self-healing mechanism in the acidic water oxidation reaction. Overall, these insights offer design principles to prepare and operate scalable, stable, and

efficient electrocatalyst systems for acidic water splitting using earth-abundant and environmentally friendly materials.

5.2. Results and discussion

5.2.1. A survey of single metal oxides

We conducted a survey of the OER activity and stability of seven promising earth-abundant metal oxides consisting of single Co, Ni, Cr, Fe, Mo, Mn, and Bi cations, for acidic water splitting. All metal oxide anodes were prepared by sputtering metal layers with an iso-thickness of 100 nm onto fluorine-doped SnO_2 (FTO) substrates followed by annealing at 450 ºC in 1 h. Characterisation of the as-prepared materials was conducted by X-ray diffraction (XRD) and X-ray photoelectron spectroscopy (XPS) analyses confirming their composition and phases (**Figure 5.1** and **Figure 5.2**). The XRD patterns (**Figure 5.1**) reveal the crystal structure of Co_3O_4, NiO, Cr_2O_3, Mn_2O_3, Fe_2O_3, MoO_3 and Bi_2O_3, with their oxidation states confirmed by high-resolution XPS spectra (**Figure 5.2**).

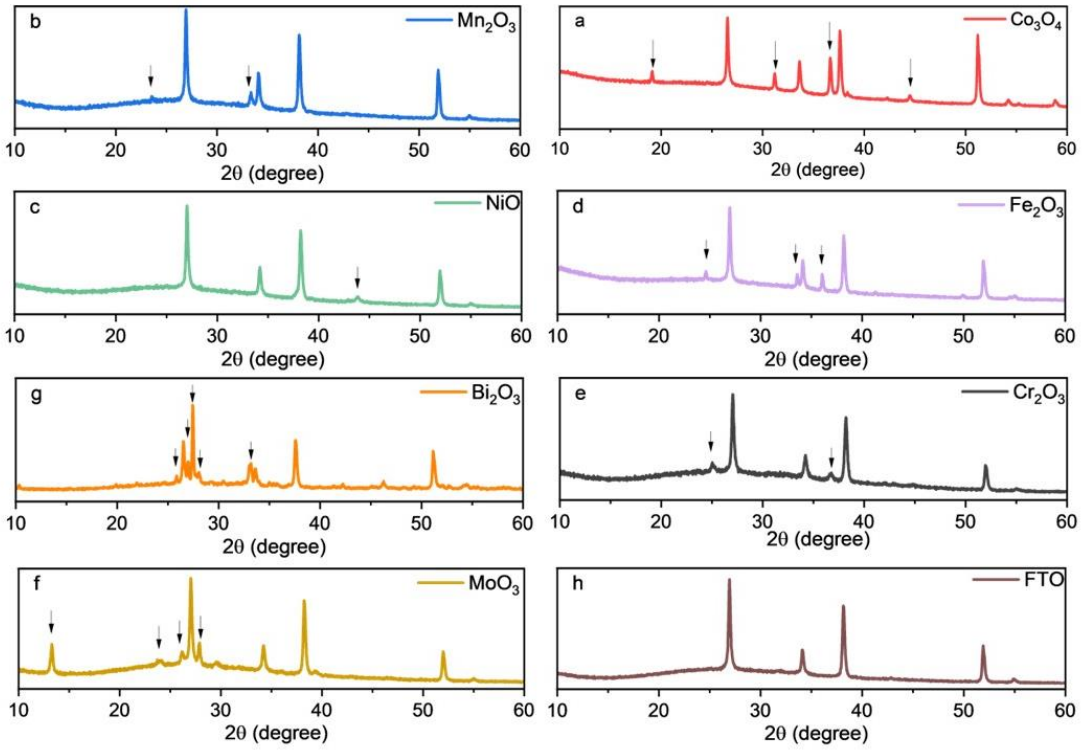

Figure 5.1 X-ray diffraction pattern of single metal oxides a) Co_3O_4, b) Mn_2O_3, c) NiO, d) Fe_2O_3, e) Cr_2O_3, f) MoO_3, g) Bi_2O_3, and h) F-doped SnO_2 (FTO) substrate (↓ denotes the diffraction peaks of each metal oxides. They reflected the diffraction peaks at a) 19 º, 31.3 º, 36.8 º, and 44.8 º belonging to the cubic phase of Co_3O_4 (PDF#43-1003), b) 23.3 º and 33 º from the cubic phase of

Mn_2O_3 (PDF#24-0508), c) 43.3 º of the hexagonal phase NiO (PDF#44-1159), d) 24.2 º, 33.2 º, and 35.7 º of the hexagonal phase Fe_2O_3 (PDF#33-0664), e) 25 º and 36.2 º of the hexagonal phase Cr_2O_3 (PDF#38-1479), f) peaks at 13 º, 23.6 º, 24.1 º, 26.2 º, and 27.9 º of monoclinic phase MoO_3 (PDF#47-1320), g) peaks at 25.8 º, 26.9 º, 27.4 º, 28 º, and 33.3 º of the tetragonal β-phase of Bi_2O_3 (PDF# 78-1793), and h) peaks at 27.6 º, 34 º, 38 º, and 51.8 º belonging SnO_2 in FTO substrate (PDF#41-1445).

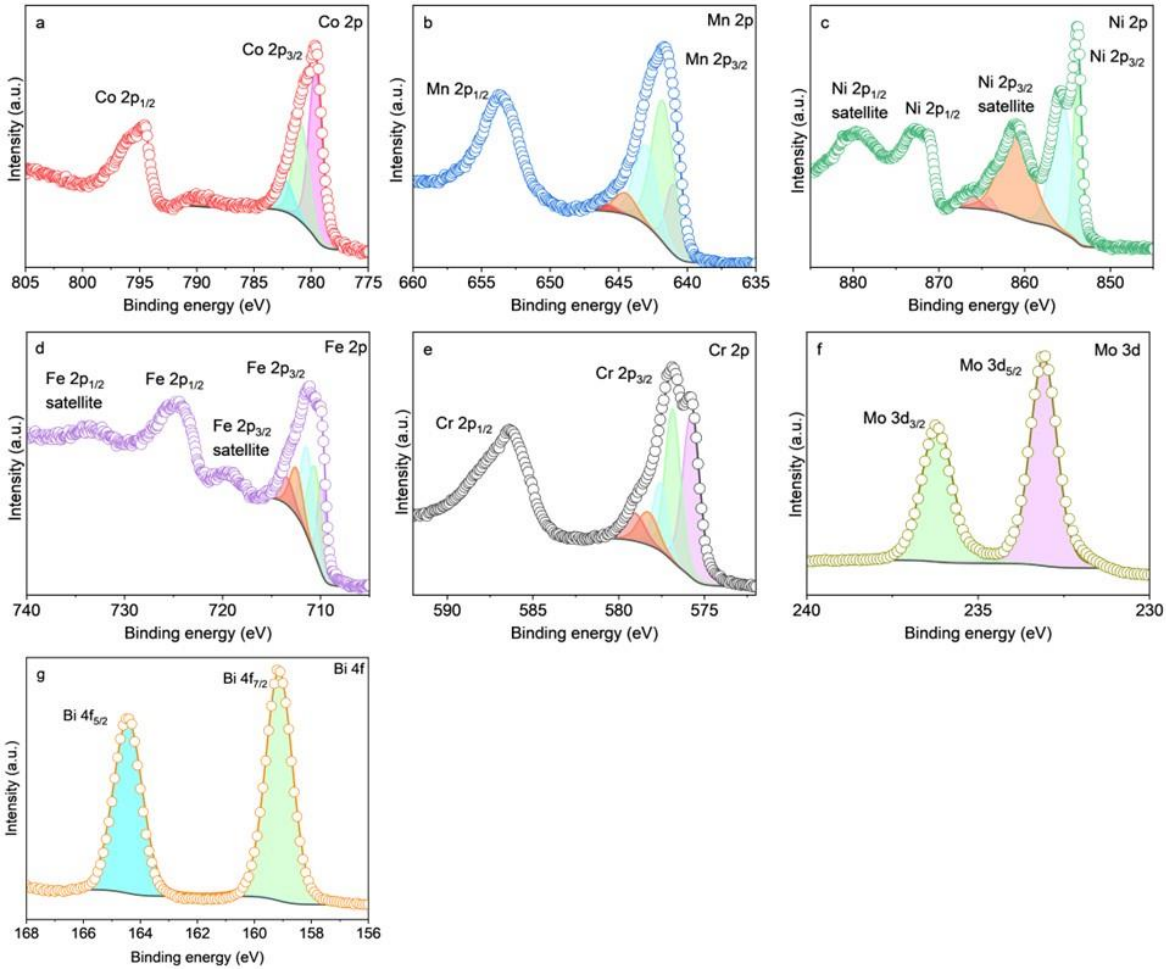

Figure 5.2 High resolution XP spectra of a) Co 2p in Co_3O_4,[39] b) Mn 2p in Mn_2O_3,[39] c) Ni 2p in NiO,[39] d) Fe 2p in Fe_2O_3, [39] e) Cr 2p in Cr_2O_3,[39] f) Mo 3d in MoO_3,[40] g) Bi 4f in Bi_2O_3.[36]

First, the acidic OER electrocatalytic activity of these single metal oxides was investigated in a 0.1 M H_2SO_4 electrolyte at pH 1 (**Figure 5.3**). Forward linear sweep voltammetry (LSV) curves (**Figure 5.3a**) show three metal oxides, Co_3O_4, NiO, and Mn_2O_3, having a notably higher OER catalytic activity than the others. Amongst them, Co_3O_4 demonstrated the highest OER activity, followed by NiO and Mn_2O_3. Their onset potential values at 10 mA cm^{-2} were determined to be 1.68, 1.72, and 1.79 V *vs*. RHE for Co_3O_4, Mn_2O_3, and NiO, respectively (**Figure 5.3b**).

Conversely, the electrocatalytic activities of Fe_2O_3, Cr_2O_3, MoO_3, and Bi_2O_3 were found to be significantly lower. This observation was corroborated by short-term chronopotentiometric (CP) curves at various current densities ranging from 1 to 20 mA cm^{-2} (**Figure 5.3c – d**). To achieve a current density of 10 mA cm^{-2}, the Co_3O_4, NiO, and Mn_2O_3 anodes required a potential of 1.98, 2.08, and 2.18 V *vs.* RHE, respectively. In contrast, Fe_2O_3, Cr_2O_3, MoO_3, and Bi_2O_3 necessitated overpotentials exceeding 2.5 V *vs.* RHE for the same current density.

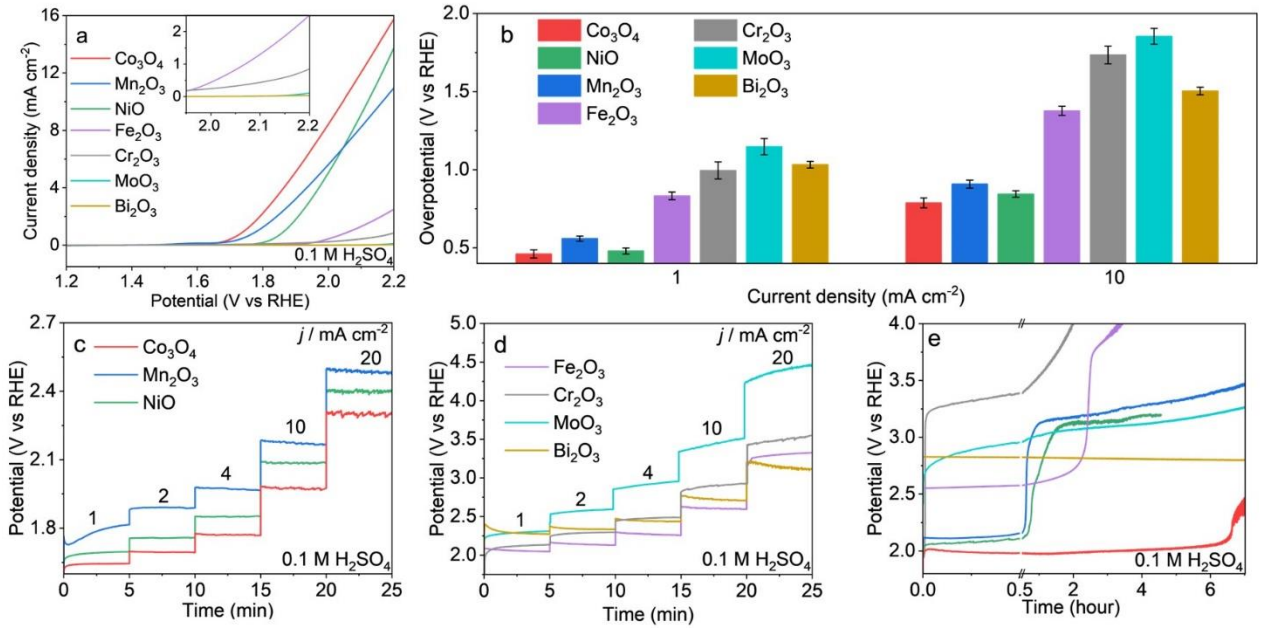

Figure 5.3 Electrochemical characterisation of single metal oxide anodes in a 0.1 M H_2SO_4 electrolyte. a) Forward linear sweep voltammetry (LSV) curves (3rd scan, scan rate 0.005 V s^{-1}), b) comparison of the potential required to achieve 1 and 10 mA cm^{-2}, c–d) chronopotentiograms at varied current densities, ranging from 1 to 20 mA cm^{-2}, and e) chronopotentiograms for stability test recorded at 10 mA cm^{-2} of Co_3O_4 (red), Mn_2O_3 (blue), NiO (green), Fe_2O_3 (pink), Cr_2O_3 (dark gray), MoO_3 (purple), and Bi_2O_3 (dark yellow).

The stability of these anodes was initially investigated by their CP curves during OER at 10 mA cm^{-2} for 7 h in a 0.1 M H_2SO_4 electrolyte (**Figure 5.3e**). The three most active transition metal oxides all revealed poor stability, with Co_3O_4 being the most stable with a constant overpotential for less than 6 h. In comparison, the NiO and Mn_2O_3 anodes reveal a rapid rise in required overpotential in less than 1 h of OER. The other less OER active transition metals lost their performance within 2 h. Overall, Bi_2O_3 was the most stable anode showing constant overpotential for over 7 h. Despite not being an active material with a considerably higher overpotential to reach 10 mA cm^{-2} (2.7 V *vs.* RHE), Bi_2O_3 demonstrated remarkable stability at various pH for over 25-h

OER galvanostatic tests (**Figure 5.4**). This is attributed to its self-healing mechanism previously reported by Thorarinsdottir et al.[36] It revealed the dissolved Bi(III) species can be oxidised to ion species with higher oxidation state ($Bi^{>3+}$) and electrodeposited onto the anode during OER, forming a thermodynamically stable phase of BiO_x, according to the Pourbaix diagram (**Figure 5.4**).

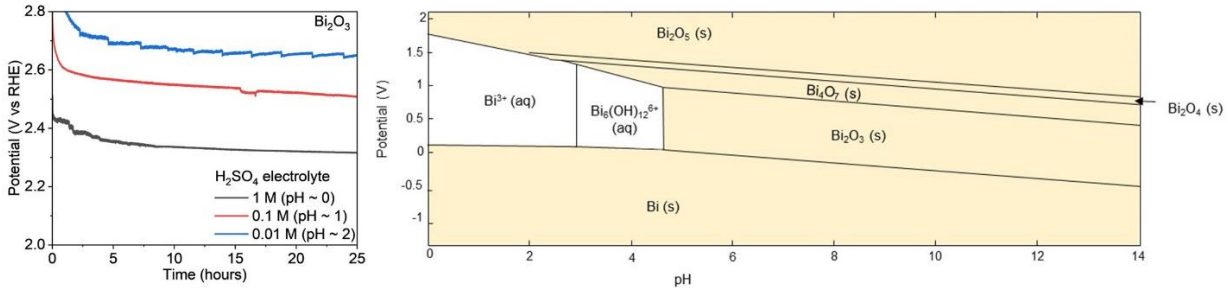

Figure 5.4 a) Galvanostatic test of Bi_2O_3 in 25 hours at 10 mA cm^{-2} in different H_2SO_4 electrolytes and b) Pourbaix diagram of bismuth extracted the Material Project database.[41]

5.2.2. Design of [M-Bi]O_x self-healing catalyst systems

The most OER active Co and Ni transition metals, identified above, were further investigated as active catalytic sites in a self-healing bismuth oxide matrix by co-sputtering of Bi to form [M-Bi]O_x matrixes (M is either Co or Ni). SEM images of the [M-Bi]O_x anodes reveal a relatively dense and uniform layer of particles, in line with the morphology expected by sputtering.[26] The surface chemical composition of the as-prepared [M-Bi]O_x was analysed by XRD and XPS (**Figure 5.5**). The XRD patterns reveal the presence of the cubic phase of Co_3O_4 (PDF#43-1003) and the hexagonal phase of NiO (PDF#44-1159) in the [Co-Bi]O_x and [Ni-Bi]O_x anodes, respectively, in addition to the tetragonal phase of Bi_2O_3 (PDF#78-1793). Overall, the diffraction peaks of these as-prepared [Co-Bi]O_x and [Ni-Bi]O_x anodes are quite similar to those of the corresponding single metal oxides (**Figure 5.1**), indicating a partially segregated structure.

The near-surface chemistry of the [M-Bi]O_x anodes was analyzed by X-ray photoelectron spectroscopy (XPS). It should be noted that the transition metal components (Co, Ni) of the compound structures have a similar chemical oxidation state to that of the corresponding single oxides (**Figure 5.2**), further confirming the formation of segregated metal oxide and Bi_2O_3 domains. The survey XPS spectra revealed the ratio between Bi and the active elements (Co/Ni) at *ca* 0.5. In the [Co-Bi]O_x anode, the Co 2p core-level photoemission shows the prominent peaks at ~780 and 795 eV of Co $2p_{3/2}$ and Co $2p_{1/2}$, respectively, which are deconvoluted as suggested by Biesinger et al..[27,39,42] In the [Ni-Bi]O_x anode, the Ni 2p high-resolution spectrum shows two prominent

multiple-split peaks at ~854.2 and 871.5 eV, assigned to Ni $2p_{3/2}$ and Ni $2p_{1/2}$, respectively, and two broad peaks at ~861 and 880 eV, corresponding to the satellite peaks of Ni $2p_{3/2}$ and Ni $2p_{1/2}$, respectively. The Ni $2p_{3/2}$ can be deconvoluted into five components as suggested in Biesinger et al.[39] In both anodes, the Bi components show the two main peaks of Bi $4f_{5/2}$ and Bi $4f_{7/2}$ at ~159.2 and 164.5 eV, respectively, attributed to Bi^{3+}.[36]

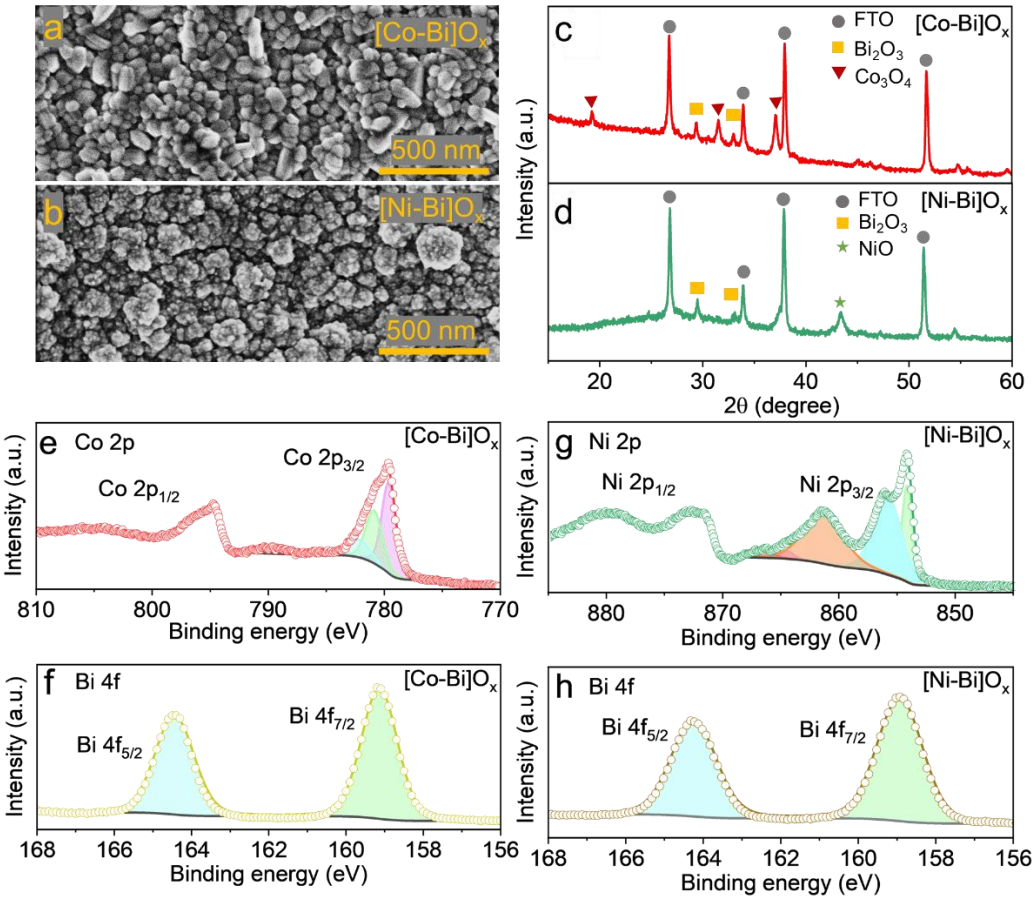

Figure 5.5 Structural characterisation of the as-prepared self-healing metal oxide compounds. a–b) Top-view SEM images, c–d) X-ray diffraction patterns, and e–h) XPS spectra of e) Co 2p, f, h) Bi 4f, and g) Ni 2p from a, c, e, f) $[Co\text{-}Bi]O_x$ and b, d, g, h) $[Ni\text{-}Bi]O_x$ anodes.

5.2.3. Electrochemical performance of the self-healing compounds

To gain insights into the self-healing mechanism, we investigated the effect of the pH on the electrochemical behavior of $[Co\text{-}Bi]O_x$ and $[Ni\text{-}Bi]O_x$ anodes. Electrochemical impedance spectroscopy (EIS) was first undertaken to study the ionic and electronic conductivity as well as charge transfer resistance of the catalyst layers (**Figure 5.6 & Table 5.1**). The results show that the charge transfer resistance decreases with increasing H_2SO_4 concentration from 0.01 to 1 M.

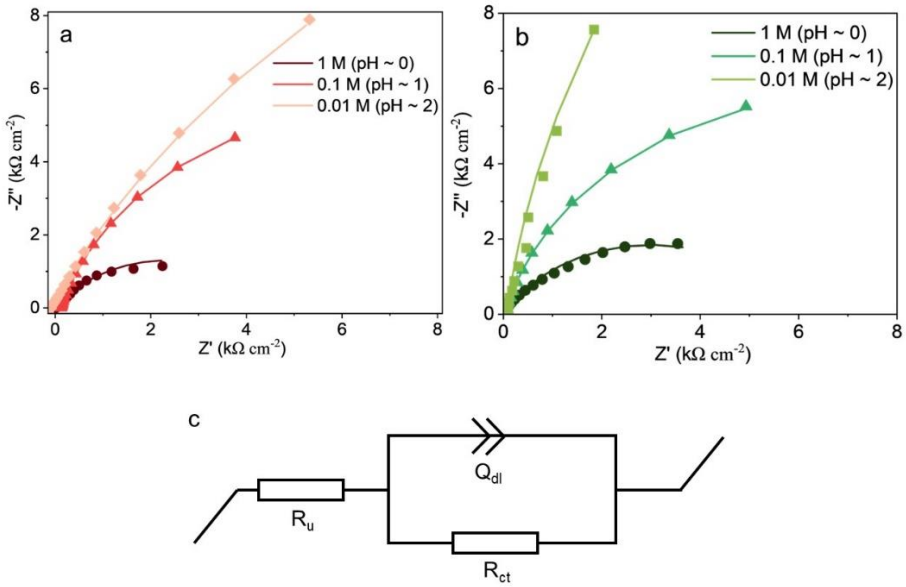

Figure 5.6 Nyquist plots of the electrochemical impedance spectroscopy (EIS) data collected at 0.3 V *vs.* RHE of a) [Co-Bi]O_x/FTO and b) [Ni-Bi]O_x/FTO (colored dots: raw EIS data; solid colored line: simulation curves after fitting with a Randle circuit.), and c) graph illustrating the Randle circuit used for EIS fitting where R_u, Q_{dl}, R_{ct} are the series resistance, the double-layer capacitance, and charge transfer resistance, respectively.

Table 5.1 Summary of electrochemical impedance spectroscopy fitting for [M-Bi]O_x anodes at 0.3 V vs. RHE in 0.1 M H_2SO_4 electrolyte.

Electrolyte	**1 M H_2SO_4**	**0.1 M H_2SO_4**	**0.01 M H_2SO_4**
		[Co-Bi]O_x	
R_u (Ω)	18.26	27.5	87.0
R_{ct} (Ω)	4658	14253	63486
Q_{dl} (F cm^{-2} $s^{\alpha-1}$)	0.315×10^{-3}	0.207×10^{-3}	0.160×10^{-3}
α_{dl}	0.649	0.684	0.705
		[Ni-Bi]O_x	
R_u (Ω)	16.2	27.7	80.0
R_{ct} (Ω)	5976	14672	75544
Q_{dl} (F cm^{-2} $s^{\alpha-1}$)	0.425×10^{-3}	0.282×10^{-3}	0.069×10^{-3}
α_{dl}	0.707	0.860	0.912

The electrochemical performance of the [Co-Bi]O_x and [Ni-Bi]O_x anodes was then investigated as a function of the H_2SO_4 concentration. **(Figure 5.7a−b)** show the linear sweep voltammetry (LSV) curves of the anodes in a 1 M, 0.1 M, and 0.01 M H_2SO_4 electrolyte with a corresponding pH of 0, 1, and 2, respectively. Notably, both anodes reveal a comparable performance to the single oxide counterparts at a pH of 1 (**Figure 5.3**). This reveals that it is possible to add up to ca 30 % of Bi

without negatively affecting the anode OER activity. Decreasing the electrolyte pH from 1 to 0 enhanced the initial OER performance, in which the potential required to reach a current of 10 mA cm^{-2} reduced from 2.05 to 1.9 V and 2.1 to 2.05 V *vs*. RHE for the [Co-Bi]O_x (**Figure 5.7a**) and the [Ni-Bi]O_x anodes (**Figure 5.7b**), respectively. Instead, increasing the electrolyte pH to 2 reduced OER activity, as indicated by the increased potential (> 2.2 V *vs*. RHE) required to achieve 10 mA cm^{-2} for both anodes.

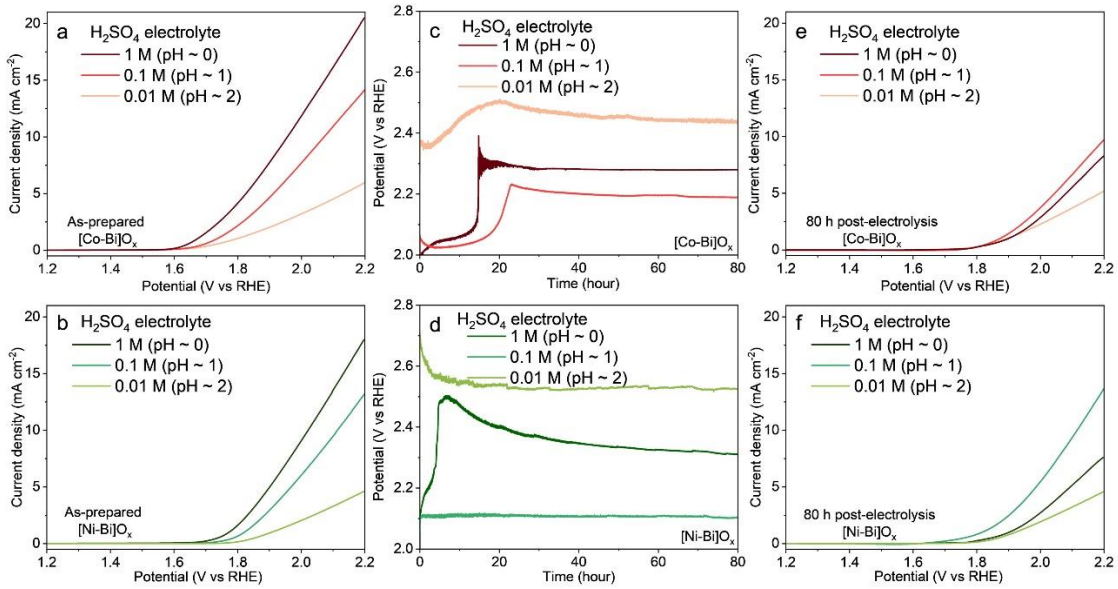

Figure 5.7 Influence of the electrolyte pH on the performance of the self-healing [Co-Bi]O_x and [Ni-Bi]O_x anodes. a−b) Forward linear sweep voltammetry (LSV) curves of as-prepared anodes, c−d) chronoamperometric (CP) curves reflecting the 80-h stability test recorded at 10 mA cm^{-2}, and e−f) LSV curves of post-electrolysis anodes. Forward LSV curves were recorded at 3rd scan, scan rate 0.005 V s^{-1}.

Investigation of the long-term stability of the [Co-Bi]O_x and [Ni-Bi]O_x anodes for 80 h OER CP test reveals distinct behaviors and activity trends (**Figure 5.7c−d**). At a constant current of 10 mA cm^{-2}, the [Co-Bi]O_x anodes reached a quasi-steady state potential of 2.28, 2.20, and 2.43 V *vs*. RHE at an electrolyte pH of 0, 1 and 2, respectively, after 20 – 30 h. Notably, the [Co-Bi]O_x anode potential at pH 2 started at 2.37 V *vs*. RHE and increased only slightly to 2.43 V *vs*. RHE. This was further confirmed by a comparison between the as-prepared and 80 h post-electrolysis samples, which showed the smallest reduction of the current density of ca 9% at 2 V *vs*. RHE at a pH of 2 (**Figure 5.8a**). The [Ni-Bi]O_x anodes reached a stable overpotential of 2.32 V *vs*. RHE after approximately 10 h of operation at 0 pH 1. This corresponds to a significant drop of performance, of *ca* 69 %, from the as-prepared anodes (**Figure 5.8b**). At a pH of 1 and 2, the [Ni-Bi]O_x anodes

display a stable overpotential of 2.1 and 2.54 V *vs*. RHE, respectively, throughout the 80h OER CP test (**Figure 5.7e**). These [Ni-Bi]O_x anodes experienced a minimal decrease in OER activity of 8 % and 5 % from the as-prepared samples at a pH of 1 and 2, respectively (**Figure 5.8b**). Although the reduction in anode performance for both the [Co-Bi]O_x and [Ni-Bi]O_x anodes was the smallest at a pH of 2, at this condition their OER activity was also the lowest. This behavior aligns with the post-electrolysis LSV curves of the anodes (**Figure 5.7e−f**), showing the electrocatalytic activity following the order of 1 > 0 > 2 pH.

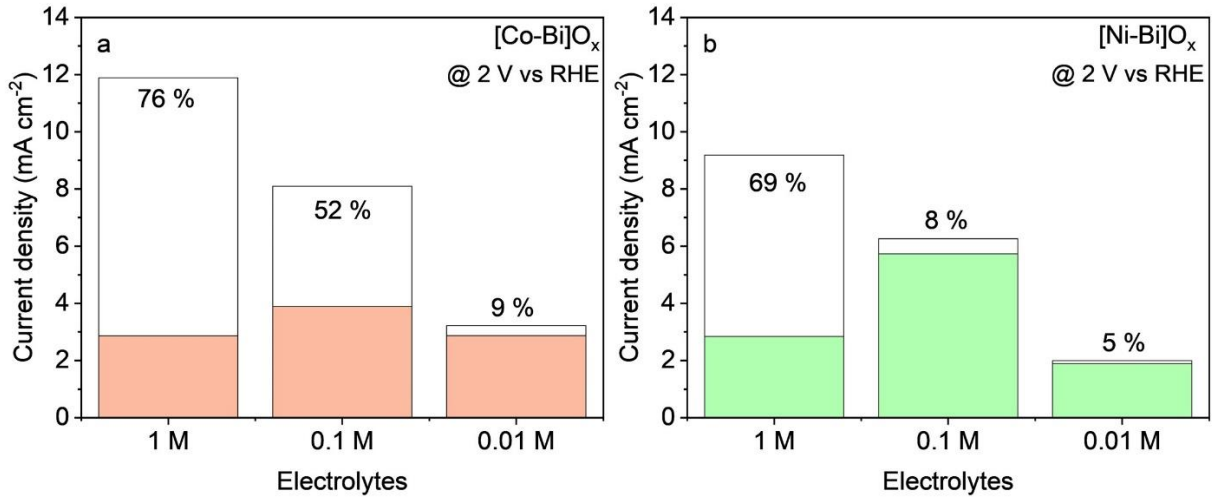

Figure 5.8 Comparison current density achieved at 2 V *vs.* RHE of as-prepared and post-electrolysis a) [Co-Bi]O_x and b) [Ni-Bi]O_x anodes in 1 M, 0.1 M, and 0.01 M H_2SO_4 electrolytes (filled bar: 80 h post-performance; unfilled bar: degraded performance).

The low performance of both [Co-Bi]O_x and [Ni-Bi]O_x anodes at a pH of 2 may potentially arise from the buffer concentration, which directly impacts the electrical conductivity and proton-coupled electron transfer (PCET) process.[29,43] In detail, a lower concentration of H_2SO_4 in the electrolyte results in less [H^+] and [SO_4^{2-}] ions, and thus lower electrical conductivity. To elucidate the impact of the buffer concentration of the anode performance, a potassium sulfate (K_2SO_4) buffer was added to the 0.01 M H_2SO_4 electrolyte (pH ~ 2), achieving a total concentration of electrolytes of 0.1 and 1 M (**Figure 5.9**). For the [Co-Bi]O_x anode, the increased buffer concentration led to a noteworthy improvement in the quasi-steady state potential. This is reflected by a *ca* 150 mV reduction in the potential required to reach 10 mA cm^{-2} after 60 h operation at 1 M and 0.1 M sulfate concentrations in comparison to that observed at a pH of 2 without the K_2SO_4 buffer. This overpotential drop is attributed to the enhanced electrolyte conductivity, as supported by the EIS analysis (**Figure 5.9** and **Table 5.2).** Also, for the [Ni-Bi]O_x anode, the addition of a 0.1 M sulfate electrolyte significantly enhances the electrocatalytic activity, resulting in a 200 mV reduction in the quasi-

steady state potential to reach 10 mA cm^{-2} at pH 2. However, when the sulfate concentration was increased to 1 M, the self-healing mechanism of the [Ni-Bi]O_x anode failed, as indicated by a complete loss of the OER performance in *ca* 60 h. Although the use of buffer supporting (K_2SO_4) in electrolyte could enhance the quasi-steady state performance of both [Co-Bi]O_x and [Ni-Bi]O_x anodes at a pH of 2, their overall performance is still lower than that achieved at a pH of 1, indicating that a 0.1 M H_2SO_4 electrolyte is the most optimal operation for these self-healing compounds.

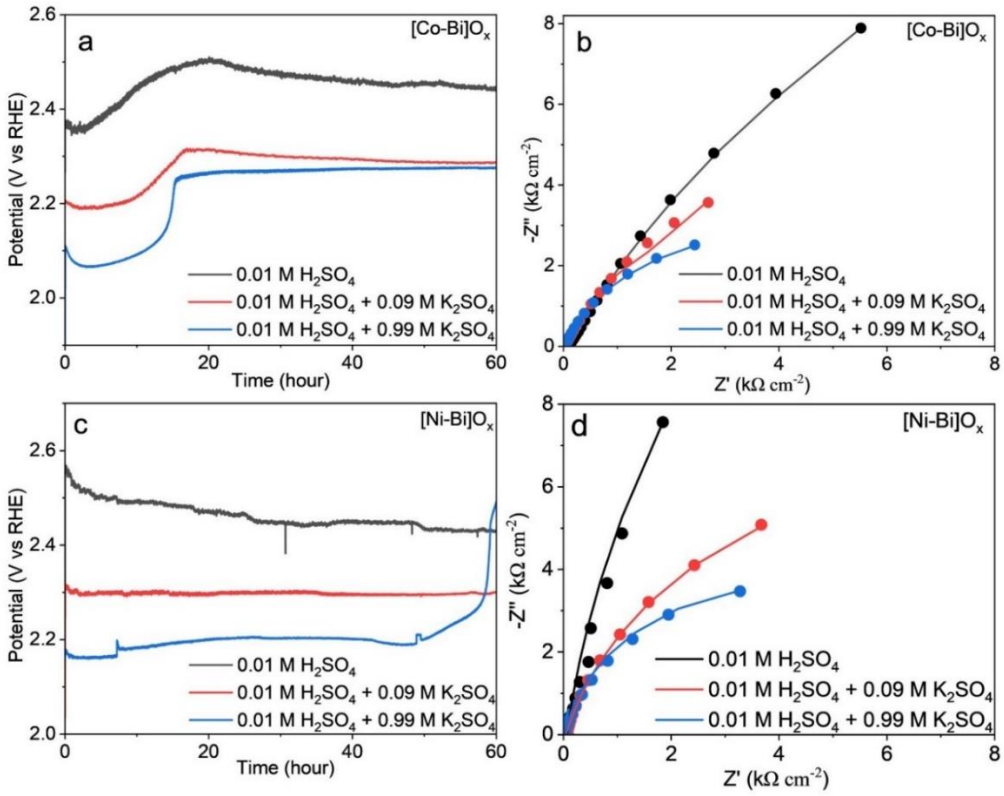

Figure 5.9 Galvanostatic stability test of a) [Co-Bi]O_x and b) [Ni-Bi]O_x in 0.01 M H_2SO_4 electrolyte with supporting buffer K_2SO_4.

Table 5.2 Summary of EIS fitting for [Co-Bi]O_x and [Ni-Bi]O_x anodes in 0.01 M H_2SO_4 electrolyte with supporting buffer K_2SO_4.

Electrolyte	**0.01 M H_2SO_4 + 0.99 M K_2SO_4**	**0.01 M H_2SO_4 + 0.09 M K_2SO_4**	**0.01 M H_2SO_4**
		[Co-Bi]O_x	
R_u (Ω)	30.5	32.29	87.0
R_{ct} (Ω)	7344	15564	63486
Q_{dl} (F cm^{-2} $s^{\alpha-1}$)	0.316×10^{-3}	0.294×10^{-3}	0.160×10^{-3}
α_{dl}	0.813	0.841	0.705

	[Ni-Bi]O_x		
R_u (Ω)	23.84	36.62	80.0
R_{ct} (Ω)	8387	15758	75544
Q_{dl} (F cm^{-2} $s^{\alpha-1}$)	0.257×10^{-3}	0.019×10^{-3}	0.069×10^{-3}
α_{dl}	0.847	0.854	0.912

To further optimize the [Co-Bi]O_x and [Ni-Bi]O_x anodes' composition by increasing the density of OER active sites, the ratio of Bi content versus the Co/Ni components varied from *ca.* 0.85 to 0. The performance was investigated by CP measurement at a pH of 1. However, reducing the Bi content from a Bi/Ni ratio of 0.5 to 0 did not result in a significant increase of the OER activity for both the as-prepared and post-electrolysis samples (**Figure 5.10**). For the [Co-Bi]O_x anodes, while decreasing the Bi content to a Bi/Co ratio of 0.25 slightly decreased the initial overpotential, the post-electrolysis performance was relatively similar (**Figure 5.10**).

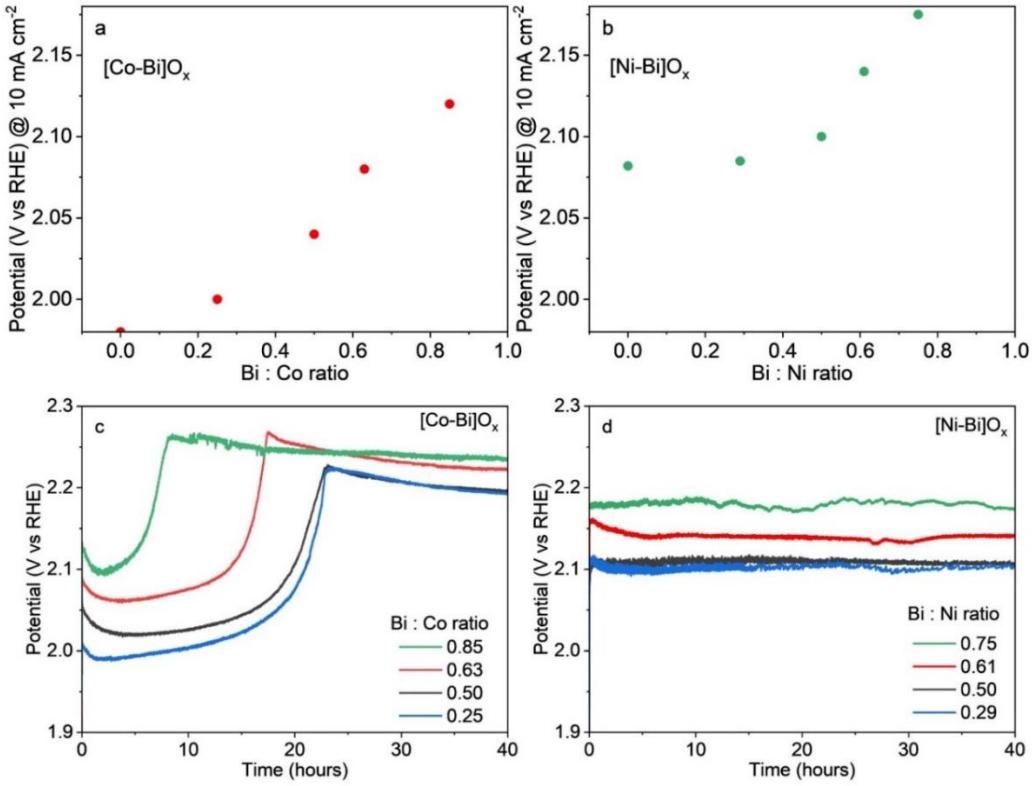

Figure 5.10 Comparison potential at 10 mA cm^{-2} of as-prepared a) [Co-Bi]O_x and b) [Ni-Bi]O_x anodes in 0.1 M H_2SO_4 electrolyte in the variation of Bi/M ratio; Galvanostatic stability test of c) [Co-Bi]O_x, and d) [Ni-Bi]O_x in 0.1 M H_2SO_4 in the variation of Bi/M ratio.

5.2.4. Evolution of the self-healing anodes structural properties

Structural characterisation was undertaken for the 80 h post-electrolysis [Co-Bi]O_x and [Ni-Bi]O_x anodes. SEM images (**Figure 5.11a-c** and **Figure 5.11f-h**) show some morphological changes

dependent on the electrolyte pH. After 80 h OER at a pH of 1 and 2, the formation of coarse particles uniformly distributed on FTO substrates was observed for both the [Co-Bi]O_x and [Ni-Bi]O_x anodes. The latter increase in particle size is attributed to the re-deposition of the catalyst during the self-healing process, leading to growth centered around the first nucleation points. In contrast, at a pH of 0 the post-electrolysis anodes show only the presence of small particles on the FTO substrates.

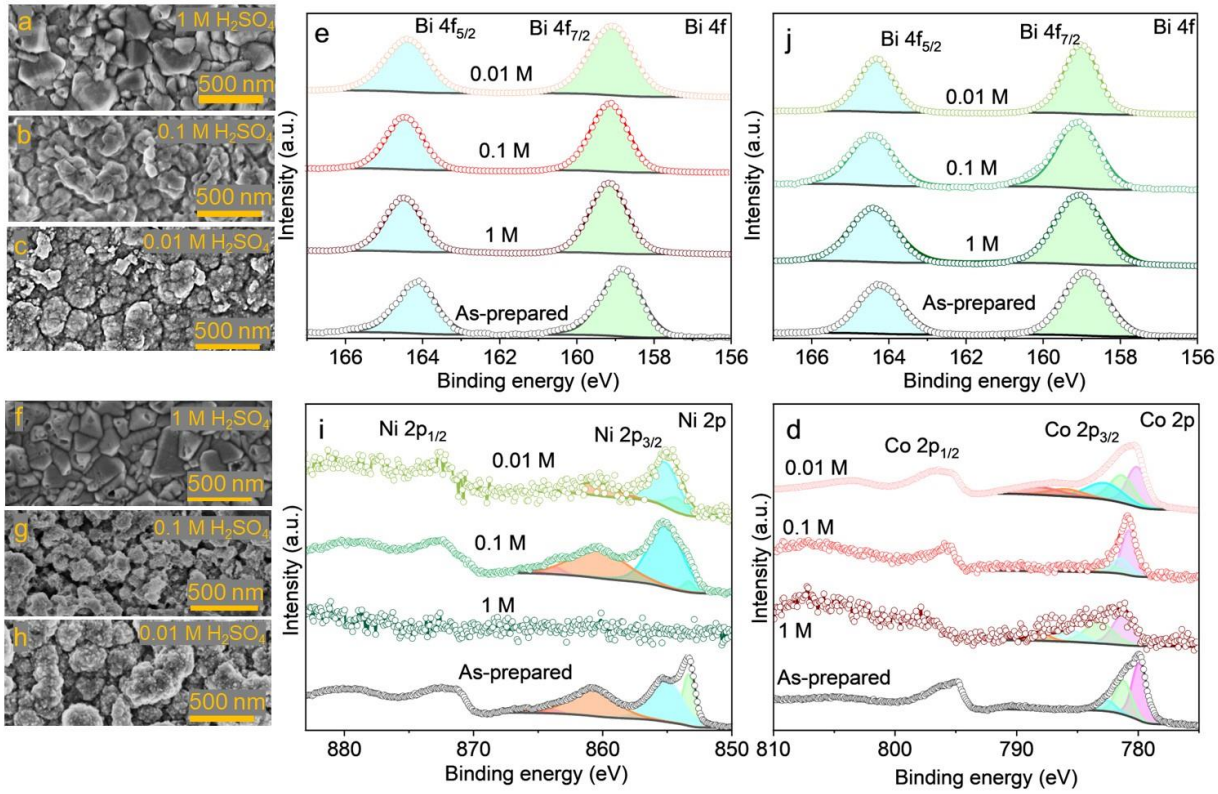

Figure 5.11 Quasi-steady-state composition of the anodes as a function of the pH. Top-view SEM images of a−c) [Co-Bi]O_x and d−f) [Ni-Bi]O_x anodes after 80 h of galvanostatic OER tests in a, d) 1 M H_2SO_4, b, e) 0.1 M H_2SO_4, and c, f) 0.01 M H_2SO_4 at 10 mA cm^{-2}. High-resolution X-ray photoelectron spectra of d) Co 2p and e) Bi 4f of [Co-Bi]O_x samples (red), i) Ni 2p and j) Bi 4f of [Ni-Bi]O_x anodes (green) before and after 80 h of galvanostatic OER tests.

The surface composition of the post-OER [Co-Bi]O_x and [Ni-Bi]O_x anodes was investigated by XPS analysis (**Figure 5.11**). The full-survey spectrum of the as-prepared [M-Bi]O_x anodes (**Figure 5.12**) revealed only the presence of the corresponding transition metals (Co or Ni), Bi, and O. After 80 h galvanostatic operation, the full-survey spectrum of all samples (**Figure 5.12**) revealed the similar surface composition of the anodes. However, while there was no noticeable variation in the shape of the high-resolution Co 2p, the peak intensity significantly decreased with decreasing electrolyte pH (**Figure 5.11d**). This is attributed to a reduction of the thermodynamically stable Co fraction in

highly acidic conditions. The atomic ratio of Co and Bi in the post-electrolysis anodes was 4:96, 13:87, and 58:42 at a pH of 0, 1 and 2, respectively. This indicates that the Co and Bi equilibrium concentration in the electrolyte depends highly on the pH. Also interesting, the higher density of active Co sites attained at a pH of 2 did not lead to the highest OER activity.

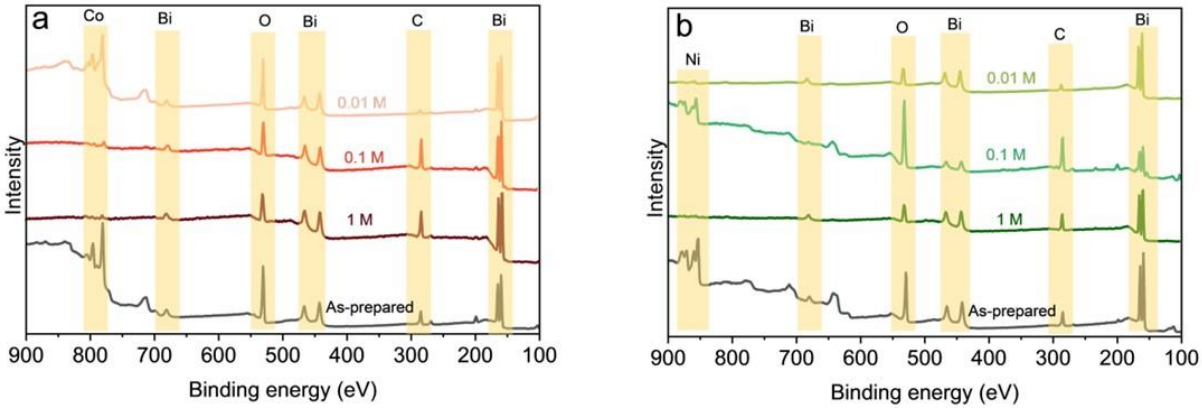

Figure 5.12 Full survey XP spectrum of as-prepared and 80-hour post-electrolysis a) [Co-Bi]O_x, and b) [Ni-Bi]O_x anodes.

In contrast the [Ni-Bi]O_x anodes revealed a change in the XPS peak shape of the post-electrolysis samples at a pH of 1 and 2 (**Figure 5.11i**). Notably, the component peak at 853.7 eV was lost, indicating the presence of only Ni(II) in the quasi-steady state anode. The signal of the Ni 2p in post-electrolysis samples at pH 2 is obviously decreased, indicating a drop of Ni in the quasi-steady state anodes from that of the as-prepared samples (Ni:Bi ratio ~ 66:34). At a pH of 1, the intensity of the Ni 2p spectra is relatively similar to the as-prepared sample, in line with the only minor reduction of Bi content. In specific, the Ni:Bi atomic ratio post-electrolysis was 0:100, 61:39, and 12:88 at a pH of 0, 1 and 2, respectively. These results show that extremely acidic conditions of pH near 0 of the 1 M H_2SO_4 electrolyte, have a too high Co and Ni atoms equilibrium to drive sufficient reincorporation of the Co and Ni active sites. This is in line with the lower OER performance of both anodes upon OER at 0 pH than at 1. Although, a pH of 2 resulted in a more stable anode composition, the low electrolyte charge carrier concentration limits the PCET process, resulting in the lowest catalytic activity. For the [Ni-Bi]O_x, a pH of 1 was the most suitable environment resulting in a quasi-steady-state activity throughout the 80 h OER test.

In terms of the Bi composition, the Bi 4f spectra (**Figure 5.11e, j**) of all post-electrolysis samples shows a similar shift of the two component peaks toward a higher binding energy level. This observation suggests an increased oxidation state of [Bi]O_x, in line with previous reports on self-healing [Bi]O_x-based compounds.[36,38] The significantly higher content of Bi in the post-

electrolysis samples reflected the stability of the BiO_x structure. The XRD patterns of the post-electrolysis samples (**Figure 5.13**) only show peaks of the Bi_2O_3 phase, with the exception of the $[Ni\text{-}Bi]O_x$ at a pH of 1 revealing an additional diffraction peak belonging to the NiO phase. These findings show that the Bi_2O_3 matrix can self-repair at sufficient rate at all pH, indicating a remarkable self-healing capability despite its low OER activity **(Figure 5.4)**. The advantage of the binary $[Co\text{-}Bi]O_x$ and $[Ni\text{-}Bi]O_x$ self-healing anodes over the pure BiO_x ones is their significantly higher OER activity. This is reflected by the significantly lower overpotential required to drive a 10 mA cm^{-2} current density over 80 h of OER.

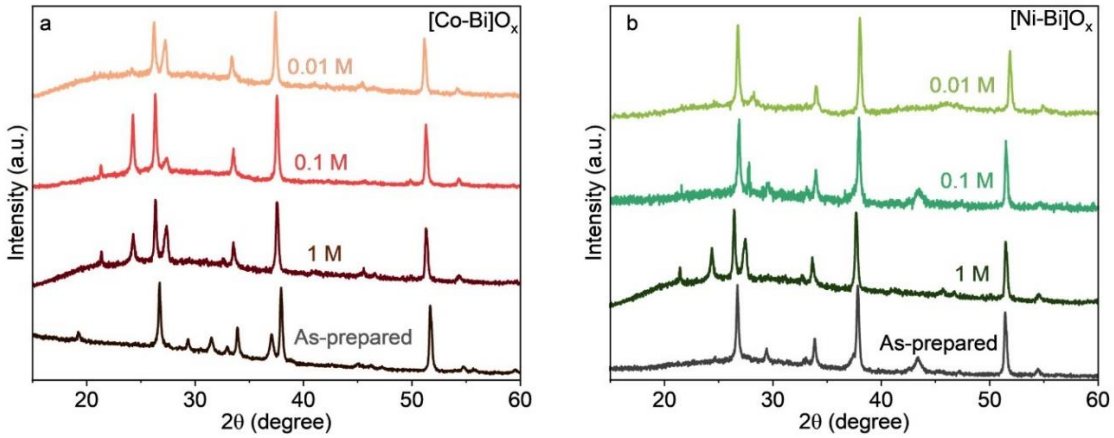

Figure 5.13 X-ray diffraction patterns of 80-h post-electrolysis a) $[Co\text{-}Bi]O_x$ and b) $[Ni\text{-}Bi]O_x$ anodes. They reflected the diffraction peaks at 21.6 º, 24.9 º, 30.7 º, and 33.2 º belonging to the monoclinic phase of Bi_2O_3 (PDF# 41-1449), and peak at 43.3 º of the hexagonal phase NiO (PDF#44-1159) of post-electrolysis samples in 0.1 M H_2SO_4 electrolyte.

5.2.5. Stable self-healing oxygen evolution at a pH of 1

The acidic OER performance of these $[Co\text{-}Bi]O_x$ and $[Ni\text{-}Bi]O_x$ anodes was investigated in detail at a pH of 1 (**Figure 5.14**), the optimal self-healing condition determined in the previous section. The short-term chronoamperometric (CP) indicated a higher OER activity of the as-prepared $[Co\text{-}Bi]O_x$ than that of the $[Ni\text{-}Bi]O_x$ anodes, with a required overpotential to reach 10 mA cm^{-2} of 2.05 and 2.1 V *vs.* RHE, respectively.

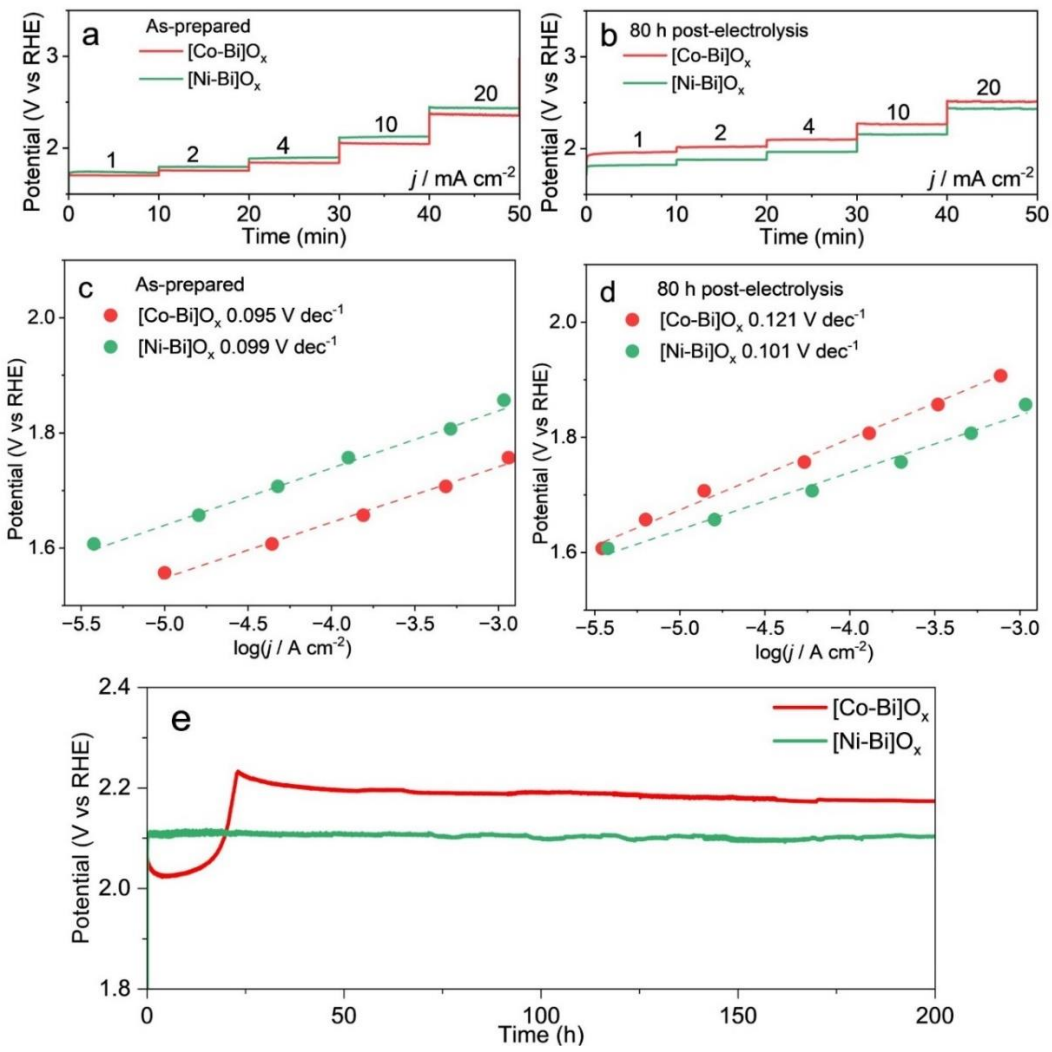

Figure 5.14 Electrochemical characterisation at a pH of 1 of the [Co-Bi]O_x (red) and [Ni-Bi]O_x (green) anodes. Tafel plots of a) as-prepared and b) post-electrolysis anodes; sweep chronopotentiograms at varied current densities 1 to 20 mA cm^{-2} of c) as-prepared and d) post-electrolysis of [M-Bi]O_x anodes; e) the 200-h stability test of mixed-metal oxides anodes recorded at 10 mA cm^{-2}.

The OER kinetics of the as-prepared anodes were evaluated by their Tafel slope, calculated through short-term chronoamperometric (CA) analysis (**Figure 5.15**). A Tafel slope of 0.095 and 0.099 V dec^{-1} was determined for the [Co-Bi]O_x and [Ni-Bi]O_x anodes, respectively. This indicates that the binary [Co-Bi]O_x has a slightly faster OER kinetic than the [Ni-Bi]O_x system. However, upon 80-h OER at a pH of 1 (0.1 M H_2SO_4 electrolyte), the CP curves revealed a considerable reduction in the performance of the [Co-Bi]O_x anode reaching a Tafel slope of 0.121 V dec^{-1}. In contrast, the [Ni-Bi]O_x anodes had a significantly better stability resulting in only a small increase of the Tafel slope to 0.101 V dec^{-1}.

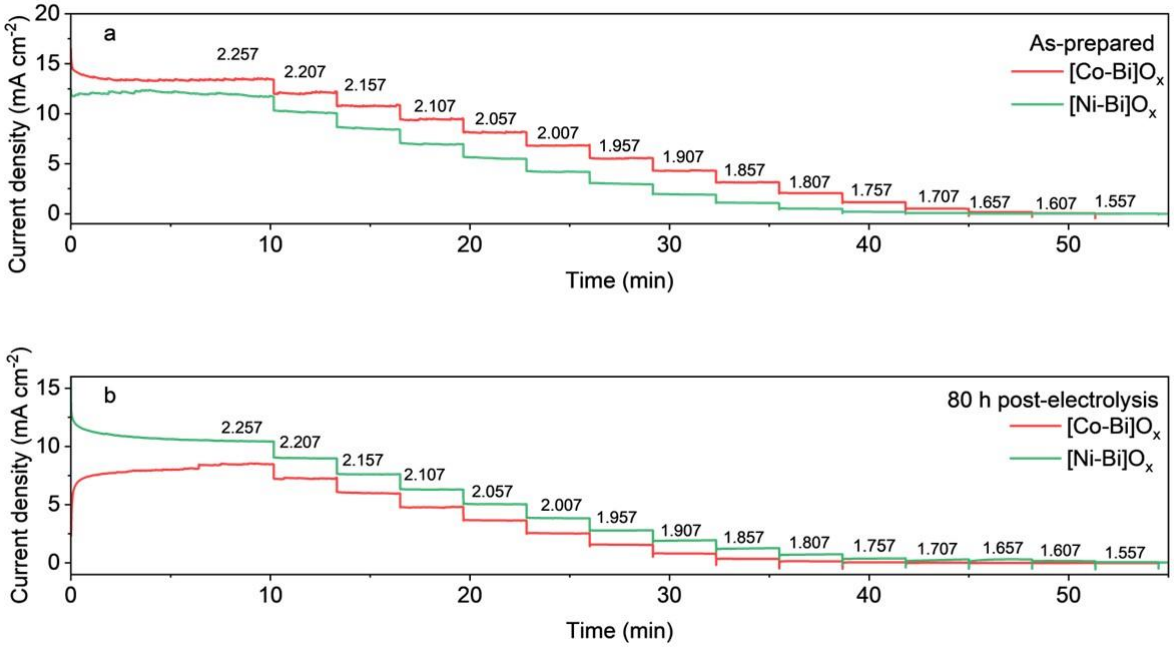

Figure 5.15 Sweep chronoamperometry at varied current potential of a) as-prepared and b) post-electrolysis [Co-Bi]O_x and [Ni-Bi]O_x anodes.

The stability of [Co-Bi]O_x and [Ni-Bi]O_x anodes was also studied by interrupting and restarting the OER via CV scans followed by CP in the 0.1 M H_2SO_4 electrolyte. In (**Figure 5.16)**, the developed anodes were tested by 140 continuous CV scans. For the first to the 30th scan, they showed a continuous and slight enhancement in performance during operation, which may suggest the *in situ* formation of more active surface of catalysts. However, the performance dropped down from the 30th to the 140th scan due to the instability of catalysts under the interruption of the OER reaction during the change of potential in the CV cycles. CP measurement was conducted after the 140-CV scan (**Figure 5.16**). Notably, the catalyst performance regenerated significantly within 2h and kept regenerating at a slower pace for up to ca 80 h. This further indicates a self-healing behaviour of the [Co-Bi]O_x and [Ni-Bi]O_x electrodes under OER operation. The post-electrolysis performance of the recovered catalysts was quite similar to that achieved in a continuous 80-h operation test (**Figure 5.7**), indicating that they reached their quasi-steady state after the regeneration process. In addition, on/off galvanostatic oxidation tests (**Figure 5.17**) highlighted the self-healing capacity of [Co-Bi]O_x and [Ni-Bi]O_x anodes by rapid recovery of the stable performance upon interruption. Specifically, they showed nearly immediate restoration of their catalytic activity as soon as a positive potential was applied after several hours of immersion in the acidic 0.1 M H_2SO_4 at open circuit conditions.

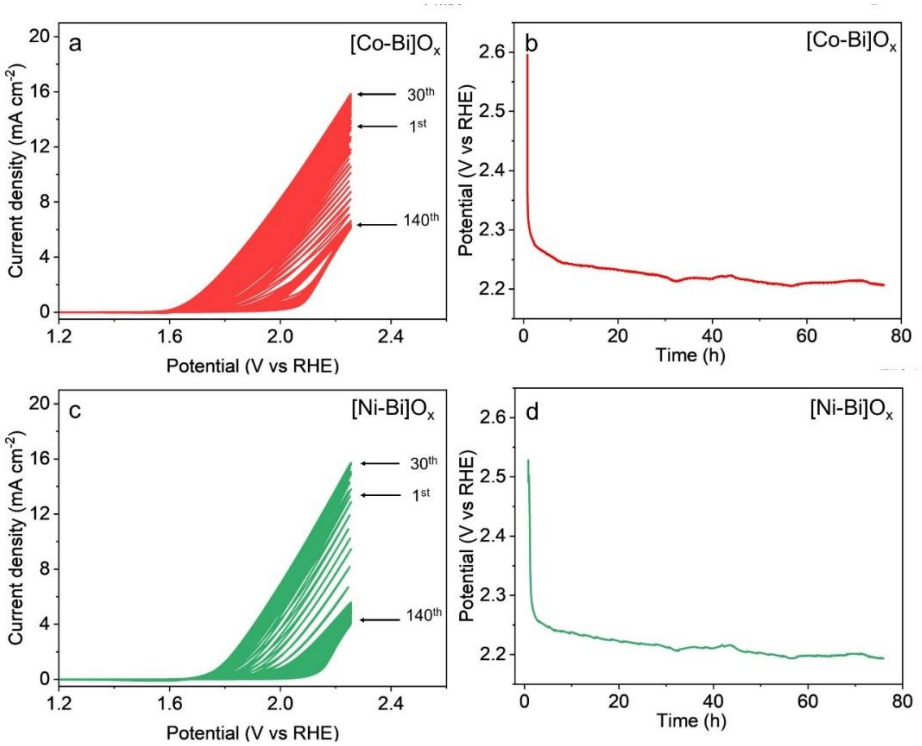

Figure 5.16 (a, c) Cyclic voltammetry (CV) curves (140 scans), (b, d) chronoamperometric (CP) curves reflecting the 80-h stability test recorded at 10 mA cm^{-2} after 140 CV scans of (a – b) [Co-Bi]O_x and (c – d) [Ni-Bi]O_x anodes.

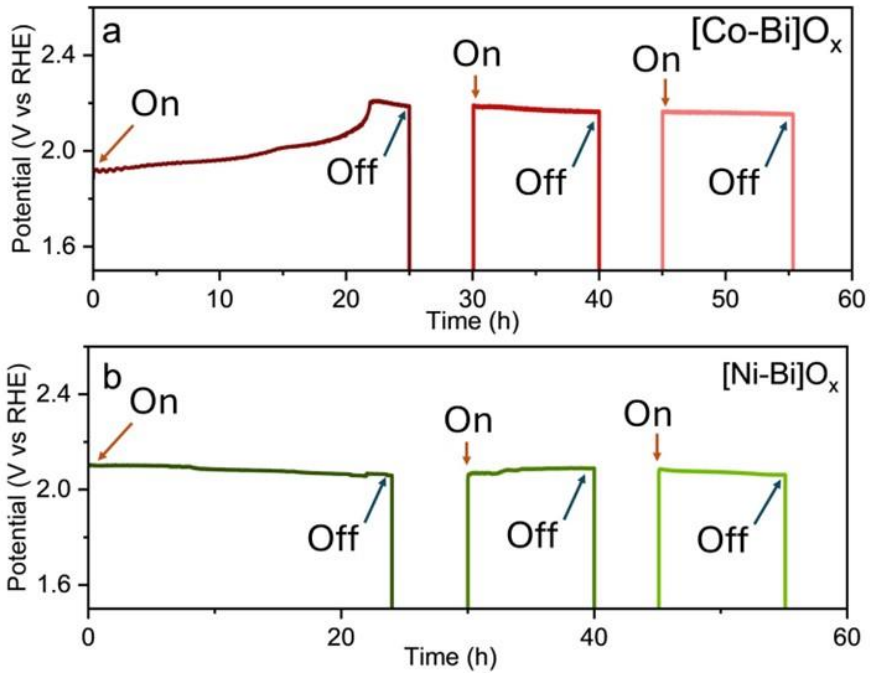

Figure 5.17 Galvanostatic oxidation (operating current density 10 mA cm^{-2}) of aqueous 0.1 M H_2SO_4 in an interrupted regime (see "ON" and "OFF" labels in figure) of (a) [Co-Bi]O_x and (b) [Ni-Bi]O_x anodes.

An analogous OER behavior of the [Co-Bi]O_x and [Ni-Bi]O_x anodes was observed with other electrolytes at the same pH of 1 (*ie*. 0.1 M HNO_3 and 0.1 M $HClO_4$) (**Figure 5.18**), indicating the minimal effect of the anion identity of the self-healing mechanism. Beyond the influence of the pH, previous studies have indicated that the presence of additional active elements in the electrolyte can impact the self-healing capability.[29,31–33] To explore this further, we investigated the effect of adding [Co^{2+}] and [Ni^{2+}] ions at a pH of 1 in the 0.1 M H_2SO_4 electrolyte on the OER performance and self-healing capability of the corresponding binary anodes (**Figure 5.19**). The OER performance of the [Co-Bi]O_x and [Ni-Bi]O_x anodes, as illustrated in the LSVs graph of (**Figure 5.19**), exhibited a reduction when the concentration of [Co^{2+}] and [Ni^{2+}] reached 2 mM, while a concentration between 0 – 1 mM did not show observable variations of the OER activity. At 10 mA cm^{-2}, the [Co-Bi]O_x achieved the lowest required potential of 2.15 V *vs*. RHE with the addition of 0.5 mM Co^{2+}. However, this is only marginally lower by 50 mV that without addition of [Co^{2+}] (**Figure 5.21**). Instead the [Ni-Bi]O_x anode overpotential for 10 mA cm^{-2} remains essentially constant upon the addition of [Ni^{2+}] from 0 to 1 mM.

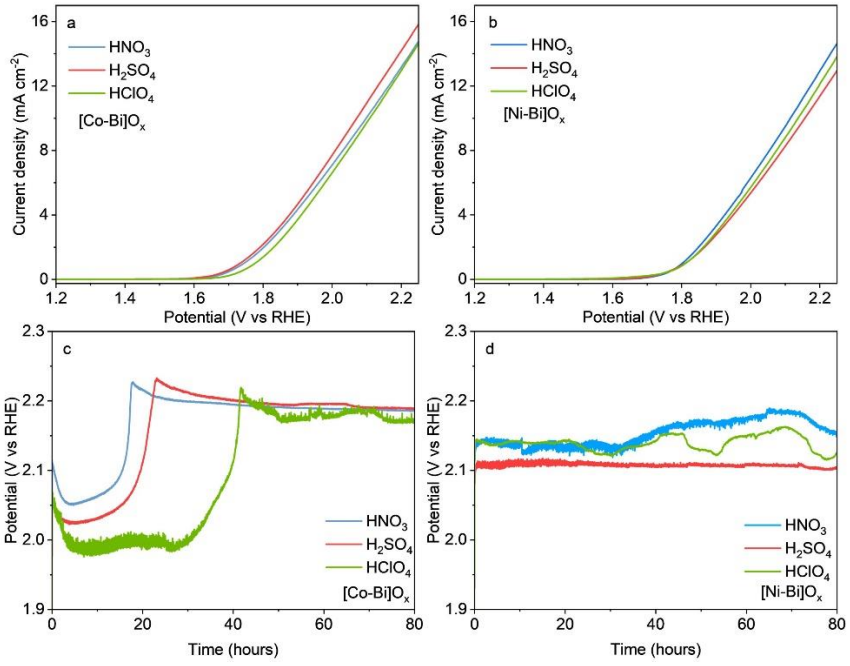

Figure 5.18 Electrochemical characterization of [Co-Bi]O_x and [Ni-Bi]O_x in 0.1 M H_2SO_4, HNO_3, $HClO_4$ electrolyte. a−b) Forward linear sweep voltammetry (LSV) curves (3rd scan, scan rate 0.005 V s^{-1}), c−d) the 80-h stability test of mixed-metal oxides anodes recorded at 10 mA cm^{-2}.

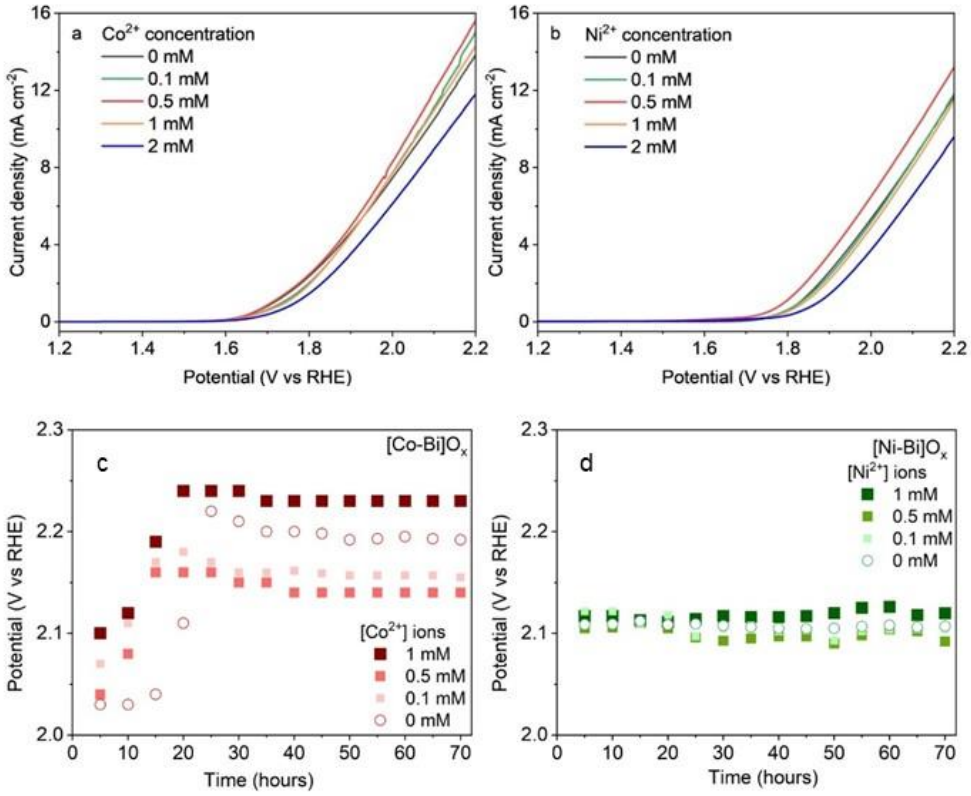

Figure 5.19 a – b) Forward linear sweep voltammetry (LSV) curves (3rd scan, scan rate 0.005 V s^{-1}) and c – d) chronopotentiometric curves reflecting the stability test of [Co-Bi]O_x and [Ni-Bi]O_x in 0.1 M H_2SO_4 electrolytes with different dissolved concentration of Co^{2+} and Ni $^{2+}$.

The stability of [Co-Bi]O_x and [Ni-Bi]O_x anodes were also evaluated under the higher range of current densities and applied potentials (**Figure 5.20**). It was reflected in the CP curves of 20 h-OER operation measured at 20, 30, and 40 mA cm^{-2}, which achieved at the high potential range from 2.2 – 3.2 V vs RHE. Although both materials performed sustained OER operation, [Ni-Bi]O_x curves demonstrated the lower activity than what obtained in [Co-Bi]O_x anode, which is contrast with the performance measured at low current density 10 mA cm^{-2}. It determined the outperformed activity and stability of [Co-Bi]O_x anodes in leverage current densities at low pH condition, which was well consistent with the favorable self-assembly mechanism of Co-based system reported previously.[29,44]

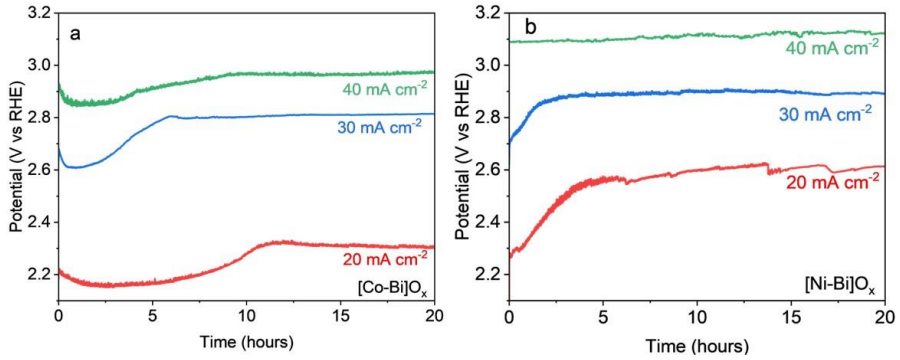

Figure 5.20 Chronopotentiometric curves reflecting the stability test of a) $[Co\text{-}Bi]O_x$ and b) $[Ni\text{-}Bi]O_x$ in 0.1 M H_2SO_4 electrolytes at different current density range.

The quasi steady-state potentials of the $[Co\text{-}Bi]O_x$ and $[Ni\text{-}Bi]O_x$ anodes were further evaluated for extended 200-h OER CP (**Figure 5.14e**). A comparison of their performance upon iR_u correction (**Figure 5.21**) against other self-healing OER electrocatalyst systems is presented in (**Table 5.3**). The quasi steady-state iR_u-corrected overpotential of the $[Co\text{-}Bi]O_x$ and $[Ni\text{-}Bi]O_x$ samples at a 10 mA cm^{-2} current density is 0.67 and 0.59 V, respectively. These values show a higher activity than previously reported self-healing electrocatalyst systems (**Table 5.3**), while providing a more environmentally friendly and earth-abundant composition. Overall, the increased OER stability and their lower overpotential demonstrate a synergistic effect of incorporating highly catalytic active transition metal sites into a stable self-healing BiO_x matrix.

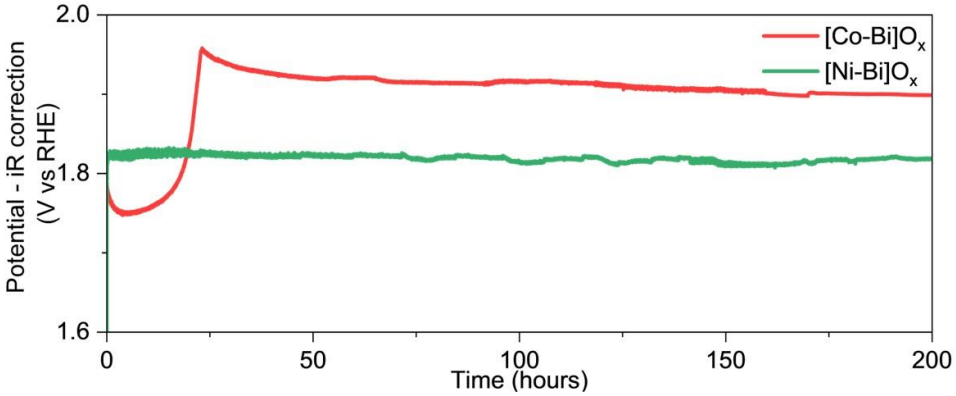

Figure 5.21 The 200-h galvanostatic test of $[Co\text{-}Bi]O_x$ and $[Ni\text{-}Bi]O_x$ anodes recorded at 10 mA cm^{-2} with iR- correction in 0.1 M H_2SO_4 electrolyte.

Table 5.3 Summary of various self-healing OECs reported recently in the literature.

Catalyst	Electrolyte	Substrate	Current density (mA cm^{-2})	*i*R-corrected overpotential (V *vs.* RHE)	Stability (hours)	Ref.
$[Ni\text{-}Bi]O_x$	0.1 M H_2SO_4	FTO	10	0.59	200	This work
$[Co\text{-}Bi]O_x$	0.1 M H_2SO_4	FTO	10	0.67	200	
$Co\text{-}MnO_2$	0.1 M $HClO_4$ containing 2.4 mg mL^{-1} Co^{2+}	Carbon fiber paper	10	0.77	260	[45]
$[Ag\text{-}Bi]O_x$	0.1 M H_2SO_4	FTO	10	0.7	400	[38]
$CoBiSnO_x$	0.1 M H_2SO_4	FTO	10	0.67	210	[37]
BiO_x	0.01 M H_2SO_4	FTO	5	1.17	110	[36]
$[Co\text{-}Fe\text{-}Pb]O_x$	0.1 M H_2SO_4 containing 0.05 mM Co^{2+} (80 °C)	FTO	10	0.56	168	[31]
$[Co\text{-}Fe\text{-}Pb]O_x$	0.1 M H_2SO_4 containing 0.25 mM Co^{2+}, 1 mM Fe^{3+} and 0.5 mM Pb^{2+} (80 °C)	FTO	500	0.7	160	[32]
$CoFePbO_x$	sulfate buffer (pH 2)	FTO	1	0.57	50	[30]
CoO_x	1 M H_3PO_4 (pH 1.6)	FTO	10	1	30	[46]

From the abovementioned studies, we can describe the mechanism of acidic self-healing electrocatalysts based on earth-abundant transition metal oxides (Co, Ni) within a Bi-matrix through the schematic in (**Figure 5.22**). The self-healing operation was achieved by a dynamic equilibrium state, where the degradation of catalysts is compensated by the concurrent reparation. The key point is that the dissolved catalyst ions, especially for the active components (Co, Ni), were redeposited onto the surface at the required OER potential with a rate equal to or exceeding the rate of metal dissolution. In these materials, the bismuth oxide serves as an acid-stable structural matrix that hosts and stabilizes the more catalytically active components (Co, Ni). The self-sustaining system was generated by the balance cycling between dissolved and solid-state ions at a sufficient potential to drive both the desired electrochemical reaction and the continuous catalyst regeneration. Although both structural (Bi) and active (Co, Ni) components suffer from the acidic attack of electrolytes, the more serious degradation occurs with the latter part due to their inherent instability. The Bi-matrix provided a framework and facilitated the regeneration of the active metal ions, which mainly impacted the electrocatalytic activity of self-healing electrocatalysts. This regeneration and sustained operation of these active electrocatalysts could not be achieved in the system without $[Bi]O_x$.

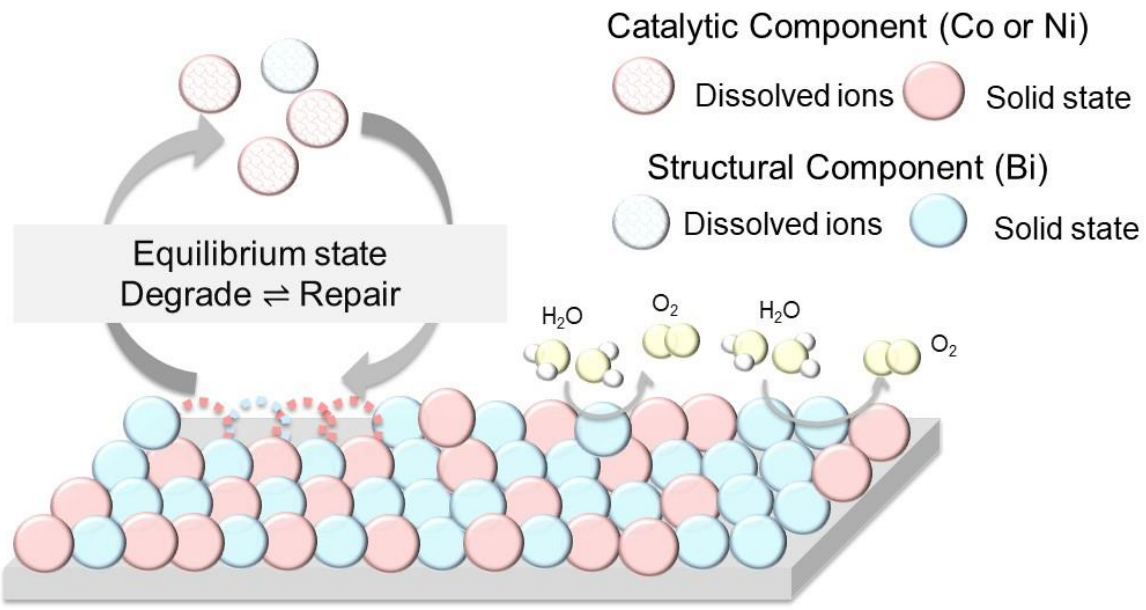

Figure 5.22 A schematic illustrating the mechanism of acidic self-healing electrocatalyst based on earth-abundant transition metal oxides and a Bi matrix.

5.3. Conclusions

This study introduced the systematic design of highly performing self-healing compounds for acidic OER based on earth-abundant transition metal oxides and a Bi matrix. Our findings demonstrate that the incorporation of optimal metal sites into the BiO_x matrix leads to acidic stable and OER active [M-Bi]O_x electrocatalysts that attain stable compositions of Co or Ni and Bi atoms. Our optimal [Co-Bi]O_x and [Ni-Bi]O_x anodes achieve a constant 10 mA cm^{-2} OER current density for over 200 h at a pH of 1 with a low overpotential of 670 and 590 mV, respectively. We also reveal key insights into the role of environmental factors such as electrolyte pH and chemical composition, buffer, and concentration of electrolytes on the self-healing mechanism of the [Co-Bi]O_x and [Ni-Bi]O_x anodes. Extremely acidic condition of pH ~ 0 in a 1 M H_2SO_4 electrolyte induce the loss of the active metals due to their high equilibrium concentration in the electrolyte interrupting the self-healing process. However, the self-healing activity of [Co-Bi]O_x and [Ni-Bi]O_x samples proved to be sufficiently effective at a pH of 1 resulting in stable operation and high OER activity. These findings provide directions for the engineering of environmentally friendly, earth-abundant and low-cost self-healing electrocatalyst systems for acidic OER supporting the global production of green hydrogen via proton membrane-based electrolysis.

5.4. Experimental section

5.4.1. Materials

All the chemical reagents and solvents for the material synthesis were used as received without any further purification. Ultrapure deionized water was used in preparing aqueous solutions in all experiments. Fluorine-doped tin oxide (FTO) glass (PV Tech, 7 $\Omega\,cm^{-1}$) was cleaned with deionized (DI) water, then ethanol and DI water sequentially. Precursor sources used in sputtering process were metal targets from AJA International USA, ≥ 99.9%.

5.4.2. Mixed Bi-based oxides anodes fabrication

Cobalt (Co), nickel (Ni), and bismuth (Bi) were deposited simultaneously onto FTO glass substrate by co-sputtering two DC magnetron guns in 1200 seconds. Argon gas was used during the deposition in the sputter coater system (AJA Intl. – ATC-2400V). The stoichiometric ratios of active metal (Co, Ni) and Bi were controlled through tuning the power of gun sources. Then, samples were annealed at 450 ºC in 1 h with the ramp rate 2 ºC min^{-1} to obtain the cobalt bismuth oxide [Co-Bi]O_x and nickel bismuth oxide [Ni-Bi]O_x.

5.4.3. Material Characterisation

The morphology of the films was investigated using a field-emission scanning electron microscope (FESEM) Zeiss Ultra Plus operating at 3 kV without coating. Samples for SEM were prepared by fixing the cut pieces of the electrode on the specimen stubs using carbon tape. X-ray diffraction (XRD) patterns were recorded by a D2 Phaser Bruker system with Cu Kα radiation of average wavelength 1.54056 Å at a scan rate of 1.17 deg min^{-1}. The XRD results were obtained by direct measurement of the samples on FTO substrates.

X-ray photoelectron spectroscopy (XPS) analysis was performed using a calibrated ESCALAB250Xi spectrometer (Thermo Scientific, UK) with a monochromated Al Kα source at a power of 120 W (13.8 kV × 8.7 mA). The base pressure in the main vacuum chamber during analysis was typically around 2 x 10^{-7} mbar. Survey spectra were acquired at a pass energy of 160 eV. To obtain more detailed information about the chemical structure, oxidation states, and so forth, high-resolution spectra were recorded at 20 eV pass energy (yielding a typical peak width for polymers of approximately 1.0 eV). Spectra were collected at normal emission. The data was analyzed using CasaXPS software version 2.3.25 PR1.0. Adventitious C 1s (284.8 eV) peak was used to calibrate the spectra.

5.4.4. Electrochemical experiments

All electrochemical measurements in this study were carried out with a BioLogic electrochemical workstation using a customized two-compartment cell separated by a Nafion@117 membrane (sourced from FuelCellStore). The electrochemical performance of the electrodes was evaluated in a three-electrode configuration using a Pt wire as the counter electrode and a double-junction Ag|AgCl|KCl(sat.) (+0.197 V *vs*. SHE) as the reference electrode. Acid sulfuric (H_2SO_4) solutions with various concentrations 1 M, 0.1 M, and 0.01 M at pH 0.08, 1.11, 1.95, respectively, were measured with a Benchtop water quality meter (Sper Scientific) and used as electrolytes. The potentials were converted to the RHE scale via the Nernst equation.

$$E_{RHE} = E_{Ag/AgCl} + 0.197 + 0.059 \times pH \qquad \textbf{(Equation 5.1)}$$

Electrochemical impedance spectra (EIS) were collected at 0.3 V *vs*. RHE, where no significant faradaic processes occur, over a frequency range of 0.1 Hz–200 kHz with a 5 mV amplitude. The uncompensated R_u values derived from EIS for FTO were 17.7 Ω at pH 0.08, 27.5 Ω at pH 1.11, and 86.9 Ω at pH 1.95.

5.5. References

[1] J. Chi, H. Yu, *Chinese J. Catal.* **2018**, *39*, 390.

[2] R. L. Germscheidt, D. E. B. Moreira, R. G. Yoshimura, N. P. Gasbarro, E. Datti, P. L. dos Santos, J. A. Bonacin, *Adv. Energy Sustain. Res.* **2021**, *2*, 2100093.

[3] A. M. Oliveira, R. R. Beswick, Y. Yan, *Curr. Opin. Chem. Eng.* **2021**, *33*, 100701.

[4] M. Carmo, D. L. Fritz, J. Mergel, D. Stolten, *Int. J. Hydrogen Energy* **2013**, *38*, 4901.

[5] S. Shiva Kumar, V. Himabindu, *Mater. Sci. Energy Technol.* **2019**, *2*, 442.

[6] E. Fabbri, T. J. Schmidt, *ACS Catal.* **2018**, *8*, 9765.

[7] Q. Wu, Y. Wang, K. Zhang, Z. Xie, K. Sun, W. An, X. Liang, X. Zou, *Mater. Chem. Front.* **2023**, *7*, 1025.

[8] F. Y. Chen, Z. Y. Wu, Z. Adler, H. Wang, *Joule* **2021**, *5*, 1704.

[9] Q. Wang, Y. Cheng, H. B. Tao, Y. Liu, X. Ma, D. Li, H. Bin Yang, B. Liu, *Angew. Chemie Int. Ed.* **2023**, DOI 10.1002/anie.202216645.

[10] H. Yoon, B. Ju, D. Kim, *Batter. Energy* **2023**, *2*, DOI 10.1002/bte2.20230017.

[11] Q. Ma, S. Mu, *Interdiscip. Mater.* **2023**, *2*, 53.

[12] Z. Chen, X. Duan, W. Wei, S. Wang, B. J. Ni, *Nano Energy* **2020**, *78*, 105392.

[13] F. Hess, *Curr. Opin. Electrochem.* **2023**, *41*, 101349.

[14] H. Xu, Y. Han, Q. Wu, Y. Jia, Q. Li, X. Yan, X. Yao, *Mater. Chem. Front.* **2023**, *7*, 1248.

[15] L. Hou, X. Gu, X. Cui, J. Tang, Z. Li, X. Liu, J. Cho, *EES Catal.* **2023**, *1*, 619.

[16] A. Patonia, R. Poudineh, *Oxford Inst. Energy Stud.* **2022**.

[17] Z. Wang, L. Lu, *Electrochem. commun.* **2023**, *151*, 107505.

[18] C. Wang, R. Deng, M. Guo, Q. Zhang, *Int. J. Hydrogen Energy* **2023**, *48*, 31920.

[19] J. Gao, H. Tao, B. Liu, *Adv. Mater.* **2021**, *33*, 1.

[20] S. Cherevko, *Curr. Opin. Electrochem.* **2023**, *38*, 101213.

[21] X. M. C. Ta, T. Trần-Phú, T. K. A. Nguyen, M. Chatti, R. Daiyan, *Appl. Phys. Rev.* **2024**, *11*, DOI 10.1063/5.0200438.

[22] Q. Wu, Q. Gao, X. Wang, Y. Qi, L. Shen, X. Tai, F. Yang, X. He, Y. Wang, Y. Yao, Y. Ren, Y. Luo, S. Sun, D. Zheng, Q. Liu, S. Alfaifi, X. Sun, B. Tang, *iScience* **2024**, *27*, 108738.

[23] K. Lee, J. Shim, H. Ji, J. Kim, H. S. Lee, H. Shin, M. S. Bootharaju, K. S. Lee, W. Ko, J. Lee, K. Kim, S. Yoo, S. Heo, J. Ryu, S. Back, B. H. Lee, Y. E. Sung, T. Hyeon, *Energy Environ. Sci.* **2024**, *17*, 3618.

[24] R. Ram, L. Xia, H. Benzidi, A. Guha, V. Golovanova, A. Garzón Manjón, D. Llorens Rauret, P. Sanz Berman, M. Dimitropoulos, B. Mundet, E. Pastor, V. Celorrio, C. A. Mesa, A. M. Das, A. Pinilla-Sánchez, S. Giménez, J. Arbiol, N. López, F. P. García de Arquer, *Science (80-.).* **2024**, *384*, 1373.

[25] A. Li, S. Kong, C. Guo, H. Ooka, K. Adachi, D. Hashizume, Q. Jiang, H. Han, J. Xiao, R. Nakamura, *Nat. Catal.* **2022**, *5*, 109.

[26] X. M. C. Ta, T. Trần-Phú, J. A. Yuwono, T. K. A. Nguyen, A. D. Bui, T. N. Truong, L. Chang, E. Magnano, R. Daiyan, A. N. Simonov, A. Tricoli, *Small* **2023**, *2304650*, 1.

[27] T. Tran-Phu, H. Chen, R. Daiyan, M. Chatti, B. Liu, R. Amal, Y. Liu, D. R. Macfarlane, A. N. Simonov, A. Tricoli, *ACS Appl. Mater. Interfaces* **2022**, *14*, 33130.

[28] J. Yu, F. A. Garcés-Pineda, J. González-Cobos, M. Peña-Díaz, C. Rogero, S. Giménez, M. C. Spadaro, J. Arbiol, S. Barja, J. R. Galán-Mascarós, *Nat. Commun.* **2022**, *13*, 4341.

[29] A. E. Thorarinsdottir, S. S. Veroneau, D. G. Nocera, *Nat. Commun.* **2022**, *13*, 1.

[30] M. Huynh, T. Ozel, C. Liu, E. C. Lau, D. G. Nocera, *Chem. Sci.* **2017**, *8*, 4779.

[31] D. Simondson, M. Chatti, S. A. Bonke, M. F. Tesch, R. Golnak, J. Xiao, D. A. Hoogeveen, P. V. Cherepanov, J. L. Gardiner, A. Tricoli, D. R. MacFarlane, A. N. Simonov, *Angew. Chemie - Int. Ed.* **2021**, *60*, 15821.

[32] M. Chatti, J. L. Gardiner, M. Fournier, B. Johannessen, T. Williams, T. R. Gengenbach, N. Pai, C. Nguyen, D. R. MacFarlane, R. K. Hocking, A. N. Simonov, *Nat. Catal.* **2019**, *2*, 457.

[33] S. A. Bonke, K. L. Abel, D. A. Hoogeveen, M. Chatti, T. Gengenbach, M. Fournier, L. Spiccia, A. N. Simonov, *Chempluschem* **2018**, *83*, 704.

[34] Q. Feng, X. Z. Yuan, G. Liu, B. Wei, Z. Zhang, H. Li, H. Wang, *J. Power Sources* **2017**, *366*, 33.

[35] M. H. Miles, E. A. Klaus, B. P. Gunn, J. R. Locker, W. E. Serafin, S. Srinivasan, *Electrochim. Acta* **1978**, *23*, 521.

[36] A. E. Thorarinsdottir, C. Costentin, S. S. Veroneau, D. G. Nocera, *Chem. Mater.* **2022**, *34*, 826.

[37] H. Du, M. Chatti, B. Kerr, C. K. Nguyen, T. Tran-Phu, D. A. Hoogeveen, P. V. Cherepanov, A. S. R. Chesman, B. Johannessen, A. Tricoli, R. K. Hocking, D. R. MacFarlane, A. N. Simonov, *ChemCatChem* **2022**, *14*, DOI 10.1002/cctc.202200013.

[38] D. Simondson, M. Chatti, J. L. Gardiner, B. V. Kerr, D. A. Hoogeveen, P. V. Cherepanov, I. C. Kuschnerus, T. D. Nguyen, B. Johannessen, S. L. Y. Chang, D. R. Macfarlane, R. K. Hocking, A. N. Simonov, *ACS Catal.* **2022**, *12*, 12912.

[39] M. C. Biesinger, B. P. Payne, A. P. Grosvenor, L. W. M. Lau, A. R. Gerson, R. S. C. Smart, *Appl. Surf. Sci.* **2011**, *257*, 2717.

[40] A. K.-V. S. W. G. and C. J. P. Alexander V. Naumkin, "NIST X-ray Photoelectron Spectroscopy Database," **n.d.**

[41] A. Jain, S. P. Ong, G. Hautier, W. Chen, W. D. Richards, S. Dacek, S. Cholia, D. Gunter, D. Skinner, G. Ceder, K. A. Persson, *APL Mater.* **2013**, *1*, DOI 10.1063/1.4812323.

[42] T. Tran-Phu, R. Daiyan, J. Leverett, Z. Fusco, A. Tadich, I. Di Bernardo, A. Kiy, T. N. Truong, Q. Zhang, H. Chen, P. Kluth, R. Amal, A. Tricoli, *Chem. Eng. J.* **2022**, *429*, 132180.

[43] N. Li, T. P. Keane, S. S. Veroneau, D. G. Nocera, *Chem. Commun.* **2020**, *56*, 10477.

[44] C. Costentin, D. G. Nocera, *Proc. Natl. Acad. Sci. U. S. A.* **2017**, *114*, 13380.

[45] X. Zhang, C. Feng, B. Dong, C. Liu, Y. Chai, *Adv. Mater.* **2023**, *35*, 1.

[46] L. G. Bloor, P. I. Molina, M. D. Symes, L. Cronin, *J. Am. Chem. Soc.* **2014**, *136*, 3304.

Chapter 6. Optimizing Surface Composition and Structure of $FeWO_4$ Photoanodes for Enhanced Water Photooxidation

As highlighted in Chapter 3, photoelectrochemical (PEC) water splitting, the second system investigated in this thesis, gains emerging interest as a promising strategy to employ solar energy to green hydrogen (H_2) production. Inspired from the attractive development of ternary metal oxide photoelectrodes reviewed in chapter 3, this chapter concentrates on developing photoanodes for efficient water photooxidation based on iron tungstate, a promising metal-tungstate materials but not yet widely studied in the role of photoelectrocatalyst. Flame spray pyrolysis (FSP) technique, a powerful technique to fabricate (photo)electrocatalysts directly onto substrates, is employed to synthesize and optimize iron tungstate photoanode.

This chapter was reprinted from the unpublished manuscript below. X. M. C. Ta, T. K. A. Nguyen, A. D. Bui, H. T. Nguyen, R. Daiyan, R. Amal, T. Tran-Phu, A. Tricoli, Optimizing Surface Composition and Structure of $FeWO_4$ Photoanodes for Enhanced Water Photooxidation. Adv. Mater. Technol. 2023, 8, 2201760. https://doi.org/10.1002/admt.202201760. Reproduced with permission.

Authorship Attribution Statement

Xuan Minh Chau Ta is the principal author of this publication, which forms part of her thesis submitted for the examination for the Doctor of Philosophy degree. The corresponding author below provided the consent for inclusion of a part or whole of the following publication in this thesis and accept the following candidate statement of contribution for this publication.

Candidate contribution:

It is the first study to synthesize the nanostructured iron tungstate ($FeWO_4$) by an ultra-fast flame synthesis route and optimize their surface composition and structure for efficient photoanode for OER. The manuscript was written, formatted, reviewed, and edited by Xuan Minh Chau Ta. This author was a main contributor, who was in charge designed, performed, or involved in all the experiments and data analysis.

Corresponding author

Prof Dr Antonio Tricoli

ABSTRACT

Photoelectrochemical water splitting is a promising approach to produce green hydrogen using solar energy. A primary bottleneck remains the lack of efficient photoanodes to catalyze the sluggish water photooxidation reaction. Engineering photoabsorbers with a narrow bandgap and suitable band edge can boost the photoelectrochemical performance. Herein, nanostructured iron tungstate ($FeWO_4$) photoanodes are engineered directly on a fluorine doped tin oxide glass substrate via a scalable and ultra-fast flame synthesis route in 13 seconds. Physiochemical, optoelectronic, and electrochemical properties of these photoanodes are systematically investigated. The key roles of charge transport, transfer, and dissolution of W and Fe ions from the $FeWO_4$ matrix within long-term performance are revealed. Optimal $FeWO_4$ photoanode with a bandgap of 1.82 eV and a FeOOH/NiOOH co-catalyst coating shows an improved water photooxidation performance, reaching a photocurrent density of 0.23 mA cm^{-2} at 1.4 V versus reversible hydrogen electrode in 1 M potassium hydroxide. It further demonstrates relatively good photostability, maintaining ≈96% of photocurrent density after 1-hour continuous photooxidation, albeit some trace of Fe, W and Ni elements dissolution in the electrolyte. Insights on the photooxidation performance of nanostructured $FeWO_4$ provide promising directions for the engineering of small band-gap catalysts for a variety of photoelectrochemical applications.

Keywords: PEC water splitting; Iron Tungstate ($FeWO_4$), Flame Spray Pyrolysis

6.1. Introduction

Green hydrogen produced from renewable energy sources such as solar electricity and water is now seen as an alternative energy carrier to replace CO_2-emitting fossil-based fuels.[1–5] Hydrogen can be produced from electrochemical water splitting, where the energy required to drive the hydrogen evolution reaction and oxygen evolution reaction is provided from electricity.[6] Reducing the electricity consumption in large-scale deployment of water electrolyzers for high-throughput hydrogen production by partially or totally utilizing solar energy is a promising approach. This is usually referred to as photoelectrochemical (PEC) water splitting. Among various solar-driven water splitting technologies, the PEC concept has been highly considered due to the low environmental impact, the simplified materials and device designs, the potential to enhance efficiency, and upscaling the system.[7–11] Analogous to the electrolysis of water, the photooxidation of water is more demanding compared to water photoreduction as the process involves four-electron transfer and high anodic polarization, limiting the overall efficiencies. The PEC process involves three major steps: (i) the light absorption by light absorption by a semiconductor with an appropriate bandgap following the photogenerated charge carriers formation; (ii) photogenerated charge separation and migration to the semiconductor-electrolyte interface; and (iii) the utilization of photogenerated charge carriers to promote the surface reactions of water reduction/ oxidation.[12] As such, engineering efficient photoanodes with suitable band edge positions and bandgap energy together with improved carrier lifetimes is of key importance. Till now, some popular photoanodes are based on the narrow band-gap semiconductor materials ($BiVO_4$, Fe_2O_3, etc.) or wide band-gap ones (TiO_2, ZnO, WO_3, etc.) which the appropriate modifications to extend light absorption range.[13–21] To enhance the photogenerated charge migration and utilization, these materials are usually treated by various strategies, co-catalyst decoration, oxygen defect construction, element doping, morphology regulation, etc.[21–27] However, their performance has approached theoretical limits, highlighting the need to explore alternative materials.

Ternary metal oxides (labeled as ABO_x, where A and B are two different cation ions) are a promising material class that can provide advantageous optoelectronic and physiochemical properties to its binary counterparts. For example, $CuWO_4$ has a bandgap energy (E_g) in the range from CuO (≈1.6 eV) to WO_3 (2.7 eV), promoting a wide range of light-harvesting applications.[21] Similarly, $ZnFe_2O_4$ has the larger hole diffusion length and narrower E_g compared to both α-Fe_2O_3 and ZnO.[28–31]. While there is a relatively small number of binary metal oxides (defined as AO_x, A is a cation ion), compositing these into ternary components can create a wide range of novel

photoanodes.[32] As the best performing $BiVO_4$ photoanode though its PEC performance is limited by its fractional sun light absorption capacity arising from its relatively large E_g of ≈2.4 eV, ternary metal-tungstates such as $FeWO_4$, $CuWO_4$ or $SnWO_4$ have recently garnered attention. Their smaller E_g, suitable edge positions for water photooxidation, and earth-abundant element compositions make them attractive for application in PEC devices and other applications such as scintillation materials, photocatalysis, sensors, and supercapacitors.[33]

Amongst ternary metal-tungstates, iron-tungstate has been considered a promising candidate for PEC water splitting. In nature, iron-tungstate is found in two different compositions namely ferberite ($FeWO_4$) and wolframite (Fe_2WO_6). Both of them are reported have a suitable bandgap in the range of 1.7–2.0 eV,[34] making them effective for capturing a relative large spectrum of solar energy in the ultraviolet to visible range. While Fe_2WO_6 has been more extensively explored, its high synthesis temperature (750–800 ºC) hinders the fabrication of tunable nanostructured morphologies and its direct assembly on conventional transparent metal oxides substrates such as fluorine-doped tin oxide (FTO) or tin-doped indium oxide glass.[35–40] Conversely, $FeWO_4$ can be synthesized at lower temperatures by various techniques such as solvothermal, hydrothermal, and sputtering, as summarized in (**Table 6.1)**. Even though previous reports achieved $FeWO_4$ with excellent electron transport and good light absorption activity,[41–45] the influence of its optoelectronic and physicochemical properties on its PEC activity remains elusive.

Here, we present the engineering of the optoelectronic and electrochemical properties of nanostructured $FeWO_4$ photoanodes by a rapid and scalable flame spray pyrolysis (FSP) route. Optoelectronic, physical, and electrochemical properties of these anodes were then systematically investigated. An optimized $FeWO_4$ photoanodes were achieved, demonstrating a photocurrent of up to 0.23 mA cm^{-2} at 1.4 V versus reversible hydrogen electrode (RHE) and reasonable photostability with no significant change in photocurrent throughout a 1 h reaction after coupling with a FeOOH/NiOOH cocatalyst layer. We believe that these first results on the engineering of the structural and morphological properties of $FeWO_4$ by flame synthesis provide a path for its further optimization and integration in PEC devices for water splitting and a variety of other photoelectrochemical applications.

Table 6.1 Summary of morphologies, synthesis methods, bandgap energies, and applications of various $FeWO_4$ structures reported recently in the literature.

Morphology[a)]	**Synthesis Method**	**Optical bandgap (eV)**	**Application**	**Performance**	**Notes**	**Reference**
Porous $FeWO_4$	Flame Synthesis	1.82	Photoanode[b)]	0.23 mA cm^{-2} @ 1.4 V[c)] pH 13.8	Flat band potential: 0.73 V versus RHE PEC stability in 1 h	This study
Bi-containing $FeWO_4$	Sputtering	1.95	Photoanode	0.35 mA cm^{-2} @ 1.23 V at pH 9	Flat band potential: 0.35 V versus RHE PEC stability in 30 min	Ref. [46]
Nanosphere $FeWO_4$	Solvothermal	2.1	Anode[d)]	1.96 mA g^{-1} @ 1.7 V 78 mV/dec Tafel slope	EC stability in 24 h	Ref. [41]
Nanorod-shaped $FeWO_4$/nickel foam	Solvothermal	n/a[e)]	Anode	10 mA cm^{-2} @ 1.51 V 54 mV/dec Tafel slope	EC stability in 30 h	Ref. [42]
$FeWO_4$ microspheres	Solvothermal	2.75	Photocatalyst[f)]	Rhodamine B degraded 89% after 20 min in H_2O_2 solution	n/a	Ref. [47]
$FeWO_4$ microstructure	Hydrothermal	2.59	n/a[e)]	n/a	n/a	Ref. [48]
$FeWO_4$ nanosheet	Hydrothermal	1.73	Photocatalyst	Methyl orange degraded 17% after 150 min	n/a	Ref. [44]

$FeWO_4$ nanopowder	Hydrothermal	2.4	n/a	n/a	n/a	Ref. [49]
Spindle-like $FeWO_4$ nanoparticles	Hydrothermal	2.17	Photocatalyst	Methyl orange degraded 74% after 30 min	n/a	Ref. [45]
$FeWO_4$ nanorod	Hydrothermal	2.16	Photocatalyst	Methyl orange degraded 89% after 60 min	n/a	Ref. [43]
Quadrilateral disk-shaped $FeWO_4$ nanocrystal	Hydrothermal	1.98	Photocatalyst	2-Propanol degradation rate constant ≈2.04 min^{-1}	n/a	Ref. [50]

[a] Light intensity for all PEC water oxidation experiments was 1 sun (Air Mass (AM) 1.5G illumination 100 mW cm^{-2}); [b] Photoanode in PEC water splitting; [c] potential versus reversible hydrogen electrode; [d] Anode in electrolysis of water; [e] data not available; [f] Photocatalyst in organic compounds degradation.

6.2. Results and discussion

Nanostructured iron tungsten photoanodes were directly grown on fluorine-doped tin oxide (FTO) glass substrates via FSP. Typically, a stochiometric ratio of W and Fe precursors were dissolved in a combustible solution, consisting of diethylene glycol monobutyl ether and ethanol. This precursor solution was fed to a custom-built atomizer and atomized by an oxygen dispersion flow to generate microdroplets before being ignited by a surrounding premixed CH_4/O_2 pilot flame. The microdroplets undergo concurring evaporation, pyrolysis and combustion forming a supersaturated vapor of the target metal oxides. Upon nucleation of the first clusters, they growth to form larger nanoparticles by means of condensation, Brownian coagulation and coalescence before self-assembling on the FTO substrates by diffusion-limited cluster-cluster aggregation.[51,52] This approach allows the direct deposition of a wide range of (photo)electrocatalysts with uniform coverage and excellent control over the mass loading in a very short time scale.[53–56] Here, the active photoanodes were directly formed on FTO glass substrates within 13 s, allowing the rapid fabrication of active photoanodes without the need of nonconductive binders and time-consuming synthesis procedures.[57,58]

It is common to perform post-thermal treatments of flame-made electrodes to optimize the crystal composition of flame-made nanostructure.[54,56–60] Here, optimization of the as-prepared iron-tungstate photoanodes was investigated by annealing at 500 and 700 °C. X-ray diffraction (XRD) spectra of as-prepared, 500, and 700 °C samples (**Figure 6.1a–b**) show strong diffraction peaks of the SnO_2 present in the FTO substrate. For the as-prepared $FeWO_4$ films, broad peaks in the range of 23–24 ° were observed, indicating low crystallinity or small crystal sizes of these anodes. After the thermal post-synthesis treatment at 500 °C, diffraction peaks at 23.7°, 24.3°, and 30.3° appeared, which are attributed to (011), (110), and (111) of the monoclinic ferberite ($FeWO_4$) with a powder diffraction file number of 74-1100.[41–47] Increasing the post-synthesis temperature to 700 °C, additional peaks at 15.5°, 18.6°, 36.1° corresponding to (010), (100), (002), respectively, of the monoclinic $FeWO_4$ phase were observed.[41–47] Raman analysis further confirmed the presence of $FeWO_4$ monoclinic phase by its characteristic vibrational peaks (**Figure 6.1c**).[43,61,62] All three samples had spectral features at 76 cm^{-1} and 125 cm^{-1}, which are attributed to lattice vibrations.[44,61] There are also peaks at 215, 270, and 390 cm^{-1} associated with the $\nu_4(B_g)$ bending models of $FeWO_4$ structure.[43,61,62]

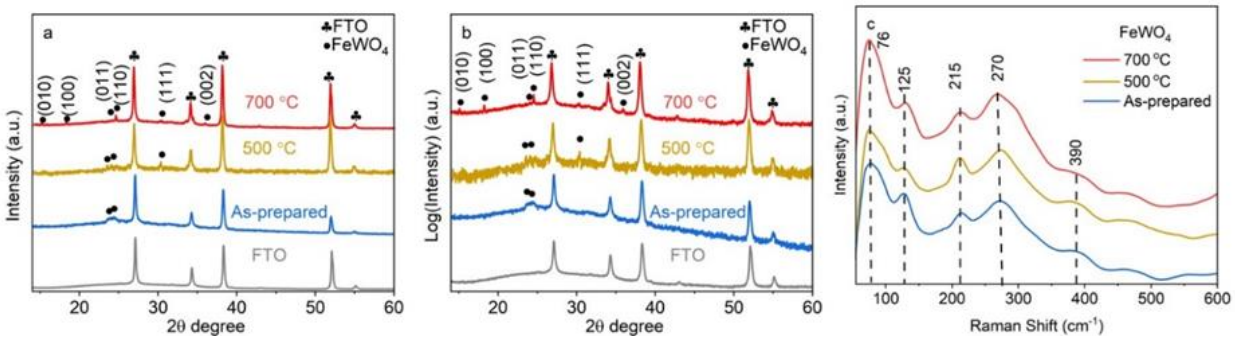

Figure 6.1 Physical characterizations of the as-prepared $FeWO_4$, $FeWO_4$ – 500 ºC, and $FeWO_4$ – 700 ºC films: a-b) XRD patterns with a) normalized, b) logarithm intensity, and c) Raman Spectra.

The morphology of flame-made $FeWO_4$ was investigated by a field-emission scanning electron microscope (FESEM) analysis. As shown in (**Figure 6.2a–c**) the as-prepared electrode consists of nanoparticles agglomerated into hierarchically porous structures and uniformly distributed on the FTO glass substrate. Increasing the thermal treatment temperature to 500 and 700 °C results in relatively similar film morphology with, however, a significant increase in the grain size of nanoparticles (**Figure 6.2d–i**). The cross-section scanning electron microscopy (SEM) images of $FeWO_4$ films prepared at different post-synthesis annealing temperatures are presented in (**Figure 6.2c,f,i**). As-prepared $FeWO_4$ films demonstrated the tree-like microsized structures throughout the film-cross section views. $FeWO_4$ films at 500 and 700 °C showed more robust and denser structure than as-prepared sample. The average thickness of three $FeWO_4$ films is estimated at about 1 μm. The effect of annealed temperatures on the $FeWO_4$ nanostructures was further investigated at 400 and 600 °C. Altogether, SEM images of these two samples (**Figure 6.3**) and the ones post-annealed at 400, 500, and 700 °C (**Figure 6.2**) indicate that increasing calcinated temperature from 400 to 700 °C caused the larger grain size of $FeWO_4$ nanoparticle.

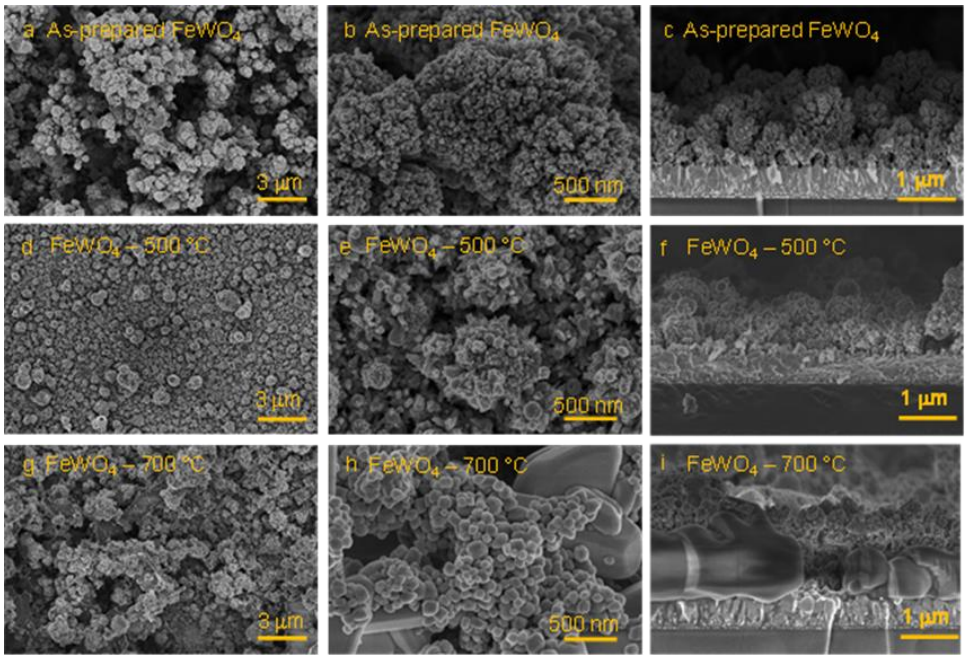

Figure 6.2 Physical characterization. a, b, d, e, g, h) Top-view and c, f, i) cross-sectional SEM images of the nanostructured $FeWO_4$ at different magnifications of a–c) as-prepared, e, f) annealed 500 °C, and g–i) 700 °C $FeWO_4$ electrodes.

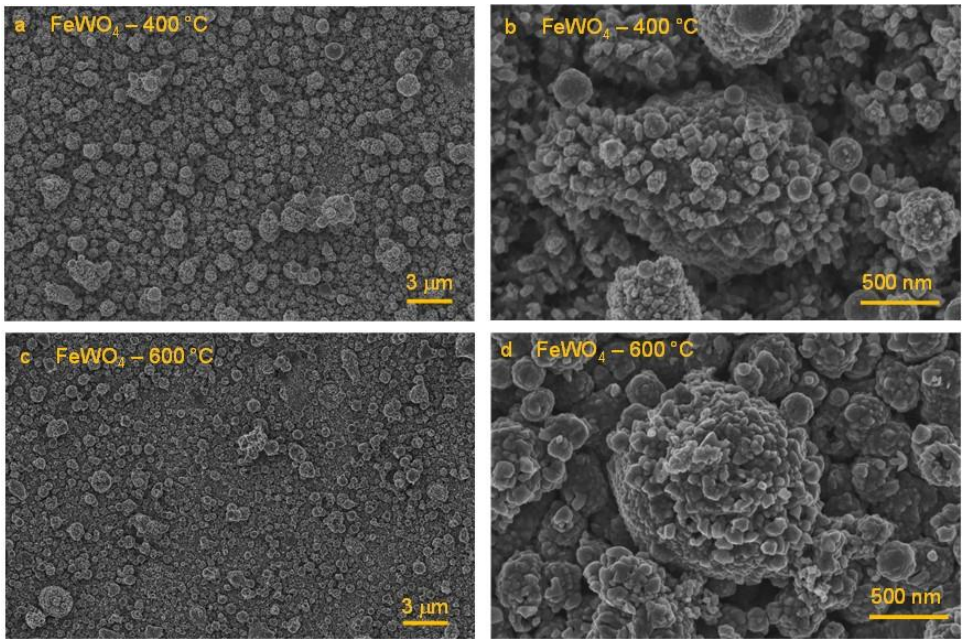

Figure 6.3 Physical characterization. SEM images of the nanostructured $FeWO_4$ at different magnifications for (a-b) annealed 400 °C and (c-d) annealed 600 °C.

Transmission electron microscopy (TEM) with energy-dispersive X-ray spectroscopy (EDS) analysis was used to study the morphology, crystallinity, and composition of $FeWO_4$ films. **(Figure 6.4 a, g, and m)** shows low-magnification TEM images of as-prepared, $FeWO_4$ –500 °C, and

$FeWO_4$ –700 °C, respectively, which present the agglomerate of nanoparticles, in line with the SEM images. Higher-magnification TEM images of as-prepared (**Figure 6.4b–e**), $FeWO_4$ –500 °C (**Figure 6.4h–k**), and $FeWO_4$ –700 °C (**Figure 6.4n–q**) samples reveal a highly crystalline structures with observed lattice fringes corresponding to (111) and (110) planes with an interatomic spacing distance of 2.9 and 3.6 Å, respectively. EDS elemental mapping (**Figure 6.4f, l, r**) displays a homogeneous distribution of Fe, W, and O in all three $FeWO_4$ photoanodes. Overall, the XRD, Raman, SEM, and TEM results confirm the generation of porous $FeWO_4$ nanostructures via flame synthesis.

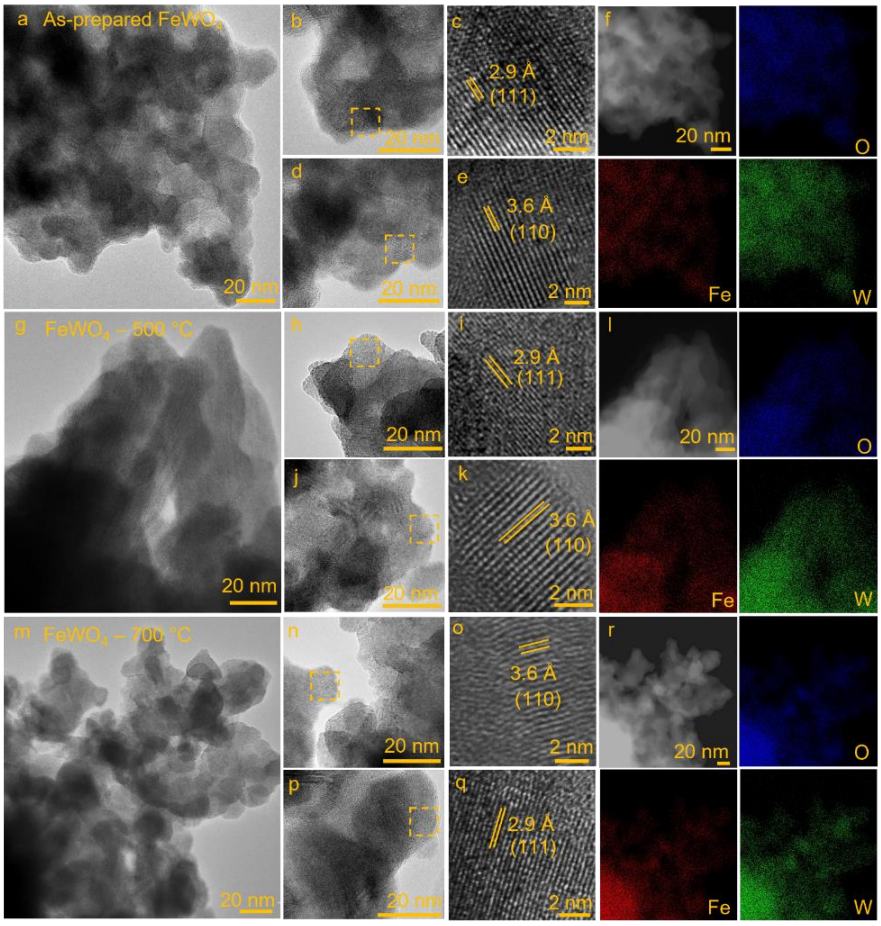

Figure 6.4 Physical characterization**.** TEM images of a–f) as-prepared, g–l) 500 °C, and m–r) 700 °C $FeWO_4$, and corresponding EDX elemental mapping.

The near-surface chemistry of $FeWO_4$ samples were probed with X-ray photoelectron spectroscopy (XPS). Survey XPS spectra of $FeWO_4$ films prepared at 500 °C, 700 °C, and before the thermal treatment (**Figure 6.5a**) reveal the presence of Fe 2p, W 4f along with O 1s, C 1s, and K (K 2s and K 2p) on the surface. K is supposed coming potassium hydroxide (KOH) solution used to clean the

residual WO_3 on the surface after flame synthesis. Core-level photoemission of Fe 2p (**Figure 6.6a**) shows two main peaks at a binding energy of 709.6 and 723.2 eV, which are attributed to Fe $2p_{1/2}$ and Fe $2p_{3/2}$, respectively.[63,64] Moreover, rigorous fitting of the Fe 2p XPS spectra proposed by Biesinger *et al.* (**Figure 6.5d**) and the broad satellite peaks at ≈732 and 719 eV indicate the presence of Fe(II) species in $FeWO_4$.[63] Likewise, the core-level spectra of W 4f (**Figure 6.6b**), with the fitted components presented in (**Figure 6.5b)**, present two specific peaks at 37.9 and 35.8 eV, which are ascribed to W $4f_{5/2}$ and W $4f_{7/2}$ states, respectively.[65] The high-resolution spectra of O 1s shown in (**Figure 6.5c)** indicate the presence of oxygen in metal oxide lattice ≈529.6 eV (orange line) as a major specie.[63] Other two photoelectron peaks of O 1s could be assigned to the possible photoemission of oxygen atoms adjacent to the oxygen vacancies in the $FeWO_4$ lattice, at the binding energy of 530.9–531.8 eV, and surface absorbed oxygens, at binding energy of 530.2–535 eV.[63,66,67] The atomic ratio between Fe and W of the as-prepared $FeWO_4$, $FeWO_4$ –500 °C, and $FeWO_4$ –700 °C films were estimated to be 1:0.99, 1:0.96, and 1: 0.90, respectively, which is in agreement with the composition structure. The XPS analyses reveal the presence of Fe^{2+} and W^{6+} in the monoclinic $FeWO_4$, with a ratio between these two components close to unity.

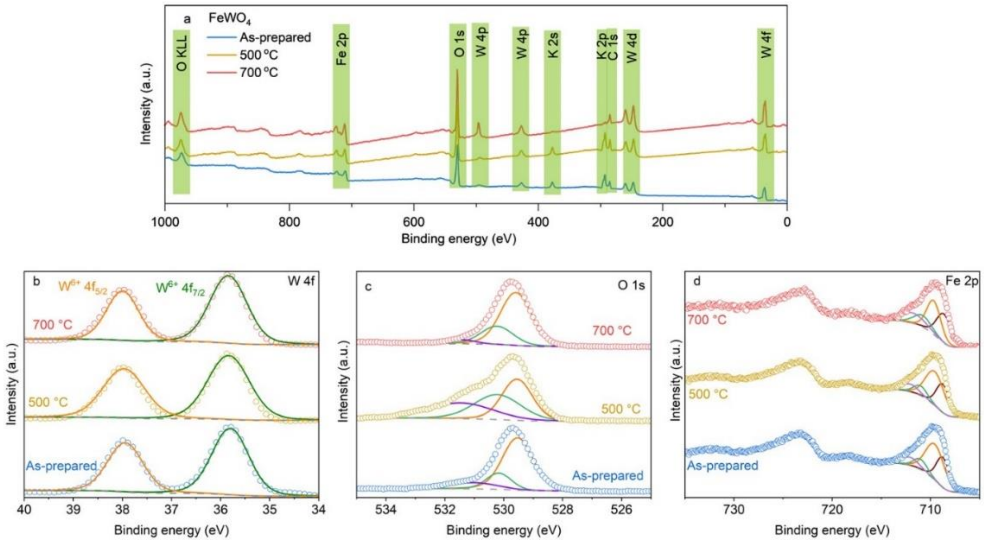

Figure 6.5 XPS analysis of the $FeWO_4$ –700, 500 °C and as-prepared films a) Full survey XPS spectra with the highlighted regions showing the photoemission of existing elements and high resolution XPS fitting spectra of b) W 4f, c) O 1s, and d) Fe 2p.

The light absorption properties of $FeWO_4$ films were investigated by ultraviolet-visible spectrophotometer (UV–Vis). These three $FeWO_4$ samples have very similar absorption spectra (**Figure 6.6c**), with the absorption edge at ≈690 nm, in line with previous reports.[41,45] The onset absorbance is gradually blue shifted when the $FeWO_4$ films were calcined at 500 and 700 °C,

suggesting a slight increase in the bandgap. The optical bandgap of these flame-made $FeWO_4$ photoanode was calculated by the Tauc plot (**Figure 6.6d**) to be ≈1.82, 1.86, and 1.91 eV for the as-prepared, $FeWO_4$–500 °C, $FeWO_4$–700 °C samples, respectively. These values are in agreement with the previous experimental and theoretical results in the literature (**Table 6.1**), ranging between 1.95 and 2.2 eV. For comparison, it can be seen that the optical bandgaps of three flame-made $FeWO_4$ films are relatively similar, and the increase in temperature of the post-thermal treatment does not have the noticeable impact on the light absorbance property.

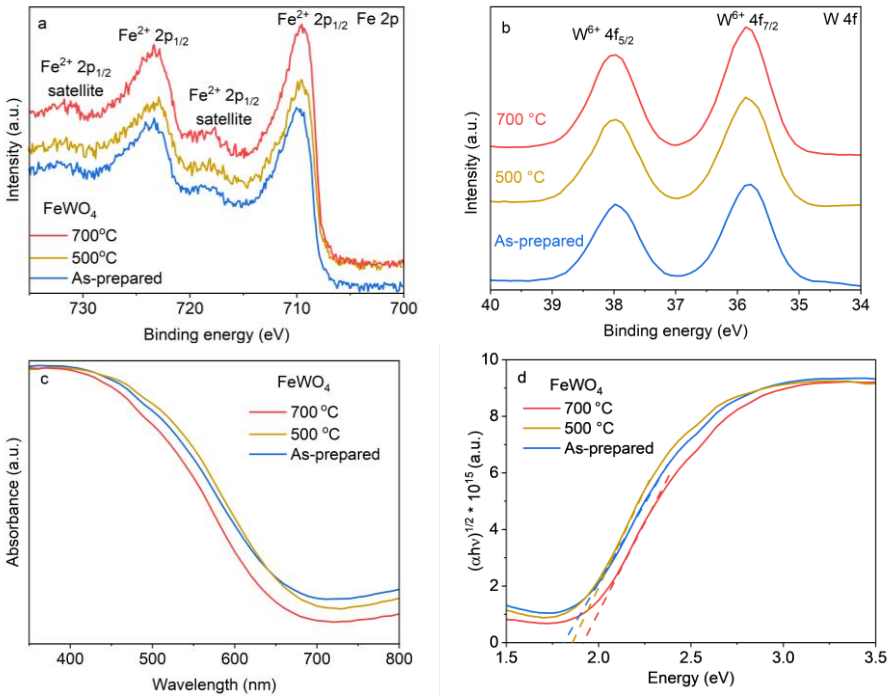

Figure 6.6 Physical characterization. High-resolution X-ray photoelectron spectra of a) Fe 2p, b) W 4f. c) UV-visible absorbance spectra and corresponding d) calculated Tauc plot.

To compare the intrinsic electrocatalytic activity of $FeWO_4$ photoanode, the electrochemically active surface area (ECSA) was first calculated using the double-layer capacitance current values derived from voltammetric measurements, shown in (**Figure 6.7a–d**).[68] The electrochemical double-layer capacitance of the catalytic surface was calculated from the slope of the capacitive current as a function of scan rates (**Figure 6.7d**).[69,70]. ECSA calculated from electrochemical double-layer and specific capacitances are presented in (**Table 6.2).** Note that for comparable ECSA, the specific capacitance and measured capacitance should be obtained in identical pH and applied potential conditions.[71] Here, a glassy carbon was used to obtain the specific capacitance (detail in the experimental), which was measured to be 0.052 mF cm^{-2} at 1.34 V versus RHE in 1 M KOH (**Figure 6.8**). This result indicates that the ECSA of as-prepared film is approximately three

times higher than those of samples obtained at 500 and 700 ºC. To investigate the impact of annealed temperatures on the surface area, the ECSA of $FeWO_4$ films at 400 and 600 ºC were also measured (**Figure 6.8a**–**b**). In summary, the capacitive current as a function of scan rate plots **(Figure 6.9c**) of $FeWO_4$ films at different synthesis treatment conditions reflected a decrease in the slope when calcinated temperature increases. Thus, higher temperature of post-synthesis treatment caused the lower ECSA, which is consistent with the results of the SEM analysis. Therefore, the growth of calcinated temperature is expected to reduce the PEC performance, which was confirmed through PEC measurement (**Figure 6.3**). Collectively, while the UV-Vis and XPS spectra indicate the similar optical property and surface composition of the investigated $FeWO_4$ photoanodes, their electrochemical results suggest that an increase in post-treated temperatures lowers ECSA.

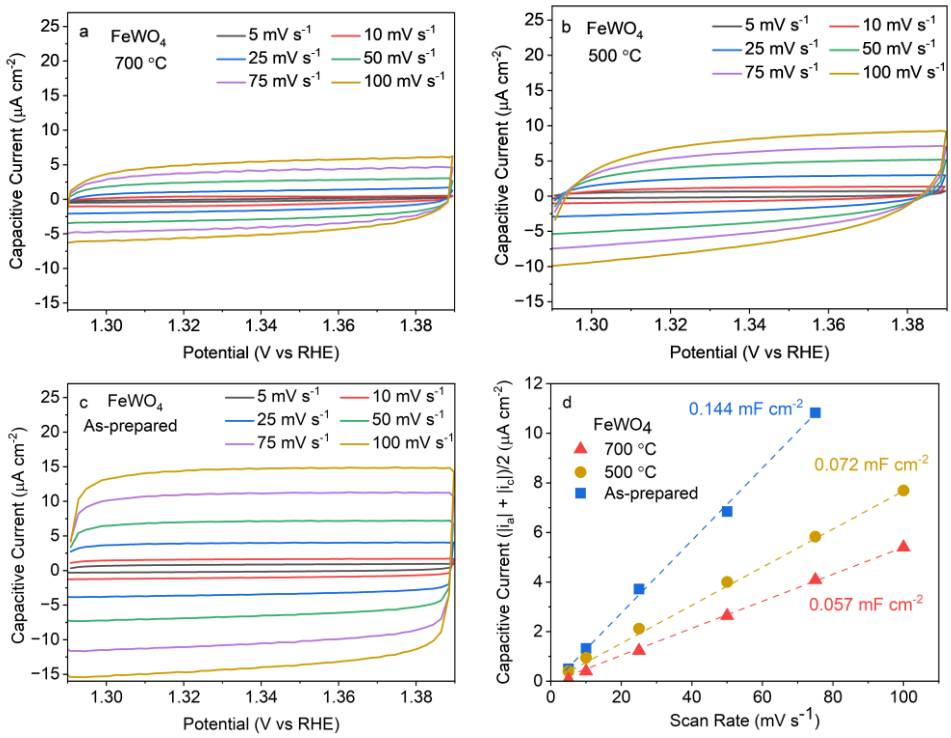

Figure 6.7 Electrochemical characterization. a–c) Capacitive current versus applied potential at different scan rates plots for a) 700 °C, b) 500 °C, c) as-prepared $FeWO_4$ photoanodes, and d) the capacitive current versus function of scan rates at 1.34 V versus RHE.

Table 6.2 Summary of the main optoelectronic and physicoelectrochemical properties of flame-made $FeWO_4$ photoanodes.

Samples	Optical Bandgap (eV)	Electrochemically Active Surface Area (cm^2)	Flat band potential (V versus RHE)	Donor density (cm_{geo}^{-3})
As-prepared	1.82	2.77	0.73	2.49×10^{21}
500 °C	1.86	1.38	0.72	9.71×10^{20}
700 °C	1.91	1.10	0.59	2.39×10^{20}

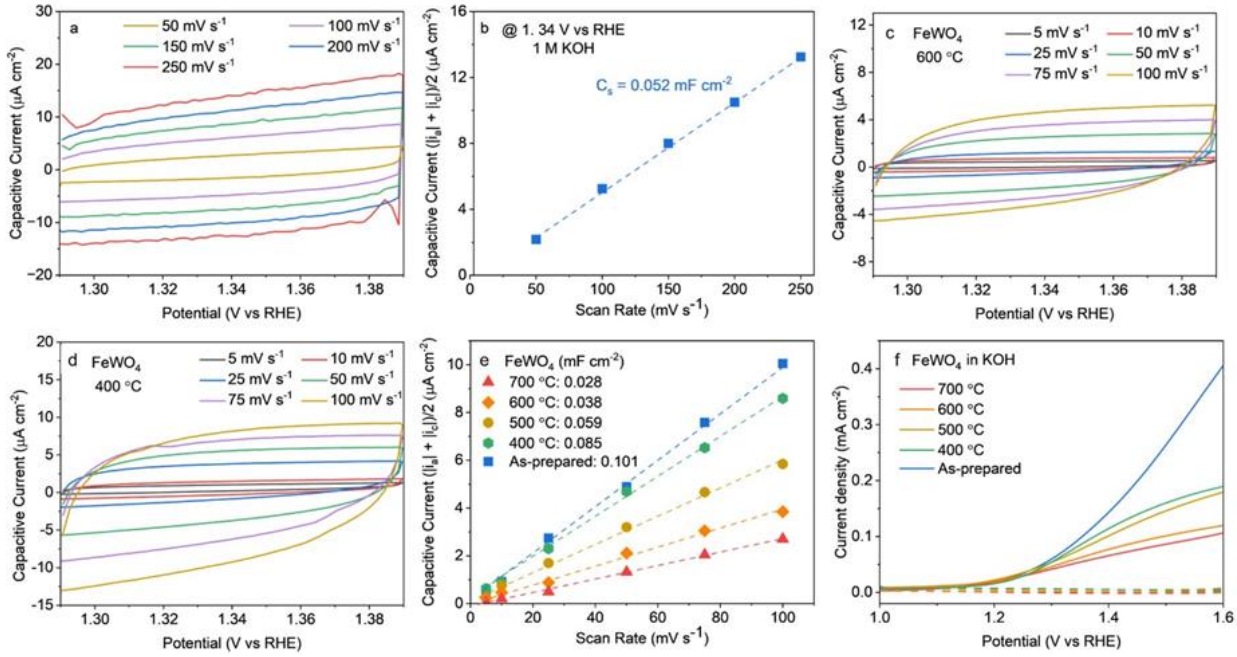

Figure 6.8 a) Capacitive current versus applied potential at different scan rates for a glassy carbon electrode, b) the capacitive current as a function of scan rates at 1.34 V versus RHE in 1 M KOH electrolyte, c–e) Capacitive current versus applied potential at different scan rates plots for c) 600 °C, d) 400 °C $FeWO_4$ photoanodes, e) the capacitive current as a function of scan rates at 1.34 V versus RHE, and f) linear sweep voltammetric (LSV) curves for water oxidation under 1 sun (100 mW cm^{-2}) of $FeWO_4$ prepared at different post-synthetic treatments conditions.

Mott – Schottky (MS) and electrochemical impedance spectroscopy (EIS) measurements were conducted to analyze the electrochemical properties of the flame-made $FeWO_4$ photoanodes with the detailed fitting parameters presented in (**Table 6.3**). To evaluate the range for MS analysis, we scanned real impedance over the wide range of frequency, which is from 0.5 to 15 kHz (**Figure 6.9a**). We found that the real impedance and the frequency start showing an independent

relationship in a frequency ranging from 10 to 15 kHz. The MS plots presented in (**Figure 6.9b–d)** of all three $FeWO_4$ films measure in different frequencies (10, 12.5, and 15 kHz) show positive slopes, confirming their n-type semiconductor behavior.[72] This n-type conductivity is supposed to attain from the synthesis conditions. There are some contradictory reports on the nature n-type or p-type of $FeWO_4$.[46,50,73–76] For example, Zhou et al.[46] reported that $FeWO_4$, synthesized by sputtering and annealing method, is n-type, while Sieber et al.[76] found this material is p-type when fabricated via a solid-state synthesis route from FeO and WO_3 precursors. These differences could be ascribed to the typical synthesis conditions (*e.g.,* temperature, pressure, and solvent), which tailor the number of vacancies, donor densities, or the crystal structures. In this work, the $FeWO_4$ photoanodes were fabricated via a hot-aerosol synthesis approach, which facilitates to the formation of oxygen vacancies,[58] and thus presenting a n-type semiconductor. The flat band potential is one of the important parameters impacting the charge transfer process across the semiconductor-electrolyte junction. Low flat band potential is expected to result in the greater (photo)electrochemical activity of anode at low onset potential. Indeed, for a given n-type semiconductor in contact with an electrolyte, the flat band potential would theoretically correspond to the photocurrent onset potential. However, in practice, the latter is usually more positive than the flat band potential depending on the surface recombination and surface modification. The flat band potential estimated from the MS plot was in the range of 0.59 – 0.73 V versus RHE for these three $FeWO_4$ films (**Table 6.2**). The annealed $FeWO_4$ films show a slight reduction of flat band potential of $FeWO_4$ –700 ºC from that of the as-prepared ones. This is tentatively attributed to the annealing process, which may decrease defect density and surface recombination sites. As-prepared $FeWO_4$ sample shows significantly lower slope than those of $FeWO_4$ films after post- calcination treatment. It reflected the higher donor density obtained from as-prepared $FeWO_4$ film. The donor densities were calculated for the geometric area and the real active surface area, which is the important factor to evaluate the area of porous photoelectrode.[68–71] All parameters used in the calculation were presented in (**Table 6.3**). The highest donor density calculated based on geometric area is 2.41×10^{21} cm^{-3} for as-prepared $FeWO_4$ film or 8.98×10^{20} cm^{-3} when normalizing in ECSA. The donor densities in ECSA are also plausible in the range of semiconductor material.[72,77–79] In comparison with annealed $FeWO_4$ films, the donor densities per geometric area of as-prepared sample is twice and ten times higher than that of $FeWO_4$ –500 ºC and $FeWO_4$ –700 ºC, respectively. The higher donor densities in as-prepared samples may increase the electrical conductivity and promote the charge transport, potentially benefiting the catalytic performance.[80–82]

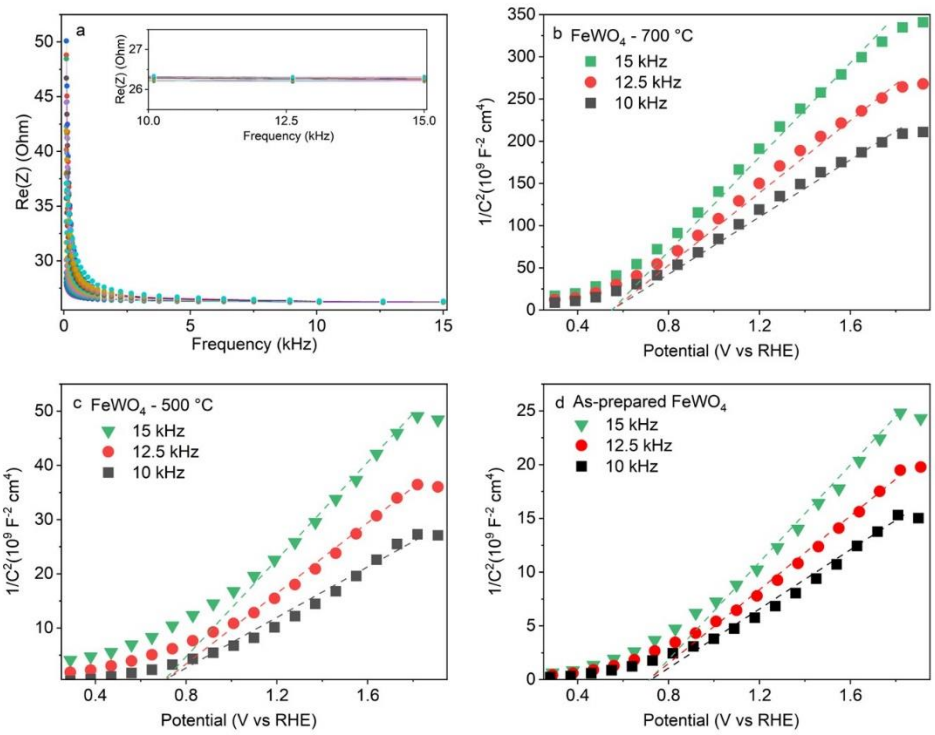

Figure 6.9 Electrochemical characterization. a) Plot of real impedance vs frequency obtained via Mott-Schottky analysis in the range 0.3 – 2 V vs RHE, b−d) Mott–Schottky plots measured at 10 kHz, 12.5 kHz, and 15 kHz of $FeWO_4$ at b) 700 °C, c) 500 °C in the dark, and d) as-prepared sample.

Table 6.3 Summary of donor density (N_D) calculation

	$FeWO_4$ – 700ºC	**$FeWO_4$ – 500ºC**	**As-prepared $FeWO_4$**
The elementary charge value (e) (C)		1.60×10^{-19}	
The relative permittivity of the semiconductor (ε)		4.86	
The permittivity in a vacuum (ε_0) (F/cm)		8.85×10^{-14}	
Slope of MS plots at 1 kHz	124×10^9	26.44×10^9	12.68×10^9
Donor density (N_D) (cm^{-3}_{geo})	2.39×10^{20}	9.71×10^{20}	2.49×10^{21}
Donor density (N_D) (cm^{-3}_{ECSA})	2.32×10^{20}	7.42×10^{20}	8.98×10^{20}

EIS measurements were also used to evaluate the kinetics of charge transfer for these $FeWO_4$ films. Nyquist plots obtained over a frequency range of 200 kHz to 0.1 Hz with 0.01 V amplitude are shown in (**Figure 6.10a**). An equivalent Randle circuit, used to fit the EIS results, is displayed in (**Figure 6.10b**), in which R_s is the series resistance, R_{ct} is the charge transfer resistance, and Q_{dl} is the constant phase element involving double-layer capacitance. The fitted values for R_s, R_{ct}, and Q_{dl}

are presented in (**Table 6.4**). The fitted values of R_{ct} are 1815 and 1758 for the $FeWO_4$ obtained at 500 °C and as-prepared samples, respectively, suggesting relatively similar charge transfer resistance of the as-prepared and $FeWO_4$ –500 °C samples. Nevertheless, the R_{ct} value of $FeWO_4$ – 700 °C film is 4586 **Ω**, which is nearly three times higher than that of the as-prepared sample. The highest charge transfer resistance from the $FeWO_4$ –700 °C photoanode could be originated from the presence of trace amounts of other $FeWO_4$ phases or minor phase segregation of iron and tungsten oxides at high post-thermal temperature,[39,40] or the reduction in the conductivity of the FTO glass substrate at higher temperature.[53]

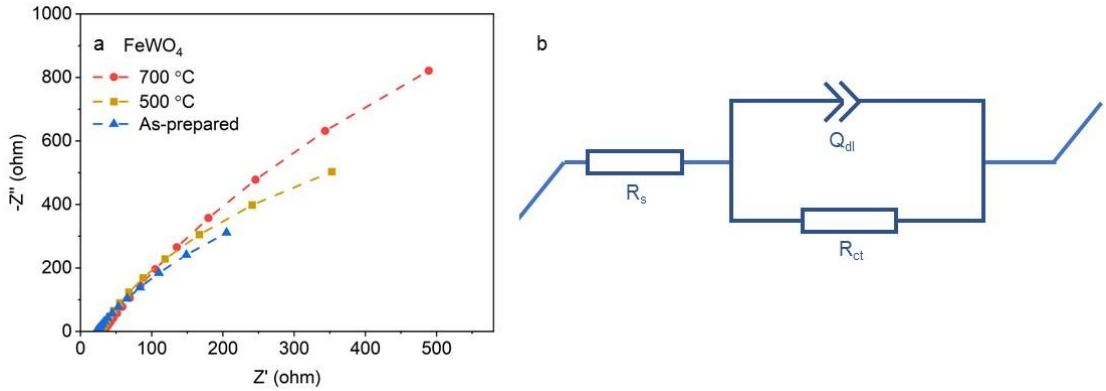

Figure 6.10 a) Nyquist plots collected by electrochemical impedance spectroscopy (EIS) measurement at 0.1 V versus RHE under dark conditions and b) Graph illustrating the Randle circuit used for electrochemical impedance spectroscopy fitting. R_s, R_{ct}, and Q_{dl} are the series resistance charge transfer resistance constant phase element involving double-layer capacitance.

Table 6.4 Summary of electrochemical impedance spectroscopy fitting for flame-made photoanodes.

	$FeWO_4$ – 700°C	**$FeWO_4$ – 500°C**	**As-prepared $FeWO_4$**
R_s (Ω)	32.33	27.53	22.10
R_{ct} (Ω)	4586	1815	1758
Q_{dl} (F cm^{-2} $s^{\alpha-1}$)	1.419×10^{-3}	2.14×10^{-3}	3.65×10^{-3}
α_{dl}	0.802	0.841	0.785

The photooxidation performance of the flame-made $FeWO_4$ photoanodes was then studied. First, the intrinsic photooxidation properties of these $FeWO_4$ photoanodes were investigated with the presence of sulfite in 1 M KOH electrolyte. The sulfite oxidation is more thermodynamically favorable (the standard redox potential of SO_3^{2-}/SO_4^{2-} reaction is –0.93 V versus normal hydrogen electrode (NHE))[83] and kinetically faster than water oxidation. As such, the surface recombination of the photogenerated carriers is negligible and hole transfer at the electrode-electrolyte interface is

generally assumed to be 100 %.[84] In the presence of sulfite (**Figure 6.11a**), the photocurrent density of as-prepared $FeWO_4$ is 0.32 mA cm^{-2} at 1.4 V versus RHE, which is ~1.5 and 3 times higher than those of $FeWO_4$ –500 ºC, $FeWO_4$ –700 ºC photoanodes, respectively, while their onset potentials are alike. Given the similar light absorption capability, the higher photocurrent density for sulfite oxidation of the as-prepared photoanode indicates lower carrier recombination in the bulk.

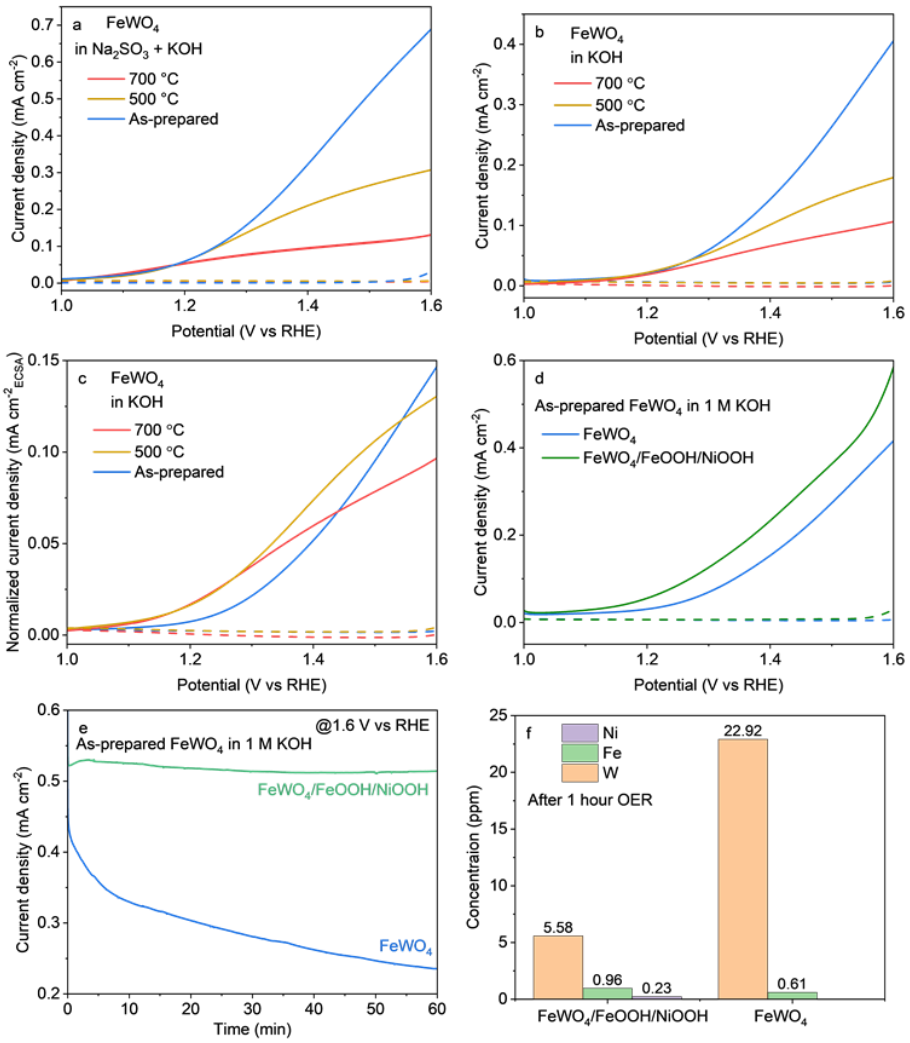

Figure 6.11 Photoelectrochemical water oxidation performance. a–c) Linear sweep voltammetric (LSV) curves of $FeWO_4$ prepared at different post-synthesis treatments conditions for a) sulfite oxidation, b) water oxidation, and c) water oxidation reaction normalized with ECSA. d) LSV and e) chronoamperometric (CA) curves at 1.6 V versus RHE of as-prepared $FeWO_4$ photoanodes with and without FeOOH/NiOOH co-catalysts. f) The inductively coupled plasma optical emission spectrometry (ICP-OES) results for the electrolytes after 1 h of PEC measurement at 1.6 V versus

RHE of as-prepared $FeWO_4$ and as-prepared $FeWO_4$/FeOOH/NiOOH. All PEC measurements were conducted under 1 sun (100 mW cm^{-2}) illumination.

The water photooxidation of these electrodes is presented below. (**Figure 6.11b)** displays the linear sweep voltammetry curves for water photooxidation of these flame-made photoanodes. Overall, the photoanodes possess similar onset potentials, which are around 1 V versus RHE, slightly higher than the flat band potential measurements (*vide supra*), and photocurrent density trend compared to the results obtained for the sulfite oxidation. The relatively high onset potential at about 1 V versus RHE was considered due to the limited PEC performance. It is possibly caused by the high energy level of surface states, which is similar to the previous reports about hematite electrodes.[85–87] Specifically, as-prepared samples achieved the highest photocurrent density at 1.4 V versus RHE, reaching 0.14 mA cm^{-2}, while these values are only 0.1 and 0.07 mA cm^{-2} for $FeWO_4$ –500 ºC, $FeWO_4$ –700 ºC photoanodes, respectively. Following the same order, the photocurrent densities of these samples approach 0.4, 0.18, and 0.09 mA cm^{-2} at 1.6 V versus RHE, respectively. The better catalytic performance of the as-prepared $FeWO_4$ compared to the other samples is attributed to its higher ECSA and electrical conductivity. To understand the intrinsic PEC activity of these $FeWO_4$ photoanodes surface, the photocurrents are normalized to the ECSA as shown in the LSV plots in (**Figure 6.11c**). Overall, the photocurrent densities normalized to the ECSA are correspondingly lower than those normalized to the geometrical areas due to the porous morphology. However, the ECSA-normalized photocurrent densities of these photoanodes are comparable, implying the similar catalytic activity of their surface. The incident photon-to-current conversion efficiencies (IPCE) of $FeWO_4$ photoanodes are shown in (**Figure 6.12a**). The as-prepared $FeWO_4$ photoanode shows a rising IPCE from about 550 nm and reaches a maximum IPCE of about 55 % at a light wavelength of 300 nm. It is higher than that obtained for annealed $FeWO_4$ films, which are in range 37–42 %. Although the absorption band edge of $FeWO_4$ films shown in UV-visible absorbance spectra is at approximately ≈690 nm, the IPCE values from 550 to 690 nm are very small. It is attributed to the significantly high recombination of electron-hole pairs due to a high number of surface and/or bulk defect states generally presented in flame-made photoanodes.[57,58] Moreover, $FeWO_4$ is predicted with intrinsically short charge carrier lifetime and diffusion lengths, which were reported in hematite electrodes and tungstate oxides anodes, such as Fe_2WO_6, $CuWO_4$, *etc*.[88–92]

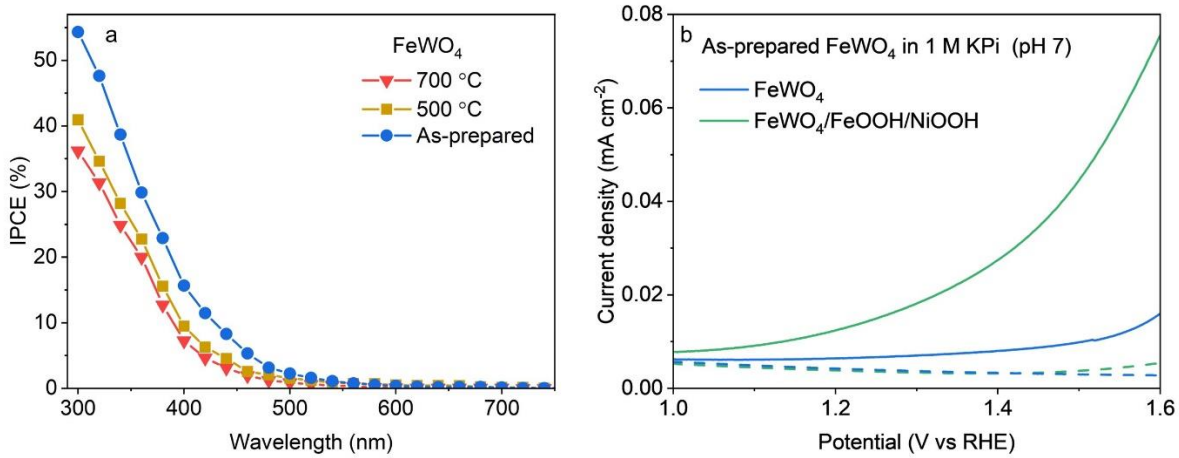

Figure 6.12 a) IPCE as a function of the wavelength measured at 1.4 V versus RHE of $FeWO_4$ prepared at different post-synthetic treatments conditions and b) linear sweep voltammetric (LSV) curves of as-prepared $FeWO_4$ photoanodes with and without FeOOH/NiOOH co-catalysts in 1 M sodium phosphate buffer (pH 7) under 1 sun (100 mW cm^{-2}) illumination.

To enhance the PEC water oxidation performance, oxygen evolution catalysts are generally incorporated with photoanodes.[54,84,93–95] FeOOH/NiOOH is reported as one of the most efficient cocatalysts in near-neutral and alkaline electrolytes; thus, it was deposited on the as-prepared $FeWO_4$ photoanode by a photoelectrodeposition method.[54,96,97] Although the photocurrent density improves slightly from 0.14 to 0.23 mA cm^{-2} at 1.4 V versus RHE and from 0.41 to 0.58 mA cm^{-2} at 1.6 V versus RHE (**Figure 6.11d**). The increased PEC performance of FeOOH/NiOOH cocatalysts on $FeWO_4$ films was further evaluated in neutral condition (pH 7). Following the LSV curves tested in 1 M KPi (**Figure 6.12b**), as-prepared $FeWO_4$ photoanode shows the limited PEC activity in neutral condition, with 0.01 mA cm^{-2} photocurrent obtained at 1.6 V versus RHE. In the presence of FeOOH/NiOOH cocatalyst, the enhanced PEC performance achieved 0.078 mA cm^{-2} photocurrent at 1.6 V versus RHE, which is still about 7 times lower than its performance in 1 M KOH (**Figure 6.11d**). A FeOOH/NiOOH cocatalyst layer is beneficial to enhance the photostability of $FeWO_4$ photoanode. The stability of as-prepared $FeWO_4$ and $FeWO_4$/FeOOH/NiOOH photoanodes were further investigated by monitoring the current density versus time at 1.6 V versus RHE. As shown in (**Figure 6.11e)**, the photocurrent density of as-prepared $FeWO_4$ film without a cocatalyst layer reduces substantially from 0.43 to 0.23 mA cm^{-2} after 1 h of continuous photoelectrochemical measurement, which accounts for ≈50 % degradation of the photocurrent. By contrast, the $FeWO_4$ photoanode with a FeOOH/NiOOH layer did not show any degradation

after the same period of time. It indicates that the reduction in the photocurrent density during the PEC test may be attributed to the dissolution of catalysts due to photocorrosion.[98,99]

To confirm this hypothesis, we carried out inductively coupled plasma–optical emission spectrometry (ICP-OES) measurements of the electrolytes after 1 h of PEC testing (**Figure 6.11f**). The data revealed significantly higher concentration of W (22.92 ppm) compared to Fe (0.61 ppm) in the electrolytes, indicating the higher dissolution rate of W in the $FeWO_4$ matrix. This could be explained by the intrinsic instability of W at high pH condition,[13,94,100] and the pH value in this study is 13.8. After introducing FeOOH/NiOOH, the concentration of W and F presented in the electrolyte are substantially decreased to 5.58 and 0.96 ppm, respectively. A small amount of Ni could be detected in the electrolyte, and this could come from the NiOOH layer. These ICP-OES and photoelectrocatalytic activity results indicate that the loss of the W from the $FeWO_4$ matrix is the primary reason causing the instability of $FeWO_4$, and that the FeOOH/NiOOH layer can improve the catalytic activity and stability of the photoanode.

6.3. Conclusions

Here, we report the ultrafast synthesis and structural engineering of $FeWO_4$ electrodes for water photooxidation reaction. Nanostructured photoanodes, with an optical bandgap of ≈1.82 eV, were fabricated within 13 s directly on FTO glass substrates via scalable flame synthesis. The impacts of post-thermal treatment temperatures on morphological structures, optical, physical, and (photo)electrochemical properties of $FeWO_4$ photoanodes are studied in detail. Increasing calcination temperature results in a reduction in electrochemically active surface area (ECSA) and electrical conductivity. As a result, the as-prepared $FeWO_4$ photoanode show higher ECSA, donor concentration, and (photo)electrochemical performance compared to the post-treated ones, achieving a photocurrent density for water oxidation of 0.23 mA cm^{-2} at 1.4 V versus RHE in 1 M KOH. The photoanode also demonstrates good photostability with the presence of FeOOH/NiOOH co-catalyst layer, retaining ≈96 % photocurrent density after 1 h of continuous photoelectrochemical measurement. Nonetheless, though having high light absorption capacity (≈1.8–1.9 eV), the photocurrents of $FeWO_4$ photoanodes are not comparable with $BiVO_4$. This could be attributed to the high recombination rate of the photogenerated carriers due to the defects, short carrier diffusion length, and/or slow reaction kinetics at the $FeWO_4$|co-catalyst interfaces. Moreover, its relatively high onset potential (≈0.8 eV) compared to that of $BiVO_4$ (≈0.2 eV) reduces the utilization of the electrical energy at low potentials. Therefore, further research should

be carried out to improve the charge transfer/separation efficiencies to utilize its excellent light absorption. This study demonstrates a rapid and scalable approach for the nanofabrication of $FeWO_4$ photoanodes and provides detailed information about the relationship between the material properties, activity and stability, setting the foundation for $FeWO_4$ further optimization and use in a variety of photoelectrochemical reactions.

6.4. Experimental section

6.4.1. Materials

All the chemical reagents and solvents for the material synthesis were used as received without any further purification. Ultrapure deionized water (resistivity 18.2 MΩ cm^{-1}) was used in preparing aqueous solutions in all experiments. Fluorine-doped tin oxide (FTO) glass (PV Tech, 7 Ω cm^{-1}) was cleaned with deionized (DI) water, then ethanol and DI water sequentially.

6.4.2. $FeWO_4$ photoanodes fabrication

A flame spray pyrolysis (FSP) system was employed to direct deposition of $FeWO_4$ onto FTO glass substrates in one-step process.[58,93,101] A solution with Fe atom and W atom concentration of 0.05 mol L^{-1} was prepared by dissolving ammonium (*meta*)tungstate hydrate (Aldrich, purity > 85 %) and iron (III) chloride (Aldrich, purity 97%) in a 1:1 v/v mixture of diethylene glycol monobutyl ether (Aldrich, purity > 98.5 %) and ethanol (Aldrich, purity > 99.5 %). This solution was supplied with a syringe pump at a rate of 5 mL min^{-1} and dispersed into a fine spray with 7 L min^{-1} oxygen at a constant pressure drop of 4.5 bar. The spray was ignited by supporting premixed methane/oxygen flames with a concentration of 1.8 and 2 L min^{-1}, respectively. A substrate holder placed at 6 cm height above the burner (HAB) was utilized for the deposition of $FeWO_4$ films on FTO substrates within 13 seconds. Then, residual WO_3 on the surface of $FeWO_4$ film was removed by cleaned with KOH following by DI water to obtain 'As-prepared $FeWO_4$' sample. The $FeWO_4$ photoelectrodes were calcined at 500 ºC for 2 hours to collect '$FeWO_4$ – 500 ºC' samples, then calcined at 700 ºC for 10 minutes for '$FeWO_4$ – 700 ºC' with 2 ºC ramming rate under air environment. '$FeWO_4$ – 400 ºC' and '$FeWO_4$ – 600 ºC' samples were deposited in the same process with '$FeWO_4$ – 500 ºC' sample but annealed at 400 ºC and 600 ºC, respectively.

6.4.3. Photoelectrodeposition of FeOOH/NiOOH

FeOOH/NiOOH co-catalyst was applied to modify the $FeWO_4$ surface following the preparation procedure of previous reports.[54,96,97] First, FeOOH was photoelectrodeposited on $FeWO_4$

electrodes using a 0.1 M $FeSO_4.7H_2O$ aqueous solution (ACS reagent, ≥99.0 %, Sigma-Aldrich) in a three-electrode cell layout with a back-side irradiation (100mW cm^{-2}, AM 1.5G) at a potential of 0.25 V vs Ag/AgCl/KCl(sat.) within 4 minutes, corresponding to a total passing charge of 4.07 mC cm^{-2}. Photoelectrodeposition of NiOOH on FeOOH-modified photanodes was undertaken using an aqueous 0.1 M $NiSO_4$ (≥99.0 %, Sigma-Aldrich) with a pH adjusted to 7.0 (using 0.1 M KOH solution), under backside irradiation (100mW cm^{-2}, AM 1.5G) at 0.11 V vs Ag/AgCl/KCl(sat.) for an optimal time of 2 minutes, which corresponds to a total passing charge of 0.926 mC cm^{-2}, followed by 1 minute electrodeposition of 0.1 M $NiSO_4$ at 1.2 V vs Ag/AgCl/KCl(sat.).

6.4.4. Material Characterization

The morphology of the films was investigated using a field-emission scanning electron microscope (FESEM) Zeiss Ultra Plus operating at 3 kV without coating and a high-resolution transmission electron microscope (HR-TEM) JEOL 2100F operating at 200 kV. Samples for SEM were prepared by fixing the cut pieces of the electrode on the specimen stubs using carbon tape, while samples for TEM were scratched off from the electrode surface and dropped on a 200 mesh holey carbon-supported copper grid.

X-ray diffraction (XRD) patterns were recorded by a D2 Phaser Bruker system with Cu Kα radiation of average wavelength 1.54056 Å at a scan rate of 1.17 deg min^{-1}. The XRD results were obtained by direct measurement of the samples on FTO substrates. To facilitate the visualization of the minor XRD peaks, the intensity of the X-ray diffraction was visualized with a linear (**Figure 6.1a**) and logarithmic (**Figure 6.1b**) intensity scale. Raman spectra were recorded at room temperature by LabRAM HR evolution CCD camera 532 delta diode laser, using grating 1800 (500 nm). The laser intensity was 100 percent. The spectra were collected at 50 seconds of acquisition time.

X-ray photoelectron spectroscopy (XPS) analysis was performed using a calibrated ESCALAB250Xi spectrometer (Thermo Scientific, UK) with a monochromated Al Kα source at a power of 120 W (13.8 kV × 8.7 mA). The base pressure in the main vacuum chamber during analysis was typically between 10^{-9} and 10^{-8} mbar. Survey spectra were acquired at pass energy of 160 eV. To obtain more detailed information about the chemical structure, oxidation states, and so forth, high-resolution spectra were recorded at 20 eV pass energy (yielding a typical peak width for polymers of approximately 1.0 eV). Spectra were collected at normal emission. The data was

analyzed using CasaXPS software version 2.3.25 PR1.0. Adventitious C 1s (284.8 eV) peak was used to calibrate the spectra.

UV–Vis absorption (*A* %) spectra of photoanodes prepared on FTO glass were calculated from (*A* = 100 - *T* -*R*), in which the transmittance (*T* %) and reflectance (*R* %) were measured by Perkin–Elmer (Lambda 1050 UV/vis/NIR) spectrophotometer and a 150mm integrating sphere. The optical bandgap (E_g) was calculated from the Tauc plot by the formula $(\alpha h\nu)^{\gamma} = A(h\nu - E_g)$, where α, *h*, ν, A, and E_g denote the absorption coefficient, Planck constant, photon's frequency, absorbance, and band gap energy, respectively.[102–105] The absorption coefficient was calculated by the formula $\alpha = (A \times \ln(10))\, L^{-1}$, in which L, the thickness of photoanode film, was 1 μm measured by SEM.[104,105] The γ factor depends on the nature of the electron transition and is equal to 1/2 to calculate the direct transition band gaps of $FeWO_4$.[103] The E_g values were thus determined by extrapolation of the linear relation to $(\alpha h\nu)^{1/2} = 0$.

The inductively coupled plasma−optical emission spectrometry (ICP-OES) performed by Agilent 5110 SVDV machine was used to analyze the Fe, W concentration in the electrolytes after 1 h PEC stability test. Samples for ICP-OES measurement were prepared by ten-fold diluting 0.5 mL electrolyte by adding 4.5 mL 2 % v/v HNO_3 solution.

6.4.5. Electrochemical and PEC experiments

All electrochemical measurements in this study were carried out with a CHI 760E (CH Instrument, Texas) electrochemical workstation. Photoelectrochemical performance of the electrodes was evaluated in a three-electrode configuration within a PTFE H-cell using a Pt wire as the counter electrode. A double-junction Ag|AgCl|KCl(sat.) (+0.197 V vs SHE) with a PTFE cover was used as the reference electrode. 1 M potassium hydroxide (KOH) solution (pH 13.6) was employed as an electrolyte, and 0.1 M sodium sulfite (Na_2SO_3) was added for the sulfite photooxidation. The potentials were converted to the reversible hydrogen electrode (RHE) scale via the Nernst equation:

$$E_{RHE} = E_{Ag/AgCl} + 0.197 + 0.059 \times pH$$ **(Equation 6.1)**

The light source was a solar simulator (LCS-100, Newport) equipped with a 100W Xe lamp and an AM 1.5G filter, calibrated with a reference cell and meter (Newport, model 91150 V). Light intensity used in PEC experiments is 1 sun (100 mW cm^{-2}). The linear sweep voltammetry was scanned from −0.2 to 0.8 V vs Ag/AgCl at 0.020 V s^{-1}. Photocurrent stability tests were conducted

by measuring the photocurrent under 1 sun (100 mW cm^{-2}) illumination at an applied bias of 0.6 V versus Ag/AgCl for 1 h.

The Mott-Schottky analysis was conducted in 1 M KOH at the frequencies of 10.0, 12.5, and 15 kHz and amplitude of 0.02 V in the dark at the potentials progressively changed from −1.0 to 0.8 V vs Ag/AgCl with 0.01 V increments. The flat-band potential (E_{FB}) and carrier density (N_D) were determined from the C^2 vs E plots using the standard relationship.

$$\frac{1}{C^2} = \frac{2}{N_D e \varepsilon \varepsilon_0}\left(E - E_{FB} - \frac{kT}{e}\right)$$

(Equation 6.2)

where C is the space charge capacitance of the semiconductor, e is the elementary charge value, ε is the relative permittivity of the semiconductor ($FeWO_4 \approx 4.86$),[73,106] ε_0 is the permittivity in a vacuum, E is the applied potential, T is the temperature, and k is the Boltzmann constant.

Electrochemical impedance spectra were collected at 0.1 V versus RHE over a frequency range of 0.1 Hz–200 kHz with a 5 mV amplitude in the dark. Electrochemically active surface area (ECSA) was investigated through the electrochemical capacitance current at 1.34 V vs RHE, which was measured by scanning cyclic voltammetry curves at different rates at the potential window of 1.29 to 1.39 V vs RHE. ECSA is calculated by comparing the double layer capacitance of the flame-made electrodes to that ECSA = C_{dl}/C_s, where C_s is the specific capacitance of an atomically smooth planar surface of the material per unit area under identical electrolyte conditions, meaning similar pH and applied potential range.[54,69–71] Here, a glassy carbon surface sourced from PINE research (AFE5T050GC with a disk diameter of 5 mm) was used to measure a specific capacitance of the planar electrode.

The incident photo-to-current efficiency (IPCE) spectra were recorded at 1.4 V versus RHE in 1 M KOH electrolyte using a 100 W Xenon lamp equipped with an Oriel Cornerstone 130 1/8 monochromator and a motorized filter wheel (model: USFW-100, Newport) to block higher order diffraction. IPCE values were calculated as below:

$$IPCE(\%) = \frac{1239.8(Vnm) \times j(mAcm^{-2})}{P_{mono}(mWcm^{-2}) \times \lambda(nm)}$$

(Equation 6.3)

where j is the photocurrent density, P_{mono} is the monochromic illumination power intensity, and λ is the wavelength at which photocurrent density and illumination power are measured.

6.5. References

[1] T. Kåberger, *Glob. Energy Interconnect.* **2018**, *1*, 48.

[2] H. Ishaq, I. Dincer, C. Crawford, *Int. J. Hydrogen Energy* **2022**, *47*, 26238.

[3] A. M. Oliveira, R. R. Beswick, Y. Yan, *Curr. Opin. Chem. Eng.* **2021**, *33*, 100701.

[4] O. Bičáková, P. Straka, *Int. J. Hydrogen Energy* **2012**, *37*, 11563.

[5] P. J. Megia, A. J. Vizcaino, J. A. Calles, A. Carrero, *Energy and Fuels* **2021**, *35*, 16403.

[6] J. Chi, H. Yu, *Chinese J. Catal.* **2018**, *39*, 390.

[7] A. Vilanova, P. Dias, T. Lopes, A. Mendes, *Chem. Soc. Rev.* **2024**, *53*, 2388.

[8] B. Turan, J.-P. Becker, F. Urbain, F. Finger, U. Rau, S. Haas, *Nat. Commun.* **2016**, *7*, 12681.

[9] B. Tam, O. Babacan, A. Kafizas, J. Nelson, *Energy Environ. Sci.* **2024**, *17*, 1677.

[10] S. Imran, M. Hussain, *Int. J. Hydrogen Energy* **2024**, *77*, 975.

[11] H. Song, S. Luo, H. Huang, B. Deng, J. Ye, *ACS Energy Lett.* **2022**, *7*, 1043.

[12] P. Subramanyam, B. Meena, V. Biju, H. Misawa, S. Challapalli, *J. Photochem. Photobiol. C Photochem. Rev.* **2022**, *51*, 100472.

[13] Y. Wang, W. Tian, C. Chen, W. Xu, L. Li, *Adv. Funct. Mater.* **2019**, *29*, 1809036.

[14] X. Yao, D. Wang, X. Zhao, S. Ma, P. S. Bassi, G. Yang, W. Chen, Z. Chen, T. Sritharan, *Energy Technol.* **2018**, *6*, 100.

[15] L. Wang, Y. Zhang, W. Li, L. Wang, *Mater. Reports Energy* **2023**, *3*, 100232.

[16] M. H. Sawal, A. A. Jalil, N. F. Khusnun, N. S. Hassan, M. B. Bahari, *Electrochim. Acta* **2023**, *467*, 143142.

[17] Z. Najaf, D. L. T. Nguyen, S. Y. Chae, O.-S. Joo, A. U. H. A. Shah, D.-V. N. Vo, V.-H. Nguyen, Q. Van Le, G. Rahman, *Int. J. Hydrogen Energy* **2021**, *46*, 23334.

[18] R. Abdullah, A. A. Jalil, M. Asmadi, N. S. Hassan, M. B. Bahari, M. Alhassan, N. M. Izzudin, M. H. Sawal, R. Saravanan, H. Karimi-Maleh, *Int. J. Hydrogen Energy* **2024**, DOI 10.1016/j.ijhydene.2024.05.461.

[19] H. Shi, H. Guo, S. Wang, G. Zhang, Y. Hu, W. Jiang, G. Liu, *Energy and Fuels* **2022**, *36*, 11404.

[20] P. Luan, J. Zhang, *ChemElectroChem* **2019**, *6*, 3227.

[21] D. K. Lee, D. Lee, M. A. Lumley, K.-S. Choi, *Chem. Soc. Rev.* **2019**, *48*, 2126.

[22] W. Lei, Y. Yu, H. Zhang, Q. Jia, S. Zhang, *Mater. Today* **2022**, *52*, 133.

[23] H. He, A. Liao, W. Guo, W. Luo, Y. Zhou, Z. Zou, *Nano Today* **2019**, *28*, 100763.

[24] J. Yang, D. Wang, H. Han, C. Li, *Acc. Chem. Res.* **2013**, *46*, 1900.

[25] M. Kumar, B. Meena, P. Subramanyam, D. Suryakala, C. Subrahmanyam, *NPG Asia Mater.* **2022**, *14*, DOI 10.1038/s41427-022-00436-x.

[26] Z. Yu, Q. Huang, X. Jiang, X. Lv, X. Xiao, M. Wang, Y. Shen, G. Wittstock, *Anal. Chem.* **2021**, *93*, 12221.

[27] D. Li, J. Shi, C. Li, *Small* **2018**, *14*, 1.

[28] Z. Luo, C. Li, D. Zhang, T. Wang, J. Gong, *Chem. Commun.* **2016**, *52*, 9013.

[29] H. Song, L. Zhu, Y. Li, Z. Lou, M. Xiao, Z. Ye, *J. Mater. Chem. A* **2015**, *3*, 8353.

[30] Y. Guo, Y. Fu, Y. Liu, S. Shen, *RSC Adv.* **2014**, *4*, 36967.

[31] J. H. Kim, J. H. Kim, J.-W. Jang, J. Y. Kim, S. H. Choi, G. Magesh, J. Lee, J. S. Lee, *Adv. Energy Mater.* **2015**, *5*, 1401933.

[32] F. F. Abdi, S. P. Berglund, R. van de Krol, in *Photoelectrochem. Sol. Fuel Prod.*, Springer International Publishing, Cham, **2016**, pp. 355–391.

[33] C.-M. Wu, S. Naseem, M.-H. Chou, J.-H. Wang, Y.-Q. Jian, *Front. Mater.* **2019**, *6*, 49.

[34] R. Schuler, F. Bianchini, T. Norby, H. Fjellvåg, *ACS Appl. Mater. Interfaces* **2021**, *13*, 7416.

[35] K. Dubey, S. Dubey, V. Sahu, R. A. Parry, A. Modi, F. Z. Haque Khan, N. K. Gaur, *Mater. Today Proc.* **2022**, *67*, 170.

[36] S. Caubergh, N. Matsubara, F. Damay, A. Maignan, F. Fauth, P. Manuel, D. D. Khalyavin, B. Vertruyen, C. Martin, *Inorg. Chem.* **2020**, *59*, 9798.

[37] M. M. Khader, M. M. Saleh, E. M. El-Naggar, *J. Solid State Electrochem.* **1998**, *2*, 170.

[38] K. Sieber, H. Leiva, K. Kourtakis, R. Kershaw, K. Dwight, A. Wold, *J. Solid State Chem.* **1983**, *47*, 361.

[39] F. F. Abdi, A. Chemseddine, S. P. Berglund, R. van de Krol, *J. Phys. Chem. C* **2017**, *121*, 153.

[40] S. Caubergh, N. Matsubara, F. Damay, F. Fauth, D. D. Khalyavin, P. Manuel, A. Mahmoud, D. Poelman, C. Martin, B. Vertruyen, *J. Phys. Chem. C* **2021**, *125*, 25907.

[41] B. Jansi Rani, G. Ravi, R. Yuvakkumar, M. Praveenkumar, S. Ravichandran, P. Muthu Mareeswaran, S. I. Hong, *ACS Omega* **2019**, *4*, 5241.

[42] M. K. Adak, A. Rajput, L. Mallick, B. Chakraborty, *ACS Appl. Energy Mater.* **2022**, *5*, 5652.

[43] Q. Gao, Z. Liu, *Prog. Nat. Sci. Mater. Int.* **2017**, *27*, 556.

[44] T. N. Kovács, G. Pokol, F. Gáber, D. Nagy, T. Igricz, I. E. Lukács, Z. Fogarassy, K. Balázsi, I. M. Szilágyi, *Mater. Res. Bull.* **2017**, *95*, 563.

[45] J. Guo, X. Zhou, Y. Lu, X. Zhang, S. Kuang, W. Hou, *J. Solid State Chem.* **2012**, *196*, 550.

[46] L. Zhou, A. Shinde, S. K. Suram, H. S. Stein, S. R. Bauers, A. Zakutayev, J. S. Duchene, G. Liu, E. A. Peterson, J. B. Neaton, J. M. Gregoire, *ACS Energy Lett.* **2018**, *3*, 2769.

[47] Z. Chen, H. Ma, J. Xia, J. Zeng, J. Di, S. Yin, L. Xu, H. Li, *Ceram. Int.* **2016**, *42*, 8997.

[48] J. Zhang, Y. Wang, S. Li, X. Wang, F. Huang, A. Xie, Y. Shen, *CrystEngComm* **2011**, *13*, 5744.

[49] F. Yu, L. Cao, J. Huang, J. Wu, *Ceram. Int.* **2013**, *39*, 4133.

[50] S. Bera, S. B. Rawal, H. J. Kim, W. I. Lee, *ACS Appl. Mater. Interfaces* **2014**, *6*, 9654.

[51] E. Goudeli, M. L. Eggersdorfer, S. E. Pratsinis, *Langmuir* **2015**, *31*, 1320.

[52] F. Pierce, C. M. Sorensen, A. Chakrabarti, *Phys. Rev. E* **2006**, *74*, 021411.

[53] H. Chen, R. Bo, T. Tran-Phu, G. Liu, A. Tricoli, *Chempluschem* **2018**, *83*, 569.

[54] T. Tran-Phu, Z. Fusco, I. Di Bernardo, J. Lipton-Duffin, C. Y. Toe, R. Daiyan, T. Gengenbach, C.-H. Lin, R. Bo, H. T. Nguyen, G. M. J. Barca, T. Wu, H. Chen, R. Amal, A. Tricoli, *Chem. Mater.* **2021**, *33*, 3553.

[55] T. Tran-Phu, R. Daiyan, Z. Fusco, Z. Ma, L. R. A. Rahim, A. Kiy, P. Kluth, X. Guo, Y. Zhu, H. Chen, R. Amal, A. Tricoli, *J. Mater. Chem. A* **2020**, *8*, 11233.

[56] G. Liu, S. K. Karuturi, H. Chen, L. Spiccia, H. H. Tan, C. Jagadish, D. Wang, A. N. Simonov, A. Tricoli, *Nano Energy* **2018**, *53*, 745.

[57] H. Chen, H. K. Mulmudi, A. Tricoli, *Chinese Chem. Lett.* **2020**, *31*, 601.

[58] T. Tran-Phu, R. Daiyan, X. M. C. Ta, R. Amal, A. Tricoli, *Adv. Funct. Mater.* **2022**, *32*, 1.

[59] G. Liu, S. K. Karuturi, A. N. Simonov, M. Fekete, H. Chen, N. Nasiri, N. H. Le, P. Reddy Narangari, M. Lysevych, T. R. Gengenbach, A. Lowe, H. H. Tan, C. Jagadish, L. Spiccia, A. Tricoli, *Adv. Energy Mater.* **2016**, *6*, 1600697.

[60] G. Liu, J. Hall, N. Nasiri, T. Gengenbach, L. Spiccia, M. H. Cheah, A. Tricoli, *ChemSusChem* **2015**, *8*, 4162.

[61] J. Ruiz-Fuertes, D. Errandonea, S. López-Moreno, J. González, O. Gomis, R. Vilaplana, F. J. Manjón, A. Muñoz, P. Rodríguez-Hernández, A. Friedrich, I. A. Tupitsyna, L. L. Nagornaya, *Phys. Rev. B - Condens. Matter Mater. Phys.* **2011**, *83*, 1.

[62] W. Hu, Y. Zhao, Z. Liu, C. W. Dunnill, D. H. Gregory, Y. Zhu, *Chem. Mater.* **2008**, *20*, 5657.

[63] M. C. Biesinger, B. P. Payne, A. P. Grosvenor, L. W. M. Lau, A. R. Gerson, R. S. C. Smart, *Appl. Surf. Sci.* **2011**, *257*, 2717.

[64] P. Mills, J. L. Sullivan, *J. Phys. D. Appl. Phys.* **1983**, *16*, 723.

[65] A. K.-V. S. W. G. and C. J. P. Alexander V. Naumkin, "NIST X-ray Photoelectron Spectroscopy Database," **n.d.**

[66] P. R. Norton, *Surf. Sci.* **1975**, *47*, 98.

[67] O. A. Chuvenkova, E. P. Domashevskaya, S. V. Ryabtsev, Y. A. Yurakov, A. E. Popov, D. A. Koyuda, D. N. Nesterov, D. E. Spirin, R. Y. Ovsyannikov, S. Y. Turishchev, *Phys. Solid State* **2015**, *57*, 153.

[68] A. J. Bard, Larry R. Faulkner, *Electrochemical Methods: Fundamentals and Applications*, Wiley, **2001**.

[69] S. Trasatti, O. A. Petrii, *J. Electroanal. Chem.* **1992**, *327*, 353.

[70] C. C. L. McCrory, S. Jung, J. C. Peters, T. F. Jaramillo, *J. Am. Chem. Soc.* **2013**, *135*, 16977.

[71] P. Connor, J. Schuch, B. Kaiser, W. Jaegermann, *Zeitschrift für Phys. Chemie* **2020**, *234*, 979.

[72] K. Sivula, *ACS Energy Lett.* **2021**, *6*, 2549.

[73] K. Hoang, *Phys. Rev. Mater.* **2017**, *1*, 024603.

[74] A. K. Chakraborty, M. R. Islam, M. H. Uddin, M. M. Rhaman, *J. Clust. Sci.* **2018**, *29*, 67.

[75] A. Godula-Jopek, D. Stolten, C. Bourasseau, *Hydrogen Production by Electrolysis*, WILEY-VCH Verlag GmbH & Co. KGaA, Weinheim, Germany, **2015**.

[76] K. Sieber, K. Kourtakis, R. Kershaw, K. Dwight, A. Wold, *Mater. Res. Bull.* **1982**, *17*, 721.

[77] A. Hankin, F. E. Bedoya-Lora, J. C. Alexander, A. Regoutz, G. H. Kelsall, *J. Mater. Chem. A* **2019**, *7*, 26162.

[78] I.-H. Toor, *J. Electrochem. Soc.* **2011**, *158*, C391.

[79] K. D. Malviya, D. Klotz, H. Dotan, D. Shlenkevich, A. Tsyganok, H. Mor, A. Rothschild, *J. Phys. Chem. C* **2017**, *121*, 4206.

[80] G. Wang, Y. Ling, H. Wang, X. Yang, C. Wang, J. Z. Zhang, Y. Li, *Energy Environ. Sci.* **2012**, *5*, 6180.

[81] W. Si, F. Haydous, U. Babic, D. Pergolesi, T. Lippert, *ACS Appl. Energy Mater.* **2019**, *2*, 5438.

[82] H. Chen, G. Liu, L. Wang, *Sci. Rep.* **2015**, *5*, 10852.

[83] T. J. B. ds. W. M. Haynes, D. R. Lide, *CRC Handbook of Chemistry and Physics: A Ready-Reference Book of Chemical and Physical Data, 97th Ed*, CRC Press, Boca Raton, **n.d.**

[84] T. W. Kim, K. S. Choi, *Science (80-.).* **2014**, *343*, 990.

[85] Z. Wang, F. Fan, S. Wang, C. Ding, Y. Zhao, C. Li, *RSC Adv.* **2016**, *6*, 85582.

[86] J. Y. Kim, G. Magesh, D. H. Youn, J.-W. Jang, J. Kubota, K. Domen, J. S. Lee, *Sci. Rep.* **2013**, *3*, 2681.

[87] C. Du, X. Yang, M. T. Mayer, H. Hoyt, J. Xie, G. McMahon, G. Bischoping, D. Wang, *Angew. Chemie Int. Ed.* **2013**, *52*, 12692.

[88] L. M. Carneiro, S. K. Cushing, C. Liu, Y. Su, P. Yang, A. P. Alivisatos, S. R. Leone, *Nat. Mater.* **2017**, *16*, 819.

[89] D. Peeters, O. Mendoza Reyes, L. Mai, A. Sadlo, S. Cwik, D. Rogalla, H. W. Becker, H. M. Schütz, J. Hirst, S. Müller, D. Friedrich, D. Mitoraj, M. Nagli, M. C. Toroker, R. Eichberger, R. Beranek, A. Devi, *J. Mater. Chem. A* **2018**, *6*, 10206.

[90] D. Kong, X. Hu, J. Geng, Y. Zhao, D. Fan, Y. Lu, W. Geng, D. Zhang, J. Liu, H. Li, X. Pu, *Appl. Surf. Sci.* **2022**, *591*, 153256.

[91] W. Guo, Z. Duan, O. Mabayoje, W. D. Chemelewski, P. Xiao, G. Henkelman, Y. Zhang, C. B. Mullins, *J. Electrochem. Soc.* **2016**, *163*, H970.

[92] B. . Zou, V. Volkov, *J. Phys. Chem. Solids* **2000**, *61*, 757.

[93] T. Tran-Phu, R. Daiyan, Z. Fusco, Z. Ma, R. Amal, A. Tricoli, *Adv. Funct. Mater.* **2020**, *30*, 1906478.

[94] C. R. Lhermitte, J. Garret Verwer, B. M. Bartlett, *J. Mater. Chem. A* **2016**, *4*, 2960.

[95] D. K. Zhong, D. R. Gamelin, *J. Am. Chem. Soc.* **2010**, *132*, 4202.

[96] T. W. Kim, K.-S. Choi, *Science (80-.).* **2014**, *343*, 990.

[97] T. Tran-Phu, H. Chen, R. Bo, I. Di Bernardo, Z. Fusco, A. N. Simonov, A. Tricoli, *Energy Technol.* **2019**, *7*, 1801052.

[98] Y. Yang, Y. Ling, G. Wang, T. Liu, F. Wang, T. Zhai, Y. Tong, Y. Li, *Nano Lett.* **2015**, *15*, 7051.

[99] B. Weng, M. Y. Qi, C. Han, Z. R. Tang, Y. J. Xu, *ACS Catal.* **2019**, *9*, 4642.

[100] R. S. Lillard, G. S. Kanner, D. P. Butt, *J. Electrochem. Soc.* **1998**, *145*, 2718.

[101] T. Tran-Phu, R. Daiyan, J. Leverett, Z. Fusco, A. Tadich, I. Di Bernardo, A. Kiy, T. N. Truong, Q. Zhang, H. Chen, P. Kluth, R. Amal, A. Tricoli, *Chem. Eng. J.* **2022**, *429*, 132180.

[102] J. Tauc, *Mater. Res. Bull.* **1968**, *3*, 37.

[103] P. Makuła, M. Pacia, W. Macyk, *J. Phys. Chem. Lett.* **2018**, *9*, 6814.

[104] A. Z. Johannes, R. K. Pingak, M. Bukit, *IOP Conf. Ser. Mater. Sci. Eng.* **2020**, *823*, 012030.

[105] Ł. Haryński, A. Olejnik, K. Grochowska, K. Siuzdak, *Opt. Mater. (Amst).* **2022**, *127*, 112205.

[106] B. Huang, J. N. Hart, *Phys. Chem. Chem. Phys.* **2020**, *22*, 1727.

Chapter 7. Conclusions and Future Outlook

7.1. Conclusions

In demand for wide employment of hydrogen (H_2) as an alternative energy source to sufficiently replace fossil fuels, water electrolysis, a key-driven technology for green H_2 production, garners significant research interest. One of the imperative factors for efficient water electrolysis system is to efficiently catalyze the challenging process, OER, which has several weaknesses regarding cost, activity, and stability. Therefore, this thesis is devoted to developing low-cost, efficient, and stable OER (photo)electrocatalysts for applications in some promising industrial and renewable-integrated water electrolysis systems. They include PEMWE, the main research interest focusing on acidic water electrolysis, and the PEC electrolyzer.

PEMWE is an emerging key technology for industrial-scale H_2 production due to its high efficiency and robust design. Nevertheless, its development is obstructed by the harsh condition at low pH, limiting the use of earth-abundant-based electrocatalysts and causing the reliance on noble materials. Especially for OER, the main challenges of non-noble-metal-based electrocatalysts are the poor stability at low pH and high oxidation conditions. Therefore, in our work, we concentrated on resolving the instability issues for earth-abundant-based OECs by some stabilization strategies, which could prolong the stable operation with no considerably negative impact on their activity. In the first research, we proposed the nanoscale-thin oxide layers prepared by ALD that could sufficiently protect the non-noble OER electrocatalyst, Co_3O_4, and increase its stability with no considerable decrease in this activity. The protective effect was controlled by the interfacial bonding energy between the main catalyst and the outer layers and their intrinsic thermodynamical stability. The acidic corrosion of electrodes was also systematically investigated by a comprehensive range of material characteristics analysis to provide insights for further stabilization studies. The optimal HfO_2 layer with a thickness at around 12 nm showed the best protective effect for Co_3O_4 catalyst, which achieved durability by more than threefold the uncoated electrode. This exemplified study of the Co_3O_4 electrocatalyst is expected to provide a potential strategy to resolve the durable issues of intrinsically active catalysts in acidic water electrolysis due to its feasibility and versatility.

Although the passivation layers deposited by ALD are proven to be effective in enhancing the stability of non-noble OER catalysts, they cannot totally prevent the degradation of catalysts under the corrosion of acidic water electrolysis. Another strategy was utilizing stable matrix constructed by self-healing materials integrated with the catalytic components, which achieved sustainable

operation in long-term OER test in acidic electrolyte. It was attributed to the quasi-equilibrium state between the solid and dissolved catalyst species in the electrolyte, where the loss of catalyst from corrosion process is at the same or slower rate than its re-electrodeposition. The efficient self-healing OEC system proposed was the mixed oxide composing the stable structural component, BiO_x, and the catalytic part based on the active Ni-based material. By a systematic investigation of the self-healing behavior of catalysts under different electrolyte conditions (pH, electrolyte composition, dissolved ions, buffer concentration), mixed oxide $[Ni\text{-}Bi]O_x$ electrocatalyst showed the most stable performance in over 200 hours in electrolyte at pH ~ 1. It is expected to provide a guide in the design of a truly stable and affordable OER electrocatalyst for PEMWE.

The second research pathway concentrates on developing photoelectrocatalysts to fuel OER in PEC water splitting. Although PEC water splitting is an attractive approach to utilizing solar energy in the electrolysis system and reducing external electricity consumption, its growth is obstructed and necessitates efficient photoelectrocatalysts for light absorption and catalyzing reaction. Instead of some conventional photoelectrocatalys ($BiVO_4$, WO_3, Fe_2O_3), which further enhancement is now very challenging, our research was directed toward the novel ternary metal oxides photoanodes, iron tungstate, by flame spray pyrolysis (FSP). FSP was determined as a highly versatile, fast, and potential technology for developing active photoelectrocatalysts with porous fractal structures and offering significant opportunities to optimize materials by post-treatment process. The systematic physicochemical and optoelectronic investigations reflected the influence of the post-thermal treatment process on the surface morphology, composition, resulting in the change of PEC activity of catalysts. The coupling with the co-catalyst FeOOH/NiOOH layer could reduce the photocorrosion and increase the photostability of photoanodes. Despite some remaining weaknesses, iron tungstate is demonstrated as a promising PEC catalyst with significant possibility for further enhancement studies.

In conclusion, this thesis proposed useful insights to develop low-cost OER (photo)electrocatalysts for water splitting reaction. Besides the activity, their significant limitation is stability, which is indeed imperative for further application in acidic electrolysis. While the nano-scale passivation layer is more versatile and can be suitable to improve the stability of different electrocatalysts, self-healing materials hold considerable potential to construct the acidic stable structure in more sustainable operation in specific operation conditions. Together, these approaches are expected to represent complementary strategies for advancing the longevity of non-noble-metal-based OER electrocatalysts in acidic environments. In the second research system, PEC water splitting is a

promising strategy for employing solar energy to fuel green H_2 production. Exploring ternary metal oxide photoelectrocatalysts and developing them based on the FSP technique can open a potential direction toward highly efficient PEC water splitting in the future.

As above, a combination of photoelectro- and electrochemical water splitting by PEC and PEMWE systems, respectively, using non-precious materials, is considered the most promising approach for advancing sustainable H_2 production. In this hybrid approach, PEMWE provides a highly efficient system with a compact design that can be modularized for deployment across a wide range of geographical locations, climates, and industrial settings. Due to this flexibility, PEMWE plays a key role in supplying the large-scale H_2 energy to satisfy industrial or transportation demands. One of the promising solutions to overcome the cost barrier of this technology is to use earth-abundant-based electrocatalysts developed by our stabilization strategies. While passivation layers provide a broadly applicable means of enhancing catalyst durability without significantly compromising activity, self-healing materials offer dynamic and sustainable operation under harsh conditions. The synergistic employment of these strategies is expected to address the stability issue of non-noble-based electrocatalysts and enhance the economic feasibility of H_2 production by PEMWE. In parallel, the employment of PEC systems, especially those driven by low-cost, flame-made photoelectrodes, has the potential to enhance overall energy efficiency and reduce the electricity input required for H_2 production, especially for regions with continuous high solar irradiance available to exploit. However, for uninterrupted and large-scale H_2 supply, it is necessary to integrate the PEC system with a reliable and efficient PEMWE. In such a hybrid arrangement, PEC can play a role to additionally increase the amount of H_2 production by the support of solar irradiation during sunny periods, while the PEMWE, with its high efficiency and fast dynamic response, operates continuously (day and night) to ensure a steady, large-scale hydrogen output.

7.2. Future Outlook

7.2.1. Optimization the preparation process

For efficient green H_2 production by water electrolysis, the activity and stability of OER (photo)electrocatalysts are undeniably important aspects. These factors, especially for activity, are directly controlled by the materials properties such as structure, morphology, composition, and defects, *i.e.*, which can be optimized in the synthesis or further treatment process. Further research on the preparation process supported by our stabilization strategies has the potential to explore the efficient acidic electrocatalysts that satisfy the industrial requirements.

In the scope of this thesis, sputtering is the primary synthesis technology, allowing the fabrication of thin film and nanostructured materials with precise control of thickness and composition. These advantages make it potential for the deposition of stable and homogeneous thin films of OER electrocatalyst in acidic water electrolysis and suitable to exemplified studies relating to stabilization strategies. In the meantime, FSP is an appropriate synthesis method to deposit and improve photoelectrocatalysts, thanks to its possibility to optimize surface morphology and composition. One of the promising strategies for further enhancement of catalysts' performance is doping, which is suitable for both preparation methods. Introducing impurities elements into the intrinsic structure is expected to modify the crystal lattice, generate defects, and promote surface activity towards OER.[1,2] Moreover, it can improve the charge carrier concentration and transportation, reduce the recombination rate, and tune the bandgap structure in the case of PEC materials.[3] In addition to doping to change bulk structural properties, another proposed research is utilizing single-atom catalysts, an emerging new class of materials giving potential to maximize the use of highly active elements on the atomic scale and significantly promote the active sites on the surface.[4] Otherwise, besides annealing, another post-synthesis procedure, for example, plasma treatment, offering new opportunities to modify surface morphology and composition to improve OER performance, can be considered to develop efficient (photo)electrocatalysts.[5–7]

7.2.2. Advanced material characterization technique

To efficiently engineer active and stable acidic OER electrocatalysts, it is imperative to understand the catalytic process and corrosion/dissolution. In-situ spectroscopy, such as X-ray photoelectron spectroscopy (XPS), X-ray absorption spectroscopy (XAS), Raman spectroscopy, and Fourier-transform infrared spectroscopy (FTIR), have been widely employed to study the catalytic processes, enabling observation of real-time changes in catalysts under actual reaction conditions.[8–13] The comprehensive study with these techniques is expected to shed light on the restructures, the adsorbed species and reaction intermediates, surface chemical states, and compositions of catalysts.[8–13] This information is beneficial to engineer the active sites, reduce the deactivation process, and promote the activity and stability of OER electrocatalyst.

In terms of stability, one of the most effective systems for tracking the dissolved metal ions from catalysts is the electrochemical scanning flow cell outlet coupling with an online inductive plasma mass spectrometer or gas chromatography during the reaction.[14,15] Investigation of the dissolution process allows for a detailed understanding of the deactivation of catalysts, which plays a crucial role in evaluating the stabilization strategy for acidic OER catalysts. Despite these advantages of

in-situ techniques, there remained challenges relating to the influence of aqueous reaction environment, extreme pH, and the generation of bubbles during the reaction. More effort should be put into designing devices, instruments, and general characterization methods to meet such needs.

7.2.3. Industrial-scale application

Despite the advancements of engineering acidic stable OER electrocatalysts in laboratory setup, the practical application possibility needs to be determined in the similar real water electrolyzer, PEMWE and more industry-relevant conditions (($j \geq 0.5$ A cm^{-2}, temperature in range 60 – 80 ^{o}C).[16,17] As such, the further studies should investigate our proposed stabilization strategies in the real-world membrane electrode assembly (MEA) cell for PEMWE applications.[18–20] Moreover, the scaling process and its effect on the stability and activity of acidic OER electrocatalysts in the PEMWE should also be considered.[16,21]

Regarding photoelectrocatalysts, further research can aim to conduct the test in the integrated and compact electrolyzer. One of the most proposed systems is the PEM (polymeric electrolyte membrane)-PEC cell, inspired by the fuel cell reactor design.[22] This system is utilized an ionically conductive polymeric membrane as a separator and support for two (photo)electrodes in PEC cell, which are appropriate to both alkaline and acidic conditions.[23,24] It is more practical for continuous operation than the conventional H-cell, which is usually applied on a laboratory test, making it easier to implement in large-scale applications and utilize natural solar energy.[25] Moreover, another appealing application of PEM-PEC devices is the H_2 production in air-based operation, which is expected to harvest water as humidity in ambient conditions.[26] The proposed concept offers a very portable system, limits issues relating to the liquid electrolytes and operation costs, and promotes the effectiveness of the PEC system. However, the transition from aqueous to vapor-phase reaction is still challenging, garnering great interest in recent years.[27]

7.3. References

[1] Z. Chen, X. Duan, W. Wei, S. Wang, B. J. Ni, *Nano Energy* **2020**, *78*, 105392.

[2] N. Wang, P. Ou, R. K. Miao, Y. Chang, Z. Wang, S.-F. Hung, J. Abed, A. Ozden, H.-Y. Chen, H.-L. Wu, J. E. Huang, D. Zhou, W. Ni, L. Fan, Y. Yan, T. Peng, D. Sinton, Y. Liu, H. Liang, E. H. Sargent, *J. Am. Chem. Soc.* **2023**, *145*, 7829.

[3] B. Yao, J. Zhang, X. Fan, J. He, Y. Li, *Small* **2019**, *15*, 1803746.

[4] W. H. Lee, Y. J. Ko, J. Y. Kim, B. K. Min, Y. J. Hwang, H. S. Oh, *Chem. Commun.* **2020**, *56*, 12687.

[5] M. Cui, R. Guo, F. Wang, Y. Zhou, W. Zhao, Y. Liu, Q. Ou, S. Zhang, *Small* **2024**, DOI 10.1002/smll.202405567.

[6] Z. Wang, Y. Zhang, E. C. Neyts, X. Cao, X. Zhang, B. W. L. Jang, C. J. Liu, *ACS Catal.* **2018**, *8*, 2093.

[7] J. Horlyck, A. Nashira, E. Lovell, R. Daiyan, N. Bedford, Y. Wei, R. Amal, J. Scott, *Materials (Basel).* **2019**, *12*, 1.

[8] S.-Y. Hong, Z.-C. Yao, X. Cheng, Z. Jiang, T. Tang, J.-S. Hu, *J. Phys. Chem. C* **2024**, *128*, 17219.

[9] T. Liu, C. Chen, Z. Pu, Q. Huang, X. Zhang, A. M. Al-Enizi, A. Nafady, S. Huang, D. Chen, S. Mu, *Small* **2024**, *20*, 1.

[10] S. Zuo, Z. Wu, H. Zhang, X. W. (David) Lou, *Adv. Energy Mater.* **2022**, *12*, DOI 10.1002/aenm.202103383.

[11] L. Liu, W. Li, X. He, J. Yang, N. Liu, *Small* **2022**, *18*, 1.

[12] Q. Ji, B. Tang, X. Zhang, C. Wang, H. Tan, J. Zhao, R. Liu, M. Sun, H. Liu, C. Jiang, J. Zeng, X. Cai, W. Yan, *Nat. Commun.* **2024**, *15*, 1.

[13] M. Chen, D. Liu, L. Qiao, P. Zhou, J. Feng, K. W. Ng, Q. Liu, S. Wang, H. Pan, *Chem. Eng. J.* **2023**, *461*, 141939.

[14] O. Kasian, S. Geiger, K. J. J. Mayrhofer, S. Cherevko, *Chem. Rec.* **2019**, *19*, 2130.

[15] I. Reichmann, V. Lloret, K. Ehelebe, P. Lauf, K. Jenewein, K. J. J. Mayrhofer, S. Cherevko, *ACS Meas. Sci. Au* **2024**, *4*, 515.

[16] Q. Wang, Y. Cheng, H. B. Tao, Y. Liu, X. Ma, D. Li, H. Bin Yang, B. Liu, *Angew. Chemie Int. Ed.* **2023**, DOI 10.1002/anie.202216645.

[17] X. M. C. Ta, T. Trần-Phú, T. K. A. Nguyen, M. Chatti, R. Daiyan, *Appl. Phys. Rev.* **2024**, *11*, DOI 10.1063/5.0200438.

[18] R. T. Liu, Z. L. Xu, F. M. Li, F. Y. Chen, J. Y. Yu, Y. Yan, Y. Chen, B. Y. Xia, *Chem. Soc. Rev.* **2023**, *52*, 5652.

[19] Z. Liu, X. Wang, G. Xie, J. Ge, *Chem. Eng. J.* **2024**, *499*, 155901.

[20] S. S. Jeon, W. Lee, H. Jeon, H. Lee, *ChemSusChem* **2024**, *17*, DOI 10.1002/cssc.202301827.

[21] F. Meharban, C. Lin, X. Wu, L. Tan, H. Wang, W. Hu, D. Zhou, X. Li, W. Luo, *Adv. Energy Mater.* **2024**, *14*, 1.

[22] T. Stoll, G. Zafeiropoulos, M. N. Tsampas, *Int. J. Hydrogen Energy* **2016**, *41*, 17807.

[23] D. O. B. Apriandanu, R. M. Surya, K. Beppu, F. Amano, *ACS Appl. Energy Mater.* **2023**, *6*, 10736.

[24] C. X. M. Ta, C. Akamoto, Y. Furusho, F. Amano, *ACS Sustain. Chem. Eng.* **2020**, *8*, 9456.

[25] T. A. Kistler, M. Y. Um, P. Agbo, *J. Electrochem. Soc.* **2020**, *167*, 066502.

[26] F. Amano, A. Shintani, H. Mukohara, Y.-M. Hwang, K. Tsurui, *Front. Chem.* **2018**, *6*, 1.

[27] F. Amano, R. M. Surya, S. P. Singh, *ChemElectroChem* **2024**, *11*, DOI 10.1002/celc.202300646.